Université de Liège

Faculté des Sciences **Département d'Astrophysique, Géophysique et Océanographie**

Exoplanet imaging with mid-infrared vector vortex coronagraphs: design, manufacture, validation and first light of the annular groove phase mask

THÈSE

présentée pour l'obtention du diplôme de

Docteur en Sciences

par

Christian Delacroix

Soutenue publiquement le 25 juin 2013 devant le Jury composé de :

Président :	Pr. Marc-Antoine Dupret
Directeur de thèse :	Pr. Serge Habraken
Examinateurs :	Dr. Olivier Absil
	Dr. Mikael Karlsson
	Dr. Markus Kasper
	Dr. Cédric Lenaerts
	Dr. Dimitri Mawet
	Pr. Jean Surdej

HOLOLAB - Optics Laboratory

Mis en page avec la classe thloria.

Acknowledgments

Je tiens tout d'abord à remercier chaleureusement mon promoteur de thèse, le Professeur Serge Habraken, pour m'avoir conseillé, guidé, et encouragé avec enthousiasme au cours de ces cinq dernières années, tout en me laissant une grande liberté et en me témoignant de son entière confiance. J'ai eu l'honneur de bénéficier de ses précieuses qualités de pédagogue, associées à son profond sens de l'humour. C'est en grande partie grâce à Serge que mes années de doctorat à Hololab constituent pour moi un souvenir professionnel exceptionnel.

Mes plus profonds remerciements vont également au Professeur Jean Surdej, que je considère avec beaucoup de respect comme un mentor, tant sur le plan scientifique que sur le plan humain, et ce depuis mes premières années à l'Université de Liège où il encadra mon stage de fin d'étude. Jean, tes encouragements et ton précieux soutien ont été, depuis le départ, un réel moteur pour ma motivation. Je t'en remercie du fond du cœur.

Je tiens également à adresser mes plus chaleureux remerciements à Olivier Absil et Dimitri Mawet, deux chercheurs Liégeois admirables, et astrophysiciens exceptionnels, de m'avoir encadré durant cette thèse, et d'avoir répondu favorablement chaque fois que j'ai sollicité leur aide.

(Un petit mot en anglais à l'équipe suédoise d'Uppsala)

My utmost gratitude also goes to the Swedish team of the Ångström laboratory, Mikael Karlsson and Pontus Forsberg, with whom I had the chance to work on diamond structures. Thank you for your friendly welcome during my scientific stay at the Uppsala University! I am totally indebted to you for having believed in our project.

Je remercie également tous ceux qui ont contribué à mener le projet AGPM à si bon terme. Merci à Denis, Cédric, Loïc et Karl du Centre Spatial de Liège, pour leur implication dans la fabrication et la métrologie des composants. Merci à Richard Olivier et Jean-Franҫis Fagnard pour la réalisation des montures et les tests cryogéniques. Merci à Valentin Christiaens, Pierre Baudoz, Anthony Boccaletti, et le Professeur Jacques Baudrand de m'avoir offert la possibilité de tester des coronographes au laboratoire de l'Observatoire de Paris. Enfin, merci à Eric Pantin, Vincent Moreau, Julien Girard, Julien Milli, et bien sûr Olivier Absil et Dimitri Mawet, ainsi que toute l'équipe de l'ESO au Chili, qui ont permis la validation de l'AGPM sur le ciel.

Outre mes collaborateurs directs, plusieurs personnes ont joué un rôle indirect mais crucial à mes yeux. C'est le cas, par exemple, de mes collègues à Hololab avec qui j'ai passé d'excellents moments, et qui sont pour la plupart devenus des amis : Caroline, Georges, Grégory, Marc, Pascal, Pierre, et surtout Fabian qui partagea mon bureau durant ces cinq dernières années. Fabian, tu m'as soutenu quand j'en avais besoin, et tu as toujours été à mon écoute avec beaucoup d'intérêt. J'ai de la chance d'avoir un ami comme toi.

Il y a aussi tous mes amis de Bruxelles, Liège et Toulouse, qui ont pâti de mon manque de disponibilité ces derniers mois, et que je remercie pour leur patience et leur compréhension : la bande des SUPAERO's, Alex, Bastien, Nico et Simon, mes copains du foot, mes camarades de la Marre, mes amis musiciens, sans oublier Nico et Cathia (merci pour cette belle année de cohabitation). En particulier, je voudrais remercier mon plus fidèle ami depuis l'enfance, Quentin, qui a

toujours su trouver le juste dosage avec moi. Quentin, je pense ne pas me tromper en disant que tu es la personne qui me connaît le mieux aujourd'hui. Tu as été là pour me soutenir, en véritable ami, dans des moments qui pour moi, tu le sais, n'ont pas été faciles. Je t'en suis éternellement redevable.

Enfin, il y a ma chère famille que je remercie pour son soutien inconditionnel, et son support moral et logistique. Merci à ma Bonne-Mamy pour ses nombreux encouragements. Merci aussi à mon oncle Etienne, qui a su m'aiguiller lorsque je perdais le cap. Enfin, merci infiniment à mes deux frères, Oliver et Antoine, qui ont participé, et ce tout au long de mes études secondaires et universitaires, à la relecture de certains de mes travaux. Mes chers frérots, je vous promets que c'est la dernière fois que je vous fais relire une thèse !

(Un petit mot en polonais à ma famille maternelle)

Ze szczególną przyjemnością pragnę wyrazić moje podziękowania członkom mojej Rodziny, moim przyjaciołom i moim kuzynom. Moja ukochana Babcia, mój kochany Wujek Heniek, i mój kochany Papa Olivier! Uczucie, jakim mnie obdarzali było dla mnie nauką poczucia moralności i motywacji. Wreszcie, chciałbym z głębi serca podziękować mojej kochanej Mamusi, która nieustannie dodawała mi otuchy i odwagi w czasie moich studiów. Mamusiu, bez Ciebie nigdy nie napisałbym tej pracy!

Je ne saurais terminer cette liste sans remercier la personne qui m'est la plus chère au monde, ma petite Claire (alias Chloupy), et pas uniquement pour la superbe couverture de ce manuscrit, réalisée par la meilleure des graphistes ! Claire, ton soutien, ta douceur et ton affection, quotidiennement manifestés, ont contribué à la rédaction de ma thèse bien plus que tu ne pourrais l'imaginer. J'admire la patience et l'indulgence dont tu as fait preuve durant ces derniers mois. Je t'aime, Claire. Tu es une femme exceptionnelle, et je voudrais te dédier cette thèse.

This research was supported by a fellowship from the Belgian National Science Foundation ("Boursier F.R.I.A.") and by the University of Liège.

Contents

Notations and acronyms

Atmospheric windows

J band	from 1.15 to 1.4 μm
H band	from 1.5 to 1.8 μm
K band	from 2.0 to 2.4 μm
L band	from 3.5 to 4.1 μm
M band	from 4.5 to 5.1 μm
N band	from 8 to 13 μm

Units

arcmin (or $'$)	minute of arc (2.90888×10^{-4} radian)
arcsec (or $''$)	second of arc (4.848137×10^{-6} radian)
mas	milli-arcsec (10^{-3} arcsec)
AU	Astronomical Unit (1.495978×10^{11} m)
pc	parsec (3.085678×10^{17} m)
Jy	Jansky (10^{-26} W m^{-2} Hz^{-1})
Myr	Mega-years (one million years)
Gyr	Giga-years (one billion years)
zodi	density unit for dust disks, equivalent to the solar zodiacal disk

Notations

$M_\odot$	Mass of the Sun (1.98892×10^{30} kg)
$R_\odot$	Radius of the Sun (6.96×10^{8} m)
$L_\odot$	Luminosity of the Sun (3.846×10^{26} W)
$M_{\rm Jup}$	Mass of Jupiter (1.8987×10^{27} kg)
$R_{\rm Jup}$	Radius of Jupiter (7.1492×10^{7} m)
$M_\oplus$	Mass of the Earth (5.97370×10^{24} kg)
$R_\oplus$	Radius of the Earth (6.37814×10^{6} m)

Acronyms

ACS	Advanced Camera for Surveys (HST)
ADI	Angular Differential Imaging
AGPM	Annular Groove Phase Mask
AO	Adaptive Optics
APP	Apodizing Phase Plate
ARG	Antireflective Grating
CoRoT	COnvection ROtation and planetary Transits
CSL	Centre Spatial de Liège
DLW	Direct Laser Writing
E-ELT	European Extremely Large Telescope
EGP	Extrasolar Giant Planet
EPICS	Exo-Planet Imaging Camera and Spectrograph (E-ELT)
ESA	European Space Agency
ESI	Earth Similarity Index
ESO	European Southern Observatory
FQPM	Four Quadrant Phase Mask
GMT	Giant Magellan Telesscope
GPI	Gemini Planet Imager (Gemini South telescope)
HWP	Half-Wave Plate
HST	Hubble Space Telescope
IWA	Inner Working Angle
JWST	James Webb SpaceTelescope (NASA/ESA project)
LBT	Large Binocular Telescope
LCP	Liquid Crystal Polymer
LOCI	Locally Optimized Combination of Images
METIS	Mid-infrared E-ELT Imager and Spectrograph (E-ELT)
NACO	Nasmyth Adaptive Optics System & COude Near Infrared CAmera (VLT)
NASA	National Aeronautic and Space Administration
NIL	Nano-Imprint Lithography
OGLE	Optical Gravitational Lensing Experiment
PALC	Prolate Apodized Lyot Coronagraph
PDMS	Polydimethylsiloxane
PIAAC	Phase-Induced Amplitude Apodization Coronagraph
PMMA	Polymethyl Methacrylate
PSF	Point Spread Function
SDI	Spectral Differential Imaging
SG	Subwavelength Grating
SNR	Signal-to-Noise Ratio
SPHERE	Spectro Polarimetric High contrast Exoplanet REsearch (VLT)
TMT	Thirty Meter Telescope
TPF	Terrestrial Planet Finder (NASA project)
VLT	Very Large Telescope (ESO)
VVC	Vector Vortex Coronagraph
XAO	Extreme Adaptive Optics
ZOG	Zeroth Order Grating

Preface

Images of broken light which dance before me like a million eyes,
They call me on and on across the universe
Thoughts meander like a restless wind inside a letter box,
They tumble blindly as they make their way
Across the universe.

The Beatles, "Across The Universe" (1969)

Are we alone in the universe?

"The right tool for the right job". That is what my Polish uncle Heniek used to tell me so many times when I was a child. At that time, he was living with us most of the year, to help my mother with raising the children and running the house. He would repair broken things, repaint walls here and there, and give our garden a brand new look in early spring. Often, my brothers and I would assist him, most of the time against our will, but still learning a lot without realizing it. Obviously, we preferred to play in the garden, rather than mowing the lawn or pruning shrubs. As soon as we got the chance, we would leave the house and go play in the forest. What we liked most was adventure, discovering new places to build our huts, and invent our own world. Years have passed, many things have changed, but I have kept this taste for adventure.

In his remarks at a Caltech YMCA lunch forum in 1956, Richard Feynman defined the scientific spirit as "the spirit of (...) the adventure into the unknown, an unknown which must be recognized as being unknown in order to be explored; the demand that the unanswerable mysteries of the universe remain unanswered; the attitude that all is uncertain; to summarize it – the humility of the intellect." For thousands of years, this taste for adventure has led mankind to take many small steps, sometimes even giant leaps, towards understanding and exploring the unknown. With the development of technologies, explorers have traveled around the Earth, discovered all the continents and islands, and climbed the highest mountains. Nowadays, airplanes cross the oceans in a few hours, astronauts can reach the moon within two or three days, traveling at speeds faster than 39,000 km/h, and automated motor vehicles are exploring the surface of the planet Mars.

The interest of mankind in observing other planets did not start in the 20th century. The planets and moons of our solar system had been observed much earlier, thanks to optics and astronomy. It started in the early 17th century, with a very small telescope constructed by Galileo to look at Jupiter, Saturn, Neptune, and some of their satellites. Since then, astronomy has come a long way. After almost 400 years of innovation, we went from Galileo's 4 cm diameter telescope to 8-10 meter wide telescopes. These are built in very optimal places, like on top of mountains or extinct volcanoes, where the air has a lower density due to altitude. Indeed, air is a serious issue for ground-based telescopes, because the light going through the atmospheric turbulence becomes blurred, and so become the images. Engineers were even able to develop satellite telescopes that go above the atmosphere like the Hubble Space Telescope. Although they are limited in size to a few meters, these space telescopes provide very stable images. Our way of doing science has also considerably evolved since the time of Galileo. First astronomers were using their eyes to look through the telescope, and their pen and book to sketch their observations. Later on, with the progress in photography techniques, they were placing photographic plates at the focal plane of the telescope, which were then developed in a darkroom to obtain an image of the observed object. Advances then continued increasingly with the advent of the electronic era. Astronomers now have very detailed digital images that they can process and analyse in much detail with computers. We therefore can have beautiful pictures of some of the many objects that make their way across the universe.

The continuous progress in astronomy has enabled the imaging of increasingly fainter objects in the sky. While major discoveries have provided answers to some existential questions (like the age of our universe, or how our solar system was created), many more remain unanswered. Among them, one of the greatest questions that has always faced humankind: Are we alone in the universe? For centuries, scientists and philosophers supposed the existence of planets outside our solar system. The Greeks were already questioning the fact that they were living on Earth, and they were wondering if a world like ours existed somewhere else in the universe, or if they were really alone. There was, at that time, absolutely no way of observing them, or even simply detecting their presence. Could there be some other worlds around the many stars of the sky? And would they be comparable to the planets of our Solar System? Today, the landscape has changed. Instead of just looking up at the sky with the naked eye, we have all these big telescopes to observe those extrasolar planets, or exoplanets, and address a major question of modern astronomy: the existence of life beyond Earth.

Objectives and outline of this work

The present thesis is dedicated to the development of a type of astronomical instrument called a coronagraph. Coronagraphy is a high contrast imaging technique that has wind in its sails. Techniques of coronagraphy are numerous; the present work concentrates on a specific concept called the AGPM, based on microstructured subwavelength gratings. Such gratings have highly compelling optical properties, and are specially appropriate for mid-infrared applications where they represent an original and almost unique solution of their kind. In this context, we first used these subwavelength gratings to develop mid-infrared half-wave plates which are optical devices that alter the polarization of light. Based on these half-wave plates, we started to develop coronagraphs. This dissertation is organized into three parts, each containing two chapters. The first part of this work presents the scientific context and the objectives of exoplanet high-contrast imaging (Chap-

ter 1), and describes the selected technological route given the panel of existing coronagraphic techniques (Chapter 2). The second part is dedicated to the use of subwavelength gratings for the development of both half-wave plates (Chapter 3) and AGPM coronagraphs (Chapter 4), including design, manufacturing and performance simulations. The third and last part of this work presents the AGPM validation results obtained in the laboratory (Chapter 5) as well as the installation and first light of the AGPM at an 8 meter telescope (Chapter 6).

Part I

The need for small inner working angle broadband coronagraphs

1

A brief history of the hunt for exoplanets

Contents

Abstract. *The last twenty years have seen major advances on multiple fronts in the detection of extrasolar planets. Discoveries of exoplanets have dramatically increased, bringing some answers to the many questions raised about the formation of our solar system, and leading to various evolutionary models. Since the discovery in the 1990s of the first exoplanets, high contrast imaging techniques have made their way as well. Direct imaging of exoplanets that was just a mirage a few years ago, is gradually becoming a reality. As of today, only a handful of systems have been imaged, mostly under specific conditions of moderate contrast and/or large angular separation between the planets and their host star. Most of these breakthrough results have been made possible thanks to the advent and continuous improvement of adaptive optics systems and data reduction methods. In this broad context, coronagraphy has, more than ever, a key role to play in order to provide the means necessary for imaging Earth-size planets, and try to answer the recurring question of the possible presence of life outside the solar system.*

1.1 Starting the hunt

In the late 1980s – less than a quarter of a century ago – the existence of extrasolar planets in the universe was yet to be proven. Of course, astronomers did suspect that some stars may be analogs of our own Sun. Along with this recognition came the hypothesis that planets could orbit these distant Suns, and that their interaction could probably be observed from Earth with telescopes. This started the hunt for exoplanets.

The very first confirmed detection occurred in 1992, with the discovery of several terrestrial-mass exoplanets around a pulsar with the radio-telescope of Arecibo (Wolszczan & Frail 1992). Three years later, the first detection of an Extra-solar Giant Planet (EGP) was confirmed (Mayor & Queloz 1995), a Jupiter-like planet orbiting the nearby Sun-like star 51 Pegasi, 40 light-years away. These discoveries led to unprecedented enthusiasm in the scientific community, for all knew that these first planets were only the tip of the iceberg. Since then, the number of exoplanets discovered every year is growing exponentially. As of May 2013, nearly 900 planets have been discovered orbiting around 700 stars (see Figure 1.1). Many others are to follow.

Exoplanets can be discovered by use of several methods, which differ by whether the planet is actually imaged or not. At first, astronomers did not image the planets but simply detect their presence by indirect methods.

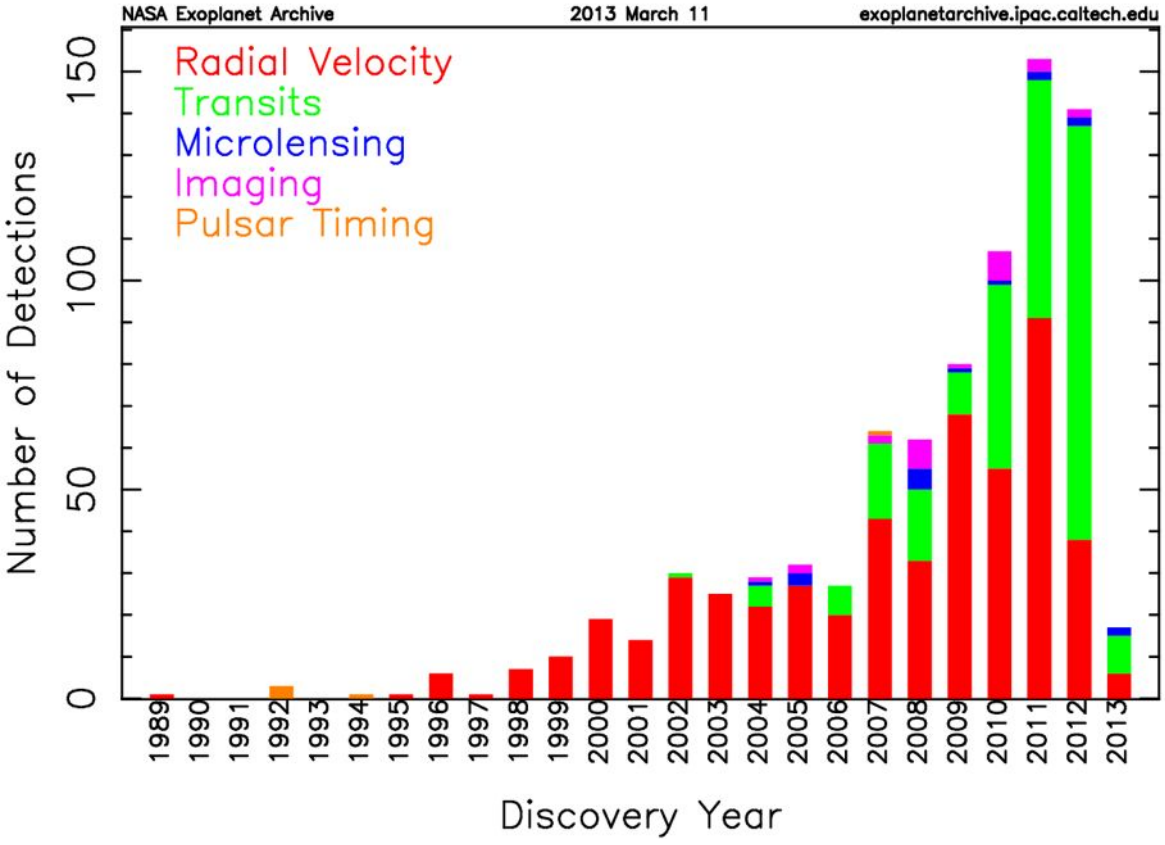

Figure 1.1: Number of confirmed detections of extrasolar planets using various discovery methods (see Section 1.2), as a function of the year of detection. The progression is exponential, as it doubles every three years. Note: The planet detected in 1989 was only confirmed several years later. © NASA Exoplanet Archive.

1.2 Indirect detection

Unlike stars, planets do not emit their own light in the visible regime. They only reflect light from their parent star, exactly like the Moon reflects light from the Sun. At a distance of a few tens of light years from us, the closest exoplanets are extremely dim light sources. They are terribly difficult to detect due to their faintness. In addition, exoplanets are completely obscured by their extremely bright host stars. As a comparison, observing directly an exoplanet would be as hard as trying to distinguish the feeble glow of a firefly laid on the edge of a lighthouse, from a distance of several hundreds of kilometers. For these reasons, almost all exoplanets have been detected so far by indirect means. *Radial velocity*, *Astrometry*, *transits*, *microlensing*, and *pulsar timing* are the main indirect methods. These will be briefly described below.

Radial velocity and astrometry

With more than 500 confirmed detections, the radial velocity method is the first and most commonly used technique for extrasolar planet detection. As the star moves in the small orbit resulting from the gravitational attraction of a planet, it will move towards Earth and then away. This perpetual back and forth movement affects the radial velocity of the star, which can be easily observed as the star's spectrum gets redshifted or blueshifted due to the Doppler effect (see Figure 1.2, left). The star spectrum is blueshifted while it moves towards Earth, and it is redshifted while it moves away. If these wavelength shifts are periodically observed, this is evidence for the presence and influence of a companion. In some very rare cases, one uses astrometry to measure the radius of the tiny circular orbit of the star. Up to now, this technique has provided only a few confirmations of radial velocity detections, and one new detection (Muterspaugh et al. 2010). One of the interesting things about the astrometry method is that it favors large orbits. The larger the orbit of the planet, the faster the motion of both the star and the planet. This is exactly the opposite of what happens with the radial velocity method, which favors small orbits where the velocity is higher.

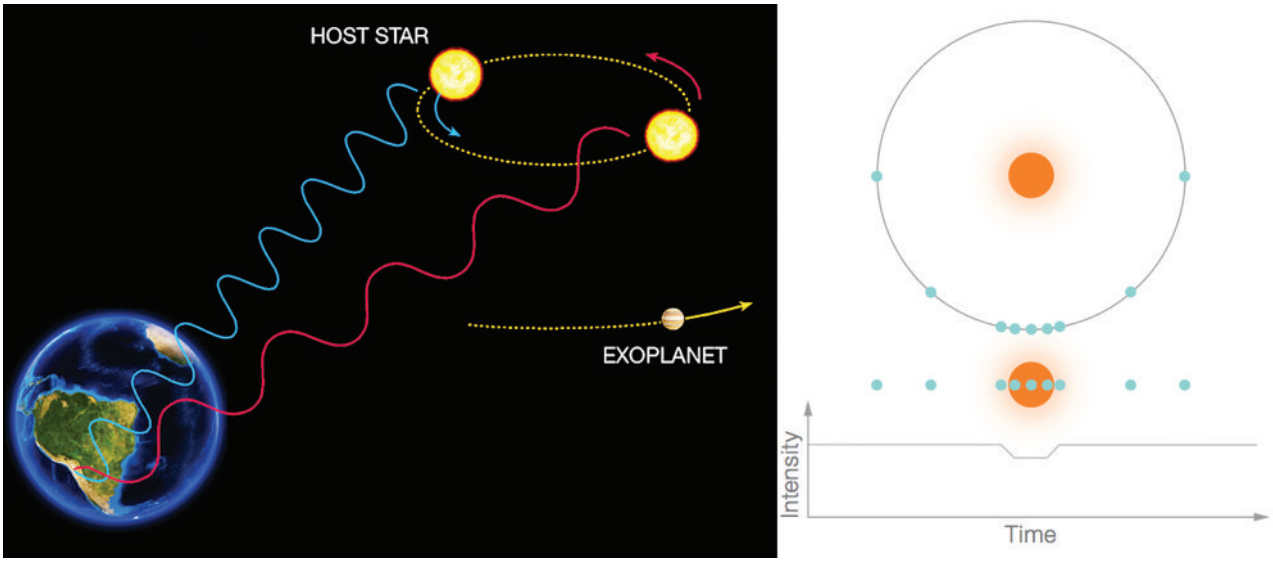

Figure 1.2: Illustration of the two principal indirect detection methods. Left, the radial velocity method: the shift of spectral lines of the star is changing due to the Doppler effect induced by a planet's gravitational pull. Right, the transit method: the brightness of the star is changing due to a planet passing in front of it. © ESO Press Releases.

Transits

In some particular configurations, an exoplanet can transit periodically on the line of sight between Earth and its host star, masking some of the starlight and creating very small attenuations in the brightness of the star (see Figure 1.2, right). Up to now, measuring these phenomena has resulted in the detection of more than 300 exoplanets, and many more are awaiting for confirmation. While radial velocity measurements provide information about the lower limit for the mass of an exoplanet, this photometric technique can determine its radius, since the amount of attenuated starlight depends on the relative size of the planet with respect to that of the star. Hence, combining the two methods makes it possible to determine the density of the planet. In case of a low density, the planet is gaseous, mainly composed of hydrogen and helium. At an intermediate level of density, the planet is supposed to have water as a major constituent. The very high densities are attributed to rocky planets, such as our Earth. During the transit, some of the starlight might also be absorbed by the planet's atmosphere, which gives insight on its composition (see Section 1.4.3, *Searching for biosignatures*). Thanks to this technique, scientists have been able to detect molecules in eight different exoplanets (e.g., Brown et al. 2002; Knutson et al. 2007; Charbonneau et al. 2002, 2008, 2009).

Microlensing

Another indirect detection method is microlensing. The gravitational field of a star may act as a lens, amplifying the light of a distant background stellar object (e.g., a star, a quasar). If a planet is orbiting around the foreground lensing star, then this planet's own gravitational field can produce a detectable contribution to the lensing effect (see Figure 1.3). The gravitational lensing effect occurring while two stars are almost exactly aligned is usually very brief, lasting for weeks or even a couple of days, since the two stars and Earth are all moving relatively to each other. In order not to miss the window, a very large number of distant stars must be continuously monitored. The first detection of an exoplanet by means of the microlensing is attributed to Bond et al. (2004), within the Optical Gravitational Lensing Experiment (OGLE) project (Udalski et al. 2003). This technique has led to the discovery of 21 planets so far.

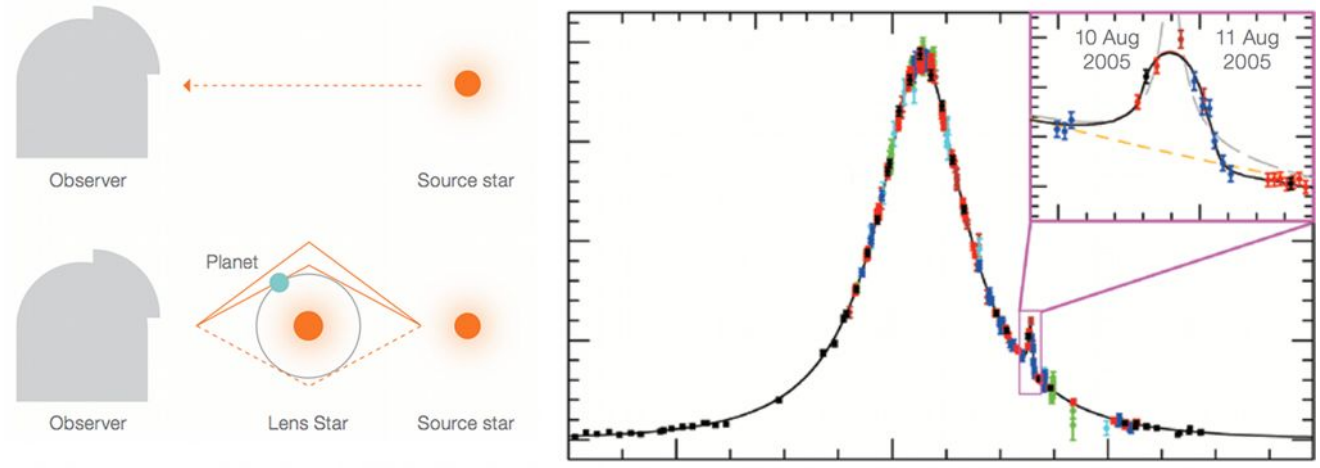

Figure 1.3: Illustration of the microlensing detection method. Left: Gravitational lensing caused by the presence of a star and an exoplanet. Right: Light curve of OGLE-2005-BLG-390. © ESO Press Releases.

Pulsar timing

The last detection method is the pulsar timing, with 15 confirmed detections so far. Pulsars are fast-spinning neutron stars. They are regularly emitting radio waves. The presence of a planet companion affects the timing of the pulses, which can be detected with high sensitivity. The pulsar timing method is capable of detecting planets with a very small mass (Silvotti et al. 2007; Lee et al. 2009). However, pulsars are pretty rare and very far away, and the high-energy radiation makes life on these planets very unlikely. For this reason, the pulsar timing method is experiencing a much lower craze than the radial velocity or the transit methods.

The four methods that we have described hereabove led to the detection of hundreds of exoplanets. As we will see in the next section, these discoveries have taught us a lot about the formation of our solar system. It appears that most of the planets discovered so far are very different from those of our own solar system.

1.3 Brave new *Giant* worlds

A large number of the exoplanets found so far are gas giant planets, similar in size to Jupiter, but orbiting very close to their host star. These *Hot Jupiters* are easy to detect using transit or radial velocity measurements because of their high mass and short orbital period (see Figure 1.4). At the beginning, such hot extra-solar giant planets (hot-EGPs) were totally new to our under-

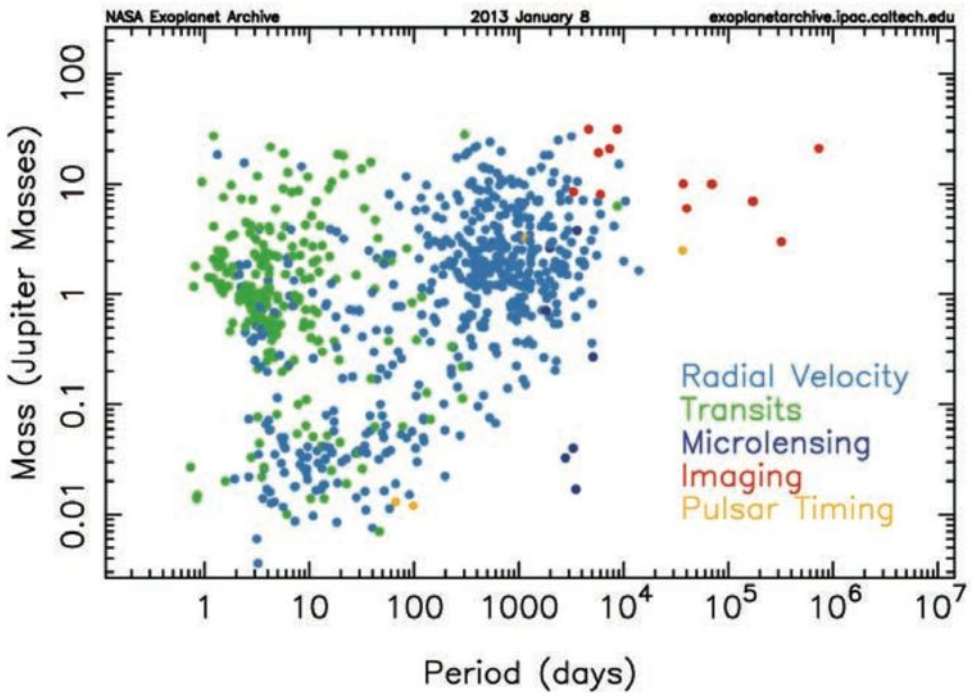

Figure 1.4: Confirmed exoplanets separated by their method of discovery and plotted with bilogarithmic scale on the axes, according to their orbital period and mass, with $1M_{\oplus} \approx 0.003M_{\mathrm{Jup}}$. Mainly Jupiter-size planets, and some super-Earths populate this diagram. Transit detections are concentrated on short period orbits. © NASA Exoplanet Archive.

standing of the formation of planets. For decades, the observation and classification of objects in our solar system had led to the conclusion that the inner terrestrial planets are small, rocky, and in relatively short orbits. In contrast, the outer jovian planets are large, have not only rocks but also much ice and gas, and are in wider orbits. The orbits of both terrestrial and jovian planets are more or less circular (actually slightly elliptical) and co-planar.

According to the classical theory of planetary formation (Pollack 1984), the planets form from a disk of material around the central star, and are created out of a collapsing cloud, some parts of which are rotating preventing them from collapsing. After a while, the central star is surrounded by a disk basically consisting of the same material as the star. It has much gas, hydrogen (H) and helium (He) in particular, some water (ice), carbon (C), nitrogen (N), oxygen (O). It also contains some heavier elements such as silicon (Si) and iron (Fe), that can form dust and rocks. In the disk, things gradually stick together. Molecules and atoms run into each other forming dust grains or ice crystals, and these continue running into each other, gradually forming bigger objects called *planetesimals*. The planetesimals bump into each other and stick together, until everything along each orbit coalesce into one large object per orbit. During this process, the ellipticity of these orbits tend to cancel out, and they all end up almost circular and co-planar. However, there is an expected difference between how this works out in the inner part and the outer part of the planetary system. In the inner system, ices evaporate and almost all the gas is pushed outward by the central star, leaving only rocky materials. In the outer system, ices are frozen and behave just like rocks, which means that planets are substantially more massive. They have enough gravity to retain gas as well, and become gaseous giant planets. This process lasts about 10 Myr (Pollack et al. 1996). According to Sasselov & Lecar (2000), it is only behind the dividing line, the so-called *snow line* (i.e., in the outer disk), that the $\sim$10 $M_\oplus$ proto-planetary cores find enough gas to accrete. The position of the snow line is determined by the temperature, hence by the luminosity of the star. Therefore, gas giants are not expected to be at the same distance away from a star, but at the place where the temperature is the same.

The discovery of EGPs appearing at locations where many scientists thought they could not exist, led to various models including planetary migration theory (Lin et al. 1996). In the following years, the quest for exoplanets led to many other discoveries, such as, e.g., the correlation between metallicity and planet occurrence (Boss 2002), or, more recently, the existence of planets with retrograde orbits with respect to the rotation of their parent star (Queloz et al. 2010). Thanks to new exoplanet discoveries, we understand that our solar system is not a universal model. A better picture of planetary formation is slowly emerging.

1.4 The search for *Earth 2.0*

Gaseous giant planets are unsuitable for hosting life as we observe it on our planet Earth, even microorganisms that can develop in extreme conditions. Since the classical paper proposed by Wald (1964), astrobiologists have tried to define more precisely the origin of life (Gilbert 1986; Maher & Stevenson 1988), addressing the question of whether life exists beyond our planet, and if it does, how humans can detect it. The principal established conditions for life on Earth are listed below.

(a) A source of **energy**. Living systems are energy transformers. This means that all organisms need to consume and produce energy. This energy can be taken from different sources, like radiation and photochemistry (both originating from the Sun light), but also minerals or reduced gases, in total absence of light (Peck Jr 1968; Matin 1978).

(b) A suitable **environment**. For life to develop on a planet, the radiation of the star is certainly essential, since it is a free source of energy. However, the planet also needs protection against some part of the radiation spectrum (X- and gamma-rays; ultraviolet radiation) which is too energetic, and produces photochemical reactions that are lethal for life systems. Such a protection on Earth is provided by the ozone (O_3) layer.

(c) The **elements** needed for metabolism and reproduction. The so-called *biogenic elements* are carbon (C), hydrogen (H), oxygen (O), nitrogen (N), sulphur (S), phosphor (P), monovalent and divalent metals like sodium (Na), potassium (K), magnesium (Mg), calcium (Ca), manganese (Mn), iron (Fe), cobalt (Co), copper (Cu) and zinc (Zn), as well as anions like that of chlorine (Cl^-). In order to determine if an exoplanet is inhabited, one must be able to study the composition of its atmosphere, by observing its spectrum, and to detect the presence of biosignatures, i.e. molecules containing these elements (see Section 1.4.3).

The above criteria are highly impregnated with our Earth-centric point of view. One cannot exclude that some of these conditions may need to be somehow adapted, giving birth to absolutely unthinkable extraterrestrial life forms. However, the most important and crucial condition for life remains the existence of water in a liquid state, and as to our current knowledge, the most likely location for liquid water to exist is on small *Earth-like* rocky planets, orbiting in the inner region of their stellar system.

1.4.1 KEPLER: the great exoplanet harvest

From the ground, one cannot see transits of Earth-size planets because of our turbulent atmosphere. Obviously, the place to look for transits is in space with telescopes such as the Hubble Space Telescope (HST). The problem with the HST is that everybody uses it for various astrophysical programs, and there is a relatively limited amount of time for any particular project. HST was also not perfectly designed for making transit observations. Therefore, new space-based telescopes have been launched for the purpose of making very high precision measurements of the brightness of stars in order to look for transits.

The last five years have encountered great success thanks to two space missions dedicated to the search for Earth-like planets: COROT and KEPLER. The COROT mission (for COnvection ROtation and planetary Transits) is conducted by the French and European space agencies (CNES and ESA). It is the first spacecraft dedicated to the detection of transiting extrasolar planets. Among the 26 confirmed extrasolar planets detected by COROT since its launch in 2006, one was the first potential extrasolar terrestrial planet to be found, with a measured diameter 1.58 times that of Earth (Léger et al. 2009). More recently, the KEPLER space observatory, named after the 17th-century astronomer Johannes Kepler, was launched with the specific mission of detecting

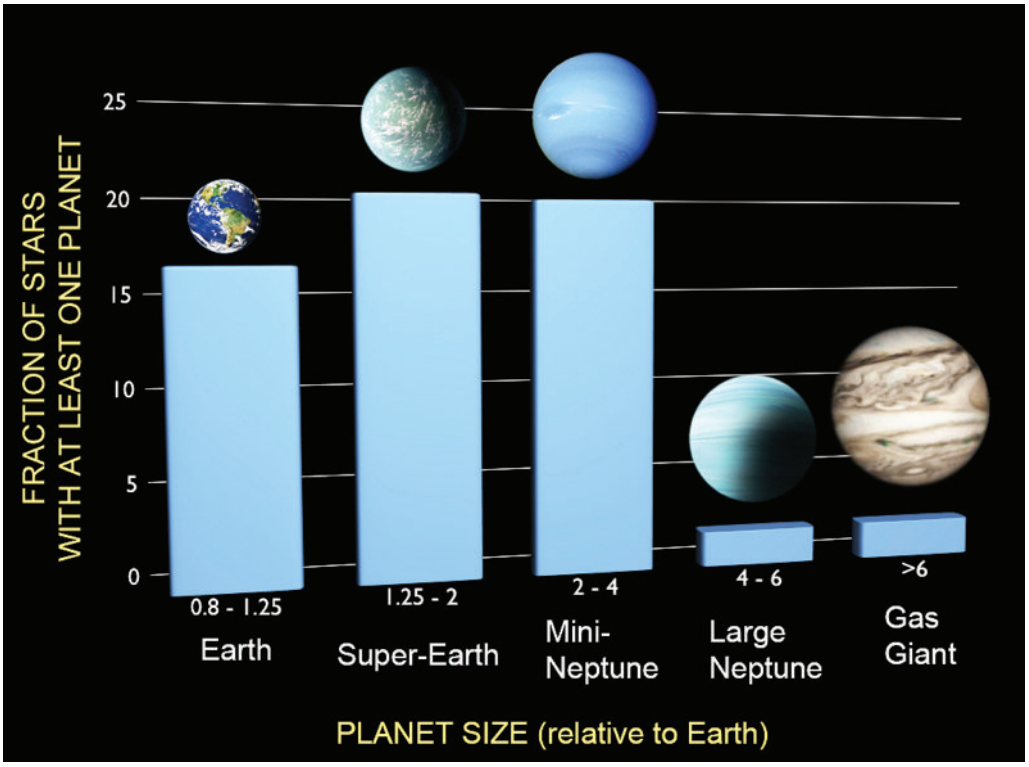

Figure 1.5: The occurrence of planets studied in a tight orbit, resulting from a new analysis of the KEPLER data, function of their size relative to Earth. The diagram shows that about one in six stars have at least one planet between 0.8 and 1.25 $R_\oplus$, about a fourth have a super-Earth (1.25 - 2 $R_\oplus$), and the same fraction have a mini-Neptune (2 - 4 $R_\oplus$). From Fressin et al. (2013a).

dozens of Earth-size extrasolar planets by surveying a close region of our Milky Way galaxy, and statistically evaluate how many of the billions of stars in our galaxy have such planets (Koch et al. 2010; Borucki et al. 2010, 2011). The general problem with transiting planets is that one only sees the ones that are in edge-on systems. Even if many stars have planets, only a small proportion of them show transits. For this reason, KEPLER was designed to look at a hundred thousand of stars.

After only two years of scanning and data processing, the results are breathtaking. KEPLER is literally harvesting exoplanets. In 2010 and 2011, it has detected more than 1200 candidates. And as of January 2013, 1500 more (Burke 2013). A huge volume of data is still under processing and analysis. Several thousand possible detections of exoplanets are awaiting confirmation. In the whole Milky Way galaxy, it is expected that there is at least one planet, on average, orbiting each star. This leads to hundreds of billions of planets (Cassan et al. 2012) and many of these planets are Earth-sized (see Figure 1.5). According to the latest news from the KEPLER's scientist team (Fressin et al. 2013a,b), about 17% of the stars situated in a region of the galaxy close to our Sun, possess an Earth-size planet in a tight orbit of 400 days or less. And 20% of them have a super-Earth. Only a few percent have a gaseous planet in close orbit.

1.4.2 First exoplanets detected in the habitable zone

The number of extrasolar planets grows from year to year, and counting exoplanets might soon become much less attractive. In fact, the real challenge, much more exciting than detecting new worlds, is to find at least one that harbors extraterrestrial life. With the discovery of the first extrasolar planets came the definition of the *habitable zone* (Kasting et al. 1993). The development of life on a rocky planet, with temperatures suitable for liquid water to be present at its surface, requires it to be located in a well defined region of the stellar system. The habitable zone of the majority of stars (i.e., main-sequence stars) is determined primarily by the mass of the star. The smaller (or less massive) the star, the weaker its radiation. Based on previous work by Kasting et al. (1993), and following recent new estimates using updated absorption databases of greenhouse gases (Kasting & Catling 2003; Kopparapu et al. 2013), the habitable zone around different types of main-sequence stars has been updated (see Figure 1.6). In the new model, Earth appears at the very edge of the habitable zone. Some extrasolar planets previously believed to be situated in habitable zones may, in fact, not be. So far, scientists have found some 3000 extrasolar planet candidates, but only a handful of these are situated in the habitable zone.

The first habitable zone candidates were gaseous giants on larger orbits. Although such planets are very unlikely to host life, they might potentially have habitable rocky moons (Williams & Pollard 2002; Barnes & O'Brien 2002; Sudarsky et al. 2003). More recently, exoplanetary science has made an important breakthrough with the discovery of some Super-Earths and Earth-size planets, with the proper orbital characteristics to be potentially habitable (see Figure 1.6). The main potentially habitable planets known as of April 2013 are presented in Table 1.1 with their order of Earth Similarity Index (ESI, Mascaro 2011), which is a function of the planet's radius, density, escape velocity, and surface temperature.

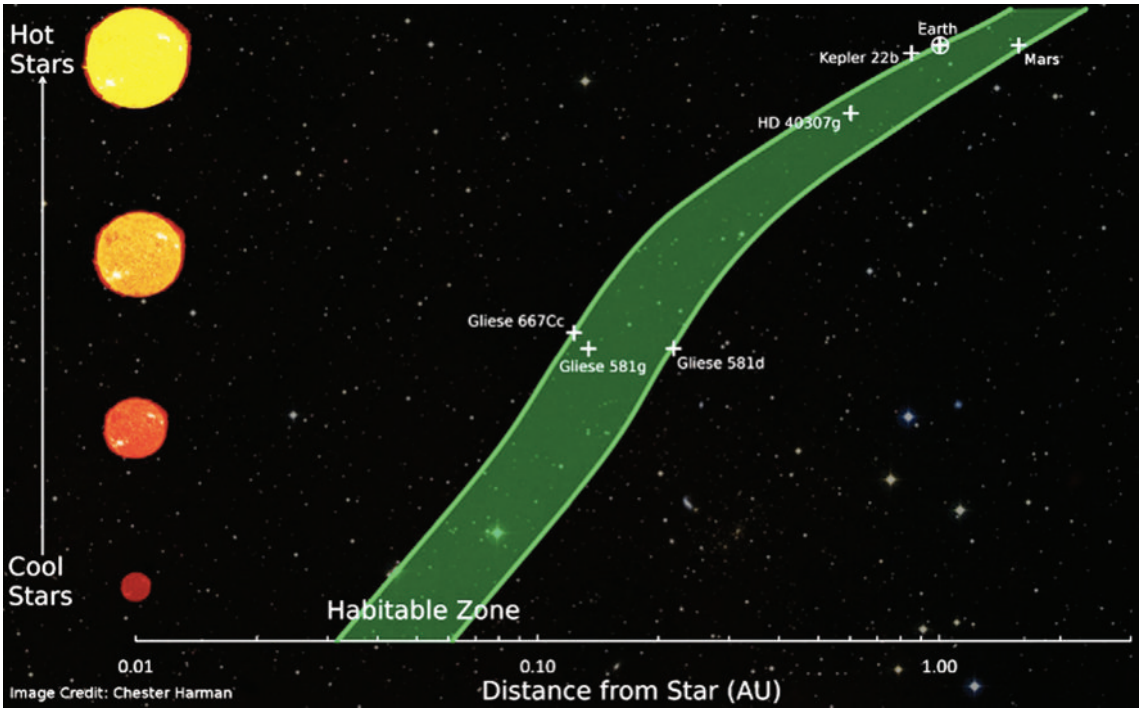

Figure 1.6: Habitable zone distances around various main-sequence stars (Kopparapu et al. 2013). Presence of Earth, Mars, and five confirmed exoplanets detected by transit. Credits: Chester Harman, *Penn State University*.

Table 1.1: Current potential habitable exoplanets, compared with Earth and Mars, ranked in order of discovery date, with their Earth Similarity Index (ESI) given by the Planetary Habitability Laboratory, *University of Puerto Rico at Arecibo* (www.phl.upr.edu).

Name	Period (d)	$M_\oplus$	ESI	Discovery	Related publications
Earth	365.2	1.0	1.00	–	–
Mars	687.0	0.1	0.66	–	–
Gliese 581 d	66.9	5.6	0.50	Apr 2007	Selsis et al. (2007)
Gliese 581 g*	36.6	3.1	**0.82**	Sep 2010	Tuomi (2011)
Gliese 667C c	28.2	4.5	0.79	Nov 2011	Anglada-Escudé et al. (2012)
Kepler-22 b	289.9	6.4	**0.81**	Dec 2011	Borucki et al. (2012)
Gliese 163 c	25.6	6.9	0.72	Sep 2012	Forveille et al. (submitted)
HD 40307 g*	197.8	7.1	0.67	Nov 2012	Tuomi et al. (2013a)
τ Ceti e*	168.1	4.3	0.74	Dec 2012	Tuomi et al. (2013b)
Kepler-62 f	267.3	**1.4**	0.69	Apr 2013	Borucki et al. (2013)
Kepler-62 e	122.4	**1.6**	**0.82**	Apr 2013	Borucki et al. (2013)

* unconfirmed exoplanets

Let us now have a look at the large number of new KEPLER exoplanet candidates announced recently by Burke (2013). Figure 1.7 shows the sizes of all the candidates, with respect to their equilibrium temperature, i.e., the theoretical planet's temperature when considered as a black body being heated only by its parent star. On the left part of this diagram, the habitable zone is shown as a green strip. The right part of the diagram is a magnification of this habitable zone. We notice that most of the planets situated inside this zone are recent results. The reason why KEPLER has needed more time to discover such cooler planets with longer orbit period is twofold: (i) several transits are necessary for a planet to be detected, which can last for 300-400 days for some of the longest orbital periods, and (ii) smaller planets show smaller dips in the light curves, which has required to significantly improve the detection algorithms.

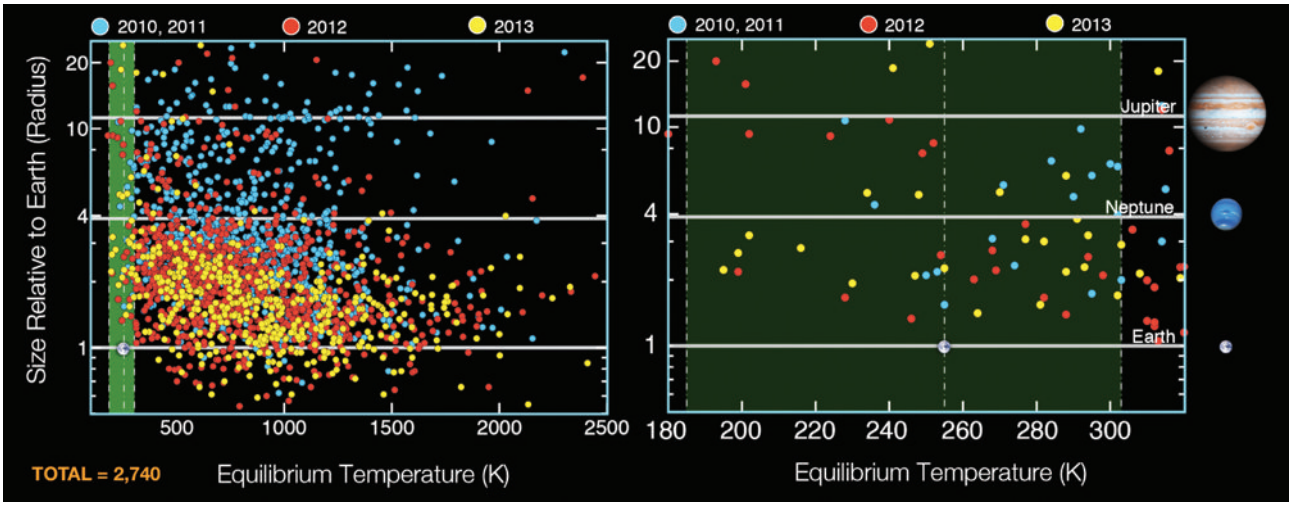

Figure 1.7: Left: KEPLER exoplanet candidates separated by year of detection, and plotted according to equilibrium temperature and size relative to Earth, with a green strip indicating the habitable zone. Right: Magnification of the habitable zone. From Burke (2013).

In addition to the large number of new candidates and the recent objects smaller than Neptune, one can notice that four of these new habitable zone candidates found by Kepler have estimated radii smaller than twice the size of Earth. Three of these are orbiting stars that are much cooler than the Sun. The fourth one, particularly interesting, is orbiting a Solar-type star, with a radius of about 1.5 Earth radius, and an orbital period of 242 days (Burke 2013). In addition to these numerous candidates, very recent results obtained by the Kepler team have confirmed two new Earth-like exoplanets around Kepler-62 with 1.4 and 1.6 Earth radii (Borucki et al. 2013), as shown in Table 1.1.

1.4.3 Searching for biosignatures

As of today, it is no longer a question of *how* to find an Earth analog, but a question of *whether* and *when*. According to the above results, this might happen within the next few years. But finding a true Earth-like habitable zone extrasolar planet will not yet be the evidence of extraterrestrial life. One must detect molecules in the atmosphere of an exoplanet. A spectrum of light that has passed through the planet atmosphere would tell a lot about its chemical composition and give important clues about what might be found on the surface. In particular, detecting ozone (O_3) and water vapour (H_2O) would constitute a relatively robust signature of biological activity as no purely abiotic process producing these elements has been identified yet (Léger et al. 1999; Selsis et al. 2002).

Some time ago, in the 1990s, during its mission towards Jupiter, the spacecraft Galileo took images of Earth. The experiment consisted in using the standard suite of exploration instruments and see if the existence of life on Earth can be detected. People had all kinds of thoughts about what would be detectable, e.g., cities and highways at night, the Great Wall of China. It turned out that none of these is actually visible from space (Sagan et al. 1993). But while observing the spectrum of Earth, the presence of H_2O can be seen at many different wavelengths, in the visible or the thermal infrared. As for O_3, it is detectable around 9 μm, and of course, it is blocking the ultra-violet severely under 350 nm (see Figure 1.8). The clearest sign of life on Earth is the fact that the atmosphere contains methane (CH_4). In fact, putting some CH_4 into an oxygen atmosphere would immediately dissociate into water vapour (H_2O) and carbon dioxide (CO_2) because of all the free oxygen. Although there should not be any CH_4 in the atmosphere, there is some, and one can detect it by looking at the infrared spectrum of the atmosphere. The presence of CH_4 in the Earth atmosphere means that there is a continuous source of CH_4 pumping into the atmosphere all the time. One of the main sources is, as Carl Sagan delicately put it, bovine flatulence. In other words, that happens from biological activity. Consequently, if one could observe the atmospheric chemistry of an exoplanet, one should look for something in there that is out of equilibrium, that could only be continually replenished by biological activity. The presence of an atmosphere with both oxygen and methane at the same time is one such indicator.

As already stated in Section 1.2, the transit method has allowed to identify some molecules for a couple of planets (Brown et al. 2002; Knutson et al. 2007; Charbonneau et al. 2002, 2008, 2009), such as e.g., water vapour (H_2O), methane (CH_4), carbon monoxide (CO), or carbon dioxide (CO_2). This technique is of course limited to planets transiting their parent stars as seen from our point of view. Moreover, for planets with a very long orbital period, it might require many decades

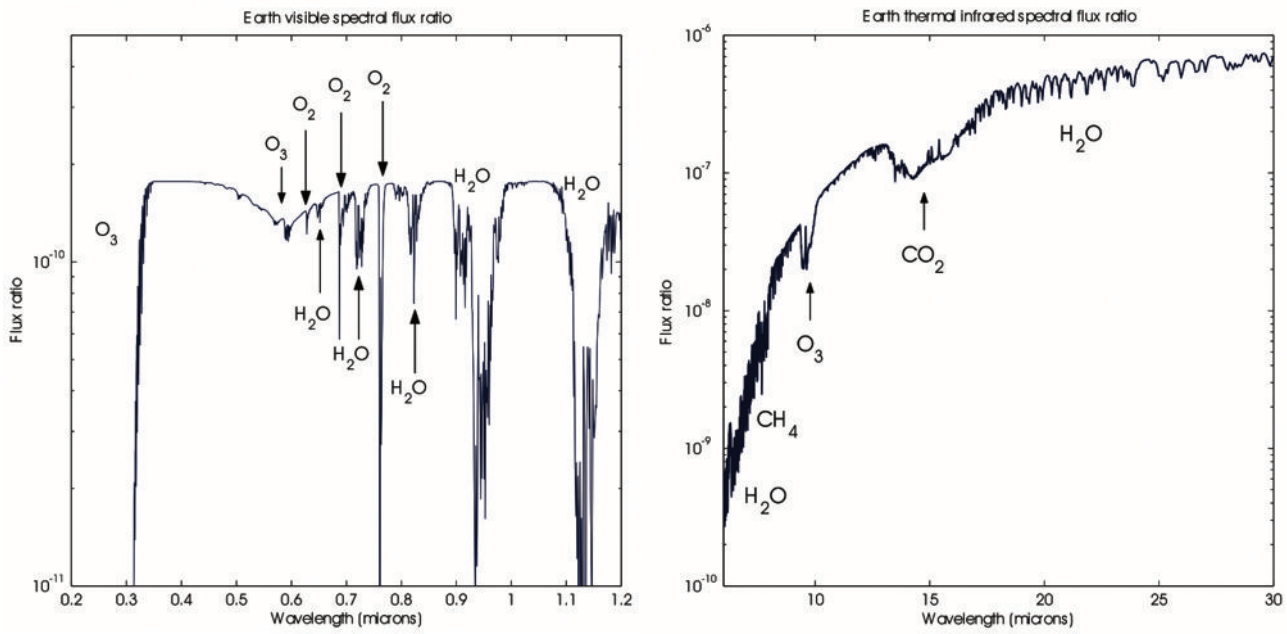

Figure 1.8: Left: Earth spectral contrast in the visible, with spectral biosignature features like O_2, O_3, H_2O. Right: Earth spectral contrast in the thermal infrared where the CO_2 and CH_4 features appear.

or centuries of observations to analyse their atmosphere composition with the transit method. If, on the other hand, one can measure directly the light reflected by the planet, separately from that of the star, it is possible to produce spectra of any planet, even the ones which do not transit in front of their host stars.

1.5 Direct detection: imaging Earth-like worlds

Direct imaging of an exoplanet consists in actually taking a picture of the light from the planet. It is fundamentally different from *indirect methods*, where one needs to observe the star in order to infer the presence of the planet. Observing planetary light directly is of great interest, as it can then be examined spectroscopically to characterise the planet, its color, the presence of land or oceans, clouds, and possibly identify biosignatures in the composition of its atmosphere. So far, only a few extrasolar planets have been discovered using *direct methods*. This lack of results reflects the great difficulty of spatially resolving a planet from its bright host star, which is due to two major difficulties:

- the angular separation between them is very small,
- the contrast between them is huge.

To successfully address these issues, one has to combine several techniques. Hereafter, we briefly describe the main technologies and techniques (i.e., adaptive optics, coronagraphy and differential imaging) that allow both high angular resolution and high dynamic range to be reached.

1.5.1 High angular resolution

In the theoretical perfect case (i.e., without optical aberrations), the image of a point source (such as a star) through a telescope is a diffraction pattern called the point spread function (PSF), known as the Airy-pattern in the case of a circular aperture. The half-width of this PSF represents the smallest angular distance between two sources that can be discerned. It is also called the resolving power, and is equal to $1.22\lambda/D$ where λ is the wavelength of observation and D the diameter of the mirror or the lens. In theory, increasing the diameter of the telescope directly improves the angular resolution and increases the collecting area for a better sensitivity to detect faint sources. Unfortunately, for ground-based telescopes, turbulence in the Earth's atmosphere limits the angular resolution, since it smears out the light from the PSF and makes it a fuzzy blob rather than a point, when taking a long exposure image of it. As a consequence, the diffracted stellar light can outshine the presence of potential faint companions, such as exoplanets, especially close to the star. While taking a short exposure image, short enough to freeze the atmospheric turbulence, one still obtains an image with many bright compact structures (called speckles). As the turbulence changes with time as the wind blows, the patterns of speckles change typically every few milliseconds. In addition to the fast fluctuating speckles, optical defects in the optics create quasi-static speckles. Both these speckles make it very difficult to separate the light of the star, from the light of the planet.

Adaptive optics

Adaptive optics (AO) is a technique for correcting spatial distortions in the input wavefronts which enables to dramatically improve image quality. It was first proposed by Babcock (1953), then later applied on the 3.6 m telescope of La Silla Observatory (ESO) by Rousset et al. (1990). This technique corrects the blurring and motion artifacts due to our turbulent atmosphere by superimposing all the speckles over each other to get only one much brighter speckle, which corresponds to the diffraction limit of the telescope (see Figure 1.9).

The AO runs in a closed-loop control system. First, the turbulence produces optical distortions that are measured hundreds of times a second with a wavefront sensor, using the light from a bright point source, usually a star. Then, the detector sends the information to a computer that calculates the shape that must be applied in real time (every millisecond or so) to a special deformable mirror (DM) placed in the optical train of the telescope. The surface of the DM reshapes by the action of hundreds or thousands of actuators, according to the instruction signals. The AO technique sharpens the image nearly to the point that it would have been delivered with no disturbing atmosphere at all.

Increasing the number of actuators is crucial, because the wavefront quality provided by AO systems directly depends on the actuator density. This wavefront quality is usually expressed in terms of Strehl ratio, that is the ratio of the peak image intensity from a point source compared to the maximum attainable intensity using an ideal optical system. From this definition, an image is conventionally considered as being diffraction limited when the Strehl is above 80%, i.e., limited only by diffraction over the system's aperture. First generation AO systems reach Strehl ratios around 40-60% in the infrared regime. Since the Strehl ratio depends on the wavelength, the image quality is much better in the mid-infrared regime (75-85% around 4 μm). Over the years, the AO technology has evolved and next generation extreme adaptive optics (XAO) systems, disposing of a much higher actuator density (Dekany et al. 2006; Racine 2006; Bouchez et al. 2010), will soon

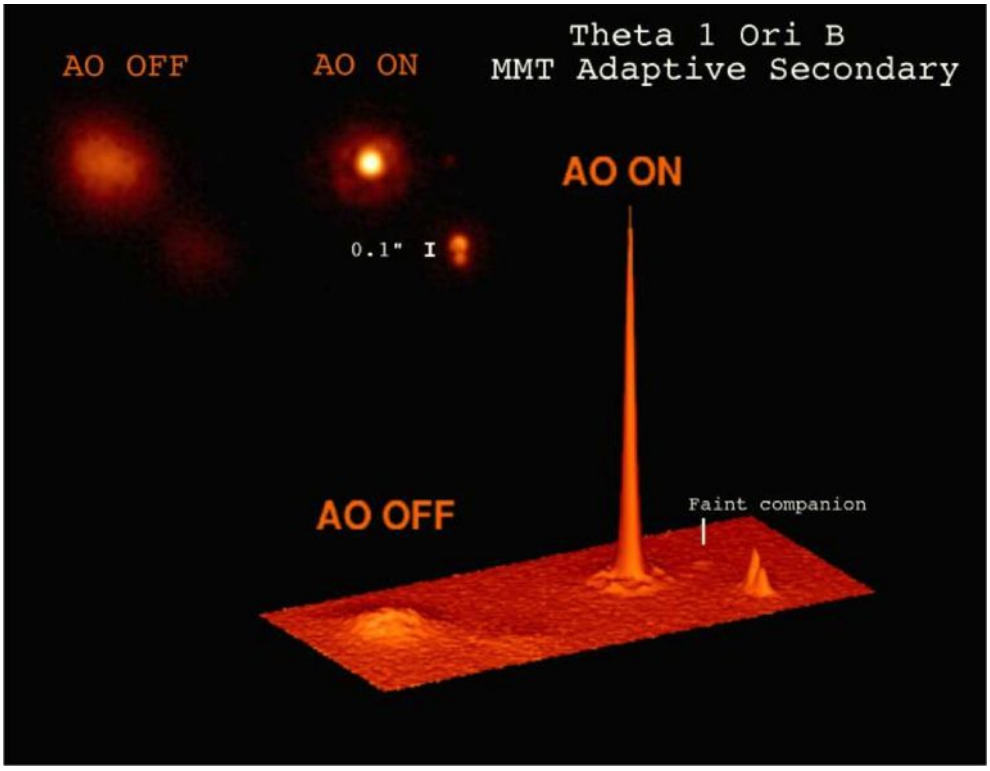

Figure 1.9: Wavefront correction of a blurred PSF provided by a classical AO system. When the AO is turned off, the image seems to be composed of a binary system. Once turned on, two additional stars appear in the image, one of them being a faint companion compared to the primary. Credits: Laird Close, *CAAO, Steward Observatory.*

provide diffraction limited images with Strehl ratios higher than 90% in the near-infrared (Beuzit et al. 2008; Macintosh et al. 2008).

1.5.2 High dynamic range

By simply pointing a telescope to a star, even one equipped with advanced XAO system, it is still difficult to take an image of an exoplanet next to the star, because the glare of the star generally prevents from seeing the planet which is much fainter. There are optical techniques to suppress the light of the star in such a way that there is no more glare any longer on top of the planet. There is a couple of different ways to blank out the light of the star, in particular two techniques that can be combined: coronagraphy (a *hardware* technique) and differential imaging (a *software* technique).

Coronagraphy

The first coronagraph (Lyot 1939) consisted of a big opaque mask designed to block the light coming from the Sun's photosphere and observe its corona. During the last 20 years, a coronagraph has become a generic term for a system that suppresses (or drastically reduces) the on-axis light of a star while permitting the light from surrounding sources to pass through the optical system. It essentially produces an artificial eclipse of bright stars, thereby removing the glare from the star

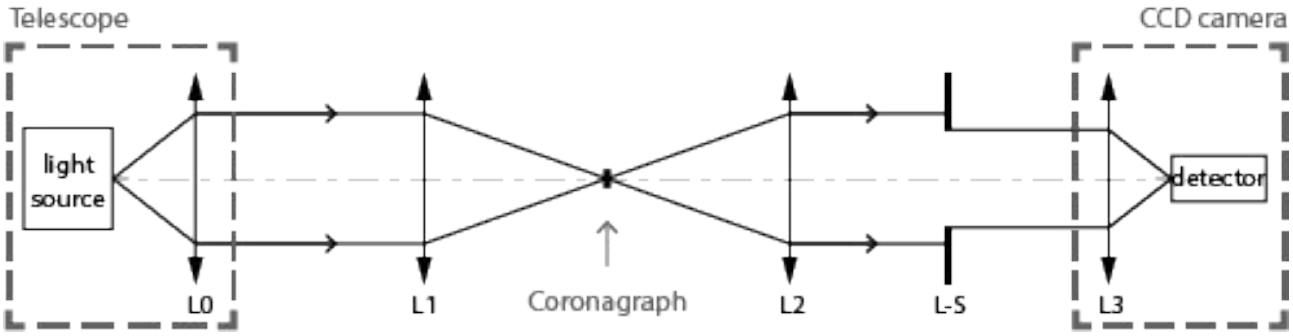

Figure 1.10: Classical coronagraphic bench layout. L0, L1, L2 and L3 correspond to converging optics. The light source is collimated by L0 to simulate the star plane waves. The next lens (L1) converges the beam from the central star on the optical axis in the first focal plane. The coronagraph (amplitude or phase) mask obscures the beam. This causes diffraction of most of the energy at the edge of the second pupil plane (defined by L2). The Lyot stop (L-S) then allows to block this diffracted energy and the image of the central star is not formed on the detector placed in the second focal plane (after L3).

to potentially reveal the faint light of planetary companions. The basic principle of coronagraphy is illustrated in Figure 1.10, with the use of lenses such as on a laboratory optical bench. In a telescope, the lenses are replaced by mirrors. L1 corresponds to the primary mirror providing a large f-number, which is the F/D ratio, where F is the focal length and D the diameter of the telescope. L2 corresponds to the secondary mirror. L-S is a pupil mask called the Lyot stop. L3 is focusing the light on a detector (CCD camera).

Coronagraphy is a powerful method for the detection of faint point-sources such as extrasolar planets in close separation from their stars, and is the main theme addressed in our work. In Chapter 2, we will describe in more details the different types of coronagraphs, and especially the subwavelength grating vector vortex coronagraph (SG-VVC) also called the annular groove phase mask (AGPM, Mawet et al. 2005a), which is the main subject of this thesis.

Differential imaging

Along with coronagraphy, another powerful method for the detection of faint point-sources such as extrasolar planets located very near their stars is differential imaging. This technique is based on numerical subtraction of images, such as a filtering process with a computer. While coronagraphy and adaptive optics provide diffraction control, differential imaging allows systematic errors calibration. Indeed, its primary goal is to eliminate the PSF aberrations caused by imperfections of the telescope mirrors and diffracted by the mechanical support structure, called the spider, holding the secondary mirror. Unlike atmospheric turbulence, this PSF noise evolves very slowly during the observation and therefore results in quasi-static speckles (Marois et al. 2003; Masciadri et al. 2005). For the last 25 years, various differential imaging methods have been proposed to suppress the PSF quasi-static noise and improve the detection limit.

The first technique is spectral differential imaging (SDI, Smith 1987; Racine et al. 1999; Lafrenière et al. 2007c), which consists in the simultaneous acquisition of images in different adjacent narrow spectral bands, within a spectral range where the star and planet spectra differ. Since quasi-static speckles result from the diffraction of stellar light, their spectral signature is

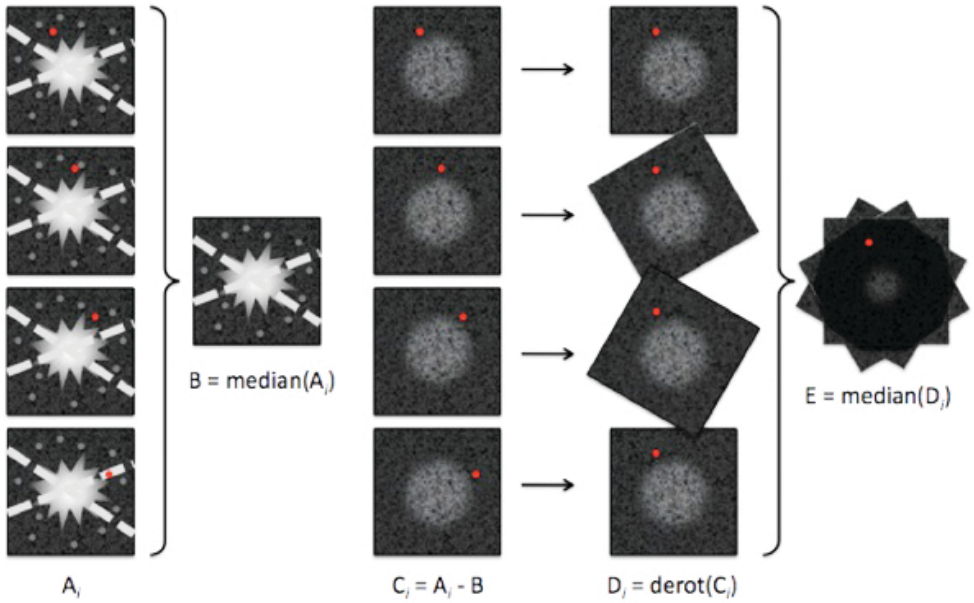

Figure 1.11: Illustration of the ADI image combination technique. A_i corresponds to the series of raw frames taken in pupil-stabilized observing mode. The halo sketched in gray is the quasi-static speckle, the red-highlighted point is the rotating planet signal. Credits: Christian Thalmann, *Max Planck Institute for Astronomy*.

different from the signature of the companion. By subtracting the different recorded images, the stellar PSF and the quasi-static speckles can be strongly attenuated, and the signature of the companion can be easier to retrieve.

Later on, the angular differential imaging (ADI, Marois et al. 2006) was developed. This technique yields performances similar to SDI, but does not require the presence of sharp spectral features in the planet spectrum. ADI is used on an alt-azimuth telescope mount. As Earth spins around its axis, the field appears to rotate. This is not the case for the quasi-static speckles, which are due to the imperfections of the telescope. ADI exploits the fact that the field and the pupil rotate with respect to each other during the observations to distinguish the star's halo from real astronomical sources, such as planet companions. As shown in Figure 1.11, for each image (A_i), a reference image (B) is constructed from other images of the same sequence, and subtracted to remove quasi-static structures (C_i). All residual images are then rotated to align the field (D_i) and are summed up (E). At the end, both the starlight and the quasi-static speckles are reduced reduced typically by an order of magnitude (Marois et al. 2006).

More recently, a more sophisticated way to perform the PSF subtraction, the locally optimized combination of images (LOCI) algorithm, was developed (Lafrenière et al. 2007b). It is inspired by the ADI method, but instead of subtracting one median PSF from all images in the series, an optimized PSF is constructed by linearly combining the reference images to minimize residuals within the scientific observation. To build the optimal artificial LOCI PSF, all images are divided into multiple ring-shaped subsections (see Figure 1.12), and for each of them, an optimised portion of the PSF is built. LOCI was first developed to work on PSF libraries, but it can also use images taken at different parallactic angles, from ADI image sequences, as reference.

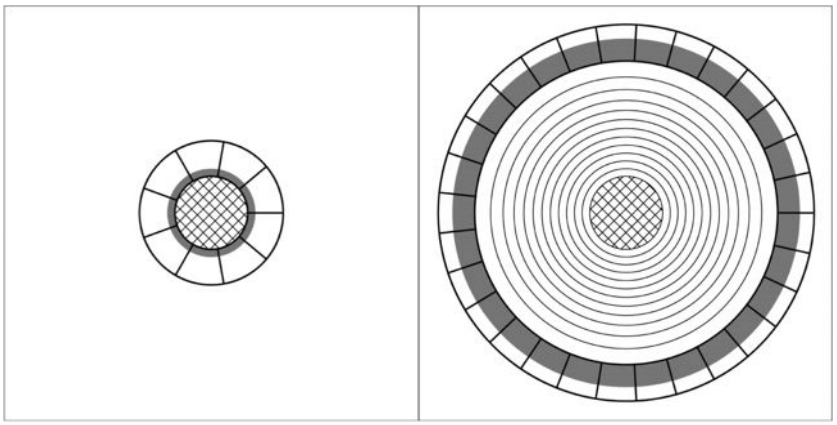

Figure 1.12: Illustration of the artificial LOCI PSF construction process. For each subsection of ring (delimited by thick lines), a portion of the optimized background is obtained by linear combination (gray shaded area). The left and right panels show the 1st and 13th subtraction annuli, respectively. From Lafrenière et al. (2007c).

1.5.3 The first images

Over recent years, astronomers have taken the first images of planets outside of our solar system. Let us recall the main direct detections made so far (see Figure 1.13), and illustrate the limits of the current direct detection capabilities for some of them.

- **2M1207 b** was imaged in 2004 with the VLT using only AO (Chauvin et al. 2004). It is a very hot gas giant orbiting a brown dwarf, about only 100 times brighter than its companion. 2M1207 b is believed to have a mass ranging from 3 to 10 $M_{\rm Jup}$, and is considered as the first imaged extrasolar planet, even though it is not orbiting a star.

- **Fomalhaut b** was imaged in 2004 and 2006 with the HST using a coronagraphic occulting spot (Kalas et al. 2005, 2008). Considered as the first directly imaged exoplanet orbiting a main sequence star, Fomalhaut b is a major discovery. We describe it below in more details.

- β **Pictoris b** was imaged in 2003 and 2009 with the VLT using AO and ADI (Lagrange et al. 2009a, 2010). The planet, with a mass around 8 $M_{\rm Jup}$, is orbiting at a semi-major axis of 8 AU from β Pictoris. This is the first time that the motion of a directly imaged planet has been followed as it moves to the other side of its host star.

- **HR 8799 b, c, d** (in 2008) and later **e** (in 2010) were imaged with the Keck and Gemini telescopes, using AO, coronagraphy, and ADI LOCI (Marois et al. 2008b, 2010). This is the first multiple-planet extrasolar system directly imaged. We also describe it in more details hereafter.

- κ **Andromedae b** was imaged in 2012 with the Subaru Telescope using AO, coronagraphy, and ADI (Carson et al. 2013). With a mass of nearly 13 $M_{\rm Jup}$, it is not clear yet if the object is an exoplanet or a brown dwarf.

- Plus a few more which could also claim the title of planet.

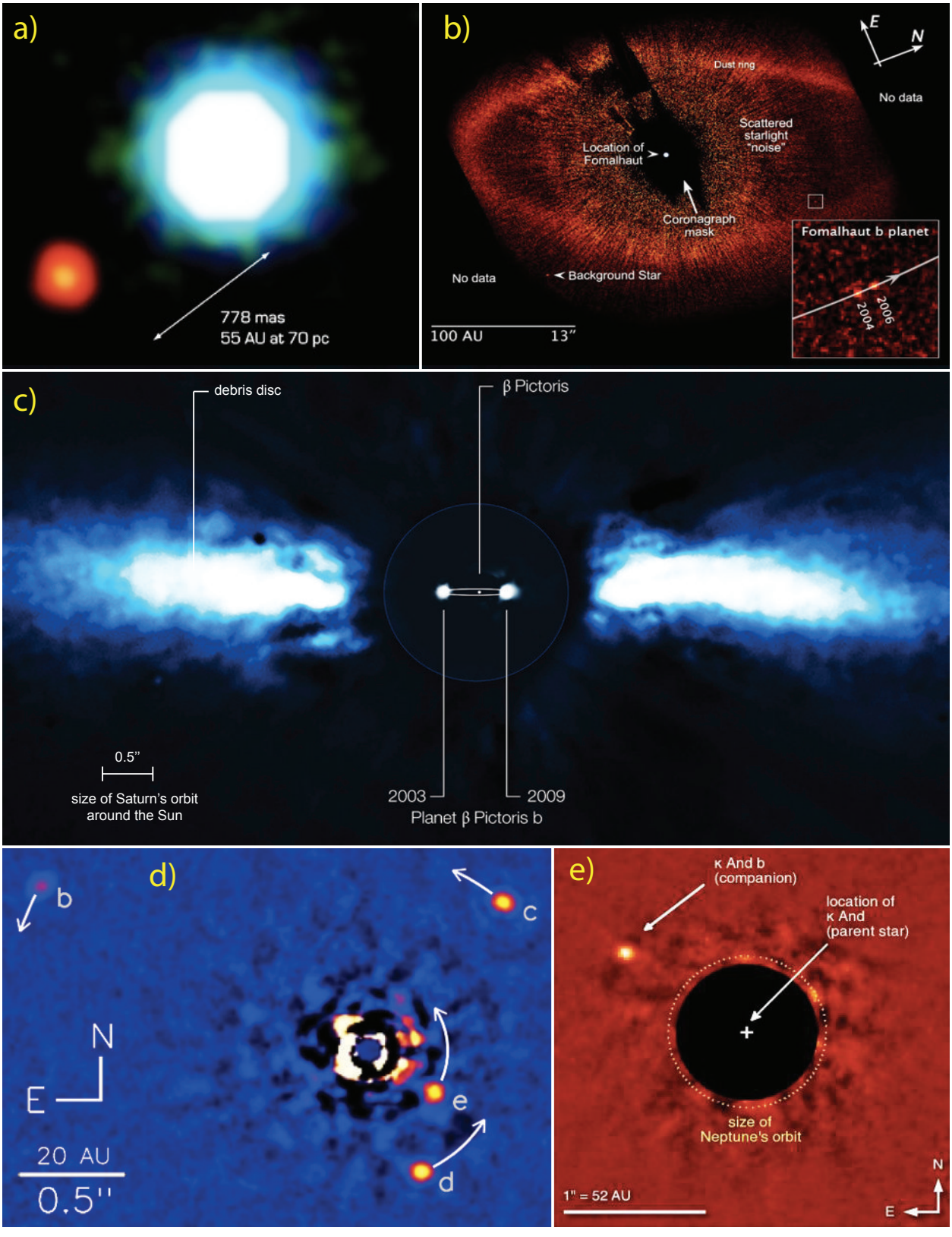

Figure 1.13: Some of the principal planets directly imaged so far. *(a) 2M1207 b* imaged in 2004. *(b) Fomalhaut b* imaged in 2004 and 2006. *(c) β Pictoris b* imaged in 2003 and 2009. *(d) HR 8799 b, c, d, e* imaged in 2008 and 2010. *(e) κ Andromedae b* imaged in 2012. References are given in the text.

Fomalhaut b

Fomalhaut is one of the twenty brightest stars in the sky, easily visible with the naked eye, and its glare makes it very difficult to detect the faint signal from a planet that may be very close to the star. The first image was taken in 2004 in visible light using a new instrument aboard the Hubble Space Telescope (HST) called the Advanced Camera for Surveys (ACS), equipped with a coronagraph (Kalas et al. 2005). At that time, the planet was not noticed immediately, but only the vast dust belt circling the star. This is an analog to our Kuiper belt, a system of icy bodies that are colliding and continually producing dust that one can see as reflected light. Following Kalas et al. (2005), the belt had several unusual features which they hypothesized could be due to the gravitational perturbations from a planet that had not been seen yet. With this hypothesis in mind, they returned to Fomalhaut in 2006 with the ACS, and obtained even deeper and more accurate images of the belt but also found a faint point source to the lower right (see Figure 1.13, b), one billion times fainter than the central star, orbiting at 115 AU (Kalas et al. 2008). Note that new results have been published this month (Kalas et al. 2013) with the space telescope imaging spectrograph (STIS).

This discovery makes it the first visible light picture of a planet orbiting another star. The planet, called Fomalhaut b, completes an orbit in roughly 800 years. It is orbiting the star Fomalhaut in a counter clock-wise motion, just within the dust belt, thereby satisfying the hypothesis that the belt is governed by the gravity of the planet. By measuring how close the planet is to the dust belt, and by combining it with the orbital motion and the brightness of the planet, one can firmly constrain the mass of the planet to be less than 3 $M_{\rm Jup}$. The lower limit to the mass of Fomalhaut b is the mass of Neptune. Neptune in our solar system does a similar thing, by sculpting the inside edge of the Kuiper belt. This discovery allows us to better understand the origin and evolution of planetary system architectures.

HR 8799 b, c, d, e

HR 8799 is located in the constellation Pegasus, 130 light years away from Earth. The star is about 1.5 $M_{\odot}$, and it has four directly imaged companions (see Figure 1.13, d). The first three planets orbiting around HR 8799 were imaged in the infrared by a canadian team in 2008, using the Gemini and the W. M. Keck observatory on Hawaii's Mauna Kea (Marois et al. 2008b). This discovery was made possible thanks to the use of the ADI technique. HR 8799 b, c and d were also recently imaged using a vortex coronagraph capable of reaching small angles behind a small, well-corrected telescope subaperture (Serabyn et al. 2010). Later, the planet e was imaged by the canadian team (Marois et al. 2010). This fourth planet is probably 9 $M_{\rm Jup}$ and it is the closest one to the host star (14.5 AU). It is followed by the planets d and c, almost as large (10 $M_{\rm Jup}$) and further out (24 AU and 38 AU). Then, planet b, the most distant planet in this multi-planet system, is 7 $M_{\rm Jup}$ and it orbits at 68 AU, just inside a disk of dusty debris similar to our Kuiper belt, a relic of the formation of the system. This multi-planet system is considered by astronomers to be young, only about 60 Myrs old. That means that the orbs of the planets are still glowing with heat leftover after their formation. The set-up of this planetary system, along with its dusty belt, suggest that it could be a scaled-up version of our solar system. Earth-like planets might also exist closer-in to the star, but if so, their are too dim to be photographed with the instruments previously used to image the four planets, and need more efficient coronagraphs, combined with better AO systems or space-based telescopes.

1.6 Conclusion

For the last ten years, detections of exoplanets have dramatically increased. Astronomers are finding a planet every two weeks in average, using indirect detection methods such as transits or radial velocity. Most of the planets discovered so far are very different from those of our own solar system. This stretches our imagination of what a planet can be, and gives us some hope about all the other exciting discoveries to be made. Discoveries of hot Jupiters have taught us a lot about the formation of our solar system, leading to various evolutionary models, including planetary migration theory. During the last five years, a series of Earth-size planets have been discovered. Among them, some are located in the habitable zone and could probably host life. In the next few years, more and more Earth-like worlds will be detected. However, taking pictures of these worlds is still far from being an easy game.

The direct imaging of Fomalhaut b is a landmark discovery among exoplanets, because it is considered as the first direct image of a planet of quite a low mass. Together with β Pictoris b and the HR 8799 system, these significant discoveries legitimize the whole field of direct imaging. The advantages of direct detection are multiple. First, it is a much faster detection than using indirect ways. Instead of waiting many years for a planet to transit in front of its host star, one can see it in a few hours with an 8-m telescope. Moreover, by analyzing the incoming light, one can study the planet composition using photometry. In this regard, the integral field spectroscopy (IFS) technique is actually providing its first results (Konopacky et al. 2013; Oppenheimer et al. 2013). Direct imaging is also sensitive to different kinds of planets, which are orbiting further away than those detected using radial velocity. In that way, it complements the searches. Finally, direct imaging allows to follow the orbit and see the planet spin around the star.

New technologies are continuously developed. Next generation extreme adaptive optics (XAO) allow high angular resolutions. Differential imaging algorithm, such as ADI LOCI, can suppress the PSF quasi-static noise and improve the detection limit. But most of all, the addition of a coronagraphic mask enhances the capability of large XAO-corrected telescopes and promises to distinguish giant planets with planetary masses around that of Jupiter with contrasts up to a few tens of thousands. The recent advances in stellar coronagraphy will be presented in the next chapter.

2

An overview of coronagraph technologies

Contents

Abstract. *The adaptive optics and data reduction techniques presented in the previous chapter have improved considerably the image quality of current 8-10 meter class telescopes, providing sharp, high resolution images and reducing the stellar scattered light. These techniques are however limited when it comes to observing faint extrasolar planets. Indeed, the direct imaging of exoplanets requires unprecedented levels of light suppression. Such high contrasts can be achieved by blocking or canceling the starlight with a coronagraph. In this chapter, we first provide an overview of the multiple stellar coronagraphy techniques that have emerged during the last decade, and review the specificities proper to a particular class of phase-masks called the vector vortex coronagraph. We then present the different vortex coronagraphy technologies, with a particular interest for the use of subwavelength gratings as a unique solution at mid-infrared wavelengths. Finally, we end this chapter with a review of the current and future coronagraphic facilities on the ground and in space.*

2.1 The coronagraph tree of life

Downstream from the telescope, the first step of imaging instruments dedicated to the direct detection of exoplanets is to reduce the light intensity from the host star without affecting the light from the planet. For this, many types of coronagraphs have been proposed, studied, tested and integrated to large telescopes. All these different types have a common ancestor: the Lyot coronagraph (see Figure 2.1). Bernard Lyot, astronomer at the Meudon Observatory from 1920 to 1952, made great progress in astronomy instrumentation. Among other things, he invented the photoelectric polarimeter, a very narrow spectral bandwidth filter, and the solar coronagraph (Lyot 1932, 1939). The latter was invented to allow regular and systematic study of the corona of the sun, which had previously been studied only at the time of total solar eclipses. The instrument reduces the light flux from the solar photosphere, without reducing the flux from the two most tenuous layers that surround it, i.e., the chromosphere and the corona. The genius of Bernard Lyot was to introduce a diaphragm to block the light diffracted by the edges of the pupil of the telescope. Today, this diaphragm bears his name: the Lyot stop. With the solar coronagraph of Lyot, the study of the solar corona has triggered many themes, such as: (i) corona polarimetry (Koomen et al. 1975), (ii) corona interactions with a comet (Curtis & Sacramento Peak Observatory Staff 1966), (iii) corona magnetic field (Wagner et al. 1974), (iv) study of solar prominences (Hirayama & Nakagomi 1974). Nowadays, several solar coronagraphs are still in use, including onboard the Solar Heliospheric Observatory (SOHO) and at the Pic du Midi Observatory.

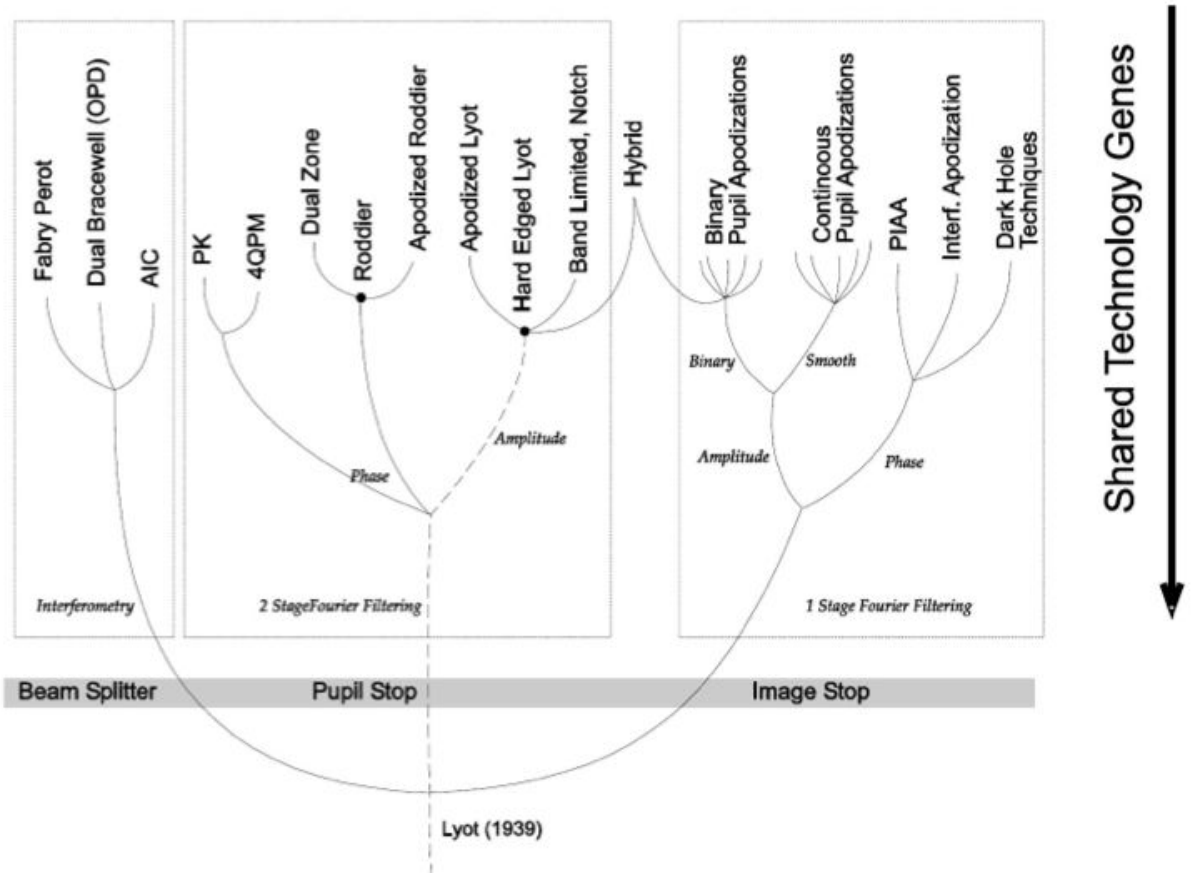

Figure 2.1: Illustration of the stellar coronagraph family tree, regrouping most of the existing coronagraphic concepts (non exhaustive), descending from the Lyot solar coronagraph. From Quirrenbach (2005).

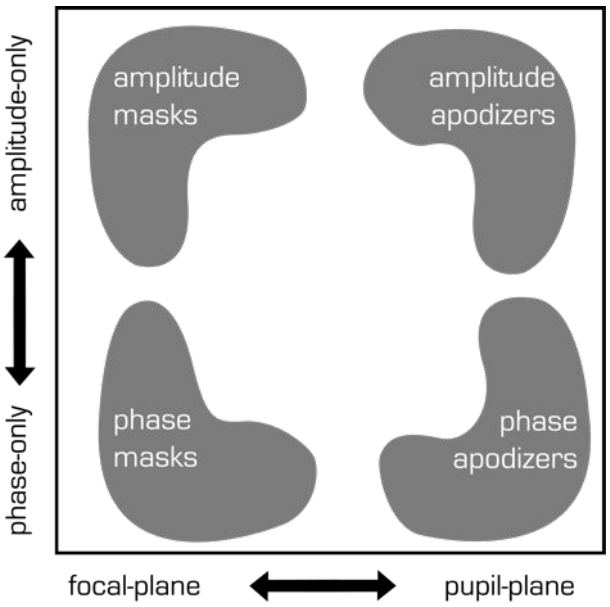

Figure 2.2: Illustration of the four major stellar coronagraph types, following two divisions: position of the Fourier spatial filter (focal-plane / pupil-plane) along the horizontal axis, and occultation method (amplitude / phase) along the vertical axis.

In the early 80s, a simple question arose. Why not adapt the solar coronagraph to the study of the tenuous environment of other objects than the Sun? This is how the Lyot coronagraph has been used to observe the rings and satellites of Saturn (Dollfus & Brunier 1980), or to study asteroids (Gradie 1986). Then the stellar coronagraph has emerged. Astronomers photographed Alpha and Beta Pictoris and R Aquarii to study their circumstellar disk (Smith & Terrile 1984; Paresce & Burrows 1986, 1987). Other teams have tried to detect brown dwarfs around nearby stars (Macintosh et al. 1992; Nakajima et al. 1994). Since astronomers were interested in the imaging of extrasolar planets (Mills et al. 1991; Nakajima 1994), it was necessary to modify the initial solar coronagraph, the angular size of a star being negligible compared to that of the Sun. Since then, new concepts of coronagraphs were invented every year. A complete description of each technique and a comparison of performances will not be provided in this manuscript (see Guyon et al. 2006; Guyon 2007; Trauger 2009). We limit our discussion to the description of the four major coronagraph types (see Section 2.2). Then, in Section 2.3, we detail the concept of vector vortex coronagraphs (VVC, Mawet et al. 2005a; Foo et al. 2005; Palacios 2005; Jenkins 2008; Swartzlander 2009; Mawet et al. 2011b; Serabyn et al. 2011), especially coronagraphs using subwavelength gratings (SG-VVC), on which this work is focused (Delacroix et al. 2010a, 2012b, 2013).

2.2 Four major stellar coronagraph types

The vast diversity of different approaches presented in Fig. 2.1 can be classified along two divisions (Mawet 2006; Trauger 2009), and regrouped into four groups (see Fig. 2.2): (i) amplitude masks, (ii) amplitude apodizers, (iii) phase apodizers, and (iv) phase masks. The primary division lays in the mechanism by which the stellar light is segregated, depending on where the Fourier spatial filters are positioned. On the one hand, the *pupil-plane* family generally uses one-stage Fourier spatial filters, positioned in the pupil plane, dumping the light in a confined region of the focal plane (also called image stop, see Fig. 2.1). On the other hand, the *focal-plane* family regroups

coronagraphs having two (or in some case more) stages of Fourier spatial filtering, one in the first focal plane, and one in the exit pupil plane (also called pupil stop, see Fig. 2.1) as with a classical Lyot coronagraph.

The secondary division relates to the occultation method implemented by the coronagraphic system. The *amplitude* coronagraphs block the light directly, similarly to the original approach of Lyot, whereas the *phase* coronagraphs induce spatially-distributed phase shifts, with the aim of rejecting the starlight out of the Lyot stop.

2.2.1 Amplitude masks

The Lyot coronagraph (also called hard-edged Lyot) suffers from two fundamental limitations: (i) it does not completely extinguish the central star, (ii) the diameter of the mask prevents observing regions close to the star. What was not a concern in the context of the study of the solar corona, has become a limiting factor for the study of stellar environments. It was therefore necessary to develop new types of coronagraphs.

Prolate apodized Lyot coronagraph

The apodization of the entrance pupil is an effective solution used on the prolate apodized Lyot coronagraph (PALC) to improve the extinction of a classical Lyot coronagraph. The Lyot mask is then used, but applied to an image of the star that became soft-edged by the apodization. The apodization is achieved using a *prolate* function (see Figure 2.3) that provides the best compromise in terms of loss of resolution and throughput (Aime et al. 2001, 2002; Soummer et al. 2003a; Aime & Soummer 2004).

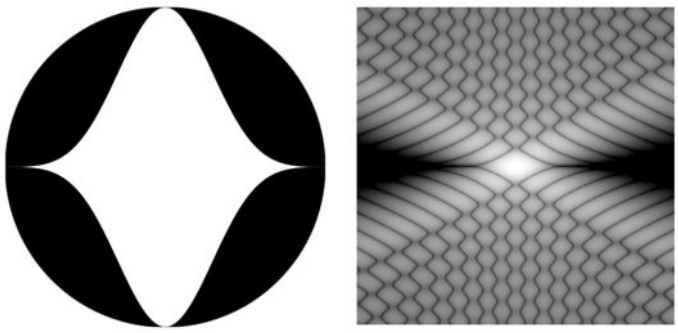

Figure 2.3: Left: Prolate function apodized aperture (Slepian 1965). Right: Corresponding PSF plotted on a logarithmic scale with black areas 10^{-10} below brightest ones. From Kasdin et al. (2003).

Band-limited and notch-filter masks

For the amplitude mask to completely remove the residual flux from the pupil, the Fourier transform of the mask must be a bounded-support function, which is to say that the mask must be an unbounded-support function (Kuchner & Traub 2002). There is a whole family of masks called *band-limited* that satisfy this condition. BL coronagraphs achieve contrasts of 10^{-9} at $3\lambda/D$ inner working angle (IWA) over a $\Delta\lambda/\lambda = 20\%$ bandwidth (Trauger 2009), but the residual flux is still

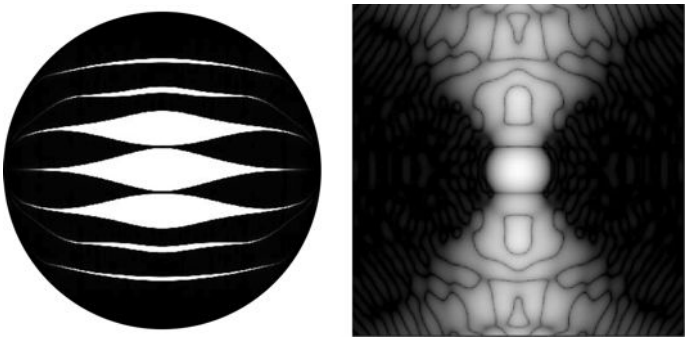

Figure 2.4: Left: The transmittance profile of a representative (the *Ripple 3* design) shaped-pupil apodization, where black indicates opaque. Right: Corresponding PSF plotted on a logarithmic scale with black areas 10^{-10} below brightest ones. From Belikov et al. (2007).

not totally canceled. Moreover, even far from the star, the mask still attenuates the companion. To address this issue, Kuchner & Spergel (2003) proposes to use *notch filters*, i.e., binary narrow band-stop filters (Kuchner et al. 2005; Shaklan & Green 2005).

2.2.2 Amplitude apodizers

The main disadvantage of occulting masks comes from their overall dimensions, thereby hiding the area of interest. As an original solution, different sorts of mask-less designs have been proposed. These are called *shaped pupil* coronagraphs. They are based on the concept of apodization proposed by Jacquinot & Roizen-Dossier (1964). This concept gave birth to many derivatives (Nisenson & Papaliolios 2001; Kasdin et al. 2003; Debes & Ge 2004; Belikov et al. 2007), such as the *Ripple 3* design illustrated in Figure 2.4. This design achieves a 10^{-9} contrast at $4\lambda/D$ with 10% bandwidth (Belikov et al. 2007; Trauger 2009). These coronagraphs, however, reduce dramatically the signal transmission. Smaller IWAs are possible with the so-called *dark hole* techniques described below in Section 2.2.3, that require a deformable mirror (DM).

Another apodizer is the phase-induced amplitude apodization coronagraph (PIAAC). It is technically an amplitude apodizer, however it also induces phase modulation. Therefore, we will present this concept in the next section, dedicated to phase apodizers.

2.2.3 Phase apodizers

Some types of coronagraph enable the apodization of the entrance pupil by modulating the phase of the incident beam, enabling imaging at small angular separation with little loss in throughput.

Pupil mapping

The phase-induced amplitude apodization coronagraph (PIAAC, also known as *pupil mapping*, see Figure 2.5) is a coronagraph apodized by phase, while the incident beam passes through two aspheric optics (Traub & Vanderbei 2003; Guyon 2003; Guyon et al. 2005, 2010b; Martinache et al. 2006, 2012a). The optics can be mirrors or lenses. The PIAAC combines high throughput, small IWA ($2\lambda/D$ for 10^{-10} contrast), low chromaticity (when mirrors are used), full 360° discovery space, and full $1\lambda/D$ angular resolution. A new approach consists in combining the full throughput and uncompromized angular resolution of the PIAAC, and the design flexibility

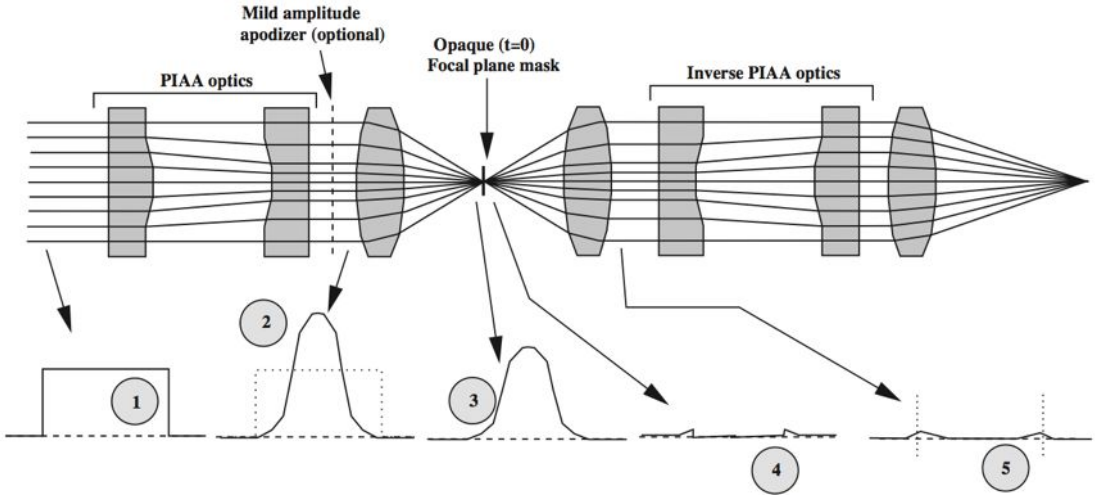

Figure 2.5: Architecture of the phase-induced amplitude apodization coronagraph (PIAAC), with graphical representations of complex amplitudes in a few relevant planes: (1) telescope entrance pupil, (2) pupil after apodization, (3) focal plane before introduction of the focal-plane mask, (4) focal plane after the focal-plane mask, and (5) exit pupil plane before truncation by the Lyot mask. From Guyon et al. (2010a).

of apodized pupil Lyot coronagraphs, to obtain a PIAA complex mask coronagraph (PIAACMC, Guyon et al. 2010a), which offers 50% throughput at $0.64\lambda/D$ while providing total extinction of an on-axis point source.

The most challenging feature is the manufacturing of aspheric mirrors to the required accuracy, due to the rapid decrease in radius of curvature at the edge of the first PIAA element. In addition, the mirrors are bounded, which leads to a limited number of frequencies in the focal plane, producing Fresnel effects, harmful to the apodization (Vanderbei 2006).

Apodizing phase plate

Another technique based on modulation of phase across the pupil is the apodizing phase plate (APP, Yang & Kostinski 2004; Codona & Angel 2004; Codona et al. 2006; Kenworthy et al. 2007). The basic idea is to introduce a weak sinusoidal phase ripple across the pupil, which acts as a weak diffraction grating, creating *antispeckles* for each speckle or diffraction structure, matching their location and amplitude, but π-shifted. The APP has been installed on NACO and achieves a 10^{-4} contrast at $2\lambda/D$ (Kenworthy et al. 2010a,c; Quanz et al. 2010, 2011). Another one has been developed for the LBT (Kenworthy et al. 2010b). Since the ripples are real, the antispeckles created on one part of the star have an antisymmetric real counterpart on the other side of the star, thereby reinforcing the speckles there. It is therefore only possible to cancel the starlight over at most one half and on a limited radial extent (e.g., from 2 to $7\lambda/D$) of the field of view around the center (see Figure 2.6).

The current limitations to the APP are: (i) the 180° coverage, (ii) the chromaticity due to the design, and (iii) the limited field of view due to the outer working angle. Indeed, phase shifts can only be accurate at one wavelength λ_0. Therefore, there will be a chromatic increase in the halo intensity that varies as $[(\lambda - \lambda_0)/\lambda_0]^2$ times the original halo intensity (Codona & Angel 2004). Further research is underway to develop an achromatic vector-APP (Snik et al. 2012).

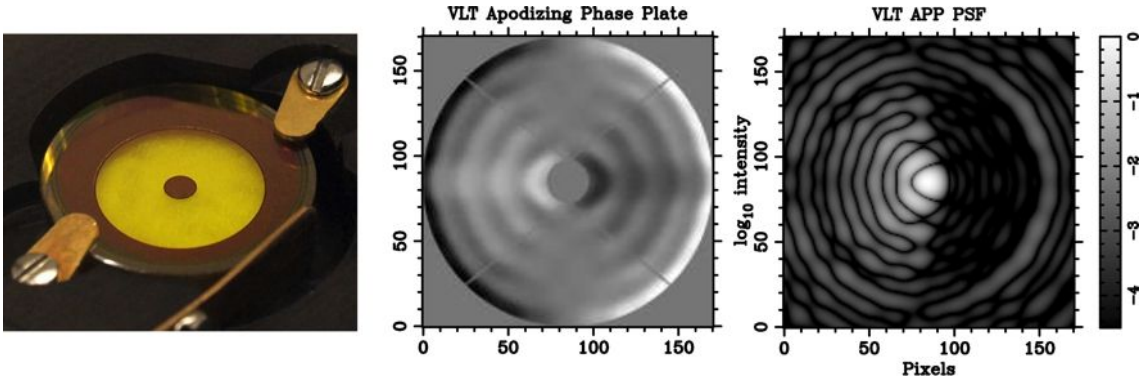

Figure 2.6: The VLT APP Design. Left: Photograph of VLT APP optics, with anti-reflection coated Zinc Selenide (light yellow area). Middle: Phase modification introduced to the VLT pupil. Right: Resultant PSF with a logarithmic intensity scale normalised to the peak flux. From Kenworthy et al. (2010c).

2.2.4 Phase masks

The phase masks constitute the fourth type of coronagraph. Just as a Lyot coronagraph, they are placed in the focal plane, but unlike the amplitude masks, they are transparent and generate phase shifts that reject, by destructive interferences, the light from the star out of the area of interest.

Roddier

Roddier & Roddier (1997) introduced a new type of coronagraph based on the the complex amplitude phase shifting, in the focal plane. A small portion of the core of the Airy pattern undergoes a π-phase shift relative to the rest of the Airy pattern. This π-phase shift is created by introducing a step e such as $\lambda = 2(n-1)e$, with n the index of the transparent material, and λ the light wavelength. The mask diameter is optimized so that all the starlight is attenuated by destructive interference (between the central portion and the outer portion), sending all the light outside the telescope aperture where it is intercepted by the Lyot stop. Compared to the Lyot coronagraph, it has higher dynamic range and smaller IWA. However, the mask is highly chromatic, for two reasons: (i) the step e is function of λ, (ii) the optimal diameter of the mask also depends on the wavelength (geometric chromatism). The chromatism of the mask can be reduced by using several steps producing different phase shifts (Soummer et al. 2003a) at the price of technical difficulties. In addition, the attenuation of the star is not total, but it can be made perfect (in the monochromatic case only) by the use of apodization by prolate functions (Soummer et al. 2003b).

Four quadrant phase mask

To solve the problem of geometric chromatism, Rouan et al. (2000) proposed another type of phase mask: the four quadrant phase mask (FQPM, Riaud et al. 2001; Boccaletti et al. 2004). The phase-shifting Roddier mask is replaced by a mask dividing the focal plane into four symmetrical parts, two of them inducing a π-phase shift (see Figure 2.7). As with the Roddier coronagraph, the π-phase shift is obtained with a phase-shift step. The light from a point source (such as a star), perfectly centered on the intersection of the four quadrants, destructively interferes and, as a result, is rejected outside the telescope pupil. As in the case of the Lyot and Roddier coronagraphs,

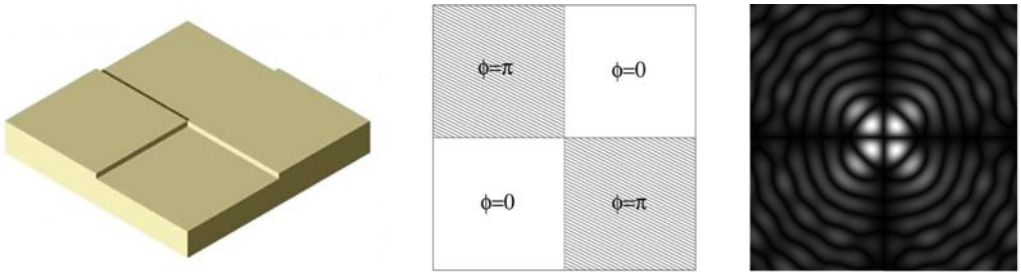

Figure 2.7: Left: Design of the four quadrant phase mask (FQPM). Middle: Two quadrants on one diagonal make the light undergo a π-phase shift, whereas the two other quadrants let it pass without shifting the phase. Right: Resulting PSF with a logarithmic intensity scale normalised to the peak flux. From Rouan et al. (2007).

the light is then blocked by a slightly undersized diaphragm (the Lyot stop). In the theoretical case, the attenuation is perfect. For an off-axis planet companion, the coronagraph effect is much weaker, especially if it is far from the center, so that its signal passes through the diaphragm and is almost not attenuated.

The FQPM is not affected by geometric chromaticism, however, it is still chromatic with respect to the phase shift. Different approaches have been proposed to make the phase shift achromatic, such as, e.g., the phase knife coronagraph (PKC, Abe et al. 2001, 2007) or the use of subwavelength gratings (Mawet et al. 2005b). Another weakness of the FQPM is its sensitivity to central obscuration and spider arm. Solutions have been proposed to reduce this degradation by beam-shaping of the entrance pupil (Lloyd et al. 2003; Abe et al. 2006) or by optimizing the Lyot stop to reduce the diffracted light (Boccaletti et al. 2004). In addition, the perfect alignment of the four quadrants is hard to manufacture.

(Vector) vortex coronagraph

The vector vortex coronagraph (VVC), or vortex coronagraph, was initially proposed as a solution to avoid the tedious task of aligning the four quadrants of the FQPM, and to suppress the transition zones which cause a loss of information. The idea is to replace the phase-shift steps by continuous phase-shift, thereby synthesizing an optical vortex (see Figure 2.8). VVCs are known for their outstanding coronagraphic properties: small IWA (down to $0.9\lambda/D$), high throughput, clear off-axis 360° discovery space, and simplicity.

Optical vortex coronagraphs (Foo et al. 2005; Mawet et al. 2005a; Palacios 2005) provide a continuous helical phase ramp, varying azimuthally around the optical axis. This phase ramp can be written $e^{\imath\phi}$, with $\phi = l\theta$, where θ is the focal plane azimuthal coordinate, and l the (even) vortex *topological charge*, i.e., the number of times the geometric phase ϕ_p (Pancharatnam 1956, see also below) accumulates 2π along a closed path s surrounding the phase singularity:

$$l = \frac{1}{2\pi} \oint \nabla \phi_p \, ds \; . \tag{2.1}$$

The phase dislocation forces the amplitude to zero at its centre, which is a singularity. Nature indeed prevents the phase from having an infinite number of values at a single point in space, which is non-physical, by simply nulling the light locally. When centred on the diffraction pattern

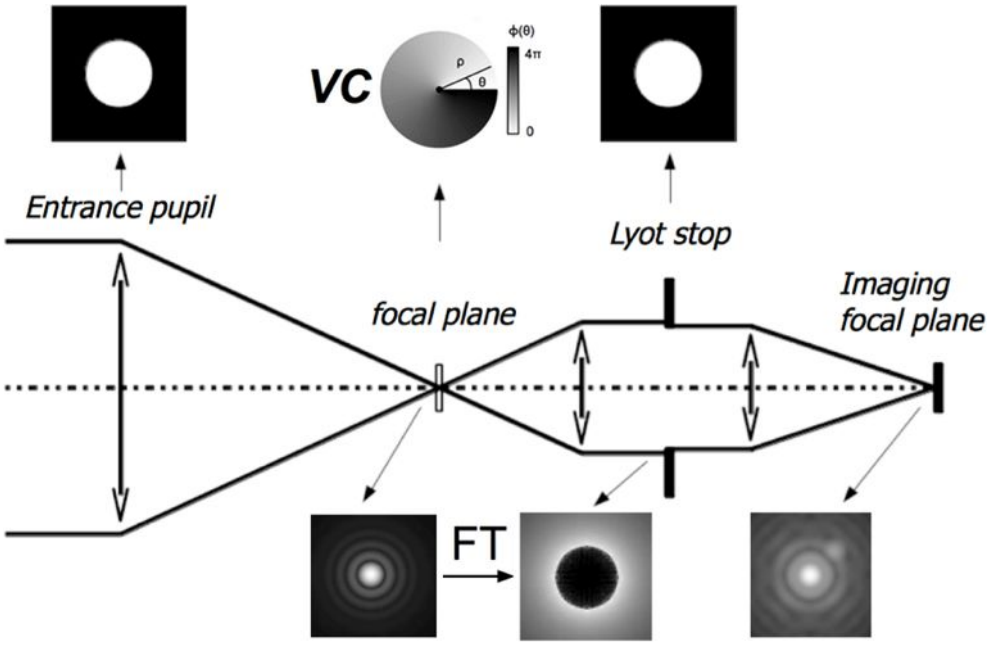

Figure 2.8: Left: An ideal unobscured circular input pupil. Middle: A transparent phase mask applies a helical phase (vortex) to a telescope's focal-plane field. Right: The light propagates downstream to a pupil image (the Lyot plane), where all of the (on-axis) starlight appears outside of the geometric image of the input pupil, where it is blocked by a Lyot stop. Light from an off-axis companion misses the center of the vortex and propagates normally.

of a star seen through a telescope, optical vortices affect the subsequent propagation by redirecting the on-axis starlight outside the geometric image of the pupil. This diffracted starlight is then blocked when passing through the Lyot stop, slightly undersized compared to the input pupil image.

The perfect starlight attenuation of an optical vortex coronagraph has been proven analytically (Mawet et al. 2005a; Foo et al. 2005; Jenkins 2008) for any non-zero even values of l by applying the result of the Weber-Schafheitlin integral[1] (Abramowitz & Stegun 1972; Sneddon 1951) to the Fourier transform of the product of a vortex ramp phase ($e^{\imath l\theta}$) with an ideal Airy pattern ($\frac{2J_1(k\rho R)}{k\rho R}$), where R is the circular input pupil radius, k the wave number, and ρ the radial coordinate in the focal plane. For instance, with a topological charge $l = 2$, the amplitude of the electric field in the Lyot-stop plane, with (r, γ) coordinates, becomes

$$E_{\mathrm{LS}}(r,\gamma) = \begin{cases} 0 & , \, r < R \\ \\ e^{\imath 2\gamma} \left(\frac{R}{r}\right)^2 & , \, r \geq R \end{cases} . \tag{2.2}$$

Optical vortices can be obtained in two different ways: *scalar* vortices or *vector(ial)* vortices. With scalar vortices, the phase ramp is directly etched in a dielectric material, such as a piece of glass shaped as a helix. The accuracy to be achieved in the glass thickness is a serious technological challenge that remains poorly mastered, even using the most recent micro-fabrication techniques. Moreover, the induced phase profile of scalar vortices is highly chromatic, which makes them unsuitable for significantly wide spectral bands, such as those commonly used in astronomical

[1]This integral reduces to Sonine's for the $l = 2$ case.

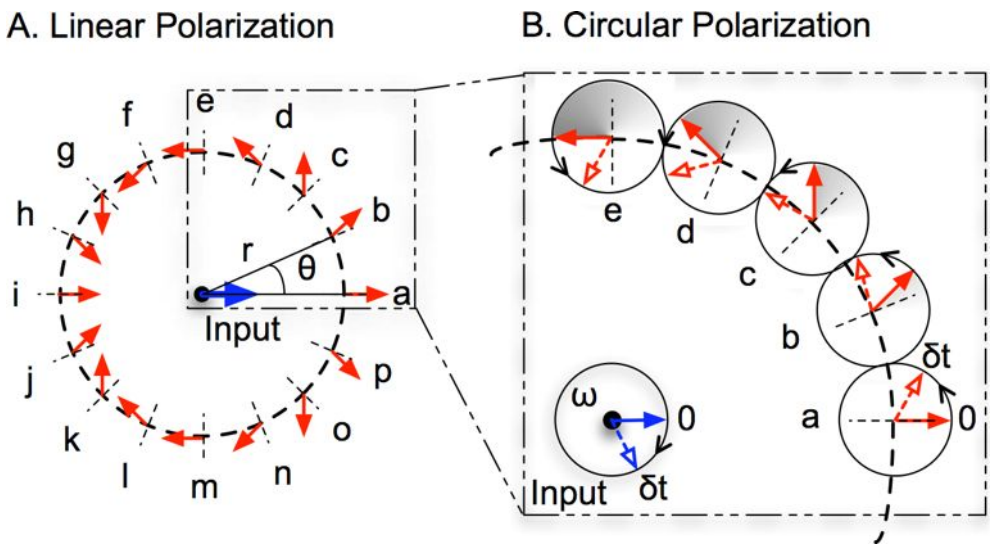

Figure 2.9: The VVC azimuthal phase ramp obtained with a rotationally symmetric half-wave plate (HWP). The rotating optical axis orientation is represented with dashed lines perpendicular to the circumference. The net effect of a HWP on a linear impinging polarization is to rotate it by $-2 \times \alpha$ where α is the angle between the incoming polarization direction and the fast optical axis. An incoming horizontal polarization (blue arrow) is transformed by the vector vortex so that it spins around its center twice as fast as the azimuthal coordinate θ (red arrows). Right: For circular polarization, the starting angle 0 is rotated, therefore the output field rotation is strictly equivalent to a phase delay. From Mawet et al. (2011b).

observations. On the other hand, vector vortices are based on a circularly symmetric half-wave plate (HWP) with an optical axis orientation that rotates about the center (see Figure 2.9). The mask affects the transverse polarisation state cyclicly around the centre to produce a phase ramp. The angle of local rotation of the polarization vector corresponds to a *geometrical* phase ϕ_p known as the Pancharatnam-Berry phase (Pancharatnam 1956; Berry 1987). A complete rotation around the center of the rotationally symmetric HWP provides a total $2 \times 2\pi$ phase ramp, which corresponds to the definition of an optical vortex of topological charge 2. It was rigorously shown (Mawet et al. 2005a; Niv et al. 2006) that vectorial vortices present the same phase ramp as scalar vortices.

Any departure from the HWP condition produces a spatially uniform chromatic leakage in the pupil, orthogonal to the main term bearing the pure geometrical phase modification. The polarization of both terms being orthogonal, one can get rid of the leakage term by inserting polarizing elements upstream and downstream the VVC. Another solution to the chromaticity issue is to build a vertical multi-layer component. The respective optical axes are mutually offset following simple geometrical rules so as to reach an enhanced achromatic retardance across a given wavelength range. A 3-layer design allows reaching the 10^{-9} contrast level over 20% bandwidth in theory, whereas a 5-layer design allows reaching further to 10^{-12} over the same bandwidth.

VVCs are the most recent members of the phase-mask coronagraph family, and are the main subject of our work, especially one sort of VVC technology called the annular groove phase mask (AGPM), and which we describe below (Section 2.3.3) in further details.

2.3 Vector vortex coronagraph technologies

In this section, we describe the three technological solutions used to manufacture VVCs:

- liquid crystal polymers (LCP),
- photonics crystals (PC),
- and subwavelength gratings (SG).

2.3.1 Liquid crystal polymers

Liquid crystal is a state of a material which is between solid crystal (long range order) and liquid phase (no long range order). The same is valid for its properties. Molecules in liquid crystal phase materials have some average alignment, making it anisotropic. Liquid crystal polymers (LCPs) combine the birefringent properties of liquid crystals with the excellent thermo-mechanical properties of polymers. The orientation of a LCP is achieved through photoalignment (see Figure 2.10). To obtain circularly symmetric HWPs, the alignment is set through a rotating exposure process, using linear polarized UV light (McEldowney et al. 2008a,b). Once aligned and cured (using standard polymer curing techniques), the polymer reaches a very stable solid state.

The LCP technology is a proven approach to generate the phase helix, both in the near-infrared and in the optical. Achromatic VVCs made out of LCP have been manufactured and installed on the 200-inch Hale telescope at Palomar in 2009. Because of their small IWA, and lack of *features* anywhere on the mask (except at the very central singularity), their discovery space is close to maximal in terms of search area for faint companions (no dead zones). They have been used behind an off-axis unobscured subaperture corrected with adaptive optics to successfully image, close binaries, brown dwarfs and extrasolar planets (Mawet et al. 2010, 2011a; Serabyn et al. 2010).

With a single-layer design, the LCP VVC is relatively chromatic by nature, since the half-wave retardance is induced only by the space variation of the optical axis orientation across the component. Alignment of liquid crystals in general and LCP specifically, is a key step in making any liquid crystal device, and requires efficient alignment techniques. As of today, many techniques

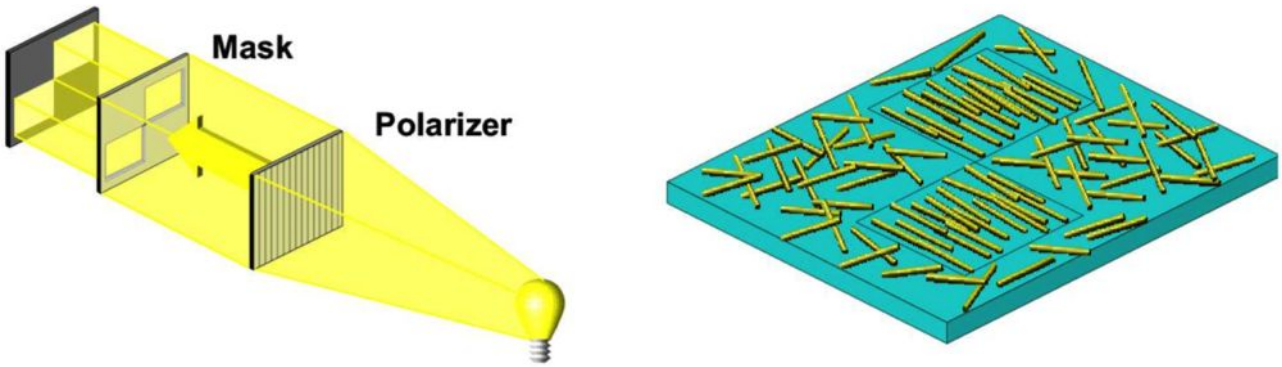

Figure 2.10: Left. Photoalignment with linear polarized UV light through an exposure mask. Right: Alignment of the LCP rods. Regions with no alignment exhibits a random orientation. From Mawet et al. (2011b).

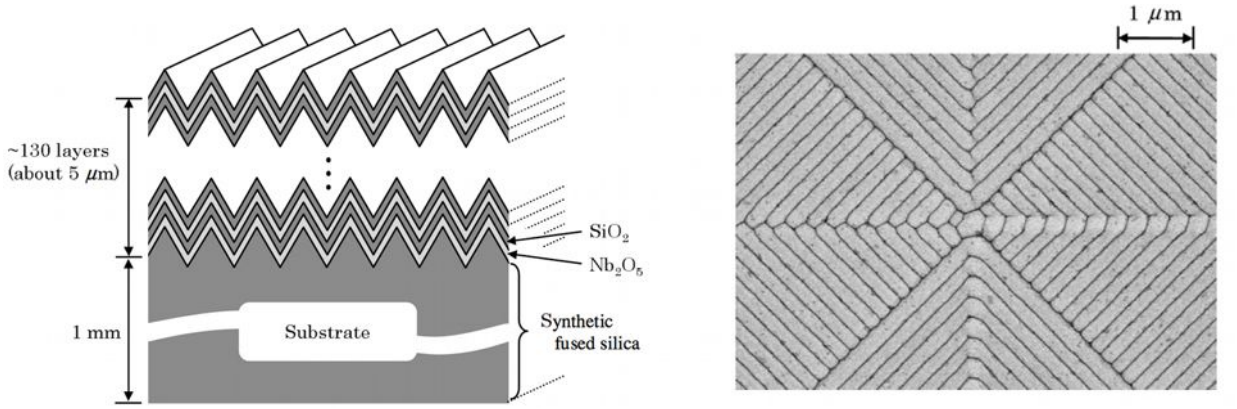

Figure 2.11: Left: Schematic cross-section of an auto-cloned photonics crystal used to synthesize a VVC. Right: Picture (zoom on the central part) of an achromatic 8-octant PC VVC made by Photonics Lattice Inc, Japan. From Murakami et al. (2010b).

are mature and are used in high volume manufacturing processes. However, a perfect alignment of the center of the VVC cannot be achieved, because of the central singularity.

2.3.2 Photonics crystals

Photonics crystals (PCs) are artificial two-dimensional and three-dimensional periodic structures. The particular technology that has been used to synthesize an eight-octant phase mask (8OPM, Murakami et al. 2010b) made out of PCs, and more recently a PC VVC (Murakami et al. 2012), is called *auto-cloning* (Kawakami et al. 1999; Kawashima et al. 2000). Auto-cloned PCs consist of patterned multilayer films fabricated by sputtering deposition (see Figure 2.11, left). The manufacturing process is performed by Photonic Lattice Inc. A periodic corrugated pattern is etched on a synthetic fused silica substrate by means of electron-beam lithography, with an accuracy of about 10 nm (see Figure 2.11, right).

Two dielectric materials (Nb_2O_5 and SiO_2) are alternately deposited on the substrate by radio-frequency sputtering, preserving the corrugated surface. The PC VVC for visible wavelengths is typically composed of about 130 layers with a thickness of about 5 microns in total (Murakami et al. 2010b). Recently, an 8OPM was tested at the high-contrast imaging testbed (HCIT, Jet Propulsion Laboratory) with active leakage filtering method (used for the achromatization). They report contrast levels of the order of $\sim 10^{-8}$ at 800 nm over 10% bandwidth.

2.3.3 Subwavelength gratings: annular-groove phase-masks

A third technological route, which we are pursuing in this thesis, is the subwavelength grating (SG) technology. This method was proposed by our team a few years ago (Mawet et al. 2005a,b). A weakness of LCP and PC VVCs is their bandwidth: they are affected by absorption at wavelengths beyond the near-infrared (H band centered at $\sim 1.65\,\mu$m, K band $\sim 2.2\,\mu$m). Furthermore, they are not intrinsically achromatic. Meanwhile, the demand for instruments in the mid-infrared (L band $\sim 3.8\,\mu$m, M band $\sim 4.8\,\mu$m, N band $\sim 10.5\,\mu$m) is growing in many domains of astrophysics. We use the dispersion of form birefringence of SGs. These gratings are particularly adapted to

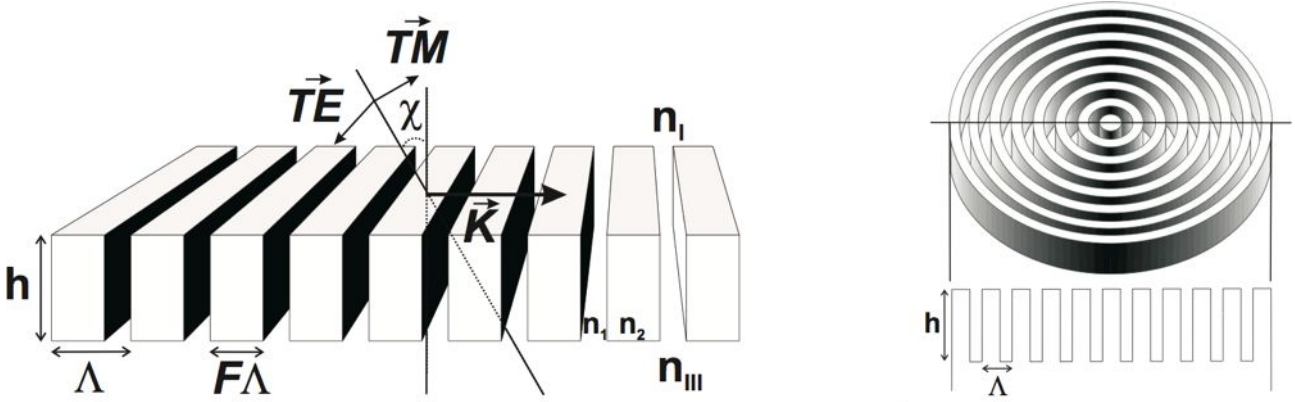

Figure 2.12: Left: Schematic diagram of a SG. The incident light beam vector is perpendicular to the grating lines. The filling factor F is such that $F\Lambda$ corresponds to the width of the grating walls. Right: Schematic diagram of the annular groove phase mask (AGPM), a SG VVC. From Mawet et al. (2005a).

longer wavelengths where the fabrication constraints are relaxed. Indeed, the subwavelength grating feature line is proportional to the wavelength (Biener et al. 2006; Niv et al. 2007).

SGs are micro-optical structures with a period Λ smaller than λ/n, λ being the observing wavelength and n the refractive index of the grating substrate (see Figure 2.12). Such structures do not diffract light as classical spectroscopic gratings. Instead, only zeroth transmitted and reflected orders are allowed to propagate outside the grating, and the incident wavefront is not affected by further aberrations. One can employ these SGs to synthesize artificial birefringent achromatic HWP (Kikuta et al. 1997), and a SG VVC can be obtained by fabricating circularly symmetric HWPs with SG. Such a design is called an annular groove phase mask (AGPM, Mawet et al. 2005a). In the next chapters of this thesis, we describe our work on SGs and the AGPM coronagraph in further details.

2.4 Current and future coronagraphic facilities

After having presented the different types of coronagraphs, and particularly the different technological routes to manufacture VVCs, we finish this chapter with a brief enumeration of the various coronagraphic facilities, existing to date or planned for the future. On the one hand, *ground-based telescopes* are limited by the presence of the Earth atmosphere, which is the cause of: (i) the formation of speckles in the image, (ii) the reduced sensitivity at longer infrared wavelengths (typically above 2 μm), due to water absorption and thermal background emission. On the other hand, space-based telescopes are neither limited in wavelengths nor by atmospheric perturbations, but they are strongly limited in terms of size by the rocket fairing they must fit in.

2.4.1 Ground-based telescopes

As already mentioned before, the capability to distinguish small details in an image is directly improved by increasing the angular resolution of the optical system being used. Since the angular resolution is inversely proportional to the size of the aperture, one needs to increase the diameter

Table 2.1: List of all optical ground-based telescopes with a primary mirror larger than 5 meters in diameter, ranked in order of construction date.

Name	Location	Diameter (m)	Latitude	Altitude (m)	Year
Hale	Mt. Palomar (California)	5	34°N	1706	1948
LOMO	Zelentchuk (Caucasus)	6	47°N	2070	1972
Gemini North	Mauna Kea (Hawaii)	8	19°N	4200	1994
Keck	Mauna Kea (Hawaii)	2×10	19°N	4200	1994
Hobby-Eberly*	Mt. Locke (Texas)	9.2	30°N	3266	1997
VLT	C. Paranal (Chile)	4×8.2	23°S	2650	1998
Subaru	Mauna Kea (Hawaii)	8.4	19°N	4200	1999
Gemini South	C. Pachon (Chile)	8.1	30°S	2738	2001
Magellan	Las Campanas (Chile)	2×6	29°S	2280	2002
LZT**	Vancouver (Canada)	6	49°N	395	2003
Salt*	Sutherland (South Africa)	11.1	32°S	1783	2005
LBT	Mt. Graham (Arizona)	2×8.2	32°N	3266	2007
GranTeCan	La Palma (Canaria)	10.4	28°N	2370	2008

* instruments moving instead of the mirror
** liquid mirror telescope

of the telescope mirror to achieve a higher angular resolution image. For centuries, telescopes with increasing size have been built, especially during the last 20 years giving rise to telescopes with primary mirrors of about 10 meters in diameter (see Table 2.1).

In the future, even more ambitious astronomical projects are programmed (see Figure 2.13, a, b, c) with extremely large primary mirrors (up to 40 meters in diameter) made up of hundreds of segments actively controlled to maintain a near-perfect optical figure, namely:

- the Thirty Meter Telescope (TMT, Nelson & Sanders 2006; Szeto et al. 2008; Crampton et al. 2009; Simard et al. 2010),
- the Giant Magellan Telescope (GMT, Johns 2008; Shectman & Johns 2010),
- the European-Extremely Large Telescope (E-ELT, Gilmozzi & Spyromilio 2007; Kasper et al. 2008, 2010, 2012; Cuby 2010; Kissler-Patig 2010; Brandl et al. 2008, 2010a).

2.4.2 Space-based telescopes

The Hubble Space Telescope (HST) has made tremendous contributions to science during more than 20 years. This unique space observatory has attained unprecedented sensitivity and yielded brilliantly sharp images. As already mentioned in Section 1.5.3, the first direct image of an exoplanet orbiting a main sequence star, Fomalhaut b, was obtained with the HST. But as often happens in science, with the development of new technologies, new challenges raise and new paths must be followed. One of these roads leads to terrestrial planet imaging. We need new space telescopes to reach our ultimate goal, which is to directly image a system that has an Earth in it, where we can actually see that Earth directly.

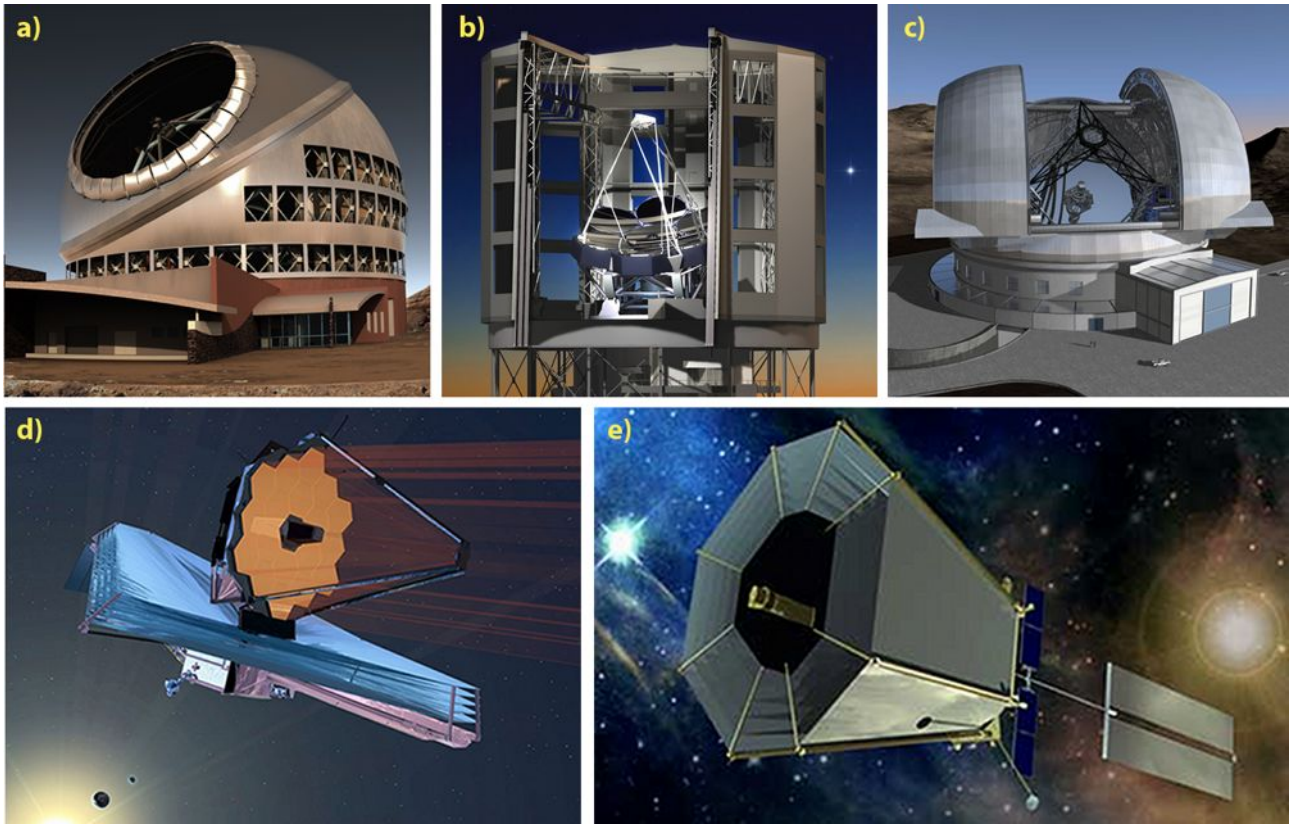

Figure 2.13: Artist's impression pictures. *(a)* The Thirty Meter Telescope (from www.tmt.org). *(b)* The Giant Magellan Telescope (www.gmto.org). *(c)* The European Extremely Large Telescope (www.eso.org). *(d)* The James Webb Space Telescope (www.jwst.nasa.gov). *(e)* The Terrestrial Planet Finder – Coronagraph (exep.jpl.nasa.gov).

James Webb Space Telescope

The James Webb Space Telescope (JWST), the next-generation space telescope, is a collaboration between NASA, Canada and ESA. It is due to be launched in 2018 (see Cosmic Vision, Fridlund et al. 2010). JWST will study the cooler and more distant objects within our Galaxy, but with an unprecedented sensitivity from 0.6 μm to 30 μm. Placed in a location permanently in Earth's shadow (see Figure 2.13, d), JWST will be about 1.5 million kilometers away. Moreover, it will be equipped with coronagraphs for probing structures similar to our own solar system, with a rich diversity of planets and dust structures.

Terrestrial Planet Finder

The Terrestrial Planet Finder (TPF) was a mission concept previously under study by NASA, and initially composed of two architectures.

- Visible light coronagraph (TPF-C): a large optical telescope (see Figure 2.13, e) with a mirror at least 3 times bigger and 100 times more precise than HST, providing a 10^{-9} contrast.
- Infrared astronomical interferometer (TPF-I): four small telescopes (2 m diameter) and one beam combiner spacecraft, flying in formation at the lagrangian point L2, using milimetric metrology to measure the distance apart from each other. This concept is similar to the Darwin project from ESA (Cockell et al. 2009).

Unfortunately, this mission has been cancelled for both technological and economical reasons. As a matter of fact, there is a 25-year so-called *roadmap* from NASA (Des Marais et al. 2003, 2008; Ehrenfreund et al. 2012), and in 2007, the TPF mission has not been selected anymore, but rather "deferred indefinitely", and more recently in 2011, it has been reported as "cancelled".

2.4.3 High contrast imaging capabilities

Among all these telescopes, let us point out the high contrast imaging capabilities, in space and from the ground, which are listed below:

- the High dynamic range imager *Project 1640* (P1640) at the Hale telescope,
- the Second generation Near Infrared Camera (NIRC-2) at the Keck telescope,
- the Nasmyth Adaptive Optics System and the COude Near Infrared CAmera (NAOS-CONICA or NACO) at the VLT,
- the Spectro Polarimetric High contrast Exoplanet REsearch (SPHERE) at the VLT,
- the Gemini Planet Imager (GPI) at the Gemini South telescope,
- the High-Contrast Coronagraphic Imager for Adaptive Optics (HiCIAO) at the Subaru telescope,
- the Subaru Coronagraphic Extreme Adaptive Optics (SCExAO) at the Subaru telescope,
- the Prototype Imaging Spectrograph for Coronagraphic Exoplanet Studies (PISCES) at the LBT,
- the Large Binocular Telescope mid-infrared camera (LMIRcam) at the LBT,
- the Planet Formation Instrument (PFI) at the TMT,
- the Exo-Planet Imaging Camera and Spectrograph (EPICS) at the E-ELT, recently renamed as Planetary Camera and Spectrograph (PCS),
- the Mid-infrared E-ELT Imager and Spectrograph (METIS) at the E-ELT,
- the Advanced Camera for Surveys (ACS) with HST,
- the Near-Infrared Camera (NIRCam) with JWST,
- the Mid-Infrared Instrument (MIRI) with JWST,
- and the Tunable Filter Imager (TFI) with JWST, recently renamed as Near Infrared Imager and Slitless Spectrograph (NIRISS).

A recent review of the state-of-the-art in exoplanet imaging has been conducted by Lawson et al. (2012) as a result of a workshop on exoplanet imaging that was held in Squaw Valley, California, in March of 2012. Contrast ratio capabilities of current and projected telescopes are compared in Figure 2.14, with 5σ detectivity curves scaled for a 1-hour observing time. A high order deformable mirror, e.g. 64 by 64 actuators, is assumed for ground-based telescopes. As shown on the figure, these facilities can be subdivided into three groups: (i) the current generation of instruments (Hale-WCS, VLT-NACO, Keck-NIRC2, and HST-ACS), (ii) the next generation of instruments (Hale-P1640, VLT-SPHERE, and GPI), and (iii) future extremely large telescopes (TMT-PFI, EELT-EPICS, and JWST-NIRCam). As a result of this comparison, we can hopefully expect substantial improvement from the next generation, both in terms of contrast and IWA.

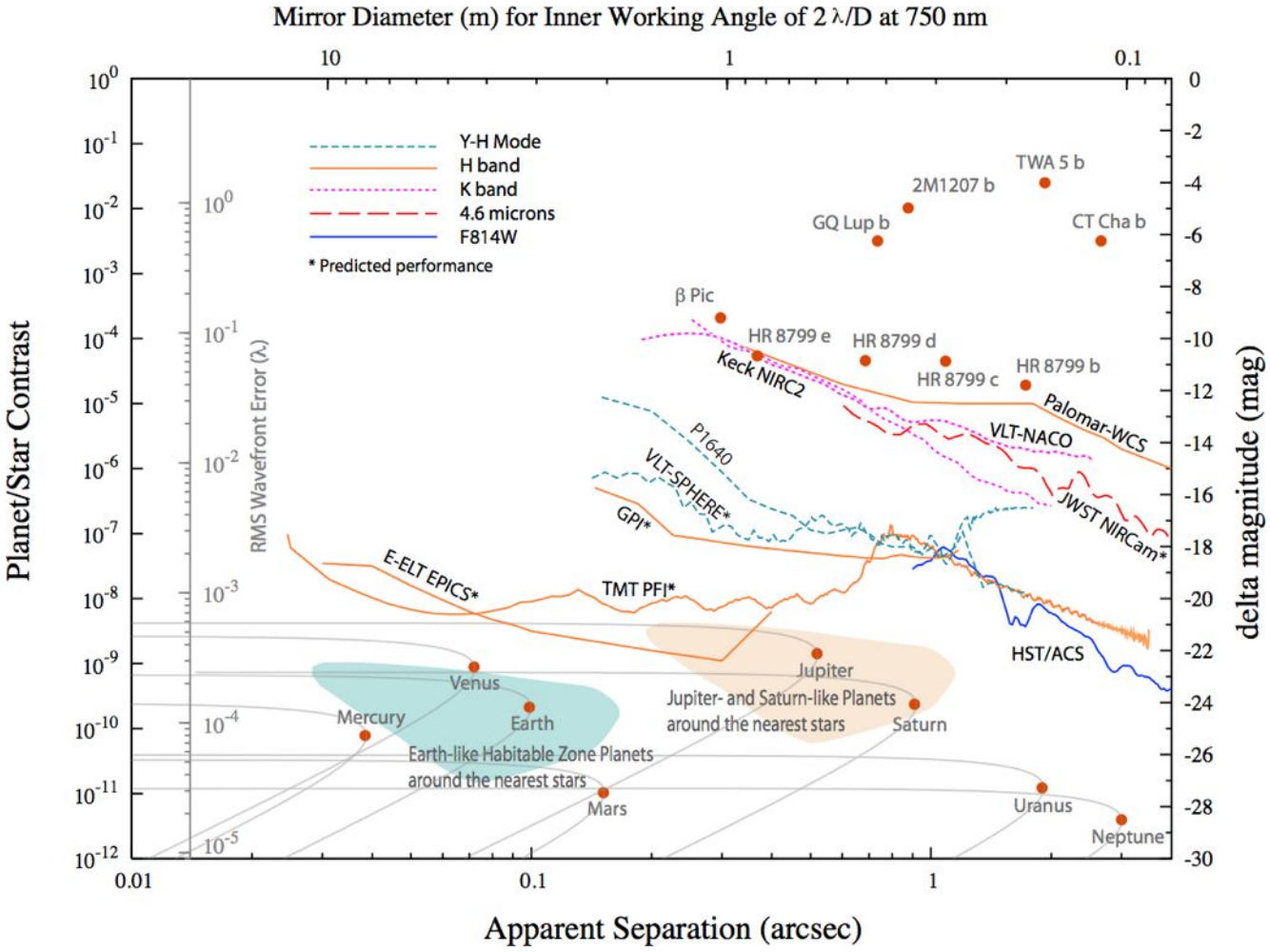

Figure 2.14: State-of-the-art in current and future high contrast imaging capabilities, in space and from the ground. The left axis shows both the planet/star contrast ratio together with the corresponding RMS wavefront quality necessary to reach it. The right axis shows the corresponding Δ magnitude relative to the central star. The x axis shows the angular separation in arcsec. An asterisk denotes the predicted contrast for future instruments. Over-plotted are the K-band fluxes for 9 imaged exoplanets. In the lower part of the figure are plotted our solar system planets as they would appear in reflected light around a Sun-like star at a distance of 10 pc. From Lawson et al. (2012).

2.5 Conclusion

In this chapter, we scanned the wide variety of coronagraph technologies developed over the last 10 years. Most of them, dedicated to hunting long-period planets, have proved rather unsuccessful and a lot of insightful lessons have been learned from the majority of non-detections. It is expected that opening the parameter space to fainter/smaller planets closer to their parent stars will bring many new objects (Crepp & Johnson 2011). Vector vortex coronagraphs (VVCs) can meet the pressing need for devices which, combined with extreme adaptive optics systems, will provide higher contrasts at small inner working angles.

As of today, the annular groove phase mask (AGPM) is the only VVC that can be used beyond the near-infrared, especially in the L band (from 3.5 to 4.1 μm) which offers significant advantages compared to shorter wavelengths (Kasper et al. 2007): (i) the increased planet/star contrast compared to shorter infrared wavelengths sufficiently compensates for the thermal background noise (which is still low enough) not to be the detection constraint, and (ii) the image quality is much higher, with Strehl ratios well above 70% and sometimes as high as 90%, thus reducing speckle noise.

In the next chapters of this thesis, we show how we managed to manufacture achromatic AGPMs for two mid-infrared spectral bands, the results of our measurements in the laboratory, and the first light at the VLT with VISIR (N band) and NACO (L band).

Part II

The road to first manufactured broadband AGPM coronagraphs

3

Achromatic subwavelength grating half-wave plates

Contents

Abstract. *Phase-masks act on the incoming starlight by modifying its phase. The process of destructive interference occurring by combining two portions of the incident light beam, π-phase shifted with respect to each other, can be ideally synthesized by use of specific optical devices called half-wave plates, generally operating at specific wavelengths. Making such components achromatic over wide infrared spectral bandwidths is however crucial for astronomical observations, as was established in Chapter 1. In the present chapter, we present our work on silica and diamond achromatic infrared half-wave plates, by use of micro-optical diffraction gratings operating in the subwavelength domain.*

3.1 Diffraction by subwavelength gratings

Diffraction by a grating can be evaluated using either scalar or vectorial theories. Scalar diffraction theories are not exact theories, since they ignore the vectorial nature of light. On the other hand, they can be convenient because they are easy to implement and little time consuming. This section summarizes the mathematical approaches of both scalar and vectorial methods, and explains how an achromatic subwavelength half-wave plate (HWP) can be optimally designed using a rigorous coupled-wave vectorial method.

3.1.1 Scalar diffraction theory

Diffraction by a grating leads to the dispersion of the incident beam into several orders of diffraction. This happens both in transmission and in reflection. For each diffraction order m, the reflected and transmitted angles, $\theta_r^{(m)}$ and $\theta_t^{(m)}$ respectively, are governed by the so-called diffraction equation:

$$n_i \sin\theta_i \pm n_{i,t} \sin\theta_{r,t}^{(m)} = -\frac{m\lambda}{\Lambda} \tag{3.1}$$

where θ_i and λ are respectively the angle and wavelength of the incident beam, Λ is the grating period, and n_i and n_t are respectively the refractive indices of the incident (superstrate) and the transmitting (substrate) media (see Figure 3.1). This equation is valid both in transmission and reflection, provided that the plus sign with the refractive index n_i corresponds to the reflection and the minus sign with the index n_t corresponds to the transmission (Palmer 2000). Equation 3.1 clearly illustrates that diffraction gratings produce a highly chromatic dispersion for non-zero orders. In the remainder of this dissertation, we consider only the diffraction orders of *transmission gratings*, which we need for manufacturing transmitting half-wave plates (HWPs).

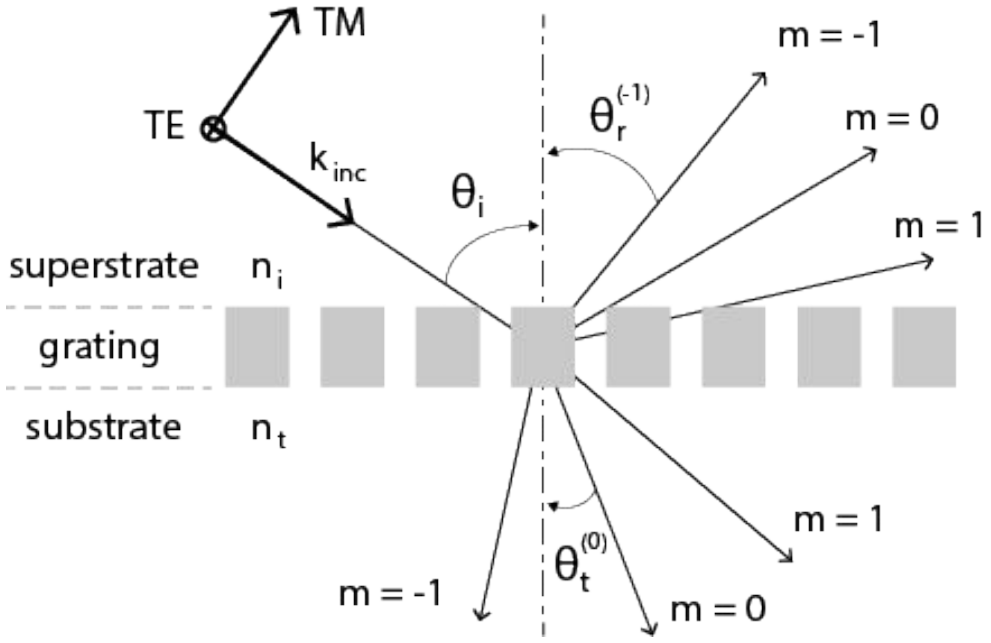

Figure 3.1: Illustration of the grating equation, intentionally limited to the first orders of diffraction in reflection and transmission for the sake clarity. Diffraction angles of the zeroth transmitted and minus first reflected orders are also shown. The incident light beam vector $\vec{k}_{inc}$ is perpendicular to the grating lines.

Following the Huygens's principle, the wavefield at a distance z behind a diffraction screen is described by a superposition of spherical waves. At a large distance $z \gg \frac{1}{2}k(x_0^2 + y_0^2)$ where x_0 and y_0 are the coordinates in the diffraction screen, we reach the so-called *far-field* regime of Fraunhofer diffraction, allowing the approximation of spherical waves by plane waves. In most practical cases, and provided that the Fraunhofer diffraction hypothesis is met, the diffracted field $U(x, y, z)$ can be simply obtained by the Fourier transform $\mathscr{F}$ of the complex amplitude in the aperture plane $U(x_0, y_0)$, which introduces a position dependent phase shift $\phi(x_0, y_0)$ such that

$$U(x, y, z) = \mathscr{F}\left\{U(x_0, y_0)\, e^{i\phi(x_0, y_0)}\right\} \tag{3.2}$$

where x and y are the coordinates in the observation plane situated at a distance z. The amplitudes of the diffraction orders are then determined by the physical structure of the periodic modulation.

In the scalar diffraction theory, the diffraction efficiency for the k^{Th} transmitted order is usually defined as the fraction (I_k) of the total transmitted intensity (I_{trans}) that is diffracted in the k^{Th} order, that is

$$\eta_k = \frac{I_k}{I_{trans}} = \frac{I_k}{\sum\limits_j I_j} \quad \text{with } j \in \mathbb{Z}\,. \tag{3.3}$$

This equation only considers transmission. Any optical loss such as reflection, absorption, or diffusion is neglected. The material is supposed to be linear, isotropic, homogeneous, and uniform.

From a practical point of view, the scalar theory is much easier and less time consuming than rigorous theories. However, it does not take into account the electromagnetic coupling at the boundaries, which is significant for gratings with a period close to the wavelength. As a matter of fact, the scalar theory is generally considered to be accurate when the grating period is larger than five to ten times the wavelength (Swanson 1989; Gremaux & Gallagher 1993; Pommet et al. 1994). Unfortunately, achromatic HWPs can only be conceived with gratings operating in the subwavelength domain, as will be explained in Section 3.2.

3.1.2 Rigorous coupled wave analysis

Common scalar theories of diffraction in gratings do not work in the subwavelength domain. In order to simulate the grating response and to calculate its form birefringence, we must consider the vectorial nature of light. Since the development of electromagnetic theories, it has been known that any form of light is composed of an electric field $\vec{E}$ and a magnetic one $\vec{H}$, both being perpendicular to the direction of propagation $\vec{k}$ and mutually orthogonal. Each of these fields can be represented by two orthogonal linearly polarized components (see Figure 3.1):

- the *transverse electric* (TE) polarization, perpendicular to the plane of incidence, i.e. the plane made by the propagation direction and a vector perpendicular to the plane of the grating surface,

- and the *transverse magnetic* (TM) polarization, parallel to the plane of incidence.

Nowadays, rigorous theories describing the behaviour of light in complex situations are commonly used. Several rigorous (or exact) theories coexist to solve diffraction problems. All these methods tackle Maxwell's equations in combination with exact boundary conditions, i.e, the continuity of the tangential components at the interface with the dielectric material. Let us cite some of the most famous vectorial diffraction methods (Petit 1980; Moharam & Gaylord 1981; Sheng 1982; Sheng et al. 1982; Maystre 1984):

- the integral method,
- the classical differential method,
- the modal method,
- the finite-difference time domain (FDTD) method,
- and the coupled-wave method.

In this thesis, we use the rigorous coupled-wave analysis (RCWA) method, also called the Fourier modal method (FMM) because it is based on a decomposition of the field on a Fourier basis. This method is called rigorous only in the sense that it solves Maxwell's equations without simplifying assumptions and without iterative techniques. The use of RCWA at the University of Liège dates back to the early 1990s. The RCWA code has been enhanced repeatedly by several generations of researchers, and reprogrammed into different languages such as LabVIEW® (Lenaerts 2005) and MATLAB® (Mawet 2006). In this context, we contributed to the ongoing evolution and continuous improvement of the RCWA software with the performing and versatile language of MATLAB®. The algorithm can solve two-dimensional gratings (in x and y) and can take conical incidence into account. The source code being available, its implementation may be easily modified to introduce new personalized grating profiles.

RCWA is an analysis method which was originally developed by Moharam & Gaylord (1981) for solving the diffraction produced by phase sinusoidal plane gratings. Since then, many improvements have been made on the RCWA method, which is now applicable to any multilayer grating profile (Li 1993, 1994), including conical incidence and metallic gratings (Lalanne & Morris 1996), and even aperiodic structures (Pisarenco et al. 2011). The algorithm that we used for RCWA, also called the *S-matrix algorithm*, converts the analytical grating-diffraction problem into a semi-analytical matrix problem: Maxwell's equations are analytically solved in the longitudinal z axis, layer by layer. As shown in Figure 3.2, the diffractive structure must be divided into rectangular slices with constant properties along the longitudinal axis. All grating layers must have the same periodicity along each dimension (Λ_x and Λ_y are constants).

We will now display the headlines of the algorithm, without going into too many mathematical considerations, which are not the purpose of this work. For a complete discussion of the RCWA algorithm, please refer to Moharam et al. (1995) and Mawet (2006). Let us start with Maxwell's equations in the ℓ^{Th} grating layer

$$\vec{\nabla} \times \vec{E}_\ell = -j\omega\mu_0 \vec{H}_\ell \ , \tag{3.4}$$

$$\vec{\nabla} \times \vec{H}_\ell = -j\omega\varepsilon_\ell(x,y)\varepsilon_0 \vec{E}_\ell \ , \tag{3.5}$$

in which ε_0 and μ_0 are the permittivity and permeability of free space, and ε_ℓ is the ℓ^{Th}-layer permittivity.

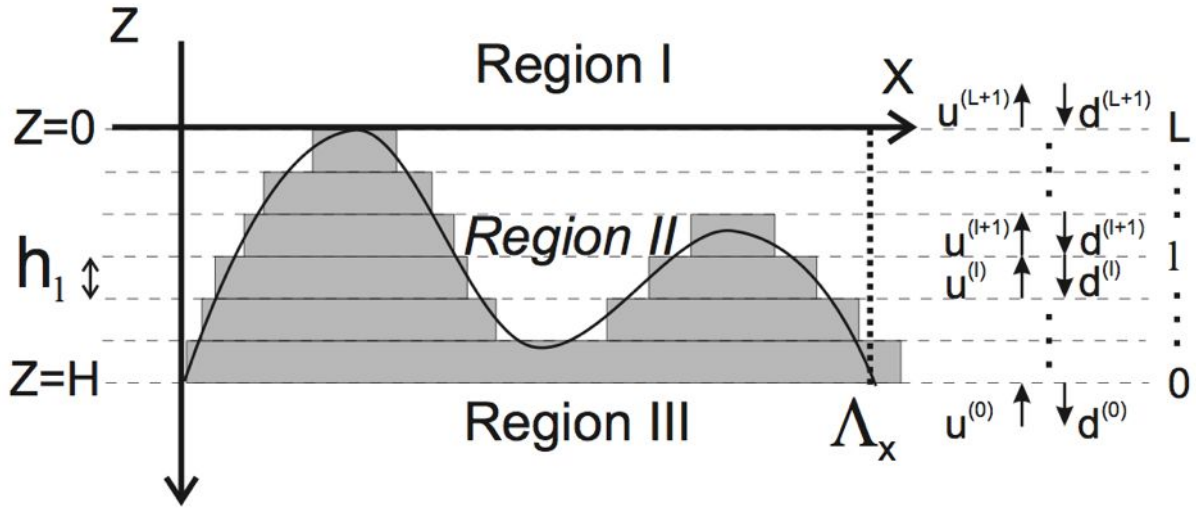

Figure 3.2: RCWA algorithm discretization of the diffractive profile along the X axis. The number of layers in the stack is L and the total thickness of the stack is $H_\ell = \sum_{\ell=1}^{L} h_\ell$. The whole stack can be divided into three regions: the incident region (Region I), the stack region (Region II), and the exit region (Region III). From Mawet (2006).

RCWA expresses the electromagnetic fields in both the incident and the transmitting regions as solutions to Maxwell's equations. The algorithm involves a Fourier expansion of the fields inside each layer into a finite number of coupled space harmonics, which are also solutions to Maxwell's equations. The tangential field components are then matched at each boundary layer within the structure to ensure continuity. The electric field $\vec{E}_\ell$ (respectively, the magnetic field $\vec{H}_\ell$) may be expressed as Fourier expansions in terms of the spatial harmonics $\vec{S}_\ell^{(m,n)}$ (respectively $\vec{U}_\ell^{(m,n)}$), with m and n being the diffraction orders of the two-dimensional grating. To numerically solve this system of coupled differential equations, the problem is expressed using matrices (in bold)

$$\begin{bmatrix} \frac{\partial^2 \mathbf{S}_{\mathbf{y},\ell}}{\partial \mathbf{z'^2}} \\ \frac{\partial^2 \mathbf{S}_{\mathbf{x},\ell}}{\partial \mathbf{z'^2}} \end{bmatrix} = \mathbf{\Omega} \begin{bmatrix} \mathbf{S}_{\mathbf{y},\ell} \\ \mathbf{S}_{\mathbf{x},\ell} \end{bmatrix} , \tag{3.6}$$

in which

$$\mathbf{\Omega} = \begin{bmatrix} \mathbf{k_x^2} + \mathbf{D}[\alpha\epsilon_\ell + (\mathbf{1}-\alpha)\mathbf{A}_\ell^{-\mathbf{1}}] & \mathbf{k_y}(\epsilon_\ell^{-\mathbf{1}}\mathbf{k_x}[\alpha\mathbf{A}_\ell^{-\mathbf{1}} + (\mathbf{1}-\alpha)\epsilon_\ell] - \mathbf{k_x}) \\ \mathbf{k_x}(\epsilon_\ell^{-\mathbf{1}}\mathbf{k_y}[\alpha\epsilon_\ell + (\mathbf{1}-\alpha)\mathbf{A}_\ell^{-\mathbf{1}}] - \mathbf{k_y}) & \mathbf{k_y^2} + \mathbf{B}[\alpha\mathbf{A}_\ell^{-\mathbf{1}} + (\mathbf{1}-\alpha)\epsilon_\ell] \end{bmatrix} \tag{3.7}$$

and

$$\mathbf{B} = \mathbf{k_x}\epsilon_\ell^{-\mathbf{1}}\mathbf{k_x} - \mathbf{I} , \tag{3.8}$$

$$\mathbf{D} = \mathbf{k_x}\epsilon_\ell^{-\mathbf{1}}\mathbf{k_y} - \mathbf{I} , \tag{3.9}$$

with ϵ_ℓ and $\mathbf{A}_\ell$ the permittivity and inverse permittivity matrices. The diagonal matrices $\mathbf{k_x}$ and $\mathbf{k_y}$ are formed from the wave vector components. If M and N are the numbers of space harmonics

retained along the X and Y axis, then $\mathbf{I}$ is the identity matrix of dimension MN. The parameter α depends on the two-dimensional grating geometry (Lalanne & Morris 1996) and ranges in the interval $[0, 1]$.

The coupled-wave equations are then solved by finding the eigenvalues and eigenvectors of $\mathbf{\Omega}$ in every layer. The transmission ($\mathbf{T_{uu},\ell}$ and $\mathbf{T_{dd},\ell}$) and reflection ($\mathbf{R_{du},\ell}$ and $\mathbf{R_{ud},\ell}$) matrices matching the boundary conditions at the appropriate interfaces, as well as the up-wave ($\mathbf{u}_\ell$) and down-wave ($\mathbf{d}_\ell$) amplitude vectors (see Figure 3.2), are then computed in a recursive way, using the S-matrix ($\mathbf{S}_\ell$) algorithm that links the waves in the layer $\ell + 1$ and those of medium 0 in the following way

$$\begin{bmatrix} \mathbf{u_{\ell+1}} \\ \mathbf{d_0} \end{bmatrix} = \mathbf{S}_\ell \begin{bmatrix} \mathbf{u_0} \\ \mathbf{d_{\ell+1}} \end{bmatrix} , \tag{3.10}$$

with

$$\mathbf{S}_\ell = \begin{bmatrix} \mathbf{T_{uu},\ell} & \mathbf{R_{ud},\ell} \\ \mathbf{R_{du},\ell} & \mathbf{T_{dd},\ell} \end{bmatrix} , \tag{3.11}$$

which finally gives $\mathbf{u_{L+1}}$ and $\mathbf{d_0}$. These vectors directly give the complex amplitudes, in the two modes (TE/TM), of mn-th reflected ($\vec{R}^{(m,n)}_{\mathrm{TE}}$ and $\vec{R}^{(m,n)}_{\mathrm{TM}}$) and transmitted ($\vec{T}^{(m,n)}_{\mathrm{TE}}$ and $\vec{T}^{(m,n)}_{\mathrm{TM}}$) orders, respectively, describing the entire diffractive characteristics of the simulated structure:

- the diffraction efficiencies for TE, in reflection $\eta^{(m,n)}_{r,\mathrm{TE}}$ and in transmission $\eta^{(m,n)}_{t,\mathrm{TE}}$,
- the diffraction efficiencies for TM, in reflection $\eta^{(m,n)}_{r,\mathrm{TM}}$ and in transmission $\eta^{(m,n)}_{t,\mathrm{TM}}$,
- and the phase shifts between TE and TM, in reflection $\Delta\Phi^{(m,n)}_{r,\mathrm{TE-TM}}$ and in transmission $\Delta\Phi^{(m,n)}_{t,\mathrm{TE-TM}}$.

Unlike scalar theories, RCWA does not make any theoretical approximation. Its only limiting factor resides in the computation parameters, such as the number of Fourier orders taken into account, or the discretization step. It also makes the assumption of an infinite grating, which is legitimate in most of applications. RCWA is very accurate regarding dielectric gratings which need few Fourier orders, and whose simple profile does not necessitate too many layers. In the rest of this chapter, we mainly use one-dimensional gratings. Therefore, we will adopt the following notations:

$$\begin{aligned} \eta^{(m)}_{\mathrm{R}} &= \tfrac{\eta^{(m)}_{\mathrm{r,TE}} + \eta^{(m)}_{\mathrm{r,TM}}}{2} , \\ \eta^{(m)}_{\mathrm{T}} &= \tfrac{\eta^{(m)}_{\mathrm{t,TE}} + \eta^{(m)}_{\mathrm{t,TM}}}{2} , \\ \Delta\Phi^{(m)}_{\mathrm{R}} &= \Delta\Phi^{(m)}_{\mathrm{r,TE-TM}} , \\ \Delta\Phi^{(m)}_{\mathrm{T}} &= \Delta\Phi^{(m)}_{\mathrm{t,TE-TM}} . \end{aligned} \tag{3.12}$$

3.2 Subwavelength grating half-wave plates

Wave plates are an essential tool for modifying the polarization of an incoming light beam. They are commonly used in many applications as retarder or phase shifter. In astrophysics, when it comes to observe a very high contrast scene, one must be able to cancel the bright source, or at least drastically reduce its intensity. This attenuation can be achieved by combining two portions of the incident light beam, one of which having undergone a π-phase shift. Therefore, a half-wave plate (HWP) is by definition the ideal tool. In many astronomical applications, HWPs are also used as polarization rotators. In this section, we explain how one can synthesize achromatic HWPs with micro-optical one-dimensional diffraction gratings, operating in the subwavelength domain.

3.2.1 Zero-order gratings

A subwavelength grating (SG) is a structure with a period Λ generally much smaller than the wavelength of the incident light λ. One of the major advantages of such a structure is that it only propagates the zeroth ($m = 0$) orders, both in transmission and in reflexion. For this reason, SG are often called zero-order gratings (ZOG). The zero-order reflection and transmission angles can be obtained with equation 3.1, for $m = 0$

$$n_i \sin\theta_i \pm n_{i,t} \sin\theta_{r,t}^{(0)} = 0 \ , \tag{3.13}$$

which gives the Snell-Descartes relations

$$\begin{cases} \theta_i = -\theta_r^{(0)} & \text{in reflection ,} \\ \\ n_i \ \sin\theta_i = n_t \ \sin\theta_t^{(0)} & \text{in transmission .} \end{cases} \tag{3.14}$$

Contrary to a classical spectroscopic diffraction grating, a SG does not disperse the light since it blocks all non-zero orders. This property can mathematically lead to a condition for having a SG, that is a maximal period size, with respect to the wavelength. Using the diffraction equation again, one can deduce the condition for the first orders, both in reflection and transmission, to be evanescent, in other words to make $\pi/2$ angles with the normal.

In the reflection case, we have

$$m = \pm 1 \ \Leftrightarrow \ \sin\theta_r^{(\pm 1)} = \mp 1 \ , \tag{3.15}$$

that leads to two inequalities

$$\begin{cases} n_i \ \sin\theta_i - n_i \ \geq \ -\frac{\lambda}{\Lambda} \\ \\ n_i \ \sin\theta_i + n_i \ \leq \ \frac{\lambda}{\Lambda} \end{cases} \tag{3.16}$$

which we can write, in the case of a positive incidence angle θ_i ,

$$\frac{\lambda}{\Lambda} \ \geq \ n_i \ \pm \ n_i \sin\theta_i \ \geq \ n_i \ + \ n_i \sin\theta_i \ . \tag{3.17}$$

Similarly, in the transmission case, we have

$$m = \pm 1 \ \Leftrightarrow \ \sin\theta_t^{(\pm 1)} = \pm 1 \ , \tag{3.18}$$

that leads to the inequality

$$\frac{\lambda}{\Lambda} \geq n_t \pm n_i \sin\theta_i \geq n_t + n_i \sin\theta_i \ . \tag{3.19}$$

From equations 3.17 and 3.19, we can write the general condition for having a SG:

$$\frac{\Lambda}{\lambda} \leq \frac{1}{n_i \sin\theta_i + \max(n_i, n_t)} \tag{3.20}$$

where θ_i is the incidence angle and n_i and n_t are the refractive indices of the incident (superstrate) and transmitting (substrate) media, respectively (see Figure 3.1).

3.2.2 Effective-medium theory

While transmitting through a SG, the zeroth order is affected by an effective refractive index n_{eff} corresponding to the average amount of material in the grating layer. This phenomenon, called homogenization, can lead to *effective index models* allowing to calculate n_{eff}. These models use the so-called *filling factor* which is illustrated in Figure 3.3.

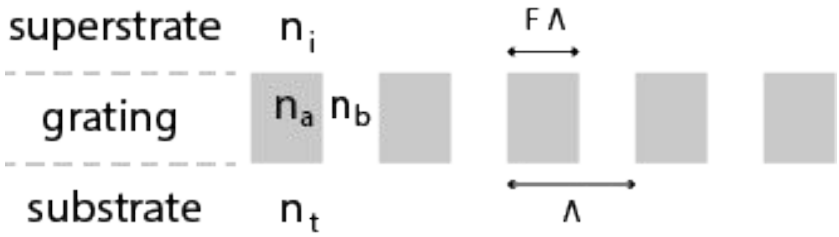

Figure 3.3: Illustration of a one-dimensional grating, with n_a and n_b the structure's refractive indices, and F the filling factor.

In the quasi-static regime, that is when $\lambda/\Lambda \ll 1$, the effective refractive index of a one-dimensional surface relief grating is calculated using the zeroth-order effective medium theory (EMT0) by a simple averaging treatment (Born & Wolf 1999) leading to the following effective indices for the TE and TM states of polarization:

$$n_{\text{eff},0}^{\text{TE}} = \left(F n_a^2 + (1-F) n_b^2\right)^{1/2} \ , \tag{3.21}$$

$$n_{\text{eff},0}^{\text{TM}} = \left(\frac{n_a^2\, n_b^2}{F n_b^2 + (1-F) n_a^2}\right)^{1/2} \ . \tag{3.22}$$

When the ratio λ/Λ is no longer negligible, one must use higher-order effective medium theories. These take into account other parameters of the whole diffraction problem (Lalanne & Lemercier-Lalanne 1997), such as the grating period Λ and the wavelength λ. As an example, the second-order effective medium theory (EMT2) allows the following expressions to be derived for the effective indices (Brundrett et al. 1994):

$$n_{\text{eff},2}^{\text{TE}} = \left[\left(n_{\text{eff},0}^{\text{TE}}\right)^2 + \frac{1}{3}\left(\frac{\Lambda}{\lambda}\right)^2 \pi^2 F^2 \left(1-F\right)^2 \left(n_a^2 - n_b^2\right)^2 \right]^{1/2} , \tag{3.23}$$

$$n_{\text{eff},2}^{\text{TM}} = \left[\left(n_{\text{eff},0}^{\text{TM}}\right)^2 + \frac{1}{3}\left(\frac{\Lambda}{\lambda}\right)^2 \pi^2 F^2 \left(1-F\right)^2 \left(\frac{1}{n_a^2} - \frac{1}{n_b^2}\right)^2 \left(n_{\text{eff},0}^{\text{TM}}\right)^6 \left(n_{\text{eff},0}^{\text{TE}}\right)^2 \right]^{1/2} . \tag{3.24}$$

However, these methods only give approximate results. Nowadays, with the increasing computation capabilities, they are generally abandoned in favor of rigorous methods such as RCWA.

3.2.3 Achromatic wave plates

A classical wave plate is a simple birefringent crystal cut into a plate. As a birefringent medium, it has two different refractive indices, n_{TE} and n_{TM}. The phase retardance $\Delta\Phi$ introduced by such a wave plate between the two polarization components is dependent on the wavelength, and is given by

$$\Delta\Phi_{\text{TE}-\text{TM}}(\lambda) = \left(\frac{2\pi}{\lambda}\right) h\, \Delta n(\lambda) \tag{3.25}$$

showing that it varies hyperbolically with the wavelength λ, while being proportional to the thickness h of the crystal, and the birefringence $\Delta n = n_{\text{TE}} - n_{\text{TM}}$, which is a non-linear function of λ. This limits the operation of single wave plates to monochromatic light. However, a large spectral bandwidth is needed in many cases, especially in astrophysics, both to increase the signal to noise ratio and to allow spectrophotometry.

Subwavelength gratings benefit from the property of birefringence, which is a dispersive *form* birefringence:

$$\Delta n_{\text{form}}(\lambda) = n_{\text{TE}}(\lambda) - n_{\text{TM}}(\lambda) . \tag{3.26}$$

The phase retardation $\Delta\Phi$ introduced by a birefringent SG becomes

$$\Delta\Phi_{\text{TE}-\text{TM}}(\lambda) = \left(\frac{2\pi}{\lambda}\right) h\, \Delta n_{\text{form}}(\lambda) \tag{3.27}$$

where h is now the optical path through the birefringent SG. By carefully selecting the grating parameters (geometry, material, incidence), the wavelength dependence in Δn_{form} can be tuned to be closely proportional to the wavelength across a wide spectral band. By doing so, the phase shift can be made constant over a wavelength range as large as possible, thereby synthesising an artificial birefringent achromatic wave plate (Kikuta et al. 1997) .

3.2.4 Selecting a material: the overriding criteria

We want to develop an achromatic HWP which will be integrated into the design of vector vortex coronagraphs, as we will see in Chapter 4. By keeping this in mind, we can scan the wide variety of dielectric materials and their properties. The design of any micro-optical component requires the selection of adequate materials, resulting from a trade off between their optical, thermal and mechanical properties. For this purpose, a study of the infrared material characteristics, such as transmission, refraction and absorption, is essential. In this section, we examine a selection of materials amongst the most frequently and successfully used for infrared optics applications, namely: IR-grade fused silica Infrasil® (SiO_2), sapphire (Al_2O_3), calcium fluoride (CaF_2), magnesium fluoride (MgF_2), barium fluoride (BaF_2), gallium arsenide ($GaAs$), silicon (Si), germanium (Ge), zinc sulfide (ZnS), zinc selenide ($ZnSe$), and diamond (C)[2].

Useful wavelength range

As we already stated in Section 2.3.3, SGs are particularly adapted to longer wavelengths where the fabrication constraints are relaxed since the subwavelength grating feature line is proportional to the wavelength (Biener et al. 2006; Niv et al. 2007). However, the visible regime is also very interesting from the astronomical point of view. We need a material that is transparent from the visible to the mid-infrared (see Figure 3.4).

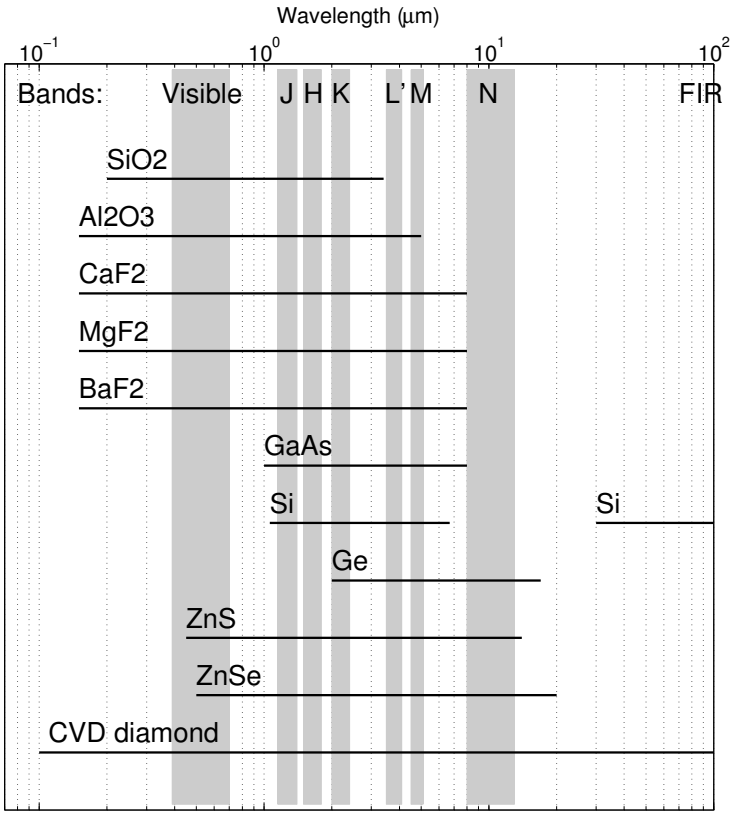

Figure 3.4: Useful wavelength ranges of some dielectric materials used for optical applications in the infrared domain, set on a logarithmic scale, together with spectral bands commonly used as astronomical filters.

[2]Diamond is an allotrope of carbon, i.e., a specific structural form of the element where the atoms are bonded in a tetrahedral lattice arrangement.

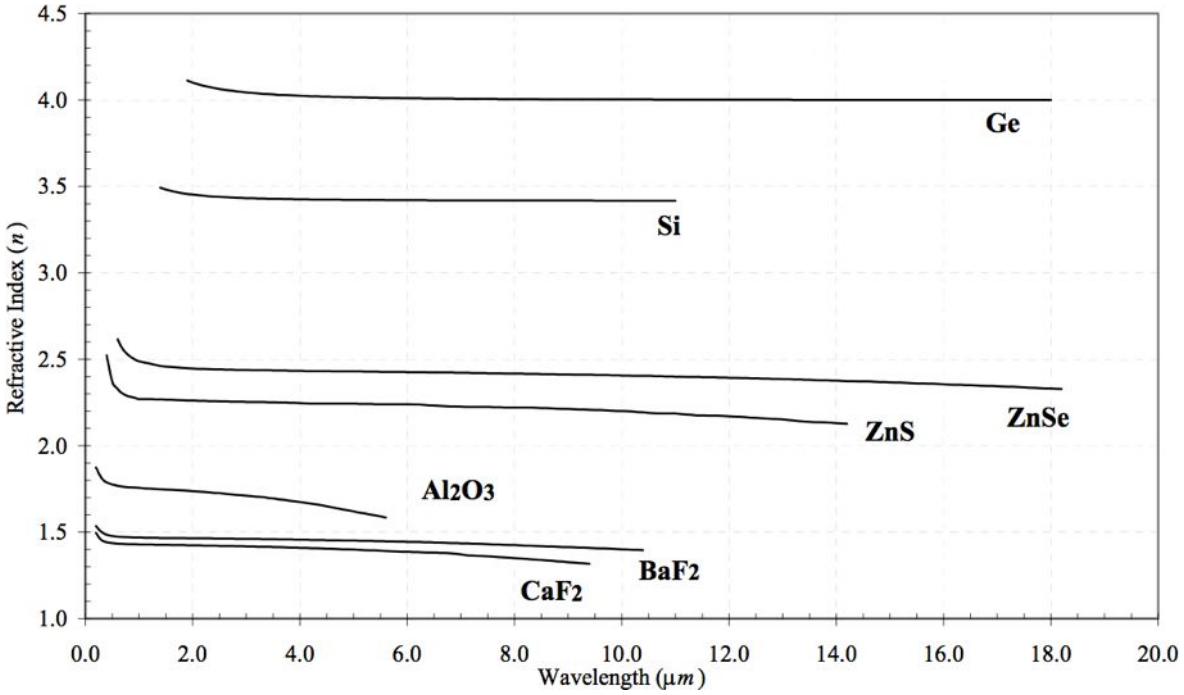

Figure 3.5: Refractive index dispersion of several common infrared substrate materials at 300K. Data from Hawkins (1998).

Some of these materials (e.g., Si, $GaAs$) are famous for their well mastered microfabrication processes, especially Si which is extensively used in micro-electronic technologies. From this aspect, we consider Si as the most interesting material for infrared applications from $\sim$1 μm to $\sim$7 μm. However, both Si and $GaAs$ are not suitable for transmission in the optical domain, as well as in the astronomical N band extending from 8 to 13 μm, due to multi-phonon absorption features as shown in Appendix A. Ge is a very interesting material for N-band applications but has a very high index ($\sim$4) and absorption, which reduce its transmittance to $\sim$45%. ZnS and $ZnSe$ are good alternatives to Ge, with lower refractive indices ($\sim$2.2 and 2.4 respectively) and a higher dispersion, useful for the HWP achromatization.

When it comes to the visible-to-near-infrared bandwidth, several materials can do the trick. From the manufacturability point of view, SiO_2 is a reasonable option for producing SGs since their fabrication process is directly inherited from Si micro-electronic technologies. However, the most interesting material is diamond, which is transparent from the UV to the far IR (see Figure 3.4). A few years ago, in the early phase of this thesis work, diamond microfabrication techniques were only at the dawn of unleashing their entire potential. Therefore, we have followed two parallel paths, which we will explain further: SiO_2 as a first option (Section 3.3) and diamond as a second option (Section 3.4).

Refractive index

A similar spectral behaviour is observed in the refractive indices of all dielectric materials (see Figure 3.5), which exhibit a decline in refractive index mainly caused by absorption, as we will see later in this section. Reducing the temperature of a dielectric material generally reduces linearly its refractive index. These similar dispersion curve shapes have been approximated by Sellmeier, Herzberger and Lorentzian mathematical functions. Modified temperature-dependent polynomial

Table 3.1: List of familiar dielectric materials mostly used from the visible to the thermal infrared. Spectral range, average transmission and refractive index are given at 300 K.

Name	Chem. formula	Range (μm)	T	n @ 2 μm
IR-grade fused silica	SiO_2	0.2 – 3.4	90%	1.46
Sapphire	Al_2O_3	0.15 – 5.0	84%	1.76
Calcium Fluoride	CaF_2	0.15 – 8.0	92%	1.43
Magnesium Fluoride	MgF_2	0.15 – 8.0	95%	1.38
Barium Fluoride	BaF_2	0.3 – 9.5	92%	1.47
Gallium Arsenide	$GaAs$	1.0 – 8.0	53%	3.14
Silicon	Si	1.06–6.7 and 30–100+	52%	3.44
Germanium	Ge	2.0 – 17.0	43%	4.1
Zinc Sulfide	ZnS	1.0 – 14.0	52%	2.27
Zinc Selenide	$ZnSe$	0.5 – 20.0	69%	2.44
CVD-diamond	C^*	0.1 – 100+	83%	2.38

* diamond is an allotrope of carbon

regressions (for Si, ZnS, and $ZnSe$) and Sellmeier equations (for diamond and Ge), proven to be the most suitable curve fitting algorithms for calculations of refractive index data (Bundy 1962; Tropf 1995; Hawkins 1998), have been implemented to the RCWA algorithm used in this thesis:

$$n_{\text{Si, ZnS, ZnSe}}(\lambda, T) = A + B\lambda + C\lambda^2 + D\lambda^3 + E\lambda^4 \ , \tag{3.28}$$

$$n_{\text{diamond, Ge}}(\lambda, T) = \sqrt{A + \frac{B\lambda^2}{(\lambda^2 - C)} + \frac{D\lambda^2}{(\lambda^2 - E)}} \ , \tag{3.29}$$

where the coefficients (A, B, C, D, and E) are temperature-dependent. These coefficients are given in Appendix A for diamond, Ge, Si, ZnS, and $ZnSe$, together with individual refractive index dispersion curves, at several temperatures. A list of refractive index values for more familiar dielectric materials is given in Table 3.1, at a wavelength of 2 μm and a temperature of 300 K.

Transmission and reflection

When a beam is impinging on the surface of an optically transparent material, part of the light is reflected from the surface and another part is transmitted to the material. Considering the specific domain of coronagraphy to which our HWP is dedicated, we can make the hypothesis that the incident medium is air ($n_{\text{air}} = 1$). In the theoretical case of natural (unpolarized) light at normal incidence ($\theta_i = 0$), the reflectance R_{theo} and transmittance T_{theo} of a polished and uncoated plane substrate, with no absorption and no scattering, can be predicted from the refractive index n of the substrate using the well-known Fresnel relations:

$$R = \frac{(n-1)^2}{(n+1)^2} \tag{3.30}$$

$$T = \frac{4n}{(n+1)^2} \tag{3.31}$$

Absorption coefficient α

Equations 3.31 and 3.30 are correct only in the theoretical case where the intensity of the incoming light I_0 is equal to the sum of the reflected and transmitted intensities. However, in practice, when light propagates through a dielectric material, part of it is absorbed. The amount of this absorption can be taken into account by defining a complex index of refraction

$$\tilde{n} = n + i\kappa \tag{3.32}$$

where the imaginary part, κ, is called the extinction coefficient. The complex wave number $\tilde{k}$ is then written

$$\tilde{k} = \frac{2\pi\,\tilde{n}}{\lambda} = \frac{2\pi n}{\lambda} + i\,\frac{2\pi\kappa}{\lambda} = k + i\,\frac{2\pi\kappa}{\lambda} \tag{3.33}$$

which, introduced into the general expression for the electric field of a plane electromagnetic wave, traveling in the z direction, gives

$$\vec{E}(z,t) = \vec{E_0}\, e^{i\left(\tilde{k}z - \omega t\right)} = \vec{E_0}\, e^{i\left(\frac{2\pi n}{\lambda}z + i\,\frac{2\pi\kappa}{\lambda}z - \omega t\right)} = e^{-\frac{2\pi\kappa}{\lambda}}\,\vec{E_0}\, e^{i\,(kz-\omega t)} \quad . \tag{3.34}$$

As a result, we see that the absorption produces an exponential decay. As the intensity of an incident wave through a solid is the conductivity (σ) of the solid multiplied by the square of the electric field vector ($I = \sigma E^2$), then the fraction of the incident light that has propagated through the material from position $z = 0$ to position $z = h$ is given by

$$\frac{I(h)}{I(0)} = \frac{\sigma E^2(h)}{\sigma E^2(0)} = e^{\frac{-4\pi\kappa}{\lambda}} \quad . \tag{3.35}$$

This leads to the definition of the absorption coefficient α, expressed in terms of the extinction coefficient κ,

$$\alpha = \frac{4\pi\kappa}{\lambda} \tag{3.36}$$

resulting in the equation of the attenuation of the intensity of light while propagating through a material layer of thickness h:

$$I = I_0\, e^{-\alpha\, h} \tag{3.37}$$

usually referred to as the Beer-Lambert law.

After the wave has traversed the first surface boundary of the substrate (referred hereafter as the *in* surface), it undergoes a second reflection from the inside of the second surface boundary (referred hereafter as the *out* surface). This second surface reflection is further reflected back from the front surface again, producing multiple internal reflections. If these reflections are all added up, the total external reflectance R_{tot} and transmittance T_{tot} become:

$$R_{\text{tot}} = R_{\text{in}} + R_{\text{out}}\, T_{\text{in}}^2\, e^{-2\alpha h} \left(1 + R_{\text{in}} R_{\text{out}}\, e^{-2\alpha h} + R_{\text{in}}^2 R_{\text{out}}^2\, e^{-4\alpha h} + ...\right) \ , \tag{3.38}$$

$$T_{\text{tot}} = T_{\text{in}}\, T_{\text{out}}\, e^{-\alpha h} \left(1 + R_{\text{out}} R_{\text{in}}\, e^{-2\alpha h} + R_{\text{out}}^2 R_{\text{in}}^2\, e^{-4\alpha h} + ...\right) \ . \tag{3.39}$$

In the case of a polished and uncoated plate, with plane parallel and identical surface boundaries, we have $R_{\text{in}} = R_{\text{out}} = R$ and $T_{\text{in}} = T_{\text{out}} = T$, and Equations 3.38 and 3.39 become:

$$R_{\text{tot}} = R + R\, T^2\, e^{-2\alpha h} \left(1 + R^2\, e^{-2\alpha h} + R^4\, e^{-4\alpha h} + ...\right) \ , \tag{3.40}$$

$$T_{\text{tot}} = T\, T\, e^{-\alpha h} \left(1 + R^2\, e^{-2\alpha h} + R^4\, e^{-4\alpha h} + ...\right) \ , \tag{3.41}$$

which are equivalent to

$$R_{\text{tot}} = R + \frac{R\, T^2\, e^{-2\alpha h}}{1 - R^2\, e^{-2\alpha h}} = R \left(1 + \frac{(1-R)^2\, e^{-2\alpha h}}{1 - R^2\, e^{-2\alpha h}}\right) \ , \tag{3.42}$$

$$T_{\text{tot}} = \frac{T\, T\, e^{-\alpha h}}{1 - R^2\, e^{-2\alpha h}} = \frac{(1-R)^2 e^{-\alpha h}}{1 - R^2\, e^{-2\alpha h}} \ . \tag{3.43}$$

Finally, the intensity (I) transmitted by a homogeneous substrate of thickness h, for an incident intensity I_0 and a well-known complex refractive index (n and κ), can be calculated by

$$I = I_0\, \frac{(1-R)^2 e^{-\alpha h}}{1 - R^2\, e^{-2\alpha h}} \tag{3.44}$$

with $R = (n-1)^2/(n+1)^2$ and $\alpha = 4\pi\kappa/\lambda$, both n and κ being wavelength-dependent.

All reflectance and transmittance curves for the principal materials which have been considered in our study, are presented in Appendix A. For all these materials, R_{tot} and T_{tot} have been computed using Equations 3.43 and 3.42, based on absorption coefficient data from Pilon (2002)

for SiO_2, and from Hawkins (1998) for Si, Ge, Zns, and $ZnSe$. In the case of diamond, we have exploited the transmittance data from Dore et al. (1998) to derive the absorption attenuation. The absorption coefficient α was then calculated by solving Equation 3.44

$$e^{-\alpha h} = \frac{-T^2 + \sqrt{T^4 + 4R^2T_{\text{tot}}^2}}{2R^2T_{\text{tot}}} \ , \tag{3.45}$$

resulting in the following expression for the extinction coefficient κ, i.e., the complex refractive index responsible for the absorption:

$$\kappa = \frac{\lambda\alpha}{4\pi} = -\left(\frac{\lambda}{4\pi h}\right) ln\left(\frac{-T^2 + \sqrt{T^4 + 4R^2T_{\text{tot}}^2}}{2R^2T_{\text{tot}}}\right) . \tag{3.46}$$

3.3 Development of silica SG HWPs

3.3.1 Silica optical properties

The substrate material for fabricating a subwavelength grating half-wave plate (SG HWP) is of paramount importance, not only in terms of its optical properties (transparency and refractive index as a function of wavelength) but also in terms of its physico-chemical properties. Indeed, microfabrication techniques are sensitive to the very nature of the material. Being inherited from the microelectronics industry, the most successful techniques are primarily applicable to silicon (Si) and its derivatives (oxides, nitrides). Therefore, our first choice of substrate material was silicon dioxide (SiO_2), also known as silica or quartz. It is compatible with Si microfabrication techniques, but in addition to the near infrared (H and K bands), unlike Si, silica is transparent to visible light. Therefore, developing a microfabrication method with SiO_2 for the infrared (K band in priority) is a long-term investment that will allow us to address the shorter wavelengths in the more distant future.

Silica is easy to produce and polish. It can be manufactured in several forms. A high-purity amorphous form is obtained with fused silica, manufactured by melting naturally occurring quartz crystals of high purity at ∼1700 K. Its high transmittance and low coefficient of thermal expansion make it a very interesting candidate for manufacturing SG HWPs for ground or space applications. Using an electrical fusing process, one can produce IR-grade fused silica (trade name Infrasil®), which has a much lower water content than UV-grade fused silica, avoiding water absorptions at 2.2 and 2.7 μm and leading to excellent infrared transmission up to 3.6 μm. The absorption occurring in fused silica in the near-infrared strongly depends on the purity of the fused quartz and in particular on the hydroxyl content (Plotnichenko 2000). The imaginary part κ (see Figure 3.6) of the complex refractive index was not always directly available from the literature, until Pilon (2002) reported referenced experimental data for fused silica at room temperature with the spectral range covered. Transmittance and reflectance curves for the 0.2 to 4 μm region are given in Appendix A.

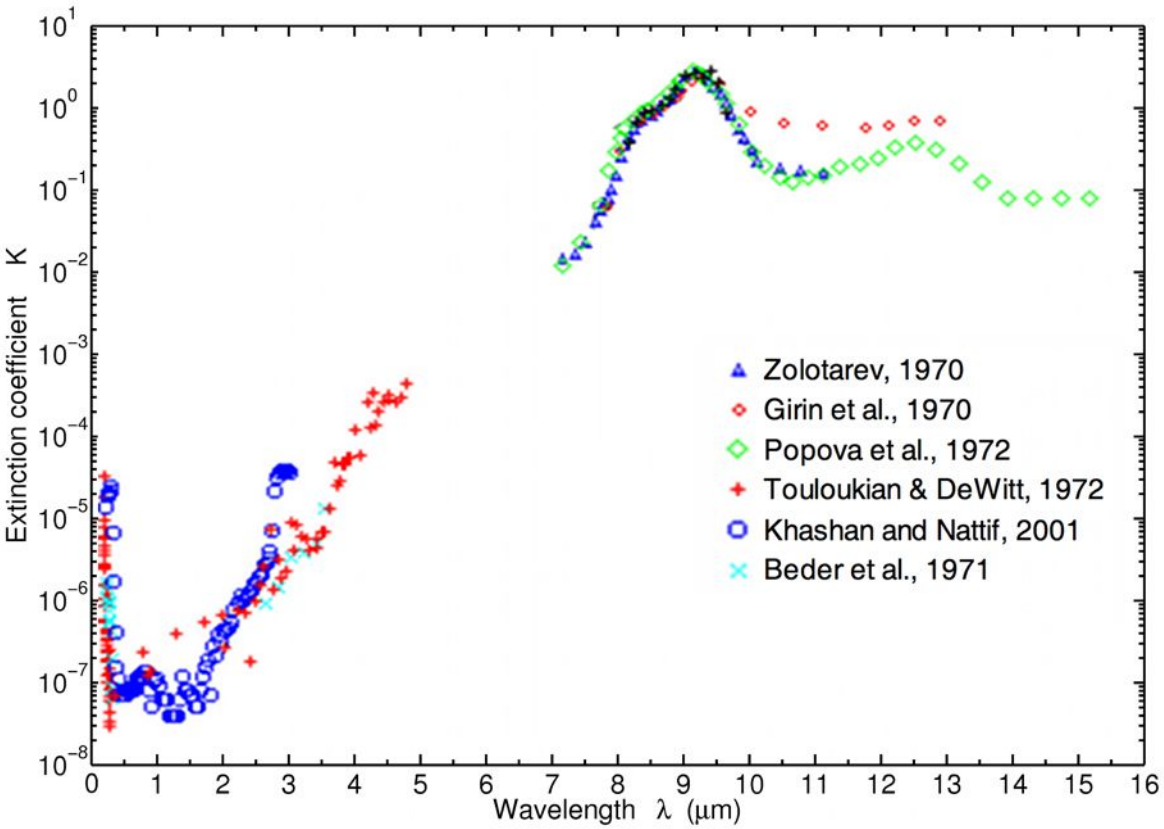

Figure 3.6: Imaginary part κ of the complex refractive index of fused silica as a function of the wavelength λ according to sources listed in the legend box. Data from Pilon (2002).

3.3.2 Design and manufacturing

Selection of optical parameters

The main disadvantage of SiO_2 is its low refractive index (see Appendix A), which requires to etch deeper structures to compensate for this weakness. In addition, compared to Si, the dispersion of its refractive index is less efficient in terms of achromatization. In fact, Si can provide an achromatic HWP for both H and K bands simultaneously, whereas SiO_2 can only do this for one at a time. For a HWP to keep its efficiency over a wide spectral band, the component must be optimized in order to minimize the phase shift error with respect to π:

$$\varepsilon(\lambda) = \Delta\Phi_{\mathrm{TE-TM}}(\lambda) - \pi \tag{3.47}$$

where $\Delta\Phi_{\mathrm{TE-TM}}$ is the phase retardation previously defined in Section 3.2.3 as

$$\Delta\Phi_{\mathrm{TE-TM}}(\lambda) = \left(\frac{2\pi}{\lambda}\right) h\ \Delta n_{\mathrm{form}}(\lambda)\ . \tag{3.48}$$

In practice, one has to make the form birefringence Δn_{form} proportional to $\lambda/2h$, h being the groove depth of the SG, or in other words the thickness of the grating. Since the error is a function of the wavelength, we must minimize the error standard deviation σ (root mean squared error) over the entire spectral band. Considering an ideal rectangular profile, we have calculated the

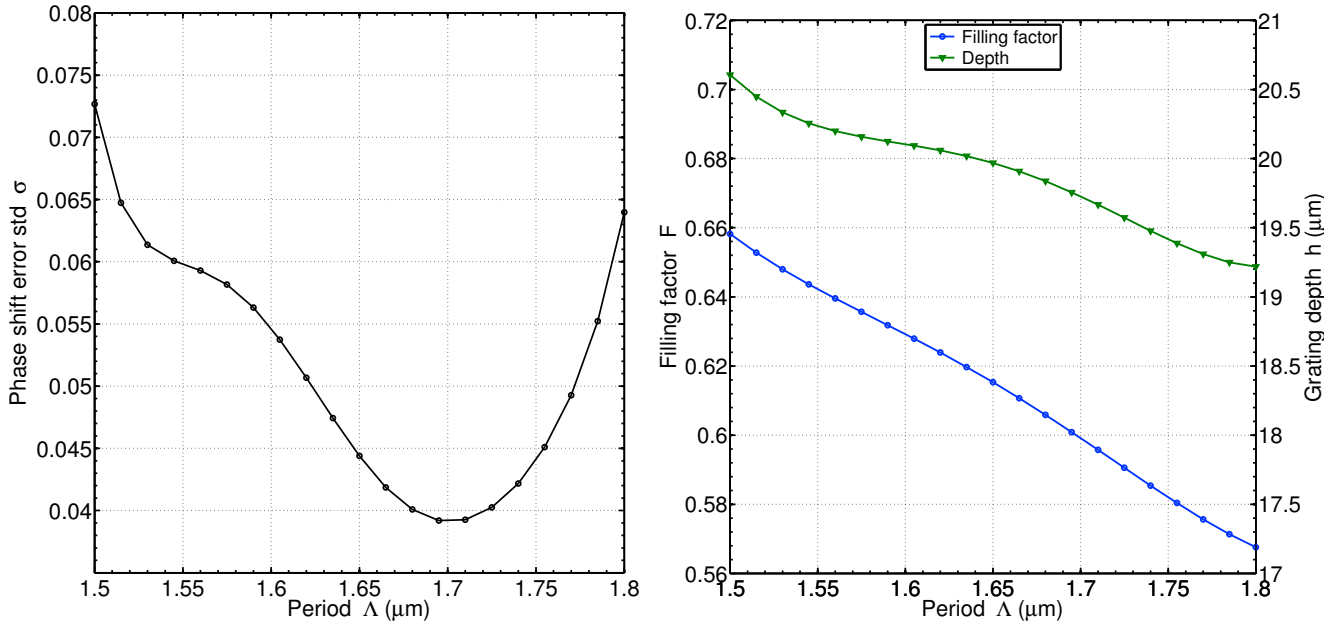

Figure 3.7: Design optimization of an SiO_2 SG HWP, function of the period Λ. Left: Phase shift error standard deviation. Right: Double plot of the grating depth h and the filling factor (F). The calculations show the optimal geometric parameters at each Λ minimizing the π-phase shift error over the whole K band (2 - 2.4μm).

form birefringence $\Delta n_{\text{form}} = \Delta n_{\text{TE-TM}}$ of a silica SG in the K band (2 - 2.4μm), for different values of the period Λ (see Figure 3.7), using a multidimensional nonlinear minimization method (Nelder-Mead algorithm, also called downhill simplex method) from the MATLAB® software. The period was constrained to be somewhat smaller than the wavelength λ, around 1.65 μm, just enough to stay in the sub-lambda regime of a zeroth order grating (ZOG). A smaller period would guarantee the non-zeroth orders to be totally evanescent, but at the cost of a much more difficult manufacturing process. In fact, the hardest part of developing SG HWP in SiO_2 is the etching of the grating. One has to etch very deep ($\sim$20 μm) and narrow ($\sim$0.7 μm) grooves in order to reach the desired form birefringence.

The most important parameter for manufacturing is the aspect ratio, which is defined as the ratio of the grating depth h to the feature line $F\Lambda$: the higher the aspect ratio, the more difficult the fabrication. Thanks to our RCWA-simulations, we have determined the geometric parameters of our rectangular profile grating illustrated in Figure 3.8.

- Period: $1.67 \leq \Lambda \leq 1.73$ μm
- Filling factor: $0.58 \leq F \leq 0.62$
- Depth: $19 \leq h \leq 20$ μm
- Aspect ratio $\simeq 17.7 - 20.6$

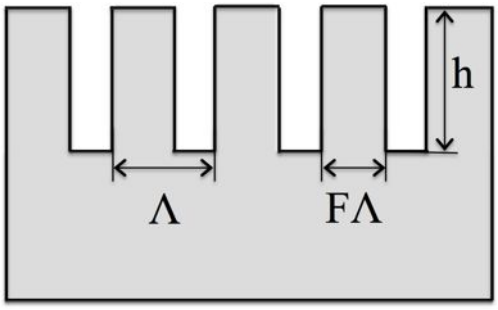

Figure 3.8: Schematic diagram of a SG, with geometrical parameters Λ, F, and h.

Expected performances

A silica SG that would have the geometrical parameters given here above, would produce a phase retardation $\Delta\Phi_{\mathrm{TE-TM}}$ close to π, with a quite small error standard deviation ($\sigma \simeq 10^{-2} rad$) in the considered K band, as presented in Figure 3.9 (top). Another interesting aspect is the transmission of the wave plate, which is very good for SiO_2. We have calculated the total reflectance $R_{\mathrm{tot}} \approx 4.5\%$ and transmittance $T_{\mathrm{tot}} \approx 89.7\%$ using Equations 3.38 and 3.39 determined in Section 3.2.4. The results are plotted in Figure 3.9 (bottom) together with the transmission (T_{in}, T_{out}) and reflection (R_{in}, R_{out}) curves on each side of the wave plate: the SG side (*in*) and the backside (*out*).

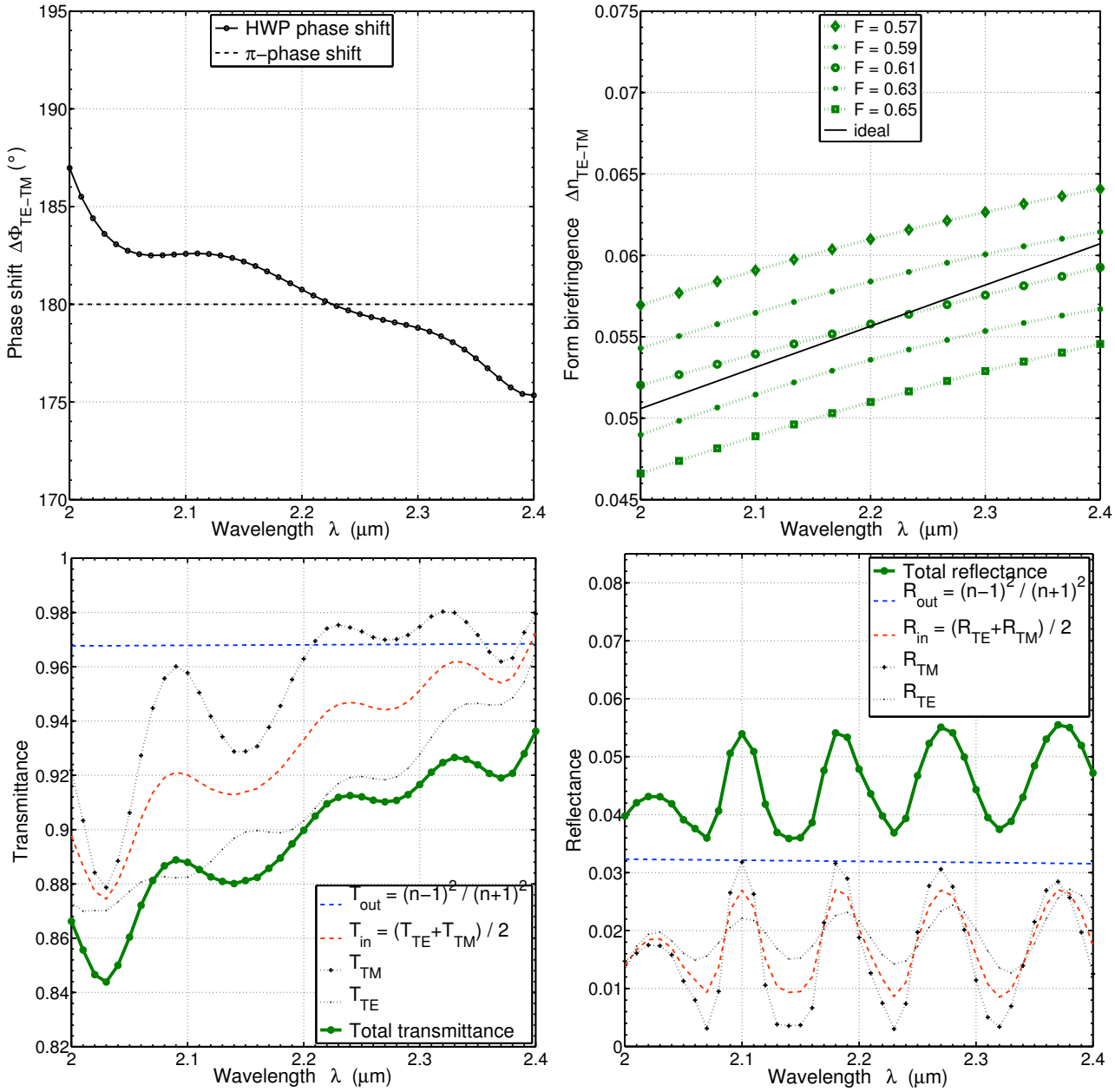

Figure 3.9: RCWA-calculated performance of a quartz SG HWP optimized for the K band. Top left: TE-TM retardance compared to a perfect π-phase shift. Top right: Form birefringence $\Delta n_{\mathrm{form}} = \Delta n_{\mathrm{TE-TM}}$ for various filling factors F between 0.57 and 0.65, compared to an ideal form birefringence proportional to $\lambda/2h$. Bottom: Reflectance (left) and transmittance (right) of a 1 mm thick K-band HWP, considering absorption occurring during multiple internal reflections.

We have then explored shorter wavelength regions, downscaling the geometrical parameters of the grating in order to keep an optimal broadband phase retardation (see Figure 3.10). We have selected four different filters spanning the visible (530 - 650 and 650 - 790 nm) and near-infrared (J band 1.15 - 1.4 μm and H band 1.5 - 1.8 μm). Each of them has a spectral resolution $R_\lambda \approx \lambda/\Delta\lambda \approx 5$, corresponding to 20% bandwidth (BW). As expected, we obtain even better results at shorter wavelengths (where the dispersion of silica is higher), coming closer to the ideal π-phase shift flat curve. The optimal grating parameters, as well as the retardation performances of all these silica subwavelength gratings are summarized in Table 3.2.

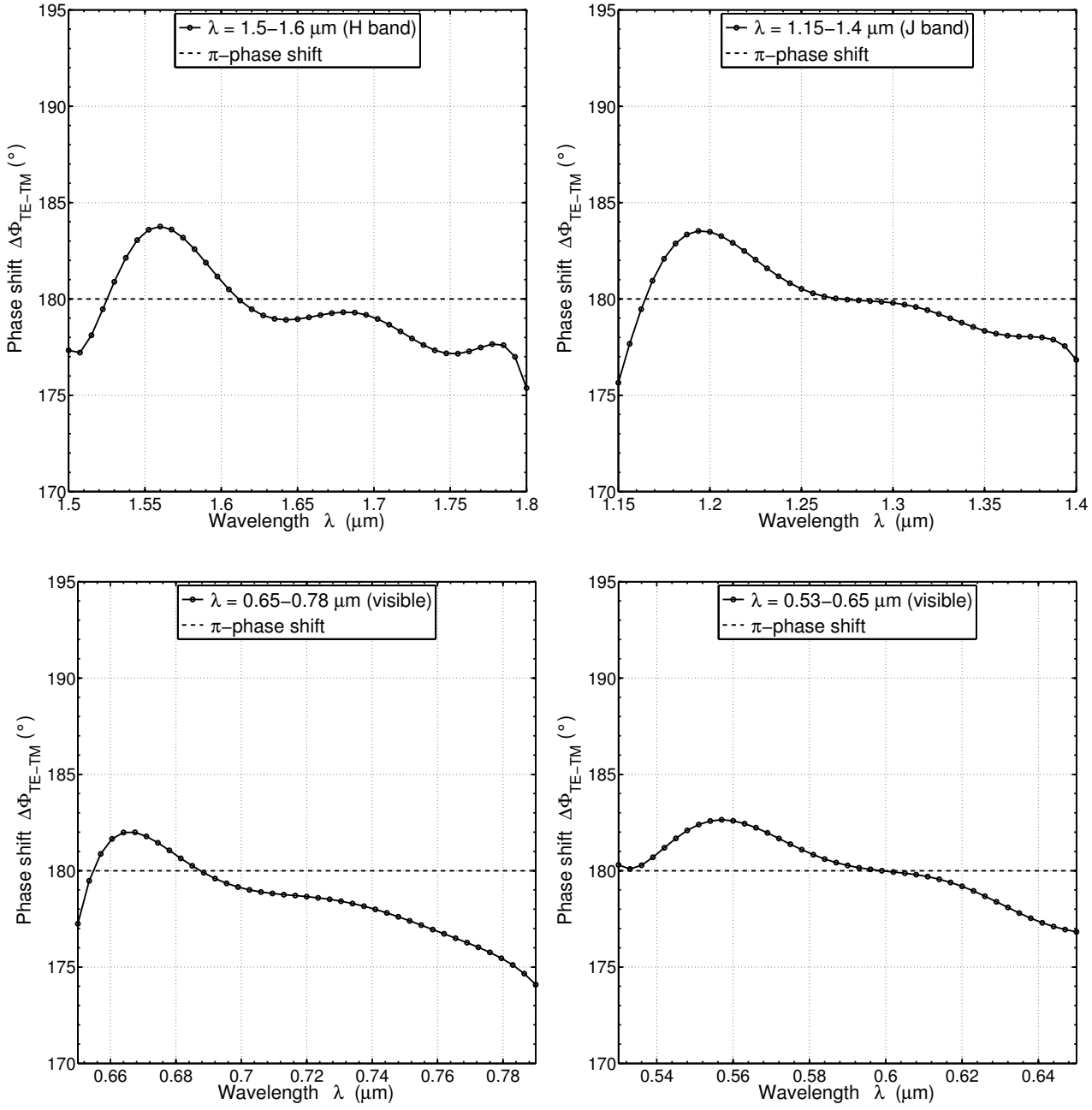

Figure 3.10: RCWA-calculated performance of quartz SG HWPs optimized for different spectral bands: H band (top left), J band (top right), 650-790 nm (bottom left), and 530-650 nm (bottom right). Each filter has a 20% bandwidth.

At this stage, we already introduce the coronagraphic performance that one can obtain with a vector optical vortex, using such subwavelength gratings. For each spectral band, we have simulated the total coronagraphic attenuation $A = 1/R$ (R being the rejection), that is the contrast provided by the coronagraph, integrated over the whole point spread function (PSF). In Table 3.2, last column, we give the contrast at the $2\lambda/d$ angular separation from the star, d corresponding to the diameter of the telescope, equivalent to $5 \times 10^{-3} \times A$. The factor 5×10^{-3} simply derives from the natural decay of the PSF intensity of a perfect pupil. In the next chapter, dedicated to the manufacturing of AGPM coronagraphs (see Chapter 4), we will explain in more details how the attenuation is calculated, and what are the possible causes of performance degradation.

Table 3.2: Geometric parameters of several achromatic SG HWPs optimized for different spectral bands using RCWA calculations. Each band has a 20 % bandwidth (BW) and each grating has a 61% filling factor. σ refers to the phase shift error standard deviation. The last two columns give the expected coronagraphic performances of annular groove phase masks (AGPMs) produced from these SGs. R refers to the rejection, equivalent to the inverse of the attenuation (A). The last column gives the achievable contrast at the $2\lambda/d$ angular separation from the star, d corresponding to the diameter of the telescope.

20% BW		SG HWP parameters				Coronagraphic performance	
Filter	Range	Λ (μm)	h (μm)	a.r.*	σ	AGPM total R	Contrast at $2\lambda/d$
K	2-2.4	1.68	19.77	19.3	5×10^{-2}	1220	4×10^{-6}
H	1.5-1.8	1.3	14.79	18.6	4.7×10^{-2}	910	5×10^{-6}
J	1.15-1.4	0.99	11.19	18.5	3.9×10^{-2}	1225	4×10^{-6}
vis.	0.65-0.79	0.54	5.94	18.0	4.7×10^{-2}	1300	3.8×10^{-6}
vis.	0.53-0.65	0.45	4.94	17.9	3.4×10^{-2}	1450	3.5×10^{-6}

* aspect ratio $= \frac{h}{F\Lambda}$ with $F \approx 61\%$ for each spectral band

Manufacturing plan

We agreed to start with the manufacturing of a K-band (2 - 2.4 μm) SG, for scientific as well as technical reasons. Indeed, in this range of wavelengths, the specifications of the feature line $F\Lambda \approx 1\,\mu$m and the "holes" $(1-F)\Lambda \approx 0.7\,\mu$m are more comfortable for the use of standard photolithographic system than at shorter wavelengths. On the scientific side, the K band is a very promising spectral region for the next generation of instruments, such as VLT-SPHERE which requires a minimal rejection $R > 500$, while our component delivers a rejection about $R = 1000 - 1500$.

Our project to build coronagraphic systems with the zero-order gratings (ZOG) technique is part of a broad and open consortium. This is the only acceptable method to obtain a viable component, given the required technological level. Therefore, we have used the experience and expertise of different collaborators (including academic institutions), all of which finding their place in the project by integrating the production of the components in their research and development activities. This separation of tasks allows flexibility and cost optimization. It also leads to a greater chance of success by taking advantage of each expertise. Hereunder, we introduce the different actors involved in the development plan, and present an organizational chart (see Figure 3.11) as well as the whole technological stack (see Figure 3.13).

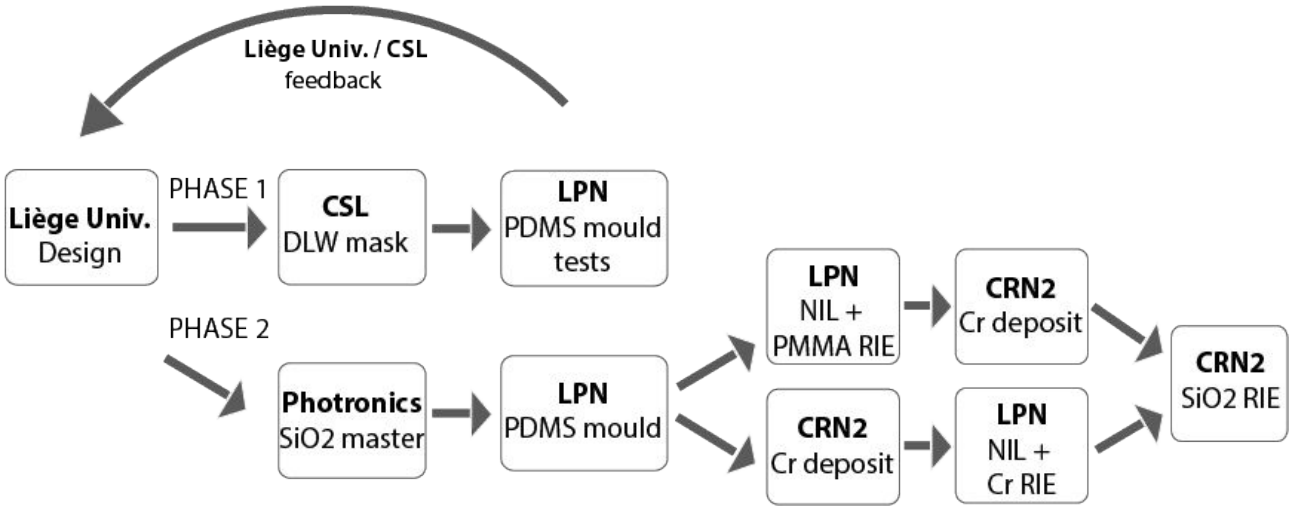

Figure 3.11: Development plan of an SiO_2 achromatic SG-HWP/AGPM. Description of the collaborators and the techniques are provided in the main text.

The **Centre Spatial de Liège (CSL)** is an applied research center at the University of Liège, focused on design, integration and calibration of space observation instruments. The CSL has demonstrated his mastery in manufacturing a mask out of photoresist, for the specifications of a K-band SG HWP by the direct laser writing (DLW) technique (see Figure 3.12). Such a mask is produced on a SiO_2 wafer. One can then obtain a master of SiO_2 by dry etching. The profile of the master is then transferred with a much higher aspect ratio into the final silica substrate using different microfabrication techniques such as nano imprint lithography (NIL) and reactive ion etching (RIE). However, the CSL does not yet totally control the etching of the master. Outsourcing this task seems to be the best solution given current CSL capabilities, but this skill might hopefully be available at the CSL within the next few years.

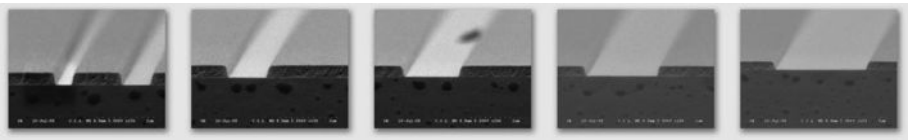

Figure 3.12: Microscopic picture of different line width (down to 0.6 μm) profiles, transferred into photoresist by direct laser writing (DLW). Courtesy of the CSL.

Photronics Inc. is a US company specialized in subwavelength photomask solutions. We have contacted them and obtained a reasonable offer for the etching of a 5-inch wafer with 7 AGPM masters with slightly different filling factors around 0.6, all etched in the same batch. The maximal depth of the grooves, given our period and filling factor specifications, is 500 nm. This is of course much less than our final goal (20 μm) because of the limited selectivity of the photolithographic mask. However, this depth concerns the etching of the master, not the final component. 500 nm is more than the minimal depth required for our process ($\sim$200 nm). Indeed, the SiO_2 master is copied by moulding into polydimethylsiloxane (PDMS, see Laboratoire de Photonique et de Nanostructures), which is then used to produce a chromium (Cr) mask on the final silica wafer, by use of nano imprint lithography (NIL) and reactive ion etching (RIE, see Centre de Recherche en Nanofabrication et Nanocaractérisation).

The French **Laboratoire de Photonique et de Nanostructures (LPN)** is equipped with NIL infrastructures and can replicate the master on a 4 inch of diameter silica wafers. The replication is performed with the assistance of a PDMS mould of the negative profile of the pattern, which is then transferred into an NIL resist mask (Amonil or Nanonex resist). The advantage of this technique is that it does not damage the master, and can be reproduced.

The Canadian **Centre de Recherche en Nanofabrication et Nanocaractérisation (CRN2)** from the University of Sherbrooke features RIE capabilities, which can etch the masked silica substrate to the required high aspect ratio.

3.3.3 Discontinuation of the silica option

The selection of silica as the perfect material for operating in the visible-to-near-infrared bandwidths has unfortunately led to an unavoidable abortion, for several reasons. First and foremost, facing the overwhelming technological challenge of this project, we have encountered two critical show-stoppers:

- the very high aspect ratio of the grating walls requires a thick metal mask layer, that may only be obtained with a very deep and neat nano-imprint lithography process,

- the reactive ion etching of the silica substrate is not mastered yet, and there is no guarantee of perfectly rectangular profiles in the grating.

The financial aspects are also crucial for such an ambitious project, and they have mainly motivated our decision to widen the consortium to many academic institutions, but as a result, we have sometimes encountered a lack of availability and responsiveness from some of them.

The main reason for having discontinued the silica option, was because in the meantime, we started to obtain very interesting results with another material: diamond. Based on our experience so far, both in designing the subwavelength grating profiles and seeking for the best manufacturing processes, we managed to develop the first broadband achromatic half-wave plates made out of diamond, as shown in the next section. Consequently, we manufactured the first AGPMs. The manufacturing of mid-infrared AGPMs made out of diamond will be described in Chapter 4, whereas the performance assessment, both in the lab and on the sky, will be presented in Part 3.

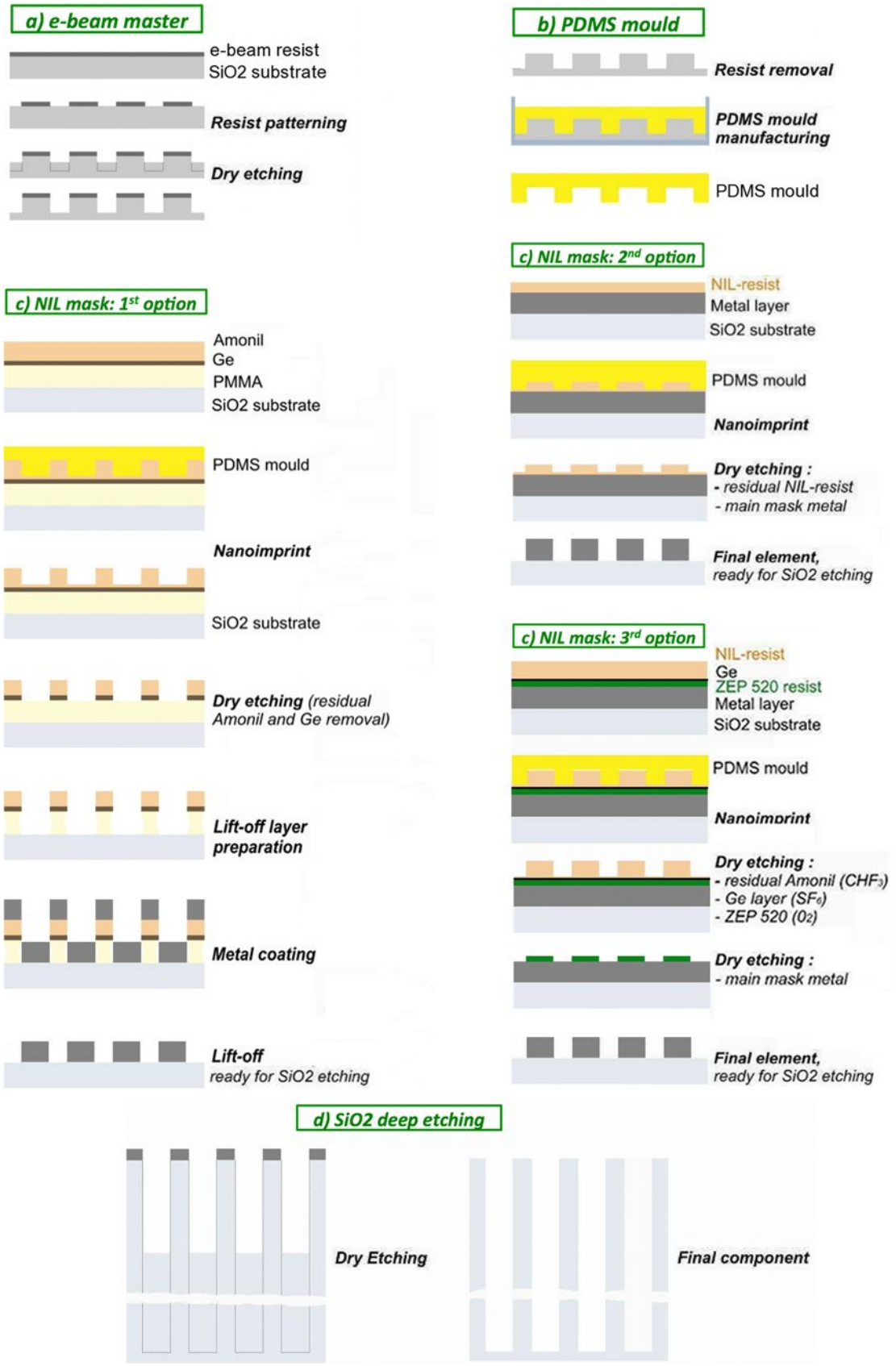

Figure 3.13: Complete technological stack of an SiO_2 achromatic SG-HWP/AGPM. The NIL mask first option is easier to implement, since it does not require etching the metal mask, but is less accurate due to the imperfect verticality of PMMA walls.

3.4 Development of diamond SG HWPs

Another material candidate, which we have investigated in parallel with our development on quartz and researches on other dielectrics, is *diamond*. The word itself is fascinating, and evokes jewelry and luxury. But as one may guess, we did not follow the path of diamond like sailors attracted by the siren songs. Beside its exploitation for gemstones, which concerns less than 2% of the total yearly production (Olson 2010), diamond is extensively used for industrial applications and scientific research. In fact, diamond is said to possess the most striking list of properties of all materials. These exceptional properties are briefly summarized hereafter.

3.4.1 Unique material properties of diamond

Diamond is a rare mineral, composed of the element carbon which has the property to exist in different forms called allotropes. Diamond is one of them. Its structure is described as two interpenetrating face-centred cubic lattices, such that each carbon atom is surrounded by four other carbon atoms and connected to them by strong covalent bonds (see Figure 3.14, left). Other elements such as Si or Ge share the same structure, but it is the very small size of tightly-bonded carbon atoms in combination with this simple and uniform arrangement that yields a substance with so many superlative properties.

– **Optical properties.** First and foremost, diamond is transparent throughout the whole infrared region, which is likely to suit many next generation instruments like SPHERE at the VLT (Beuzit et al. 2006; Kasper et al. 2012), or EPICS and METIS at the future E-ELT (Gilmozzi & Spyromilio 2007; Kasper et al. 2008; Brandl et al. 2008). It has actually one of the widest transmission windows, from the ultraviolet ∼200 nm up to the microwave ∼1 mm (Bundy 1962), with some intrinsic multiphonon absorption bands in the $2.5 - 6.7\mu$m range

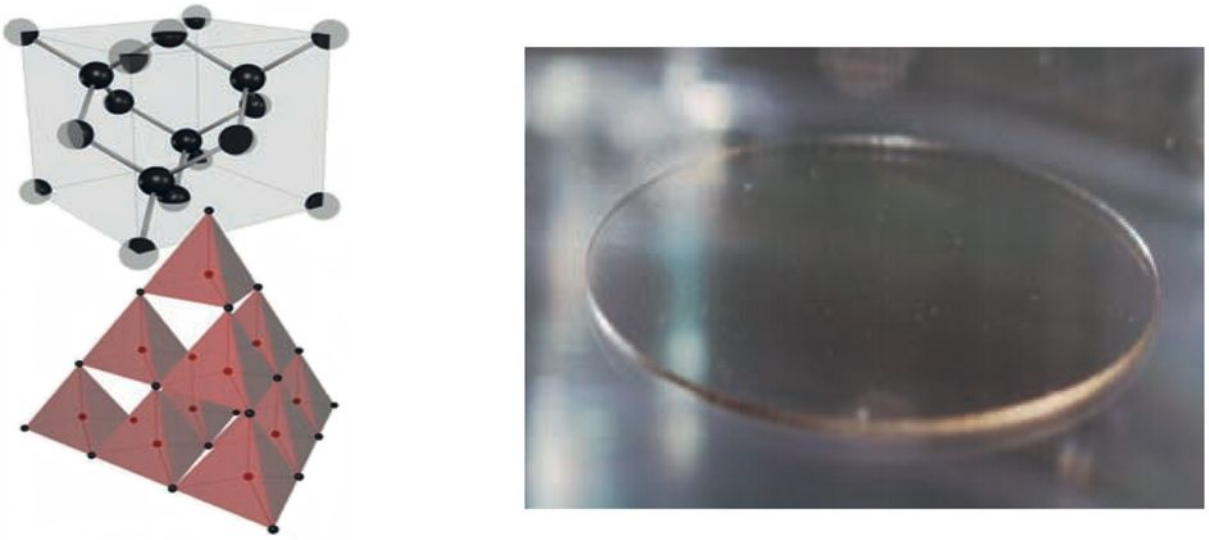

Figure 3.14: Left: Arrangement of atoms in the diamond crystal structure (top) and the structure described as a stack of tetrahedrons (bottom). Right: 2 cm diameter, 300 μm thick disk of microcrystalline CVD diamond of optical quality. Courtesy of Pontus Forsberg.

(Edwards & Philipp 1991; Thomas & Tropf 1994). Beside its high optical dispersion and high luster that help make it the world's most popular gemstone, diamond is also a privileged material for subwavelength grating (SG) coronagraphs because of its high refractive index, ∼2.42 in the visible and ∼2.38 from 1.5 μm to the thermal infrared, which is crucial since it is directly linked to the required grating aspect ratio (i.e., the ratio between the depth and the feature line). In return, this high refractive index leads to a high reflectance, which is unfavorable to transmitting coronagraphs such as the AGPM, although it is not as high as other infrared materials such as Si or Ge (see transmittance curves in Appendix A). In some way, one can say that the refractive index of diamond is the best compromise regarding SG coronagraphs. Materials with very high refractive index such as silicon (3.4) are not compatible with our applications, because they necessarily require complex antireflective coatings on top of the subwavelength grating.

– **Non optical properties.** Diamond has a low density (3.52 kg/m^3) and is the toughest and hardest (10 on Mohs scale) natural substance on Earth. In addition, it has the highest thermal conductivity of all solids and a very low thermal expansion, it is a good electrical isolator, and it is resistant to all usual chemicals, acids, and most of the alkalies. These mechanical, thermal, electronic and chemical properties make diamond an excellent candidate for space-qualified components, which is of great interest for optical instrumentation onboard future spacecraft telescopes. In fact, some exotic materials with equivalent refractive index exist, but they are not compatible with our applications because of many non-optical disadvantages (brittle, deform easily, etc.).

Synthetic diamond

The outstanding properties of diamond have been known for decades by the scientific community, and numerous applications have benefited from them. However, many new applications have often selected diamond as the most suitable candidate, but were forced to reject it on grounds of cost and possible availability. This situation is about to change thanks to improving production capabilities of synthetic diamond, and most of all, the very recent progress in machining diamond to desired micrometric (and even nanometric) surface structures.

Diamond can either be extracted from diamond mines, or produced synthetically. The total production of natural diamond is about 30 tons a year, where as the synthetic diamond yearly production is close to 900 tons (Olson 2010). The two existing methods to produce all this diamond in the laboratory are oriented towards different application purposes. The first method, called the high pressure high temperature (HPHT) approach, consists in dissolving graphite (carbon's most common allotrope) in a molten metal, and allowing it to crystalize into diamond. It is the easiest way of production on an industrial scale. The second method, requires chemical vapor deposition (CVD) equipments, and consists in growing diamond in a vacuum chamber containing gaseous methane (CH_4), allowing for finer control of impurities. CVD diamond is the best choice for research and development of many high tech optical applications such as SG-HWPs and AGPM coronagraphs.

3.4.2 Publication: Design, manufacturing, and performance analysis of mid-infrared achromatic half-wave plates with diamond subwavelength gratings

In the following paper (Delacroix et al. 2012b), published in August 2012 in the peer-reviewed journal Applied Optics from the Optical Society of America, we present the end-to-end development of a broadband subwavelength grating half-wave plate (SG-HWP) made out of diamond. The design of the gratings was performed using RCWA calculations, in complete synergy with the manufacturing process carried out by our collaborators at the Uppsala University, in Sweden. The targeted spectral bandwidth 11 - 13.2 μm is located within the mid-infrared N band. Microscopic measurements show results very close to the desired specifications, and realistic estimated performances of the manufactured SG-HWP are finally provided, taking into account some uncertainties over the verticality of the grating grooves. The rationale for the development of this component is to enable the manufacturing of an N-band annular groove phase mask (AGPM) as we will explain in the next section. We will also see in Chapter 6 how the final N-band coronagraph was installed in 2012 on the VLT/VISIR instrument, and the confirmation of its expected performance through first light at the telescope.

Design, manufacturing, and performance analysis of mid-infrared achromatic half-wave plates with diamond subwavelength gratings

Christian Delacroix,[1,*] Pontus Forsberg,[2] Mikael Karlsson,[2] Dimitri Mawet,[3] Olivier Absil,[4] Charles Hanot,[4] Jean Surdej,[4] and Serge Habraken[1]

[1]Hololab, Université de Liège, Allée du 6 Août 17 B5a, B-4000 Liège, Belgium

[2]Ångström Laboratory, Uppsala University, Lägerhyddsvägen 1, SE-751 21 Uppsala, Sweden

[3]European Southern Observatory (ESO), Alonso de Córdova 3107, Vitacura, 763 0355 Santiago, Chile

[4]IAGL, Université de Liège, Allée du 6 Août 17 B5c, B-4000 Liège, Belgium

*Corresponding author: delacroix@astro.ulg.ac.be

Received 3 May 2012; revised 10 July 2012; accepted 10 July 2012;
posted 20 July 2012 (Doc. ID 167832); published 16 August 2012

In this paper, we present a solution for creating robust monolithic achromatic half-wave plates (HWPs) for the infrared, based on the form birefringence of subwavelength gratings (SWGs) made out of diamond. We use the rigorous coupled wave analysis to design the gratings. Our analysis shows that diamond, besides its outstanding physical and mechanical properties, is a suitable substrate to manufacture mid-infrared HWPs, thanks to its high refractive index, which allows etching SWGs with lower aspect ratio. Based on our optimized design, we manufactured a diamond HWP for the 11–13.2 μm region, with an estimated mean retardance $\sim 3.143 \pm 0.061$ rad ($180.08 \pm 3.51°$). In addition, an antireflective grating was etched on the backside of the wave plate, allowing a total transmittance between 89% and 95% over the band.

OCIS codes: 050.1950, 050.5080, 050.6624.

1. Introduction

Wave plates are essential tools for modulating the polarization of an incoming light beam. They are commonly used in many applications as retarders or phase shifters. In astrophysics, when it comes to observing a very high-contrast scene, one must be able to cancel the bright source, or at least drastically reduce its intensity. This attenuation can be achieved by combining two portions of the incident light beam, one of which having to undergo a half wavelength (or π) phase shift. Therefore, a half-wave plate (HWP) is by definition the ideal tool. The retardance of a zero-order wave plate varies hyperbolically with the wavelength, which limits the operation of single wave plates to monochromatic light. However, a large spectral bandwidth is needed in many cases, especially in astrophysics, both to increase the signal-to-noise ratio and to allow spectrophotometry.

Different varieties of achromatic wave plates exist. Achromatic prism retarders [1], for instance, operate in total internal reflection. They are voluminous and not suitable for applications operating in transmission. Another way of achieving broadband performance is stacking several crystal wave plates together [2] and orienting their birefringent axes using a Pancharatnam method [3]. A thick combination of multiorder wave plates is needed, because of the weak natural birefringence of crystals, which results in an increased absorption of IR radiation. Achromatic retarders can also be produced by using

1559-128X/12/245897-06$15.00/0

liquid crystals (LCs) [4], liquid crystal polymers (LCPs) [5], or photonic crystals (PhCs) [6,7] as the birefringent materials. A weakness of these liquid or photonic crystal retarders is their bandwidth: they do not transmit at wavelengths beyond the near-infrared (H-band centered at ~1.65 μm, K-band ~2.2 μm) [8]. Meanwhile, the demand for instruments in the mid-infrared (L-band ~3.8 μm, M-band ~4.8 μm, N-band ~10.5 μm) is increasing in many domains of astrophysics. Therefore, we are pursuing a different technological route to synthesize the π phase shift. We use the dispersion of form birefringence of subwavelength gratings (SWGs) [9,10], which are particularly adapted to longer wavelengths.

In this paper, we present the results of our work on achromatic wave plates. After a brief introduction to SWGs (Section 2), we demonstrate in Section 3 that diamond is a good choice of material for mid-IR SWGs. In Section 4, we attempt to optimize a design for a diamond HWP with respect to manufacturability and performance. In Section 5, we briefly describe the fabrication of a diamond achromatic HWP dedicated to the mid-IR (11–13.2 μm). We calculate its theoretical efficiency with computer simulations based on the rigorous coupled wave analysis (RCWA). Finally, we conclude with the perspectives for present and future instruments.

2. Achromatic Half-wave Plates (HWPs)

A. Subwavelength gratings (SWGs)

Many new optical devices have been made with SWGs, such as high-efficiency diffraction gratings, polarization-selective gratings, wave plates, and monolithic antireflective structures [11]. SWGs are micro-optical structures with a period Λ smaller than λ/n, λ being the observed wavelength of the incident light and n the refractive index of the grating substrate. Such structures do not diffract light as a classical spectroscopic grating does. Instead, only zeroth transmitted and reflected orders are allowed to propagate outside the grating, and the incident wavefront is not affected by further aberrations. The condition for having an SWG is defined by the grating equation, which determines whether a diffraction order propagates or not through the grating,

$$\frac{\Lambda}{\lambda} \leq \frac{1}{n_I \sin\theta + \max(n_{\mathrm{I}}, n_{\mathrm{II}})}, \tag{1}$$

where θ is the incidence angle and n_{I} and n_{II} are the refractive indices of the incident (superstrate) and transmitting (substrate) media, respectively.

One can employ these SWGs to synthesize artificial birefringent achromatic wave plates [9]. A birefringent medium, such as a grating (see Fig. 1), has two different refractive indices, n_{TE} and n_{TM}, with regard to the polarization states TE (transverse electric, parallel to the grating grooves) and TM (transverse magnetic, orthogonal to the grating grooves). The phase retardation $\Delta\Phi$ introduced by a birefringent SWG between the two polarization components is dependent on the wavelength, and is given by

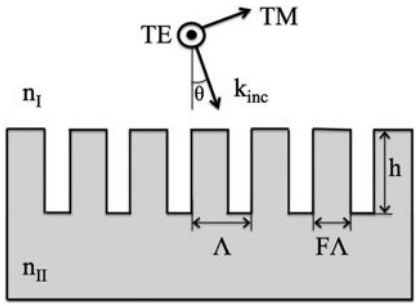

Fig. 1. Schematic diagram of a SWG. The incident light beam vector k_{inc} is perpendicular to the grating lines. The filling factor F is such that $F\Lambda$ corresponds to the width of the grating walls.

$$\Delta\Phi_{\mathrm{TE-TM}}(\lambda) = \left(\frac{2\pi}{\lambda}\right) h\, \Delta n_{\mathrm{form}}(\lambda) \tag{2}$$

where

$$\Delta n_{\mathrm{form}}(\lambda) = n_{\mathrm{TE}}(\lambda) - n_{\mathrm{TM}}(\lambda). \tag{3}$$

h is the optical path through the birefringent medium. In order to produce an achromatic wave plate, the product of the two factors in λ on the right-hand side of Eq. (2) needs to be a constant over a wavelength range as large as possible. By varying the grating parameters (geometry, material, incidence), the wavelength dependence in Δn_{form} should be tuned to be closely proportional to the wavelength across a wide spectral band.

B. Rigorous Coupled Wave Analysis (RCWA)

Common scalar theories of diffraction in gratings do not work in the subwavelength domain. In order to simulate the grating response and to calculate its form birefringence, we must consider the vectorial nature of light. For this purpose, we have performed numerical simulations using the RCWA. RCWA is an analysis method that is applicable to any multilayer grating profile [12,13]. The algorithm converts the grating-diffraction problem into a matrix problem, and solves the Maxwell equations from layer to layer. The solution corresponds to the reflection and transmission matrices in the two modes (TE/TM), describing the entire diffractive characteristics of the simulated structure: the diffraction efficiencies ($\eta_{\mathrm{TE}}^{(m)}$) and ($\eta_{\mathrm{TM}}^{(m)}$), and the phase shift ($\Delta\Phi_{\mathrm{TE-TM}}$).

3. Choosing an Appropriate Material: Diamond

For an HWP to keep its efficiency over a wide spectral band, the component must be optimized in order to minimize the phase shift error with respect to π:

$$\varepsilon(\lambda) = \Delta\Phi_{\mathrm{TE-TM}}(\lambda) - \pi. \tag{4}$$

Since the error is a function of the wavelength, we minimize the root mean squared (RMS) error $\varepsilon_{\mathrm{rms}}$

over the entire spectral band. We have performed RCWA simulations to optimize the grating parameters for a refractive index ranging from 1.5 to 2.8, and for several specific mid-IR spectral bands, corresponding to the transmission windows of the Earth atmosphere: L (3.5–4.1 μm), M (4.5–5.1 μm), and N (8–13 μm). Other solutions beyond 3 μm are cumbersome and involve exotic materials. Considering an ideal rectangular profile, we optimized the parameters F, h, and Λ (Fig. 1) using a multidimensional nonlinear minimization method (Nelder-Mead algorithm, also called downhill simplex method) from the MATLAB software. The period was constrained to be smaller than the SWG limit λ/n. With these optimized parameters, the mean phase shift error is very small ($\varepsilon_{\mathrm{rms}} \simeq 10^{-4}$ rad) in the considered spectral bands. We also introduced another parameter, the aspect ratio ρ,

$$\rho = \frac{h}{\min[F\Lambda; (1-F)\Lambda]}, \tag{5}$$

which is the height-to-width ratio of either the walls or the grooves. This parameter must be made as small as possible since features with high aspect ratio are difficult to manufacture. In our simulations, the N-band was separated into two parts of comparable bandwidth (~20%), thereby avoiding the strong ozone absorption band around 10 μm. In Fig. 2, the optimal aspect ratio is plotted against refractive index. Minima in these plots indicate a suitable substrate refractive index for the grating. For the longest wavelengths (N-band mostly), the aspect ratio ρ is much lower for high refractive indices (>2.25), while for the shorter wavelengths, the filling factor F varies strongly, which results in a very fluctuating aspect ratio due to its definition as a minimum of either the wall or void thickness. We conclude that using substrates with high refractive indices (e.g., diamond, ZnSe, Ge) can make the microfabrication of SWGs for achromatic HWPs much easier. Some exotic materials with lower refractive index exist, but they are not compatible with our applications because of many disadvantages (brittle, deform easily, etc.). Materials with very high refractive index such as silicon (~3.4) are not compatible either, because they necessarily require complex antireflective coatings on top of the SWG.

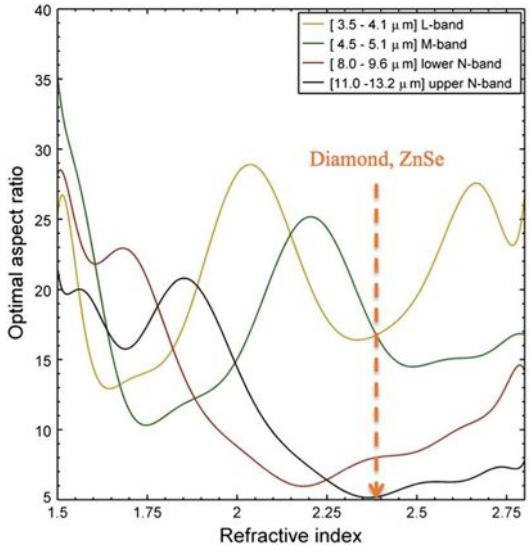

Fig. 2. (Color online) RCWA simulation: the aspect ratio of the gratings for a minimized mean phase shift error as a function of the refractive index.

Among the materials commonly used in the N-band, one good candidate is diamond, with a refractive index ~2.38 for the region of interest (from 3 to 13 μm). The use of diamond substrates leads to many advantages. First and foremost, it has a wide transmission window [14]. In addition, its mechanical properties are outstanding (low density = 3.52 kg/m^3; very high hardness = 10 on the Mohs scale; very high elasticity). Also, its thermal (excellent conductor, inertia) and chemical (resistant to usual chemicals, acids, and most of the alkalies) properties make it an excellent candidate to be space qualified.

4. Design of a Diamond Wave Plate

The larger periods and lower aspect ratios of the N-band HWP should make this grating easier to fabricate compared to bands of shorter wavelengths, as shown in Section 3. Here we will focus on a HWP for the long-wavelength part of the N-band (11–13.2 μm) for a forthcoming astronomical application (VLT/VISIR) [15]. The design of the grating was conducted in synergy with the manufacturing [16]. In particular, the slope of the sidewalls (see Fig. 3) must be taken into account and the aspect ratios must be kept within the range of what can be etched in the material.

The etch process used induces a slope $\alpha \simeq 2.7°$ (Fig. 3). During the fabrication process, small errors in line width, slope, and grating depth occur. In particular, the depth h and the slope α are difficult to measure precisely. A design that performs well even under small changes in these parameters was therefore sought. We have computed two-dimensional (2D) maps of the RMS error ($\varepsilon_{\mathrm{rms}}$) as a function of the filling factor (F) and of the depth (h), for several values of α ranging from 2.6 to 2.8°. We also calculated the mean and standard deviation of all these maps (see Fig. 4).

To obtain a good compromise between the mean value and the standard deviation, the optimum values are $h = 13.7$ μm and $F = 0.4$, which correspond to a line width (on the top) $F\Lambda = 1.84$ μm. In the first

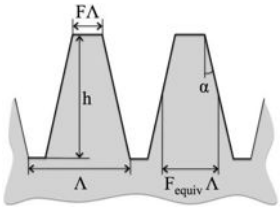

Fig. 3. Schematic diagram of a trapezoidal grating. The grating walls have a slope α and an average width $F_{\mathrm{equiv}}\Lambda$.

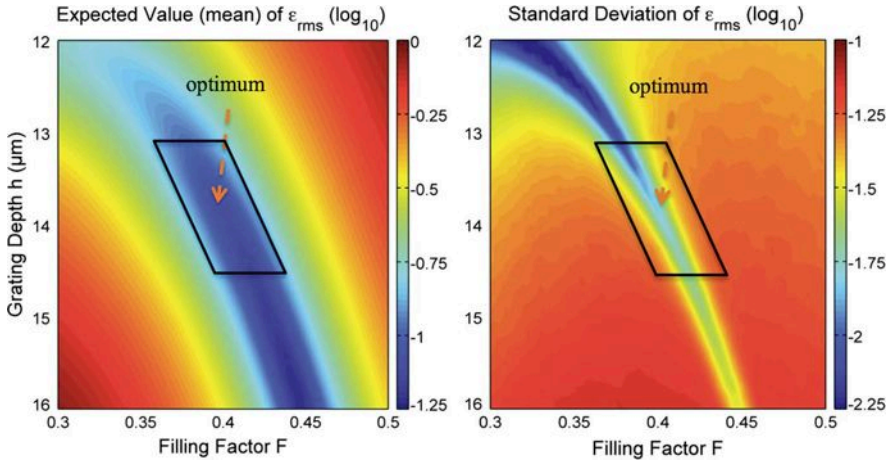

Fig. 4. (Color online) RCWA multiparametric simulation: mean (left) and standard deviation (right) of the RMS phase shift error (logarithmic scale) over the upper N-band, with α ranging from 2.6 to 2.8°. The period is set to $\Lambda = 4.6$ μm (SWG limit).

approximation, one can tell that the relation between the optimum line width and depth is quasi linear, with a regression coefficient approximately equal to 10. This is very useful for the manufacturing process, to compensate line width errors with the etching depth. For instance, if the line width is smaller than the optimum (e.g., –50 nm), one can etch a shallower grating (–500 nm).

5. Manufacturing and Performance Analysis

A. Manufacturing

The pattern was first written in photoresist on a silicon wafer by direct laser writing. This pattern was then transferred to the diamond substrate using a nanoimprint lithography process and finally dry etched in the diamond via several masking layers in an inductively coupled plasma reactor. The details of this process will be published elsewhere. The dense oxygen/argon plasma used is very stable, but the etch rate varies with depth and width of the grooves.

As mentioned before, precise measurements of the depth and profile of the subwavelength structure are difficult. The grooves are too narrow for using atomic force microscopy or white light interferometry. The best measurements were obtained by cracking the sample and observing the cross section with a scanning electron microscope (SEM). As can be seen in Fig. 5 the sidewalls have a slight angle of 2.6–2.8° from the vertical. Ions deflected in glancing impacts with the sidewalls cause trenching at the bottom of the wall. In a narrow groove such as this, trenching gives rise to the triangular ridge along the center of the groove.

B. Expected Performances

Cracking the sample is naturally not possible for the final HWPs. For these an estimate of the depth was acquired by comparing several SEM images taken at different angles. The distance between two recognizable features, one at the top and one at the bottom of a groove, was measured in micrographs recorded at tilt angles between 5 and 26°. From the variation in this distance with angle, the depth could be calculated. The depth measured by this method on cracked samples was in good agreement with cross section images (within 2%). Our prototypes have met the specifications: line width $\simeq$1.8 μm (sidewall angle $\simeq$2.7°), period 4.6 μm, and depth $\simeq$13.7 μm. As shown in Fig. 6, the retardance of the manufactured HWP is nearly ideal in the center of the spectral band. The mean and standard deviation of the phase shift over the whole upper N-band (11–13.2 μm) equal $\sim 3.143 \pm 0.061$ rad (180.08 ± 3.51°).

C. Antireflective Grating (ARG)

Incoherent reflections with different phase shift may interfere with the main beam and degrade performance of the component. The natural reflection of the diamond at N-band is $\sim$17% for one interface. Although the achromatic HWP was not designed with reducing reflections in mind, it still serves this purpose to some degree. As shown in Fig. 7, the theoretical transmittance is quite good between 11.5 and 13 μm because the diffraction grating actually acts as an antireflective layer at this wavelength.

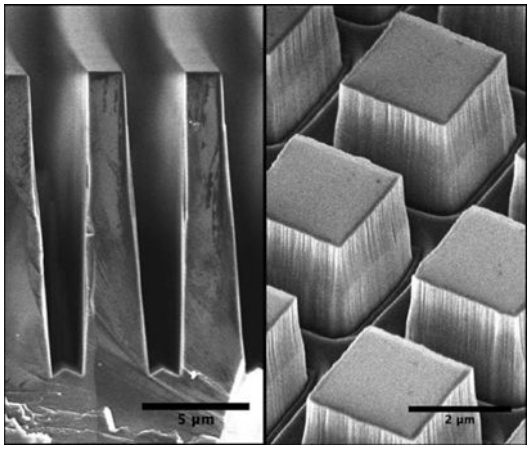

Fig. 5. SEM-micrographs of a diamond achromatic HWP. Left: cross sectional view of the grooves. Right: antireflective structure on the backside.

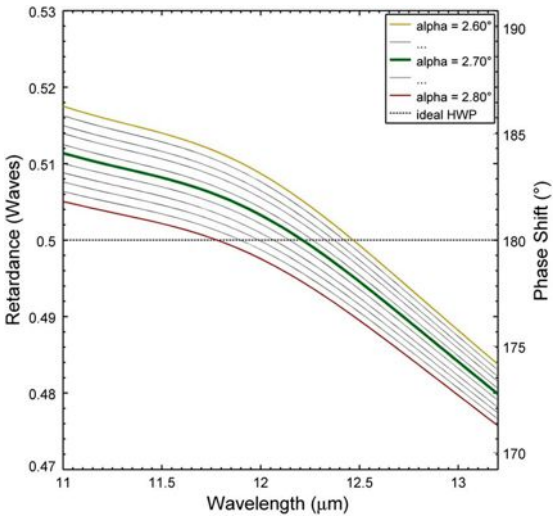

Fig. 6. (Color online) Retardance for a diamond HWP with optimal specifications at $\alpha = 2.6$–$2.8°$ (slope of the walls). Bandwidth: 11–13.2 μm.

In addition, an ARG was designed to reduce surface reflections using a diffraction grating analysis program (GSOLVER, version 4.20c., Grating Solver Development Co., USA). The program uses algorithms based on RCWA to calculate values of the zero-order transmission. A 2D SWG formed by binary square ($2.6 \times 2.6 \times 2$ μm) shaped structures with a 4 μm period was etched on the backside of the HWP to reduce the reflection from 17% to less than 0.5% in the wavelength region of interest (see Fig. 8). Etching the ARG was much less demanding than the HWP structure, but there is still trenching and the sidewalls are not perfectly vertical [11] (Fig. 5). Since there was some deviation from the calculated structure, the etch time was optimized by testing the performance. The transmittance of

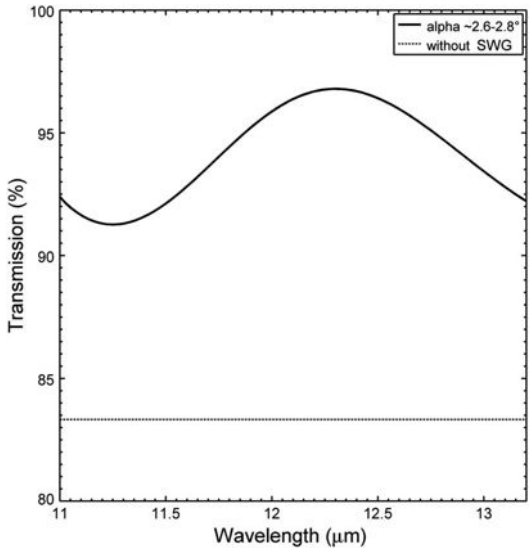

Fig. 7. Transmission spectrum of a SWG etched on diamond with HWP optimal specifications, with sidewall angle (2.6–2.8°). The dotted line shows the natural transmission of the diamond at N-band, without the SWG (~83%).

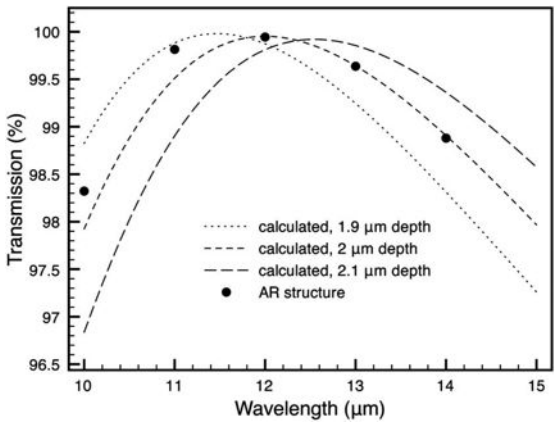

Fig. 8. Transmission spectrum of one diamond interface with ARG measured with a spectrophotometer. The calculated transmission values for three different depths are also shown.

diamond substrates with a single sided ARG was measured in a Perkin Elmer 983 infrared spectrophotometer. After removing the effects of interference within the sample and comparing with an unetched sample, the transmittance of a single AR interface has been determined (Fig. 8). As can be seen, the bandwidth of the manufactured structure was slightly larger than the calculated one. This may be due to the somewhat tilted sidewalls. The total transmittance of the finished HWP components was between 89% and 95% over the band.

6. Conclusion and Directions for Future Research

Diamond is a good material for manufacturing achromatic HWPs for mid-IR wavelengths. By optimizing the gratings with manufacturing limitations in mind, components dedicated to the upper N-band (~12 μm) could be achieved including an antireflective solution on their backside. Diamond HWPs are likely to be used for many applications, particularly for optical vortices in astrophysics. The diamond HWP shown in this paper has been developed to enable the manufacturing of an N-band annular groove phase mask (AGPM), which will be installed in 2012 on the VISIR instrument at the VLT, and is also an excellent candidate for METIS at the future European Extremely Large Telescope. This specific application will be the subject of a forthcoming paper. Moreover, a new process using e-beam lithography is now being explored to reach smaller grating periods, and thereby shorter operating wavelengths. These AGPMs are being evaluated for implementation on high-contrast imaging instruments such as NACO (L-band ~3.8 μm) and SPHERE (K-band ~2.2 μm) at the Very Large Telescope in Chile.

The first author is grateful to the financial support of the Belgian Fonds de la Recherche Scientifique (FRIA) and Fonds de solidarité ULg. We also gratefully acknowledge financial support from the Swedish Diamond Center (financed by Uppsala University), and the Communauté française de

Belgique—Actions de recherche concertées—Académie universitaire Wallonie-Europe.

References

1. R. M. A. Azzam and C. L. Spinu, "Achromatic angle-insensitive infrared quarter-wave retarder based on total internal reflection at the Si-SiO_2 interface," J. Opt. Soc. Am. A **21**, 2019–2022 (2004).
2. J.-B. Masson and G. Gallot, "Terahertz achromatic quarter-wave plate," Opt. Lett. **31**, 265–267 (2006).
3. S. Pancharatnam, "Achromatic combinations of birefringent plates—Part II. An achromatic quarter wave plate," Proc. Indian Acad. Sci. A **42**, 24–31 (1955).
4. J. Schirmer and T. Schmidt-Kaler, "Liquid crystal phase retarder with broad spectral range," Opt. Commun. **176**, 313–317 (2000).
5. D. Mawet, E. Serabyn, K. Liewer, Ch. Hanot, S. McEldowney, D. Shemo, and N. O'Brien, "Optical vectorial vortex coronagraphs using liquid crystal polymers: theory, manufacturing and laboratory demonstration," Opt. Express **17**, 1902–1918 (2009).
6. D. R. Solli, C. F. McCormick, and J. M. Hickmann, "Polarization-dependent reflective dispersion relations of photonic crystals for waveplate mirror construction," J. Lightwave Technol. **24**, 3864–3867 (2006).
7. N. Murakami, J. Nishikawa, K. Yokochi, M. Tamura, N. Baba, and L. Abe, "Achromatic eight-octant phase-mask coronagraph using photonic crystal," Astrophys. J. **714**, 772–777 (2010).
8. D. Mawet, E. Serabyn, K. Liewer, R. Burruss, J. Hickey, and D. Shemo, "The vector vortex coronagraph: laboratory results and first light at Palomar Observatory," Astrophys. J. **709**, 53–57 (2010).
9. H. Kikuta, Y. Ohira, and K. Iwata, "Achromatic quarter-wave plates using the dispersion of form birefringence," Appl. Opt. **36**, 1566–1572 (1997).
10. G. Nordin and P. Deguzman, "Broadband form birefringent quarter-wave plate for the mid-infrared wavelength region," Opt. Express **5**, 163–168 (1999).
11. M. Karlsson and F. Nikolajeff, "Diamond micro-optics: microlenses and antireflection structured surfaces for the infrared spectral region," Opt. Express **11**, 502–507 (2003).
12. M. G. Moharam and T. K. Gaylord, "Rigorous coupled-wave analysis of planar-grating diffraction," J. Opt. Soc. Am. **71**, 811–818 (1981).
13. L. Li, "Multilayer modal method for diffraction gratings of arbitrary profile, depth, and permittivity," J. Opt. Soc. Am. **10**, 2581–2591 (1993).
14. F. P. Bundy, "Melting point of graphite at high pressure: heat of fusion," Science **137**, 1055–1057 (1962).
15. P. O. Lagage, J. W. Pel, M. Authier, J. Belorgey, A. Claret, C. Doucet, D. Dubreuil, G. Durand, E. Elswijk, P. Girardot, H. U. Käufl, G. Kroes, M. Lortholary, Y. Lussignol, M. Marchesi, E. Pantin, R. Peletier, J.-F. Pirard, J. Pragt, Y. Rio, T. Schoenmaker, R. Siebenmorgen, A. Silber, A. Smette, M. Sterzik, and C. Veyssiere, "Successful commissioning of VISIR: the mid-infrared VLT Instrument," The Messenger **117**, 12–16 (2004).
16. C. Delacroix, P. Forsberg, M. Karlsson, D. Mawet, C. Lenaerts, S. Habraken, C. Hanot, J. Surdej, A. Boccaletti, and J. Baudrand, "Annular groove phase mask coronagraph in diamond for mid-IR wavelengths: manufacturing assessment and performance analysis," Proc. SPIE **7731**, 77314W (2010).

4

A performance study of manufactured diamond AGPMs

Contents

Abstract. *Based on the results presented in the previous chapter, obtained with a diamond subwavelength grating half-wave plate, we expose in the present chapter the complete development of broadband diamond annular groove phase masks (AGPMs) dedicated to mid-infrared wavelengths. First, we define some of the metrics that are generally used to quantify the attenuation produced by a coronagraph, and the basics of the destructive interference processes occurring in a phase-mask such as the AGPM. Then, the definition of optimal designs in synergy with the fabrication process is exposed. We also explain the different metrology techniques that were used to precisely characterize the shape of the subwavelength gratings. Finally, we present the expected performances of several manufactured components, as well as the micro-lithography and associated techniques which have been used to fabricate them.*

4.1 From half-wave plates to AGPMs

As already stated in Section 2.2.4, an annular groove phase mask (AGPM) is a vector vortex coronagraph (VVC) providing a continuous helical phase ramp, varying azimuthally around the optical center. In other words, it is simply a halfwave plate (HWP) in which the optical axes rotate about the center. While studying SG-HWP (Chapter 3), we have defined the phase retardation $\Delta\Phi_{TE-TM}(\lambda)$ in Equation 3.27, and the phase shift error $\varepsilon(\lambda)$ with respect to π in Equation 3.47. We have then optimized the grating parameters by minimizing the π-phase shift error standard deviation σ, over the whole bandwidth. In the present case of an AGPM, we must minimize another metrics in order to optimize the coronagraph's ability to attenuate the central starlight. In practice, the so-called figure of merit is not univocally defined among the astronomers community. Different metrics exist:

- the contrast in luminance $\Delta L'$ expressed in magnitudes as a function of radial offset (in λ/d units) from the center ;

- the peak-to-peak (PTP) rejection as the ratio of the maximum intensity of the direct image to the maximum intensity of the coronagraphic image, which also exists in its inverse version, the PTP attenuation;

- or else, the total rejection R as the ratio of total intensity of the direct image to that of the coronagraphic image, and which also exists in its inverse version, that is the total attenuation $N = \frac{1}{R}$.

Although the PTP attenuation is a widely employed metrics to quantify the coronagraphic performance, it supposes that the coronagraphic image point spread function (PSF) is similar in shape to the non-coronagraphic (direct) image PSF. In reality, the presence of the AGPM slightly changes the PSF profile near the axis. This phenomenon is characteristic of all coronagraphs. Therefore, in this thesis, we mainly use the total attenuation metrics N, also called the *null depth* or *nulling*, which is a more robust metrics since it is insensitive to the PSF change. The null depth is thus defined as the ratio between the coronagraphic (I_{coro}) and the off-axis (I_{off}) PSF profiles, integrated over the whole field (Ω):

$$N(\lambda) = R^{-1}(\lambda) = \iint_{\Omega} \frac{I_{\text{coro}}(\lambda)}{I_{\text{off}}(\lambda)} d\,\Omega \ . \tag{4.1}$$

Let us now evaluate the total null depth for an AGPM limited by chromatism. Therefore, we consider that the coronagraphic and the off-axis PSF profiles are parallel, and we can drop the double integral in equation 4.1. By definition, the coronagraphic PSF profile I_{coro} is obtained by locally creating a destructive interference between two coherent wavefronts, of complex amplitudes

$$U_j(\lambda) = A_j(\lambda)\, e^{i\,\Phi_j} = A_j(\lambda)\, e^{i\left[\frac{2\pi}{\lambda}\, z_j + \phi_j(\lambda)\right]} \qquad \text{with } j = 1 \text{ or } 2\ , \tag{4.2}$$

where A_j are the real amplitudes ($A_j^2 = I_j$), Φ_j the global phase, z_j the optical path delays (OPD), and ϕ_j the phase shifts experienced by each wavefront j. If we suppose in first approximation that the intensities of both wavefronts are equal ($I_1 = I_2 = I_0$), the transmitted intensity at the recombination of the two wavefronts $I(\lambda) = |U_1(\lambda) + U_2(\lambda)|^2$ can be calculated using

$$\begin{aligned} \Re\left[U_1(\lambda) + U_2(\lambda)\right] &= \sqrt{I_0}\,\left[\sin\Phi_1 + \sin\Phi_2\right]\ , \\ \Im\left[U_1(\lambda) + U_2(\lambda)\right] &= \sqrt{I_0}\,\left[\cos\Phi_1 + \cos\Phi_2\right]\ , \end{aligned} \tag{4.3}$$

leading to

$$\begin{aligned} I(\lambda) &= \Re\left[U_1(\lambda) + U_2(\lambda)\right]^2 + \Im\left[U_1(\lambda) + U_2(\lambda)\right]^2 \\ &= I_0\left(\sin^2\Phi_1 + \cos^2\Phi_1 + \sin^2\Phi_2 + \cos^2\Phi_2 + 2\sin\Phi_1\sin\Phi_2 + 2\cos\Phi_1\cos\Phi_2\right) \\ &= I_0\left(2 + 2\cos(\Phi_2 - \Phi_1)\right) \\ &= 2\,I_0\left[1 + \cos\left(\tfrac{2\pi}{\lambda}(z_2 - z_1) + (\phi_2(\lambda) - \phi_1(\lambda))\right)\right] \end{aligned} \tag{4.4}$$

which in the case of a proper set-up arrangement with equal OPDs ($z_1 = z_2$) becomes

$$I(\lambda) = 2\,I_0\left(1 + \cos\Delta\phi(\lambda)\right)\ . \tag{4.5}$$

From equation 4.5, we can show that with a perfect HWP, that is with a phase shift $\Delta\phi = \pi$, the nulling is total:

$$N = \frac{I_{\text{coro}}}{I_{\text{off}}} = \frac{\min(I(\lambda))}{\max(I(\lambda))} = \frac{2\,I_0\,(1-1)}{2\,I_0\,(1+1)} = 0\ . \tag{4.6}$$

4.1.1 Phase mismatch

In practice, as we have seen in Chapter 3, the π-phase shift $\Delta\phi$ is not perfect at each wavelength. By taking the error $\varepsilon(\lambda)$ into account, Equation 4.5 becomes

$$I(\lambda) = 2\,I_0\left(1 + \cos\left(\pi + \varepsilon(\lambda)\right)\right) = 2\,I_0\left(1 - \cos\varepsilon(\lambda)\right)\ , \tag{4.7}$$

and since ε is normally very small, we can approximate Equation 4.7 by a Maclaurin series of second order:

$$I(\lambda) = 2\,I_0\left(\frac{\varepsilon(\lambda)^2}{2}\right)\ . \tag{4.8}$$

By integration over the bandwidth $\Delta\lambda$, we can formulate the residual intensity of the destructive input (I_{coro}) in terms of the phase shift error standard deviation $\sigma = \int_{\Delta\lambda} \varepsilon(\lambda)^2 d\lambda \,/\, \Delta\lambda$

$$I_{\text{coro}} = \int_{\Delta\lambda} \min(I(\lambda)) d\lambda = \int_{\Delta\lambda} I_0 \, \varepsilon(\lambda)^2 \, d\lambda = I_0 \, \sigma \, \Delta\lambda \ , \tag{4.9}$$

and the total intensity of the constructive input (I_{off}) corresponding to the PSF without coronagraph

$$I_{\text{off}} = \int_{\Delta\lambda} \max(I(\lambda)) d\lambda = \int_{\Delta\lambda} 2I_0(1+1) d\lambda = 4 \, I_0 \, \Delta\lambda \ , \tag{4.10}$$

resulting in the expression of the null depth, calculated with phase mismatch only:

$$N = \frac{I_{\text{coro}}}{I_{\text{off}}} = \frac{I_0 \, \sigma \, \Delta\lambda}{4 \, I_0 \, \Delta\lambda} = \frac{\sigma}{4} \ . \tag{4.11}$$

4.1.2 Intensity mismatch

So far, we have maintained the assumption that the amount of light in each wavefront was the same, which is not always true. Slightly unequal wavefront intensities will induce a non-null transmission on the optical axis, and thus contribute as a background emission. Taking the intensity mismatch ($A_1 \neq A_2$) into account, Equation 4.5 becomes

$$\begin{aligned} I(\lambda) &= A_1^2 + A_2^2 + 2A_1A_2 \cos \Delta\phi(\lambda) \\ &= A_1^2 + A_2^2 - 2A_1A_2 \cos \varepsilon(\lambda) \\ &= A_1^2 + A_2^2 - 2A_1A_2 (1 + \tfrac{\varepsilon(\lambda)^2}{2}) \end{aligned} \tag{4.12}$$

from which we can express the null depth as a function of the wavelength

$$N(\lambda) = \frac{I_{\text{coro}}(\lambda)}{I_{\text{off}}(\lambda)} = \frac{\min(I(\lambda))}{\max(I(\lambda))} = \frac{(A_1 - A_2)^2 - \varepsilon(\lambda)^2 \, A_1A_2}{(A_1 + A_2)^2} \ , \tag{4.13}$$

and assuming an intensity ratio $q(\lambda) = I_2 \,/ I_1 = A_2^2 \,/ A_1^2$ between the two polarisation components, TE and TM, the null depth becomes

$$N(\lambda) = \frac{[1 - \sqrt{q(\lambda)}]^2 + \varepsilon(\lambda)^2 \sqrt{q(\lambda)}}{[1 + \sqrt{q(\lambda)}]^2} \ . \tag{4.14}$$

In the theoretical case where the coronagraphic profile remains identical to the original PSF profile, this formula of the null depth is also valid for the PTP attenuation, which was demonstrated in an ideal case by Mawet et al. (2005a).

4.2 Design of diamond AGPMs

4.2.1 Synergy between design and manufacturing

In the wake of our successful results obtained with a diamond SG-HWP dedicated to the upper half of the N-band (centered around 12 μm), and encouraged by the continuous improvements in diamond microfabrication techniques of our collaborators from the Ångström laboratory, we started to manufacture diamond AGPM coronagraphs. Most of our developments and accomplishments were achieved as a result of our strong partnership with the Swedish team, and their remarkable work. I had myself the chance to spend one month in the laboratory of Uppsala for the manufacturing of our first prototypes. At that time, the AGPM was starting to shape up (see Delacroix et al. 2010a), but the aspect ratio was still too small, and the surface on top of the grating was quite rough, leading to unwanted scattering. About three years later, the grating teeth now look brilliant (see Figure 4.1), and the manufacturing process is well mastered and reproducible.

The design of the grating was conducted in complete synergy with the manufacturing. Optimal grating parameters were calculated by RCWA, bearing in mind fabrication constraints and expected limitations. In particular, the slope of the sidewalls was taken into account and the aspect ratio was kept within the range of what can be etched in the material. After the first achievements, and as soon as the manufacturing process was developed, these optimizations were re-calculated with better estimates of sidewall angles. This loop was repeated for several iterations, until the process was precise enough for N-band AGPMs to be manufactured with desired specifications. One of these was then installed on VLT/VISIR, as we will discuss in Chapter 6. In the meantime, we started working on much finer gratings meant for the L band (3.5 - 4.1 μm),

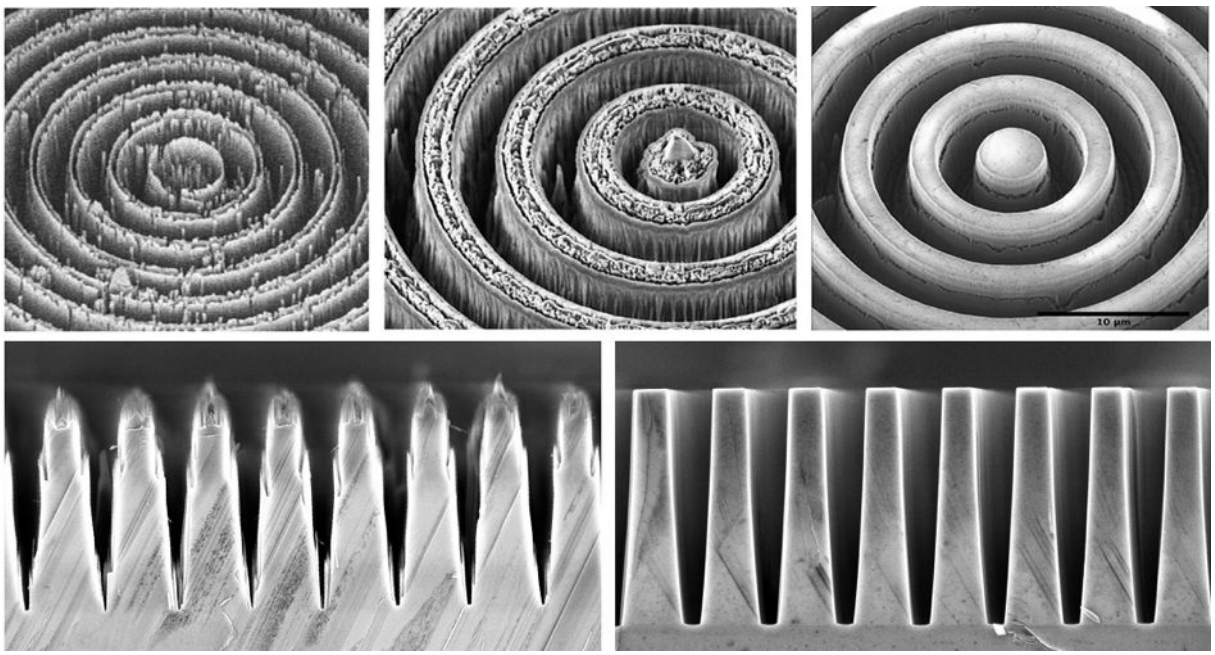

Figure 4.1: Evolution of the manufacturing of diamond AGPMs. Top: N-band AGPMs, with periods ∼4.6 μm, manufactured in November 2009, October 2010, and February 2012 (from left to right). Bottom: cracked spares of L-band AGPMs, with periods ∼1.4 μm, manufactured in March 2011 and September 2012 (from left to right). Courtesy of the Ångström laboratory.

which is more difficult for two reasons: (i) the period is about three times smaller for the L band than for the N band, which requires a much higher precision, and (ii) the etch rate and sidewall angle depend more strongly on the groove width as the grooves get narrower (see Forsberg 2013). Again, iterations between design and manufacturing were necessary to adapt the specifications to the fabrication limitations, and yet again, this successfully led to the manufacturing of L-band AGPMs which were then tested on a coronagraphic bench (see Chapter 5) and installed at the telescope (see Chapter 6).

The design calculations and expected performances of the manufactured AGPMs are presented hereafter, whereas the fabrication procedure is described in Section 4.3.

4.2.2 Selection of optimal parameters

As in the case of a SG-HWP, the grating parameters of the AGPM were optimized by means of RCWA. This time, the figure of merit is not the phase-shift error standard deviation σ anymore, but the null depth $N(\lambda)$ averaged over the whole bandwidth. As determined in Equation 4.14, the null depth is function of the wavelength since it must take both the phase shift error $\varepsilon(\lambda)$ and the intensity ratio $q(\lambda)$ into account. These two wavelength-dependent functions involve all the geometrical parameters illustrated in Figure 4.2, including a new parameter: the sidewall angle α. Indeed, it soon appeared obvious that a perfect rectangular shape was beyond the fabrication capabilities, and that we would have to cope with a trapezoidal groove shape.

At first, we focused on the upper part of the N band (11–13.2 μm), fixing the period the the ZOG limit $\Lambda = 4.6$ μm. This choice was motivated by manufacturability reasons: the longer the wavelength, the larger the period. Besides, compared to quartz, diamond has a much higher refractive index which allows shallower structures, so that the aspect ratio was less of a problem than the overall grating dimensions. After some iterations between manufacturing and design, we could estimate that the sidewall angle, for our specific N-band AGPM profile, is comprised between 2.5° and 3°. This result guided the design simulations towards new optimal parameters. A whole set of multiparametric RCWA simulations was obtained for multiple values of the sidewall angle α ranging from 2.5° to 3°, calculating the mean null depth μ over the 11–13.2 μm bandwidth, function of the filling factor F and the grating depth h. The results of this optimization campaign

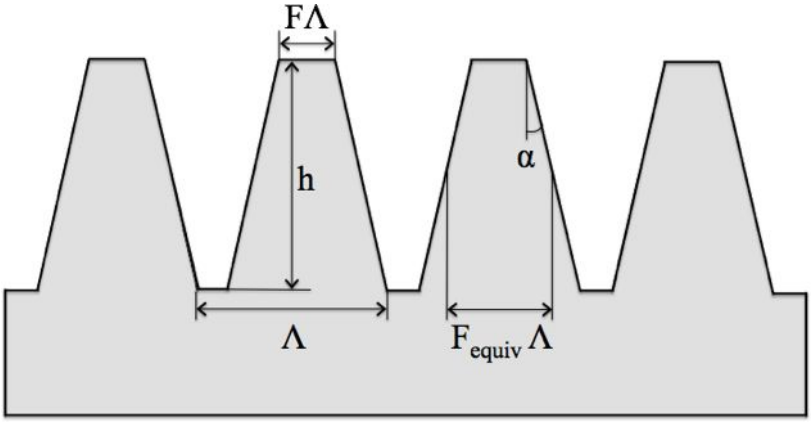

Figure 4.2: Schematic diagram of a trapezoidal grating of period Λ. The filling factor F is such that the width on top of the walls, called feature line, is $F\Lambda$. The grating sidewalls have an angle α and an average width $F_{equiv}\,\Lambda$.

are illustrated in Figure 4.3, and show that the mean null depth μ is at least as good as 10^{-3} on a narrow area of the parameter space (dark blue zone). The best null depths are achieved for $F \approx 0.45$ and $h \approx 16\,\mu$m. This optimal solution however presents two major limitations: (i) the required depth is quite hard to achieve given the etching capacities, and (ii) the null depth is more sensitive to sidewall angle variations (Figure 4.3, bottom right). Moreover, these slope variations tend to increase with the grating depth. A more relaxed specifications set was thus preferable. Based on these observations, we have fixed the filling factor to $F = 0.4$ and simulated the complete spectral performance for several scenarios of h and α values (Figures 4.4 and 4.5).

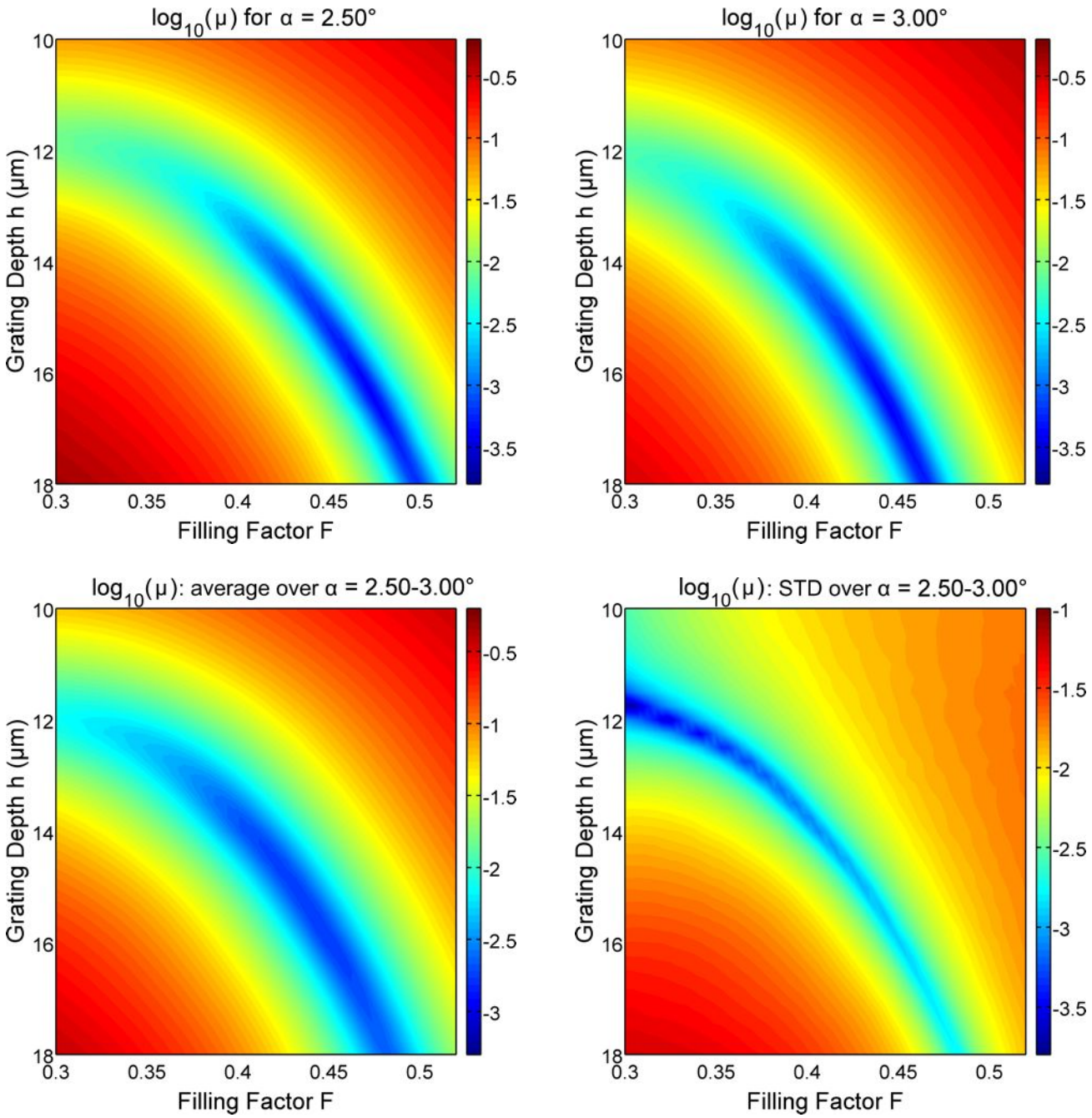

Figure 4.3: Multiparametric RCWA simulations of diamond AGPM's average null depth μ (logarithmic scale) over the upper half of the N band (11–13.2 μm), function of h and F. Top: μ-maps for a sidewall angle $\alpha = 2.5°$ (left) and 3° (right). Bottom: Average (left) and standard deviation (right) of a μ-maps sequence ranging from $\alpha = 2.5$ to 3°.

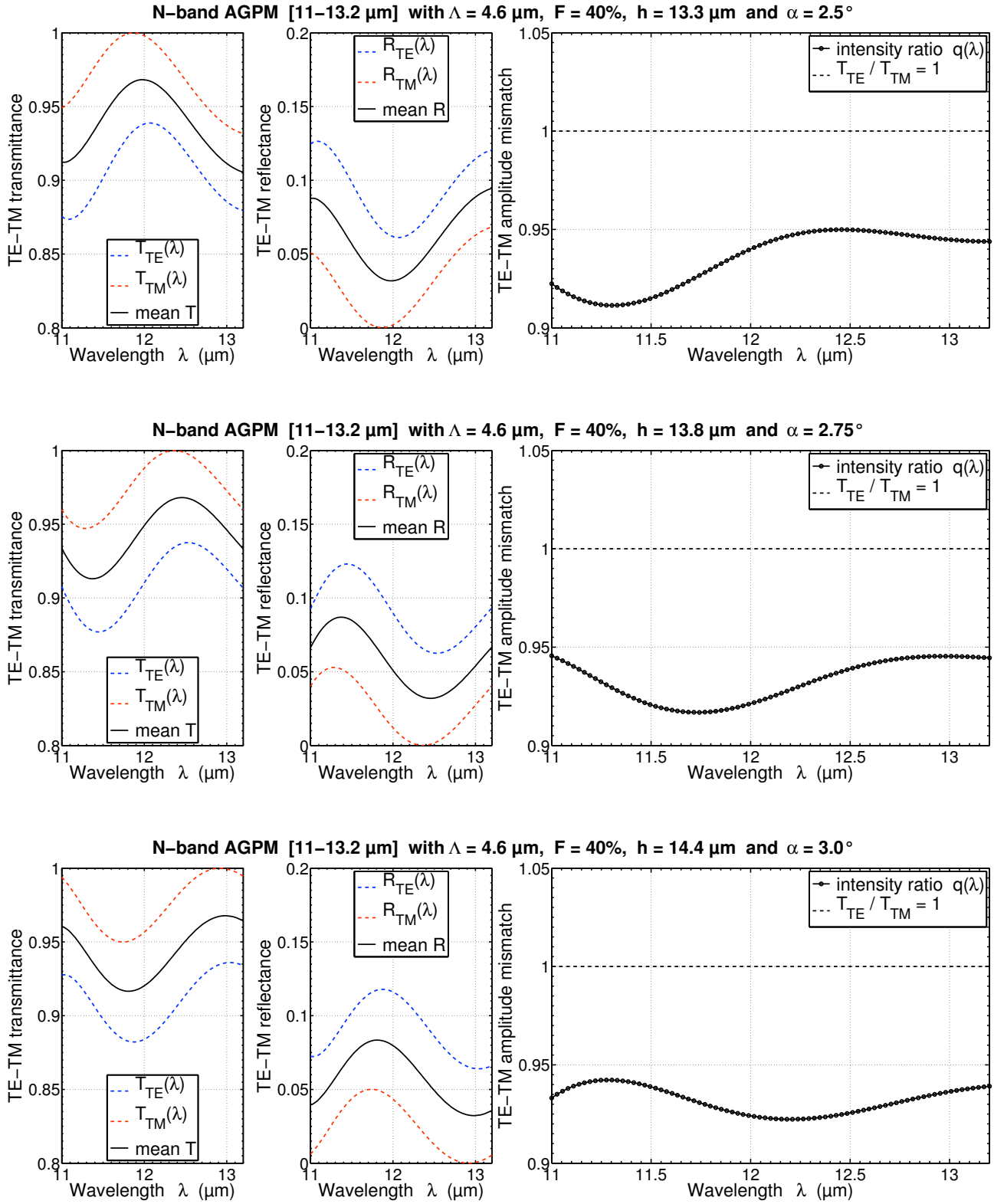

Figure 4.4: Spectral performance RCWA simulations of diamond N-band AGPMs with fixed period $\Lambda = 4.6\,\mu$m and filling factor $F = 0.4$. The figure shows three plots corresponding to optimal couples of grating depth $h = 13.3/13.8/14.4\,\mu$m and sidewall angles $\alpha = 2.5/2.75/3.0°$ (from top to bottom). The subplots illustrate the TE-TM transmittance and reflectance (left) and the intensity ratio $q(\lambda)$ (right) over the whole bandwidth.

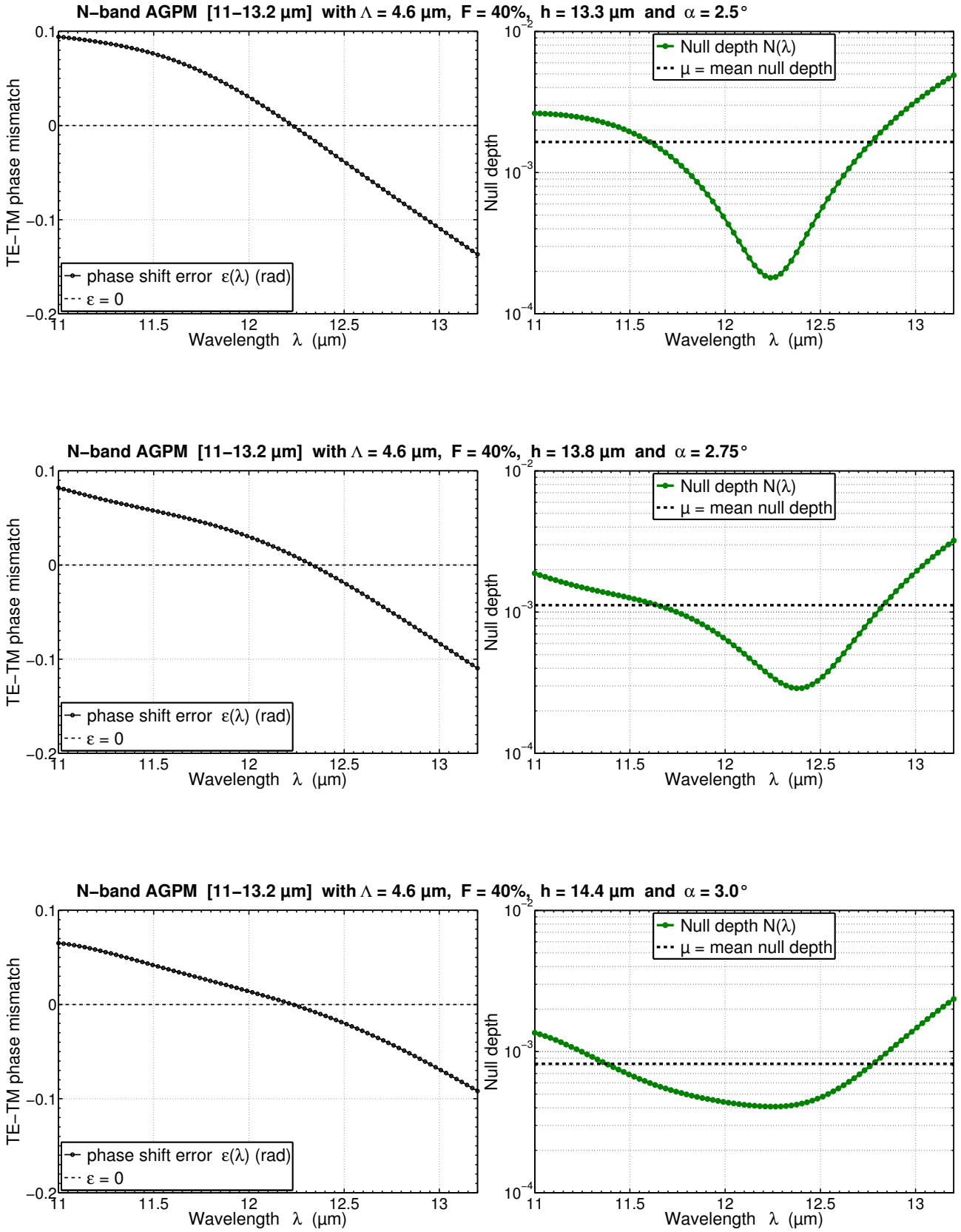

Figure 4.5: Same parametric configuration as in Figure 4.4. The subplots illustrate the phase shift error $\varepsilon(\lambda)$ (left) and the null depth $N(\lambda)$ (right) over the whole bandwidth.

There is much we can learn from Figures 4.4 and 4.5. First, we are confident that, even with a sub-optimal solution, that is with a filling factor $F = 0.4$ deliberately fixed at a smaller value than the optimum $F = 0.45$, we still have a possibility to reach a mean null depth $\mu \approx 10^{-3}$. It is worth recalling that, considering the natural decay of the PSF intensity of a perfect pupil, a total attenuation of 10^{-3} is equivalent to a contrast of 5×10^{-6} at an angular separation of $2\lambda/d$. In other words, with an 8 meter diameter telescope, the theoretical contrast would be $\Delta L' \approx 13.3$ magnitudes at 0.6 arcseconds (0.″6). This is higher than required for current telescope instruments, which are still limited by wavefront spatial distortion.

Secondly, by looking at Figure 4.4, we notice that the grating reflection is ∼7%, which is much smaller than the natural reflection of a simple air/diamond interface at N band ∼17%. In fact, the high transmittance ∼93% is due to the grating. Although it was not designed with reducing reflections in mind, it still serves this purpose to some degree and acts like an antireflective structure. However, the AGPM transmittance is also impacted by the backside reflection and the absorption. To improve the total transmittance, an antireflective grating (ARG) can be etched directly on the backside of the diamond substrate (Karlsson & Nikolajeff 2003). This was done for some of the manufactured components, as will be discussed in Chapter 5.

Finally, by comparing the $\varepsilon(\lambda)$ and $q(\lambda)$ curves, we can see how the intensity mismatch and the phase mismatch compensate each other, thereby minimizing the null depth over the whole bandwidth. Consequently, an AGPM can be made achromatic even if the phase-shift is not necessarily as close as possible to π, unlike in the case of a half-wave plate.

4.2.3 Expected performances of manufactured mid-infrared AGPMs

In addition to the development of N-band AGPMs, we have also explored the parameter space of an L-band (3.5–4.1 μm) component. Our strategy with the L band was very similar to the one with the N band. The main difference resides in the global size of the parameters, which is intrinsic to the three times smaller wavelength. As a result, the period was constrained to be smaller than the ZOG limit λ/n, that is $\Lambda \approx 1.42\,\mu$m. A whole new set of multiparametric μ-maps was calculated using RCWA simulations. Besides, the sidewall angle was estimated with a better precision. Indeed, for the N-band components, the profile parameters could only be measured in best effort through microscopy techniques, as described in Section 4.3.2, leading to an estimated $\alpha \approx 2.75°$. In the case of L band, microscopy results were correlated to laboratory characterization of several L-band AGPMs to derive their true profile specifications, including α. These laboratory measurements are detailed in Chapter 5.

In total, eight AGPMs have been manufactured so far, four for each spectral band, namely AGPM-N1 to AGPM-N4, and AGPM-L1 to AGPM-L4. The expected performances of these components are presented in Figure 4.6. AGPM-N1 was the first attempt. It was etched as deep as possible, which resulted in strongly narrowed feature lines, hence a highly reduced null depth. AGPM-N2 is not represented as it was damaged during manufacturing process. AGPM-N4 shows the best N-band performance, and was therefore installed on the VLT/VISIR instrument (see Chapter 6). All N-band null depths were calculated with fixed period $\Lambda = 4.6\,\mu$m and angle $\alpha = 2.75°$, whereas for L-band AGPMs, only the period was fixed to $\Lambda = 1.42\,\mu$m. The other parameters were measured combining metrology and laboratory characterization. The sidewall angles of the manufactured L-band components slightly vary from 2.4° to 3.25°. AGPM-L1 and AGPM-L2 were initial tests, etched with the exact same methods as N-band components. Furthermore, the e-beam-written master used in the patterning of these two had too narrow lines, explaining their steeper walls (smaller angles) and lower expected performance. AGPM-L3 was an

experiment with a different etch recipe giving a grating profile of trapezoidal walls with triangular tops, designed to reduce the problem of ghost reflections (see Chapter 6). Its depth is therefore intentionally too high, and as a result, it is not represented on the average μ-map of Figure 4.6. However, it shows very good null depth capacities, and was therefore installed on VLT/NACO (see Chapter 6). AGPM-L4, finally, was fabricated with a close to optimal depth for its actual filling factor and sidewall angle. It is the best diamond AGPM coronagraph to date. Its installation on LMIRCam, the L-band camera of the LBTI, is currently going on. Thanks to the very high Strehl ratio delivered by the LBT adaptive optics at L band (>95%, Esposito et al. 2011), we expect that AGPM-L4 will unleash its full potential on this instrument.

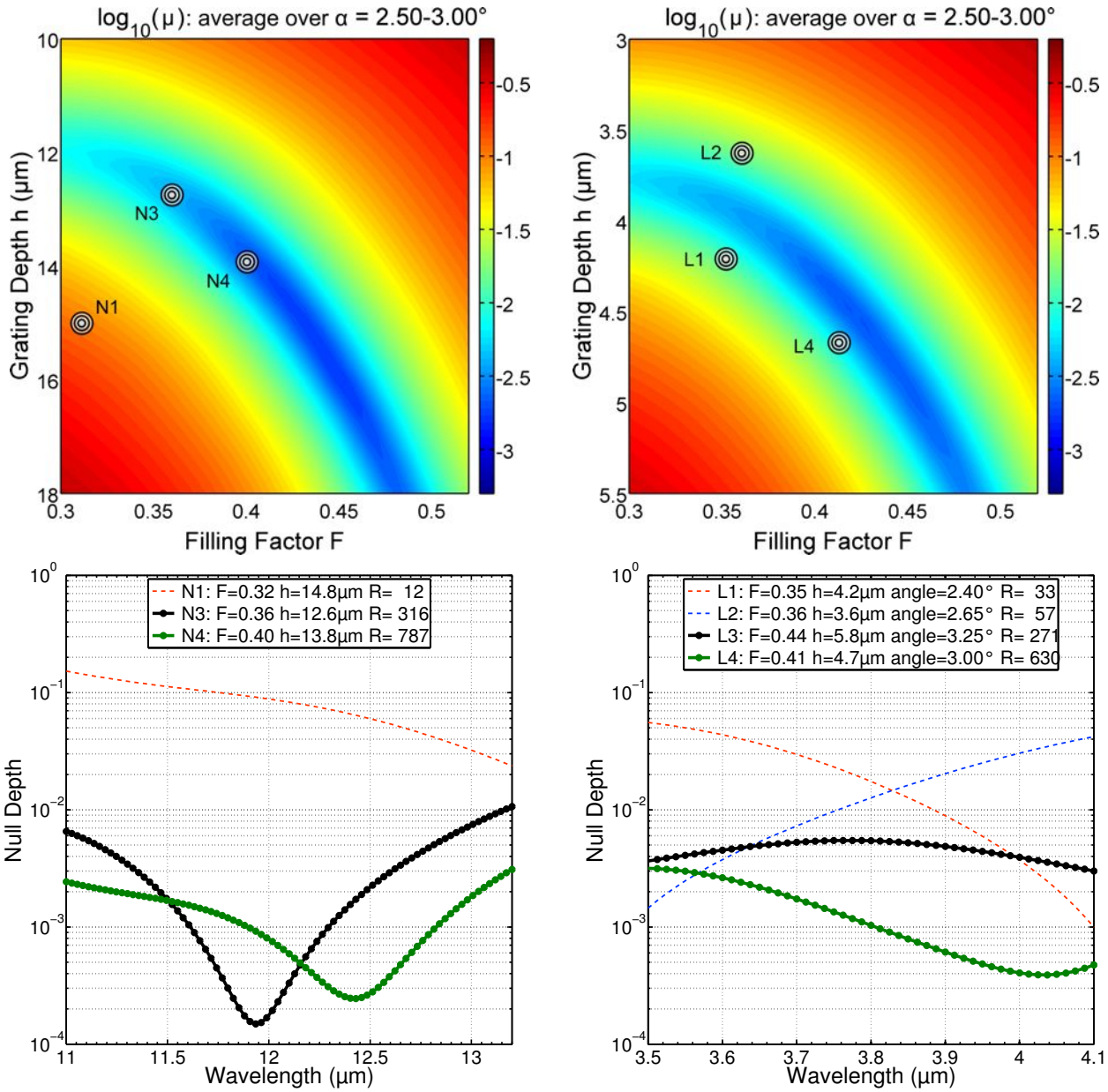

Figure 4.6: Top: Manufactured N-band (left) and L-band (right) AGPM's parameters represented on the corresponding μ-maps. Bottom: Expected null depth (logarithmic scale) of several manufactured AGPMs at N-band with measured period $\Lambda = 4.6\,\mu$m (left), and at L-band with measured period $\Lambda = 1.42\,\mu$m (right). Slightly different sidewall angles were measured for L-band AGPMs, and estimated to $\alpha = 2.75°$ for N-band AGPMs.

4.2.4 Downscaling to the near-infrared and visible regimes

It says something about the maturity of the fabrication process that we were able to produce nearly optimal grating parameters with so few trials. The grating parameters are now well established. It is very likely that new optimal designs dedicated to other wavelengths, and conserving the same fabrication recipe, would lead to filling factors $F \approx 40\%$ and sidewall angles $\alpha \approx 3°$. It is however possible to reach even higher attenuation by slightly increasing the filling factor. Given our highly satisfying results, we have explored other parameter spaces for shorter wavelengths. Figure 4.7 shows the null depth expected performances for different near-infrared and visible spec-

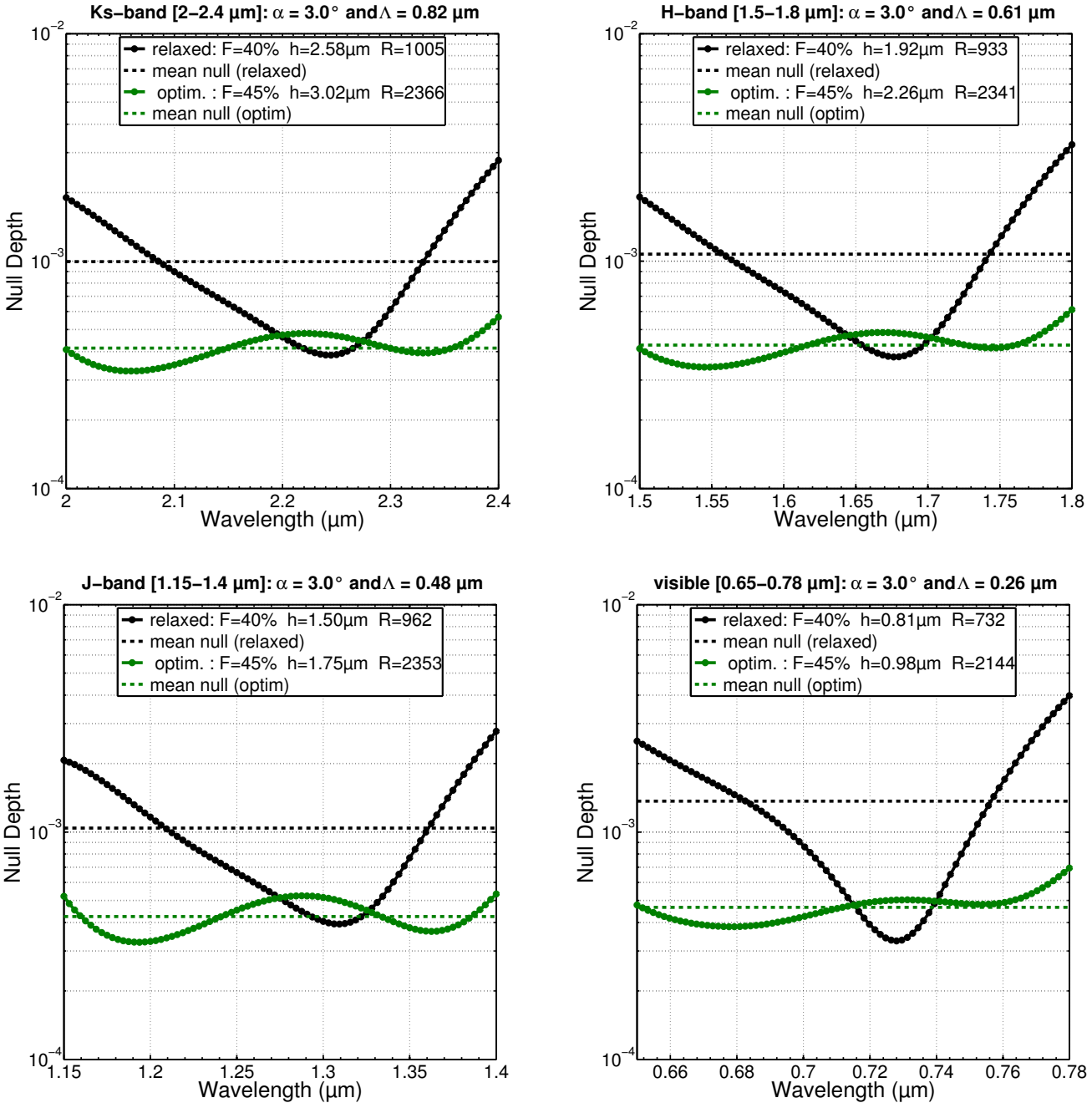

Figure 4.7: Spectral performance RCWA simulations of near-infrared (K, H, and J bands) and visible spectra AGPMs, with fixed sidewall angle $\alpha = 3°$. The null depth is calculated both with relaxed specifications ($F = 45\%$), and with optimal specifications (F unfixed).

tral regions, for two parameters sets: the first one with relaxed specifications for a fixed filling factor $F = 40\%$, and the second one with optimal specifications ($F = 45\%$). Results show similar null depth levels $N = 10^{-3}$ to 10^{-4}. These AGPMs, if manufactured, could be excellent candidates to be integrated on future instruments, both for space missions and ground-based telescopes, e.g., E-ELT/PCS (EPICS).

In the last part of this Section, we summarize the results of our RCWA simulations in Table 4.1, with all the parameters and performances of the whole set of diamond AGPM coronagraphs. We include fabricated mid-infrared AGPMs, as well as potentially manufacturable optimal designs, for all studied spectral bandwidths, from the mid-infrared to the visible light spectrum.

Table 4.1: Geometric parameters of several diamond AGPM designs (fabricated, optimal with $F = 0.4$, and optimal with $F = 0.45$) optimized for different spectral bands (20% bandwidth) using RCWA calculations. The last two columns give the expected coronagraphic performance. R refers to the total rejection, equivalent to the inverse of the total attenuation or null depth N. The last column gives the achievable contrast at a $2\lambda/D$ angular separation from the star, D corresponding to the diameter of the telescope.

20% BW		Grating parameters				Total rejec./atten.		Contr. at $2\lambda/D$
Filter	Range	$\Lambda(\mu m)$	$\alpha(^\circ)$	F	$h(\mu m)$	R	$N = R^{-1}$	$(5 \times 10^{-3})N$
Fabricated								
N1	11-13.2	4.6	2.75	0.32	14.8	12	8.3×10^{-2}	4.2×10^{-4}
N3	11-13.2	4.6	2.75	0.36	12.6	316	3.2×10^{-3}	1.6×10^{-5}
N4	11-13.2	4.6	2.75	0.40	13.8	787	1.3×10^{-3}	6.4×10^{-6}
L1	3.5-4.1	1.42	2.40	0.35	4.2	33	3.0×10^{-2}	1.5×10^{-4}
L2	3.5-4.1	1.42	2.65	0.36	3.6	57	1.8×10^{-2}	8.8×10^{-5}
L3	3.5-4.1	1.42	3.25	0.44	5.8	271	3.7×10^{-3}	1.8×10^{-5}
L4	3.5-4.1	1.42	3.00	0.41	4.7	630	1.6×10^{-3}	7.9×10^{-6}
Optimal		**with** $F = 0.40$						
N	11-13.2	4.6	3.0	0.40	14.4	1096	9.1×10^{-4}	4.6×10^{-6}
L	3.5-4.1	1.42	3.0	0.40	4.47	1134	8.8×10^{-4}	4.4×10^{-6}
K	2.0-2.4	0.82	3.0	0.40	2.58	1005	9.9×10^{-4}	5.0×10^{-6}
H	1.5-1.8	0.61	3.0	0.40	1.92	933	1.1×10^{-3}	5.4×10^{-6}
J	1.15-1.4	0.48	3.0	0.40	1.50	962	1.0×10^{-3}	5.2×10^{-6}
vis.	0.65-0.79	0.26	3.0	0.40	0.81	732	1.4×10^{-3}	6.8×10^{-6}
Optimal		**with** $F = 0.45$						
N	11-13.2	4.6	3.0	0.45	16.9	2354	4.2×10^{-4}	2.1×10^{-6}
L	3.5-4.1	1.42	3.0	0.45	5.21	2457	4.1×10^{-4}	2.0×10^{-6}
K	2.0-2.4	0.82	3.0	0.45	3.02	2366	4.2×10^{-4}	2.1×10^{-6}
H	1.5-1.8	0.61	3.0	0.45	2.26	2341	4.3×10^{-4}	2.1×10^{-6}
J	1.15-1.4	0.48	3.0	0.45	1.75	2353	4.2×10^{-4}	2.1×10^{-6}
vis.	0.65-0.79	0.26	3.0	0.45	0.98	2144	4.7×10^{-4}	2.3×10^{-6}

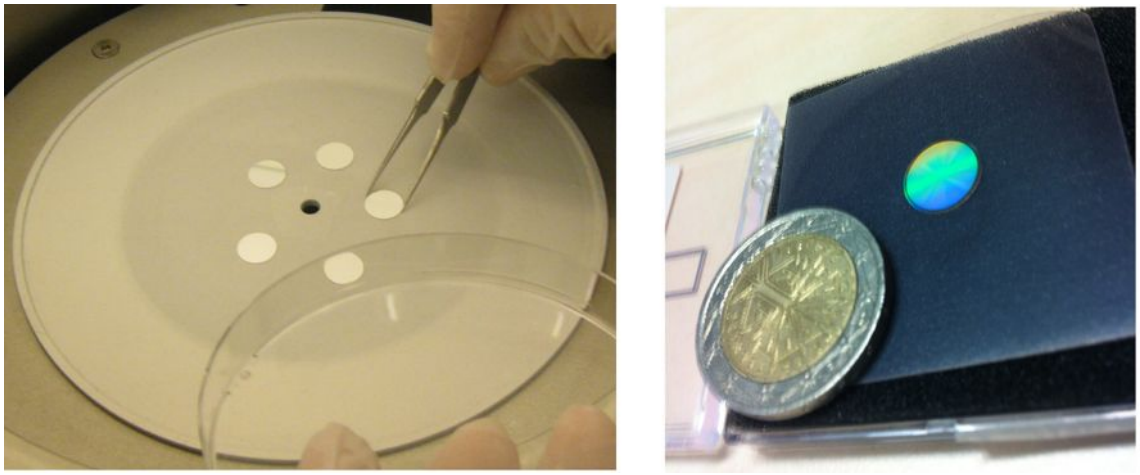

Figure 4.8: Left: 10 mm diameter, 0.3 mm thick microcrystalline CVD diamond substrates of optical quality. The five disks were coated in the same batch with a 500 nm aluminum layer. Right: One of these disks with a subwavelength grating etched on top of it. Reflection of visible light produces a colorful diffraction pattern.

4.3 Manufacturing and metrology

Thanks to the expertise of the Ångström Laboratory in the microfabrication of diamond optical components, the targeted specifications have been reached with high precision. For the first time, AGPMs have been produced. In this section, we briefly describe the fabrication method developed by our Swedish collaborators. We also explain the different metrology techniques that were used to precisely characterize the shape of the subwavelength gratings. For more details about the manufacturing process, we refer to Karlsson et al. (2010), Forsberg & Karlsson (2013a), and Forsberg (2013).

4.3.1 Manufacturing at the Ångström Laboratory

The microfabrication has been conducted at the Ångström Laboratory (Uppsala), using circular diamond substrates (diameter = 10 - 20 mm / thickness = 0.3 mm) of optical quality (see Figure 4.8). The fabrication method was especially developed and optimized for this particular process. It consists of the following steps, illustrated in Figure 4.10. First, an aluminum layer (several hundreds of nm, depending on the groove depth) is sputtered on top of the diamond substrate, and a polymer film is spun onto the *Al*-coating. This polymer, which is a special nano-imprint lithography (NIL) resist, must be spun and baked several times, with more resist added in between, in order to achieve a layer thick enough while minimizing the size of the created edge bead. Indeed, an unwanted edge bead (see Figure 4.9) is generated during the spin coating and

Figure 4.9: Illustration of the edge bead effect. Courtesy of Pontus Forsberg.

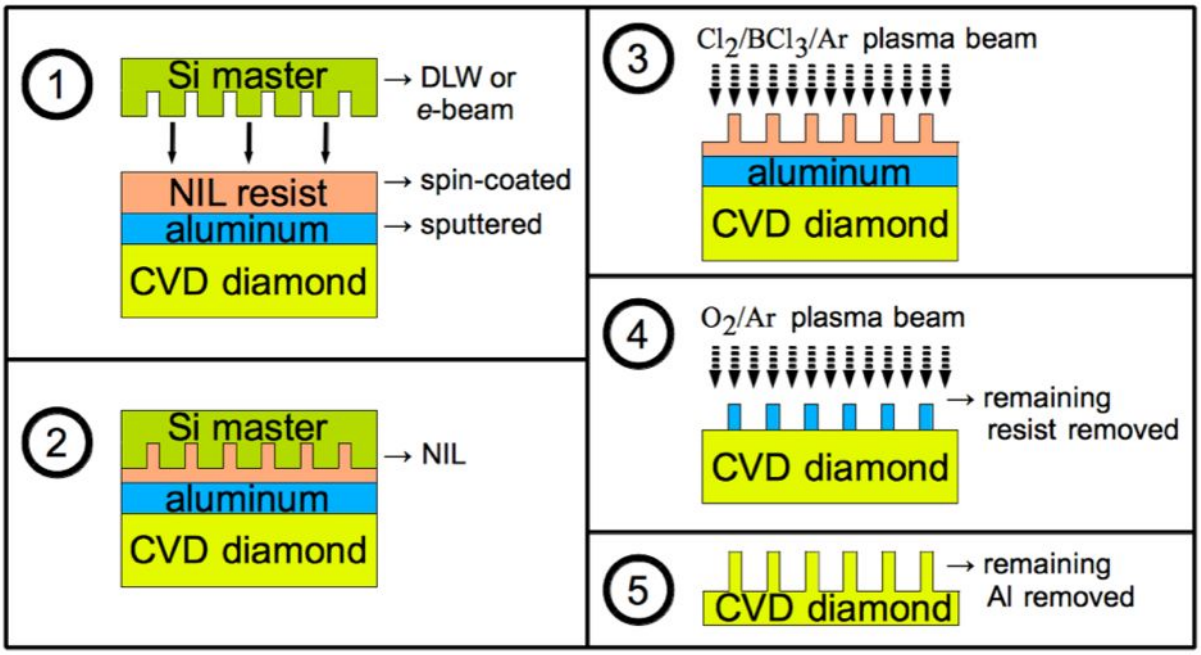

Figure 4.10: Illustration of the microfabrication process of diamond AGPMs.

reduces the effective grating area by about 10 - 20% in the worst case. Next, the surface relief master, previously prepared either by direct laser writing (DLW) or by electron-beam (e-beam) lithography, is imprinted in the NIL-resist following a specific NIL process, and then transferred into the underlying aluminum by use of a reactive ion etching process including inductively coupled plasma (RIE-ICP). The aluminum is etched in a $Cl_2/BCl_3/Ar$ chemistry until it is etched through. The remaining resist is removed in acetone, and the Al-mask carefully inspected by atomic force microscopy (AFM) and white light interferometry. The Al-mask pattern is then transferred to the diamond substrate by RIE-ICP in a O_2/Ar chemistry, and the remaining aluminum is removed with solvent. Let us mention that the master used for the NIL and fabricated by DLW in a 100 μm Ni-coated silicon wafer, is first cleaned by sonication in acetone and isopropanol, before being sputtered with chromium (30 nm) and gold (100 nm). The master is then cut into a circle to fit inside the edge bead on the diamond sample. Finally the master is treated with octadecanethiol in isopropanol to reduce sticking problems after imprinting.

4.3.2 Different metrology techniques

Microscopic metrology at the Ångström Laboratory

A classical surface metrology was carried out at the Ångström Laboratory, using scanning electron microscopy (SEM), atomic force microscopy (AFM) and white light interferometry. These various microscopy techniques can be used to measure the grating parameters of the etched components. The precision of the grating period Λ depends on the fabrication of the master. For the first N-band AGPMs, the measured error on the period is less than 5 nm, which is not affecting significantly the performances at 11 μm. For these, the master was fabricated by DLW, as described in Figure 4.10. In the case of L-band (or future near-infrared) AGPMs, with smaller specifications, this precision is improved by creating the master with e-beam lithography instead of DLW. An e-beam master is theoretically precise within a 1 nm range.

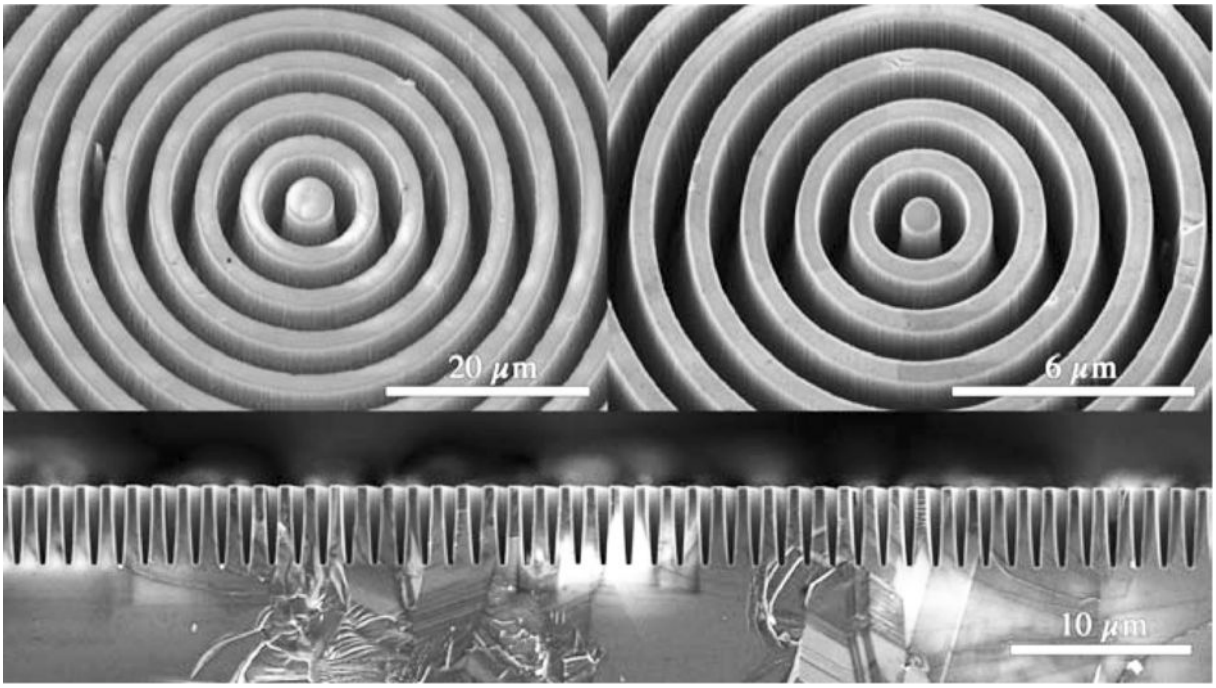

Figure 4.11: SEM micrographs of the best two AGPMs to date, for the N band (upper left) and L band (upper right). At the bottom is a cross section view of a dummy sample cracked in the process of making the L-band AGPM. Courtesy of the Ångström laboratory.

Concerning the depth h of the grooves, it must be determined by SEM. The grooves are too deep for AFM and too narrow for white light interferometry. The grating depth is actually determined by carefully measuring the distance between a point at the top of the grating and one at the bottom in several SEM micrographs taken with different tilt angles. Some of the measures are carried out during the fabrication process, in between each etching step, to control the depth in order to reach the specifications with a precision of around 100 nm (see Forsberg 2013).

The most difficult parameter to control during the fabrication process appears to be the filling factor F (or the width of the grooves), since it varies in time during the etching. As it penetrates deeper into the substrate, the plasma beam becomes thinner, so that the sides of the etched grooves are not perfectly vertical. Consequently, the profile of the ridges takes a trapezoidal shape, defined by the sidewall angle α. The only efficient way of measuring all parameters is by cracking the diamond sample (see Figure 4.11). Of course, this technique destroys the component. Therefore it must be applied on a dummy sample, etched within the same batch as the final AGPM, so that both gratings have more or less the same shape.

Diffractometry at the HOLOLAB optics laboratory

Complementary to the conventional microscopic metrology, a diffraction metrology (diffractometry) was carried on in our laboratory. For this purpose, a dedicated optical bench was installed and calibrated (see Figure 4.12, left). Its goal is to characterize the TE-TM polarizations and phase shifts induced by the AGPM. However, it is not adapted to make measures at mid-infrared wavelengths, since it is equipped with only visible and near-infrared sources, up to 2.2 μm (K band). For longer wavelengths, optical equipments (fibers, detectors) and low temperature devices (cryostats) represent a significant increase in costs, and are not planned yet. Proper polarimetric measurements with this test bench will have to wait for the first K-band and H-band AGPMs to

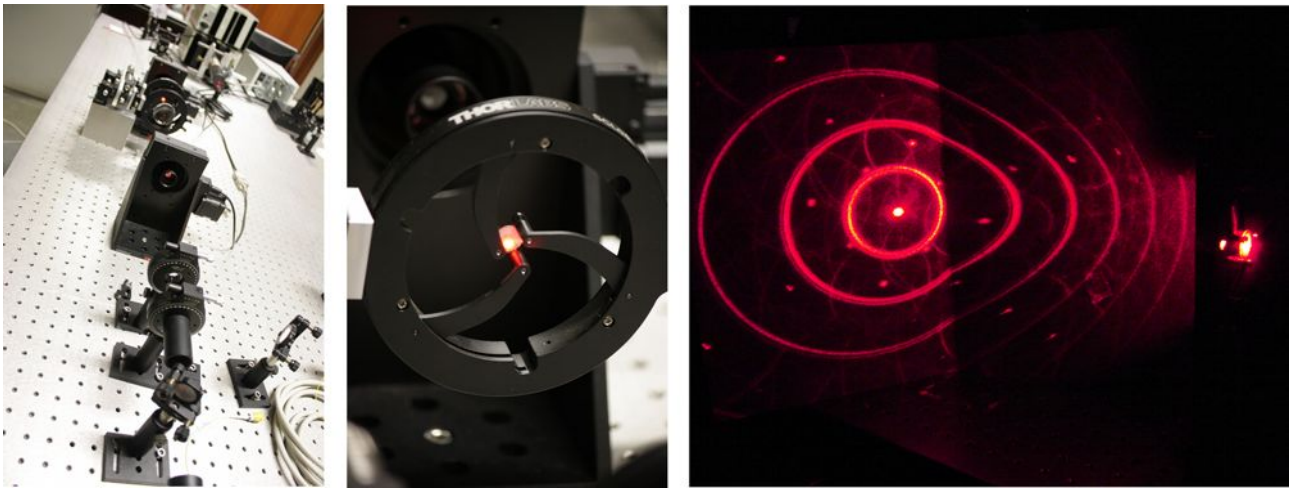

Figure 4.12: Left: Optical layout of the HOLOLAB polarimetric and diffractometric test bench. Middle: N-band AGPM in its holder. Right: Several annular transmitted diffraction orders observed at 632.8 nm.

come on the scene.

At shorter wavelengths, L-band and N-band AGPMs are of course not sublambda, and diffraction through the grating produces non-zero orders. By means of diffractometry, that is by measuring diffraction efficiencies and deviation angles of these orders, one can confirm at least the general shape of the grating. The period Λ can be easily and very quickly checked with the grating equation, defined in Section 3.1, with an acceptable precision ($\sim$50 nm). We use a red *HeNe* laser source at 632.8 nm, so that we can clearly see the orders (see Figure 4.12, right), and we measure their transmitted angles $\theta^{(m)}$. The period is then obtained with the following relation derived from Equation 3.1:

$$\Lambda = \frac{m\,\lambda}{\sin\theta^{(m)} n(\lambda)} = \frac{m}{\sin\theta^{(m)}} \times \frac{632.8 \times 10^{-9}}{2.4122} = \frac{m}{\sin\theta^{(m)}} \times 2.6233 \times 10^{-7}\ . \tag{4.15}$$

One can also measure the diffraction efficiency of each order. The diffusion (or scattering) being quite high at 632.8 nm, the measurements are not accurate enough to deduce the grating profile with precision. For instance, the zeroth order efficiency $\eta^{(0)}$ varies from $\sim$10 to $\sim$30%. By measuring the total integrated scattering TIS $\approx 50\%$ at normal incidence $\theta_i = 0$, we can evaluate the RMS roughness Δh of the component with the following expression (see Träger 2012, p.280)

$$\mathrm{TIS} = \left(\frac{4\pi \cos\theta_i\, \Delta h}{\lambda}\right)^2 \tag{4.16}$$

which gives an RMS roughness $\Delta h \approx 30$ nm. It is worth mentioning that 15 nm is the RMS value for a clean diamond substrate, provided by the supplier *Element6*. In the mid-infrared, we can expect a very low quantity of TIS, $\sim 1\%$ at L band and $\sim 0.1\%$ at N band.

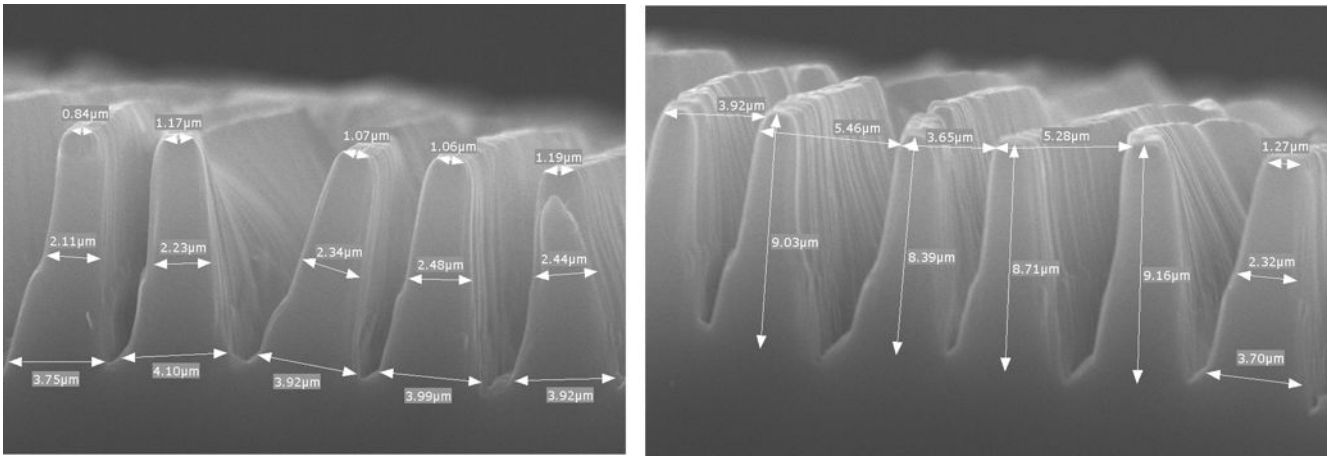

Figure 4.13: N-band AGPM silicone moulding at the CSL, giving estimations of the width (left) and depth (right) of the grooves.

Silicone moulding at the CSL

Cracking the sample is the best way of measuring the grating shape, and hence determining precisely the grating parameters. It is however only possible to do so on a dummy sample. For the final component, we need a non-destructive method. We have used a silicone moulding process (see Figure 4.13), developed at the Centre Spatial de Liège (CSL). This technique gives a good idea of the grating depth and width of the final component, but is very limited with respect to the sidewall angle estimation, since the moulding gets deformed while extracting it from the AGPM.

4.4 Conclusion

In this chapter, we have presented the results of our work on designing diamond subwavelength gratings. This design was developed in complete synergy with the manufacturing, taking into account the strengths and weaknesses of diamond microfabrication techniques. With the help of the Ångström laboratory, we managed to manufacture an achromatic half-wave plate (HWP) for the N band (11 - 13.2 μm). Thanks to an ingenious metrology, the grating parameters could be estimated with an adequate precision, giving instructions for the design specifications to adapt to the etching capabilities.

The development of this diamond HWP was a decisive step to enable the manufacturing of N-band annular groove phase masks (AGPMs). From there, we managed to fabricate several diamond AGPMs for the N band, but also for the L band (3.5 - 4.1 μm), thereby demonstrating that diamond is a very suitable material for mid-infrared coronagraphy thanks to of its exceptional properties. This result is crucial in a context where the AGPM is currently the only vector vortex coronagraph (VVC) that can be used beyond the near-infrared, especially at L band, which offers significant advantages compared to shorter wavelengths (Kasper et al. 2007). Expected null depths were calculated through RCWA simulations, both in the N band and in the L band.

Downscaling the parameters, we have then established the baseline for future AGPMs dedicated to the near-IR and the visible. Now that the fabrication is well-mastered, we believe that the next generation of diamond AGPMs is likely to suit many current and future instruments, both on ground and in space. In particular, the AGPM is a perfect candidate for high-contrast imaging instruments such as METIS and EPICS at the future E-ELT, as well as SPHERE at the VLT.

Part III

Nulling the light: in the lab and on the sky

5

Laboratory demonstration for the L band at the LESIA

Contents

Abstract. *In the past few years, various coronagraphy concepts have been used in the visible and near-infrared regimes, while coronagraphic applications in the mid-infrared have remained largely unexplored. In this chapter, we first expose our motivations for developing AGPMs for the L band (3.5 - 4.1 µm). Then, we discuss the antireflective solutions that need to be integrated to our components, in order to suppress the so-called ghost signal generated by internal reflections, which affects the coronagraphic performance. Finally, we present our laboratory results obtained on a coronagraphic bench at the Observatoire de Paris, fully in line with our projections based on rigorous coupled wave analysis discussed in the previous chapter.*

5.1 Motivations for the L band

The fabrication of diamond AGPMs presented in Chapter 4 has led to remarkable results. It gave birth to eight components, optimized for either the N band, or the L band. Some of them promise high nulling performances, predicted by RCWA simulations of the theoretical null depth. To validate the AGPM technology, simple computational assessment is however not sufficient. One has to prove it by real measurements of attenuation. These measurements can be performed in the laboratory, on a well-calibrated coronagraphic test bench. Such an installation, however, requires very specific optical equipments (sources, fibers, mirrors, detectors). Especially, a cryostat is absolutely necessary to maintain low cryogenic temperatures, and hence low background emission. All these components come with a price, and the longer the operational wavelength, the more expensive the equipments. In practice, infrared coronagraphic test benches are not common. Making demonstrations in the N band was not possible, and we concentrated our efforts on the L band, which is even more interesting on the scientific side, as we describe here after.

In recent years, the demand for L-band high contrast imaging tools, such as vector vortex coronagraphs (VVC), is particularly increasing. The reasons for this great interest are multiple.

1. **Higher planet-to-star flux ratio**. As already stated earlier in this thesis (see Section 2.5), the planet-to-star brightness ratio is predicted to be more favourable in the L band than at shorter wavelengths, so that lower mass, older objects can be addressed. Figure 5.1 shows the planet-to-star flux ratio calculated with the evolutionary models of Burrows et al. (2004) for a Jupiter-mass planet at several ages. The model clearly predicts non-black-body spectral energy distributions, with pronounced absorption in H_2O, CH_4, and NH_3 molecular bands. The flux ratio between the star and planet is 10 to 100 times larger at 4 μm than it is at shorter wavelengths (J, H and K).

2. **Useful photometric band**. The L band provides compelling photometric capabilities, making it the perfect complement to shorter wavelengths high contrast imager in order to constrain evolutionary models. It can help disentangle between true companions and background objects more quickly and allows assessing their physical characteristics such as temperature, mass and radius with more confidence.

3. **Favorable image quality**. An additional advantage of L band over shorter wavelengths is the better image quality and stability, reducing speckle noise. Since the AGPM removes only the coherent part of the PSF, a prime image quality is ideal for the coronagraph to perform more efficiently. The Strehl ratio increases as $\lambda^{6/5}$, which in practice translates into 70-90% Strehl ratios in the L band, for a first-generation AO system such as NACO (14×14 actuators). The next generation XAO facilities (40×40 actuators on ERIS, 2015-2016) will yield Strehl ratios >95%.

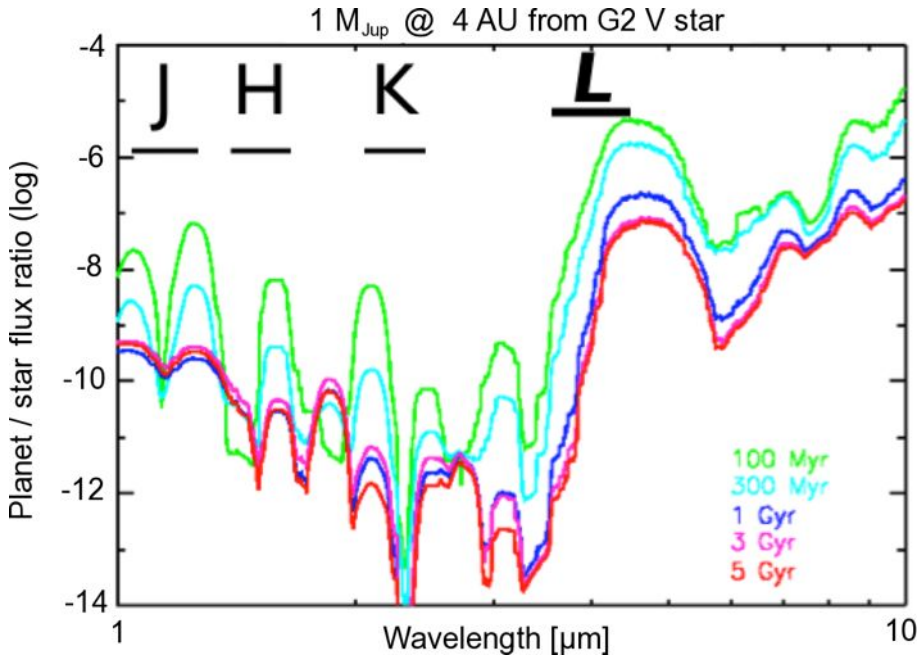

Figure 5.1: Expected planet/star flux ratio for non-irradiated Jupiter-mass planets at various ages, based on the models of Burrows et al. (2004), and assuming a Sun-like host star.

4. **Recent successful images**. In the past few years, observing at L band has been very successful in high-contrast imaging of circumstellar disks (Moerchen et al. 2007; Quanz et al. 2011) and exoplanets (Lagrange et al. 2010; Marois et al. 2010; Quanz et al. 2010; Kenworthy et al. 2013). The exoplanet images around HR8799 and β Pictoris, shown in Section 1.5.3, Figure 1.13, all pop out of the background/speckle field with an optimal signal-to-noise ratio. That is surely a good reason to continue exploring in this spectral range.

These advantages by far compensate for the inconvenience of the L band compared to shorter wavelengths, that are: (i) increased sky background, and (ii) loss in resolution. Around 3.8 μm, the background emission is still at acceptable levels (Kasper et al. 2007). The sensitivity limit is about $L = 17$ mag after 1 hour of integration time on a 10 meter class telescope operated at a world-class astronomical site, which still allows detecting Jupiter-mass planets around bright stars. Furthermore, efficient background subtraction can be achieved by use of post-processing techniques, leaving only photon noise as a significant contribution. Concerning the angular resolution (λ/D), it is of course not as good as at shorter wavelengths, but still compelling. Considering an 8-m class telescope, the resolution in the L band is about 100 mas. This corresponds to 1 AU at 10 pc. For comparison, K and H bands typically provide resolutions around 60 and 40 mas, respectively.

As a conclusion, the L band is definitely a sweet spot for high contrast coronagraphy, especially if small inner working angle (IWA) phase-mask coronagraphs are available. In this context, the AGPM will be competitive, for it is designed to reduce the stellar contribution up to $\Delta L' = 10$ mag at very small IWA (down to $0.9\lambda/D$). An L-band AGPM on an AO-assisted 10-m class telescope should be capable of imaging giant planets at a projected separation of only about 1 AU from stars located at 10 pc.

5.2 The need for an antireflective structure

Fresnel reflections from surfaces in optical systems are cumbersome for two principal reasons: (i) the total power loss can be considerable, particularly when there are many surfaces in the system, and (ii) stray light that is due to the reflections tends to reduce the contrast provided by imaging devices. Many solutions exist to reduce considerably these reflections.

5.2.1 Optical coatings

Optical coatings are the standard anti-reflective structures. They consist of a single-layer film (of refractive index $n_{\rm ar}$) deposited at the interface between the incidence medium (n_i) and the substrate (n_t). The reflected beams, from the top and the bottom of the film, can then interfere destructively, canceling each other (see Figure 5.2). In the case of normal incidence ($\theta_i = 0$), the film should be an odd number of quarter wavelengths thick: $h = m\lambda/(4n_{\rm ar})$, where m is an odd integer.

The drawback of these films is that the reflection can only be suppressed for specific wavelength and incidence angles. Antireflective coatings can be made to work over wider wavelength bands by stacking two or more films on top of each other. However, they are rather expensive and unfortunately often a source of critical issues in numerous applications, since they exhibit adhesion issues and thermal mismatch. Moreover, they are rarely transparent to the infrared, which reduces the choice of materials. These problems are of course exacerbated in astrophysical applications, especially in space where stability constraints are emphasized. In the specific case of diamond, some of the desirable surface characteristics, such as the physical robustness and chemical resistance, would be lost if one were to add a film of a different material.

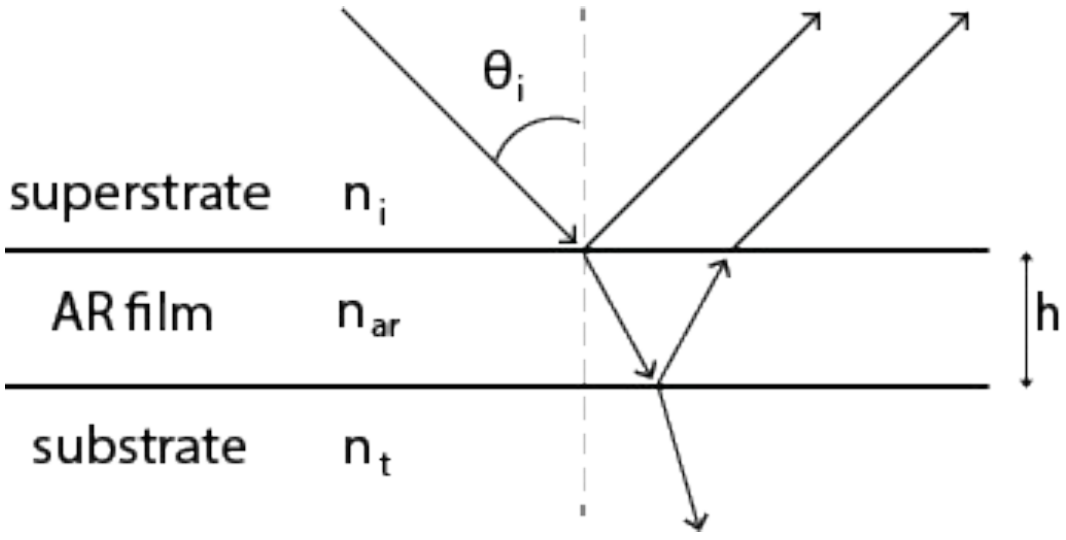

Figure 5.2: Antireflective structure obtained with an optical coating of thickness h. The two reflections occurring at each side of the coating interfere destructively.

5.2.2 Antireflective gratings

Subwavelength gratings can also be envisaged to reduce unwanted reflections. A one-dimensional antireflective gratings (ARG) with a simple rectangular profile can be used instead of the single-layer film to cancel the reflection. The film refractive index is then replaced by the grating effective index ($n_{\mathrm{ar}} = n_{\mathrm{eff}}$), which depends on the filling factor as already stated in Section 3.2. By appropriately tuning the filling factor, the effective index can be chosen to provide the exact impedance matching ($n_{\mathrm{eff}} = \sqrt{n_i n_t}$) between the substrate and the incidence medium. This leads to a substantially better performance than with a traditional single-layer treatment where the actual choice of materials is always limited.

One-dimensional ARG are anisotropic and can only be used for a single polarization at a time. In our case, light coming from the star is unpolarized, therefore a two-dimensional ARG (x and y axes) is generally used as optimal profile. 2D-symmetric profiles can be obtained by recording two 1D profiles, flipped by 90 degrees with respect to each other. These ARGs can be directly etched into the optical component substrate, thereby avoiding many physical and chemical side effects. Moreover, they can be designed by use of RCWA (Moharam et al. 1995). To us, ARGs represent a very pragmatic approach, since their manufacturing process is in direct relation with the one employed to etch the pattern of the AGPM. It uses the same lithography techniques, but it is easier as it requires much lower aspect ratios.

Two-dimensional ARG can be made of many different profiles. As our guideline is pragmatic and in direct relation with standard manufacturing processes, we will focus on binary gratings. These are gratings with only two levels in thickness, in other words, rectangular profiles. They are not totally achromatic but they can cover wavelength bands large enough for our type of application. Besides, they are optimized for specific incident angles, which is in good agreement with coronagraphs usually operating at normal incidence. Similarly to multi-layer optical coatings, one can design ARGs performant over wider spectral bandwidths by stacking two or more binary steps. Each level is then equivalent to a film, and the filling factor must be reduced from level to level. With an infinite number of levels, and if the filling factor varies from 0 at the top of the grating to 1 at the bottom, the grating will have a pyramidal profile, with continuously sloping sides. Such a profile provides dramatic improvements compared to a binary rectangular grating, even more with deep pyramids (see Figure 5.3). Such inclined surfaces can be etched directly into diamond to produce broadband antireflective structures with an average transmission of 96.4% for wavelengths between 10 and 50 μm (Forsberg & Karlsson 2013b).

In the L band, one can reach even higher transmission in theory, as shown in Figure 5.3. However, these pyramidal gratings require very high precision in the fabrication. Small deviation or asperities in any of the grating parameters can highly reduce the effectiveness. Therefore, we did not risk to etch such structures on the backside of our L-band AGPMs. Rather, we opted for binary rectangular gratings, a much better mastered technique.

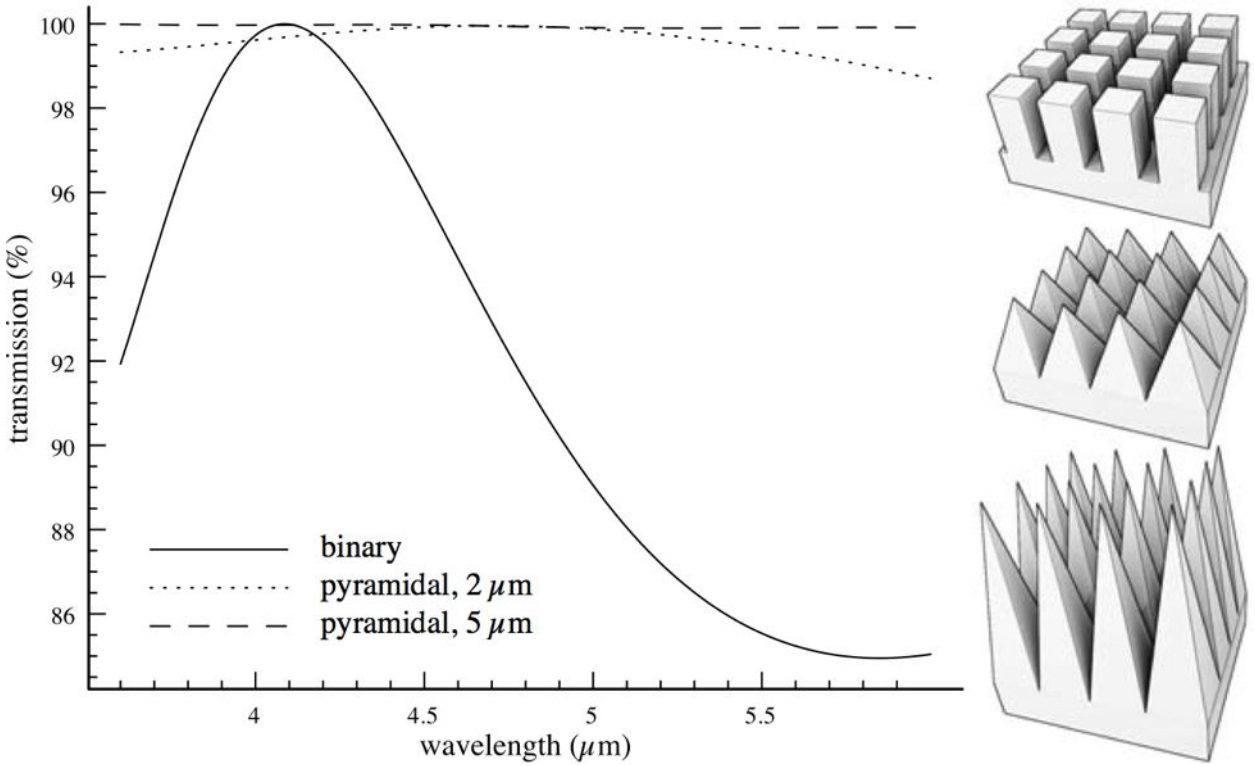

Figure 5.3: RCWA-calculated transmission across a $\Lambda = 1.5\,\mu$m diamond antireflective grating, with different profiles: one binary grating with $F = 0.65$ and $h = 2\,\mu$m, and two pyramidal gratings with $h = 2$ or 5 μm. The transmission of the deep pyramidal grating varies between 99.90% and 99.98%. From Forsberg (2013).

5.2.3 AGPM transmission performance

During our first laboratory tests with the L-band AGPMs, we noticed that their performance was much lower than predicted by the theoretical simulations. We suspected that the light reflected inside the component was producing a so-called ghost signal that was not cancelled by the optical vortex. This observation motivated our choice to etch binary rectangular antireflective gratings, such as those presented hereabove, on the backside of the AGPMs. When we returned to the laboratory at the LESIA in Paris, we confirmed the expected performance as will be shown hereafter, in Section 5.3. In the present section, we will show the importance of the antireflective grating efficiency, and its considerable impact on the coronagraphic performance of the AGPM. We will present the results of our simulations, to demonstrate that improving the transmission (with better antireflective solutions), on both sides of the AGPM, is an easy route to improve the null depth.

Antireflective gratings were etched at the Ångström laboratory on several manufactured AGPMs. The optimal parameters were calculated by RCWA simulations. The first ARGs were etched on N-band components. The period and thickness were fixed to $\Lambda = 4\,\mu$m and $h = 2\,\mu$m, respectively, and the filling factor was $F = 0.65$. Downscaling these parameters to L-band AGPMs was quite straightforward. The refractive index of diamond does not change much from N to L ($n \approx 2.38$), so the filling factor is pretty much the same. The other parameters must be reduced proportionally to the wavelength, which corresponds to a period $\sim$1.3 μm and a thickness $\sim$0.63 μm for L-band AGPMs.

We have calculated the total reflectance R_{tot} and transmittance T_{tot} of several manufactured AGPMs, using Equations 3.38 and 3.39 determined in Section 3.2.4. These equations take into account both sides of the component, as well as the absorption occurring in the substrate during multiple internal reflections. The absorption was calculated from absorption coefficient data presented in Appendix A, for a 300 μm thick substrate. The results are plotted in Figure 5.4 in the case of AGPM-L4, together with the transmission and reflection curves on each side of the wave plate (*in* and *out*). The situation *without ARG* is compared to the situation *with ARG*.

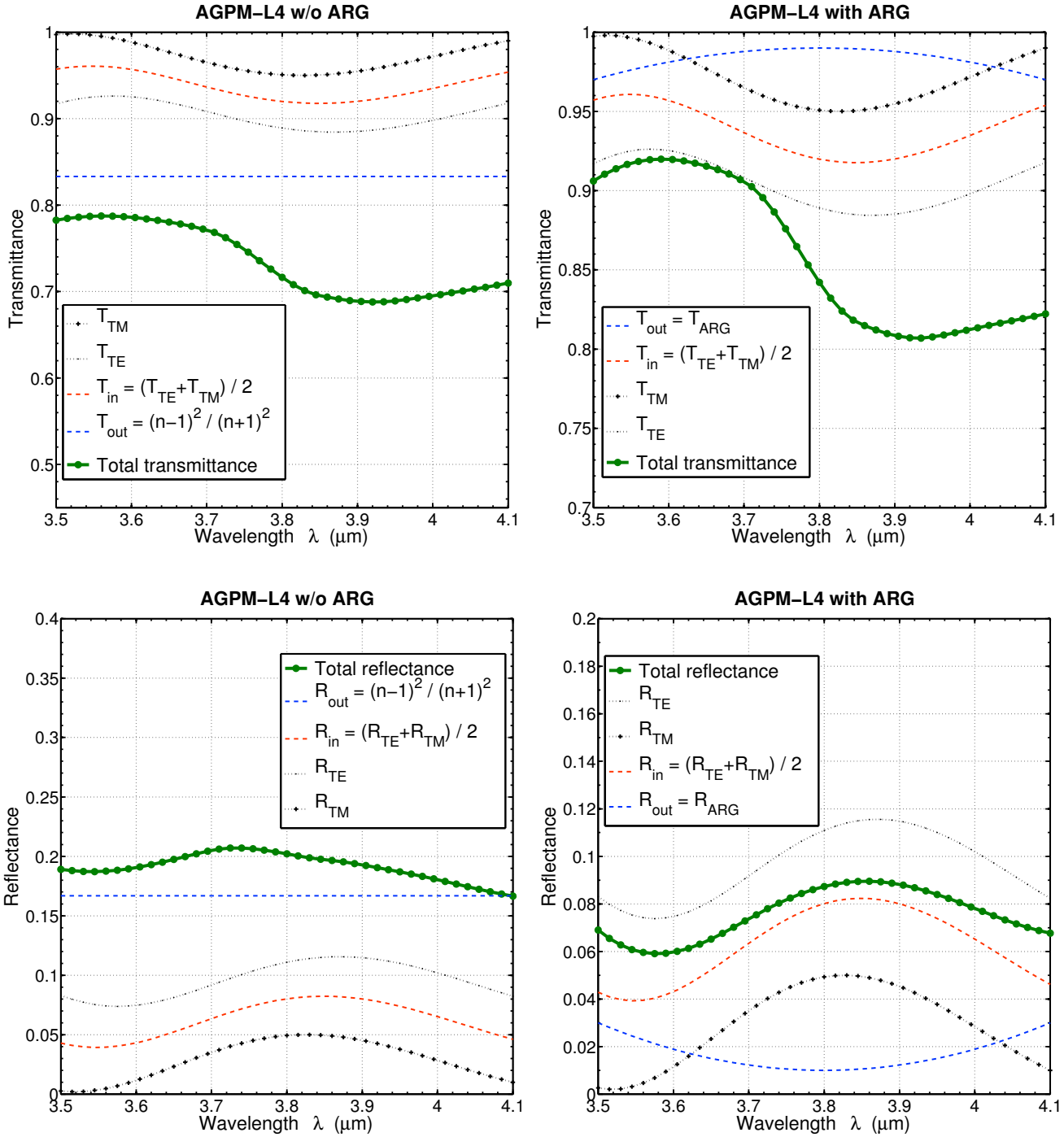

Figure 5.4: RCWA-calculated transmittance (top) and reflectance (bottom) of AGPM-L4. Situations without ARG (left) and with ARG (right) are compared. Multiple internal reflections inside the 300 μm thick component are considered. Absorption is stronger around 3.9-4 μm.

In theory, the ARG on AGPM-L4 reduces the backside reflection from 17% down to an average of just ∼2% across the band. As illustrated in Figure 5.4, the overall reflection is reduced from 19.1% down to 7.6%. This performance is even better at N band than at L band, thanks to less severe specifications, hence higher precision. Indeed, ARGs etched on N-band components reduce the backside reflection down to ∼0.5%. In the next figures, we present the total transmittance curves for AGPM-L3 (Figure 5.5), AGPM-N3 (Figure 5.6), and AGPM-N4 (Figure 5.7).

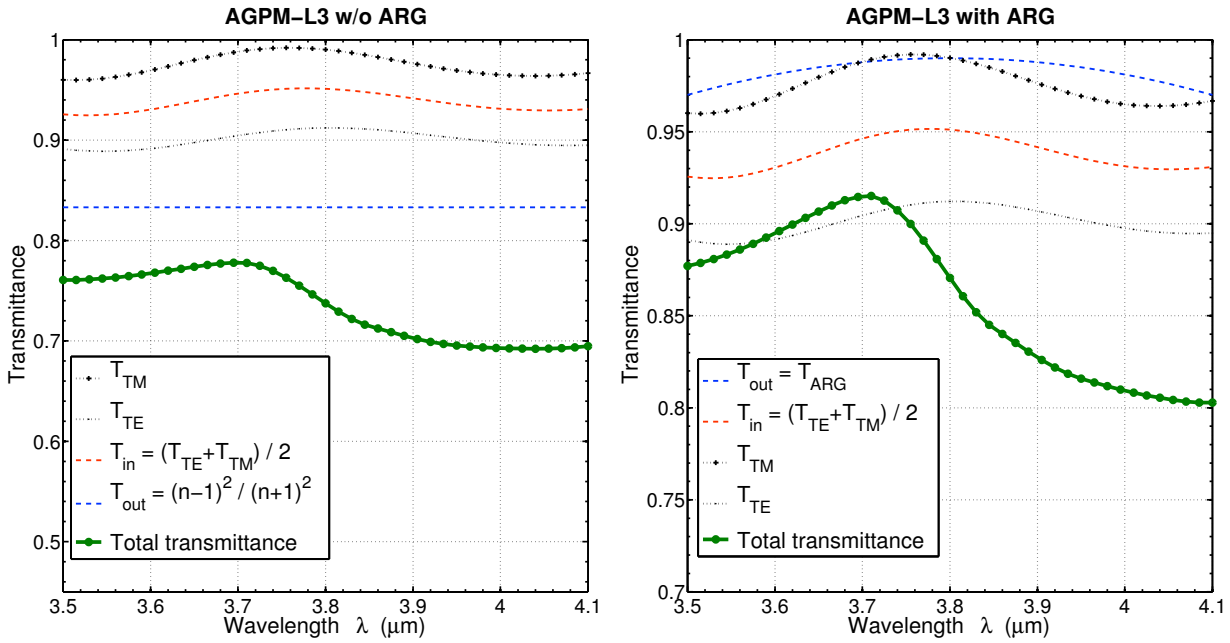

Figure 5.5: RCWA-calculated transmittance of AGPM-L3. Situations without ARG (left) and with ARG (right) are compared.

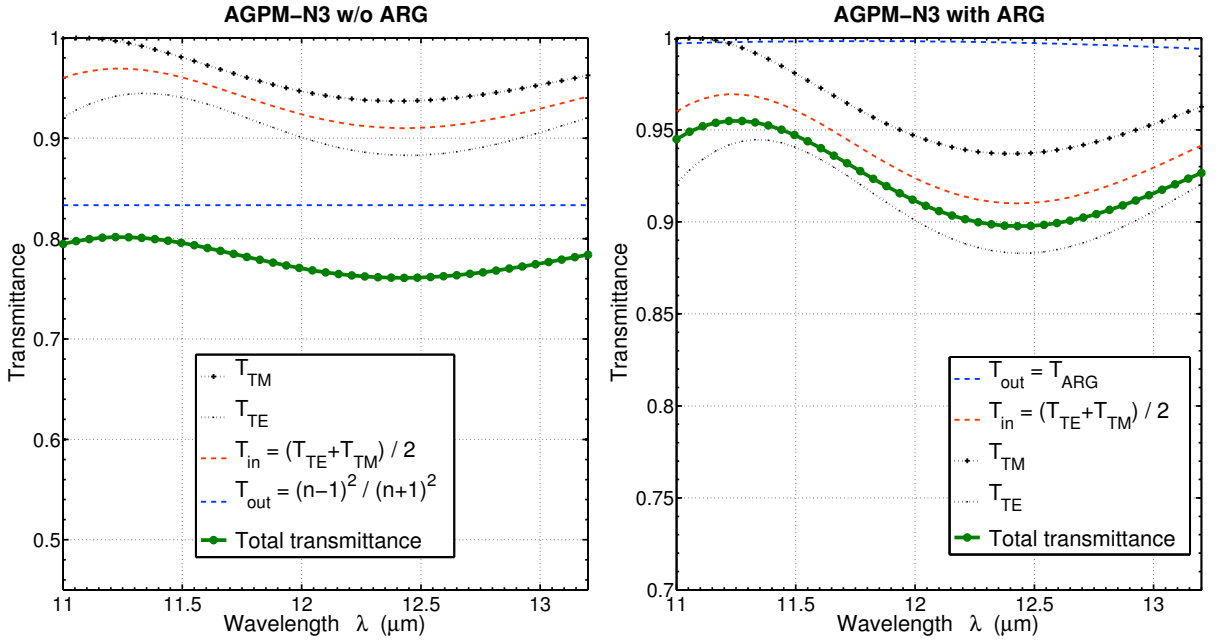

Figure 5.6: Same graphics as in Figure 5.5, but for AGPM-N3. In this spectral band (11-13.2 μm), reflection is better attenuated than in the L band, and the absorption is much lower.

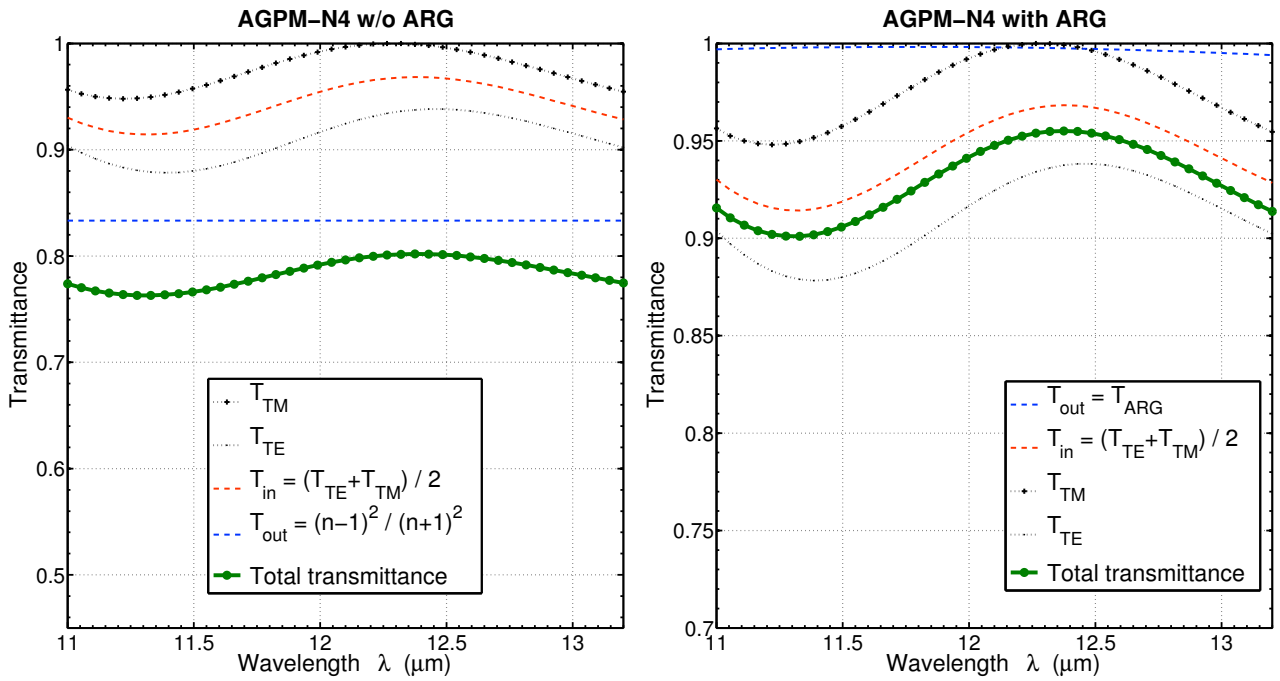

Figure 5.7: Same graphics as in Figure 5.6, but for AGPM-N4.

5.2.4 Influence of the ghost signal

The theoretical null depths of the manufactured AGPMs, presented in Section 4.2.3, were calculated regardless of the internal reflections contribution. To estimate the true expected performance of the components, the ghost signal from double (and even multiple) reflections in the component should also be added. The light going straight through the AGPM is nulled by the coronagraph, whereas the ghost signal is not correctly nulled, since it reflects on the AGPM grating, once or several times. The transmission of the coronagraphic signal is given by

$$T_{\text{coro}} = T_{\text{in}}\, T_{\text{out}}\, e^{-\alpha h} \tag{5.1}$$

where T_{in} is the transmittance of the AGPM grating surface, T_{out} the transmittance of the backside surface, α the absorption coefficient, and h the substrate thickness. T_{in}, on the one hand, is generally quite high because the AGPM grating, while not designed to be antireflective, also reduces the reflectivity to around 3-7%. T_{out}, on the other hand, can be close to 99% if the backside is etched with an ARG.

The ghost transmittance is then calculated by subtracting the coronagraphic transmission from the total transmission:

$$T_{\text{ghost}} = T_{\text{tot}} - T_{\text{coro}}\ . \tag{5.2}$$

By combining Equation 5.1, Equation 5.2, and Equation 3.39 (total transmittance with multiple internal reflections), we obtain

$$T_{\text{ghost}} = T_{\text{in}}\, T_{\text{out}}\, e^{-\alpha h} \left(1 + R_{\text{out}} R_{\text{in}}\, e^{-2\alpha h} + R_{\text{out}}^2 R_{\text{in}}^2\, e^{-4\alpha h} + ...\right) - T_{\text{in}}\, T_{\text{out}}\, e^{-\alpha h} \tag{5.3}$$

which can be approximated by

$$T_{\text{ghost}} = \frac{T_{\text{in}}\, T_{\text{out}}\, R_{\text{out}}\, R_{\text{in}}\, e^{-3\alpha h}}{1 - R_{\text{out}} R_{\text{in}}\, e^{-2\alpha h}} \ . \tag{5.4}$$

This ghost signal contributes to the transmitted non-coronagraphic light, and should be added to the total null depth :

$$N_{\text{AGPM}} = N_{\text{theo}} + N_{\text{ghost}} \tag{5.5}$$

with

$$N_{\text{ghost}} = \frac{T_{\text{ghost}}}{T_{\text{tot}}} = 1 - \frac{T_{\text{coro}}}{T_{\text{tot}}} \cong R_{\text{out}}\, R_{\text{in}}\, e^{-2\alpha h} \ . \tag{5.6}$$

Equation 5.6 shows that, in first approximation, the ghost signal can be evaluated by taking only double reflection into account. The contribution of the ghost to the null depth is obtained by multiplying the reflectivities of the back and front of the component, with the absorption occurring twice along the way. This contribution should be around $\approx 9 \times 10^{-4}$ for our L-band AGPMs, or even as low as $\approx 2 \times 10^{-4}$ for the N-band ones. This is a small number, but in the same range as the calculated null depths in the best L-band cases. Adding them together, we find that the expected null depth for our best L-band component (AGPM-L4) is around $\approx 2 \times 10^{-3}$, which is still very good.

We have simulated the performance of our best components (AGPM-N3, AGPM-N4, AGPM-L3, and AGPM-L4) by use of RCWA, as illustrated in Figure 5.8. We also summarize the mean null depth performance for all these components in Table 5.1.

Table 5.1: Transmission and reflection performance of the best manufactured components (AGPM-N3, AGPM-N4, AGPM-L3, and AGPM-L4), with and without an ARG. The null depth is calculated by taking the ghost contribution into account, and compared to the theoretical null depth.

						Null depth	
	T_{tot} (%)		R_{tot} (%)		w/o ghost	with ghost	
AGPM	w/o ARG	with ARG	w/o ARG	with ARG	N_{theo}	w/o ARG	with ARG
N3	77.9	92.2	20.9	6.7	3.2×10^{-3}	1.3×10^{-2}	3.4×10^{-3}
N4	78.3	92.9	20.4	6.0	1.3×10^{-3}	1.1×10^{-2}	1.4×10^{-3}
L3	73.4	85.9	19.1	7.5	3.7×10^{-3}	1.4×10^{-2}	4.7×10^{-3}
L4	73.4	85.9	19.1	7.6	1.6×10^{-3}	1.0×10^{-2}	2.5×10^{-3}

The results presented in Table 5.1 and Figure 5.8 are obtained by RCWA simulations, and only the transmissions and reflections have been measured so far. Of course, this is not sufficient to validate the AGPM concept. The null depth performance needs to be verified in the laboratory, by real attenuation measurements on a well-calibrated coronagraphic test bench. This will be the subject of the next section.

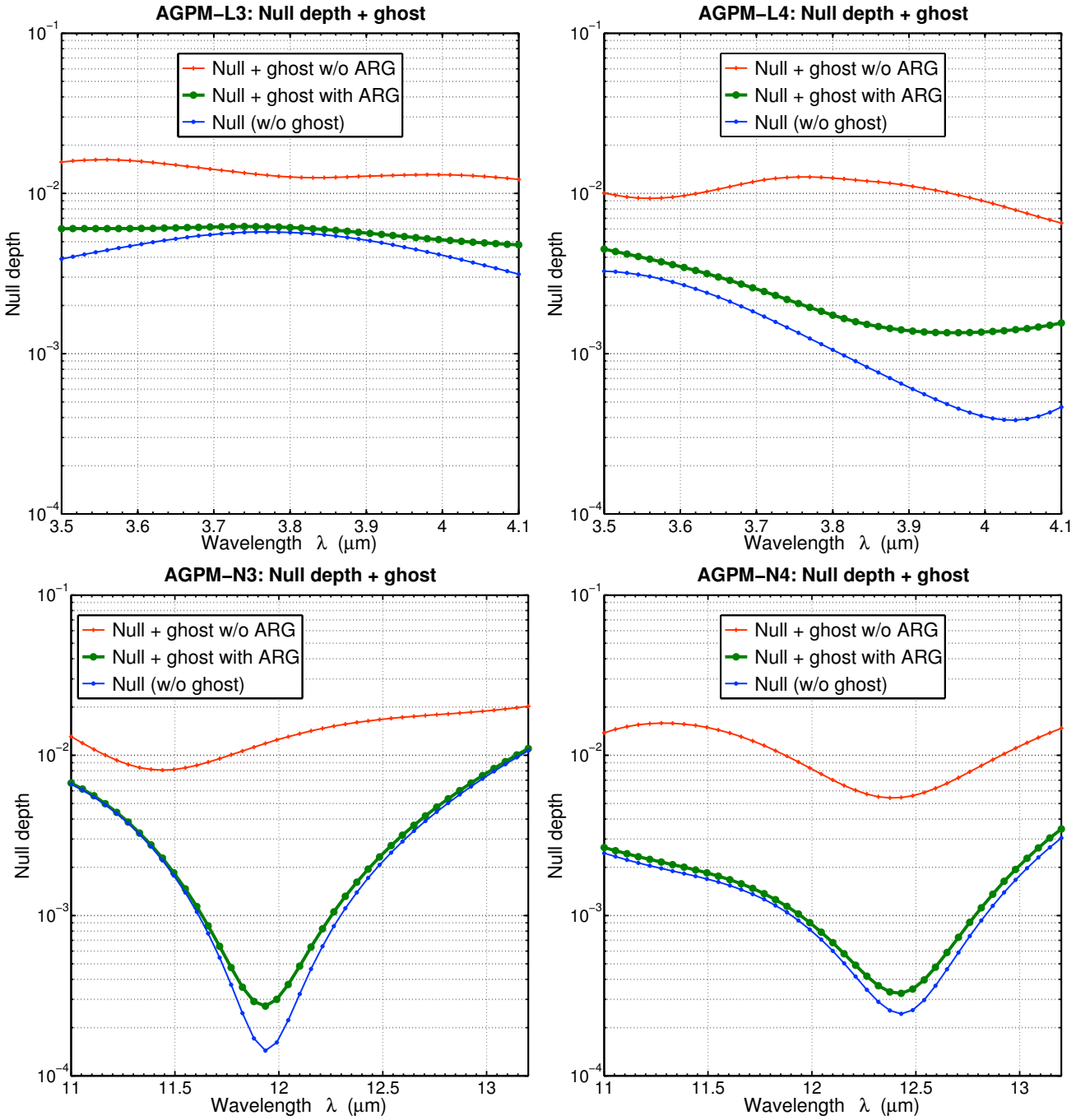

Figure 5.8: RCWA-calculated nulling performance of the best manufactured components (AGPM-N3, AGPM-N4, AGPM-L3, and AGPM-L4). The theoretical null depth is compared to the total null depth taking the ghost signal into account, with and without an ARG. Improving the transmission (with better antireflective solutions), on both sides of the AGPM, is an easy route to improve its performance.

5.3 Measured performance and comparison with theory

5.3.1 YACADIRE: the coronagraphic bench of the LESIA

Making demonstrations in the mid-infrared is a very difficult task that requires very specific optical equipments (sources, fibers, mirrors, detectors). As already stated before, testing the N-band AGPMs was impractical, as they work at a too long wavelength for the usual test benches. So far, only preliminary tests with VLT/VISIR have been made with these, as will be discussed in Chapter 6. Therefore, we focused our efforts on testing the L-band components, which is even more interesting regarding the many advantages of the L band described in Section 5.1. All the L-band AGPMs have been tested at the Laboratoire d'études spatiales et d'instrumentation en astrophysique (LESIA), from the Observatoire de Paris.

The coronagraphic bench of the LESIA is called YACADIRE, for YAmina CAlibration Detector Infra Red Euros (see Figure 5.9). YACADIRE was initially designed to: (i) simulate and control the thermal and optical environmental conditions of an infrared detector in vacuum, and (ii) calibrate the detector in these conditions. YACADIRE is located in a class 10,000 clean room. This facility was first designed for the ROSETTA and VENUS-EXPRESS missions (Ghomchi et al. 1999), with the idea of being adaptable to other experiences, thus with a certain degree of flexibility. Since then, the optical bench was used for qualification tests for the MIRI (Baudoz et al. 2004) and SPHERE (Boccaletti et al. 2008) coronagraphs. YACADIRE is equipped with an $HgCdTe$ infrared detector placed in a cryostat cooled down to 60 K, which is ideal to maintain low background emission for taking measurements at L band. It also posses a rotating filter wheel, cooled inside the cryostat chamber, where we have inserted our L-band filter as described hereafter.

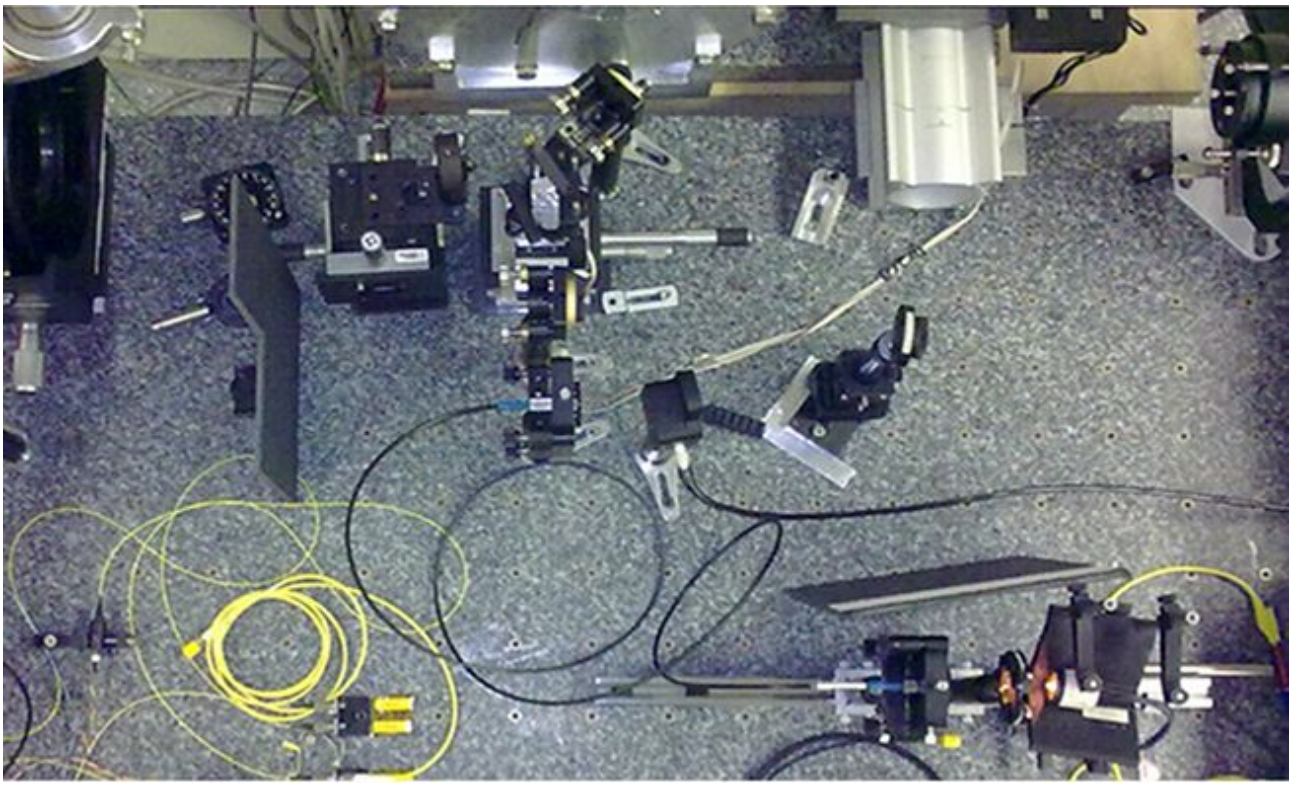

Figure 5.9: Overhead view of the YACADIRE optical test bench at the LESIA, Observatoire de Meudon in Paris. The complete optical setup (detailed scheme) is described in Section 5.3.3.

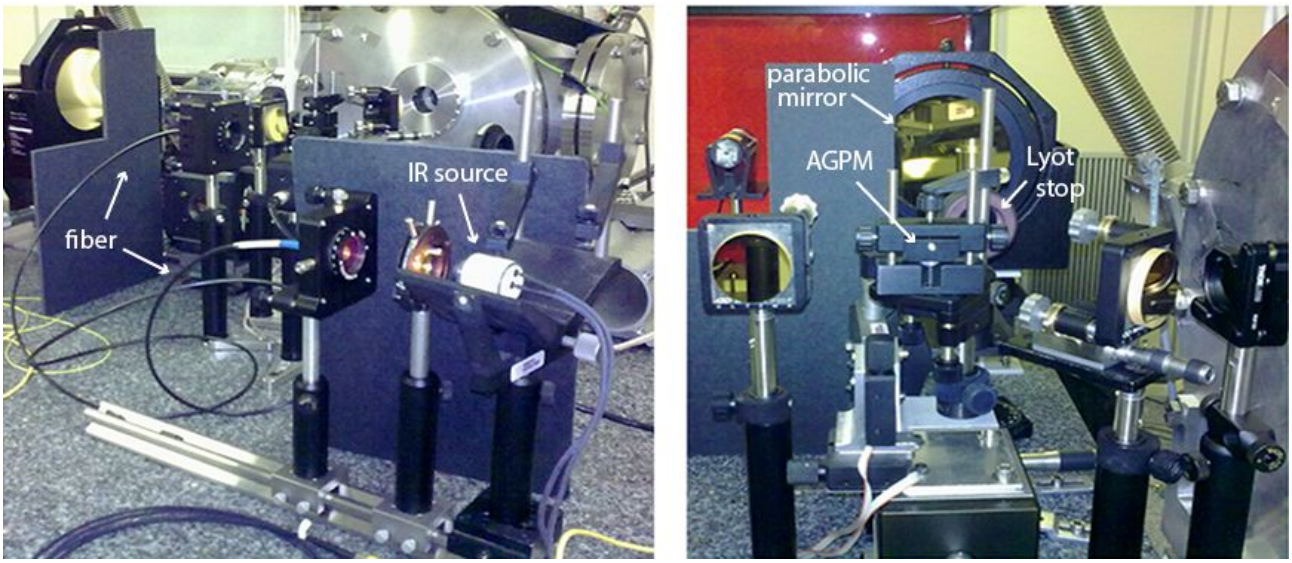

Figure 5.10: Yacadire test bench adapted to L-band coronagraphy. Left: A tungsten lamp is used to feed a single-mode fibre (our star simulator) transmitting wavelengths up to 5 μm. Right: The AGPM to be tested is placed in an intermediate focal plane between two parabolic mirrors. A Lyot stop blocking the diffracted light is then located after the second parabolic mirror, reducing the pupil to 80% of its diameter.

5.3.2 Adapting the bench to the L band

We have acquired three filters from the company SPECTROGON, with different bandwidths. One wide L-band filter (3.5-4.0 μm) and two narrow filters around 3.8 μm and 4.04 μm respectively. The wide filter was placed in the filter wheel, inside the cryostat. It was thus accurately cooled and did not contribute to background emissions. The other two filters were successively placed on the (warm) bench. There was unfortunately only one slot inside the cryostat for placing a filter. We performed many measurements with all the possible filter configurations. The best results were achieved with the wide filter alone. Both narrow filters did not provide good results for two probable reasons: (i) they contributed to the background since they were not cooled, and (ii) they were too narrow, especially the 4040 filter, which was barely overlapping with the wide filter (see Figure 5.11). The main reason seems to be the second one.

The complete setup of the coronagraphic test bench is presented in our paper hereafter, with the results of our measurements.

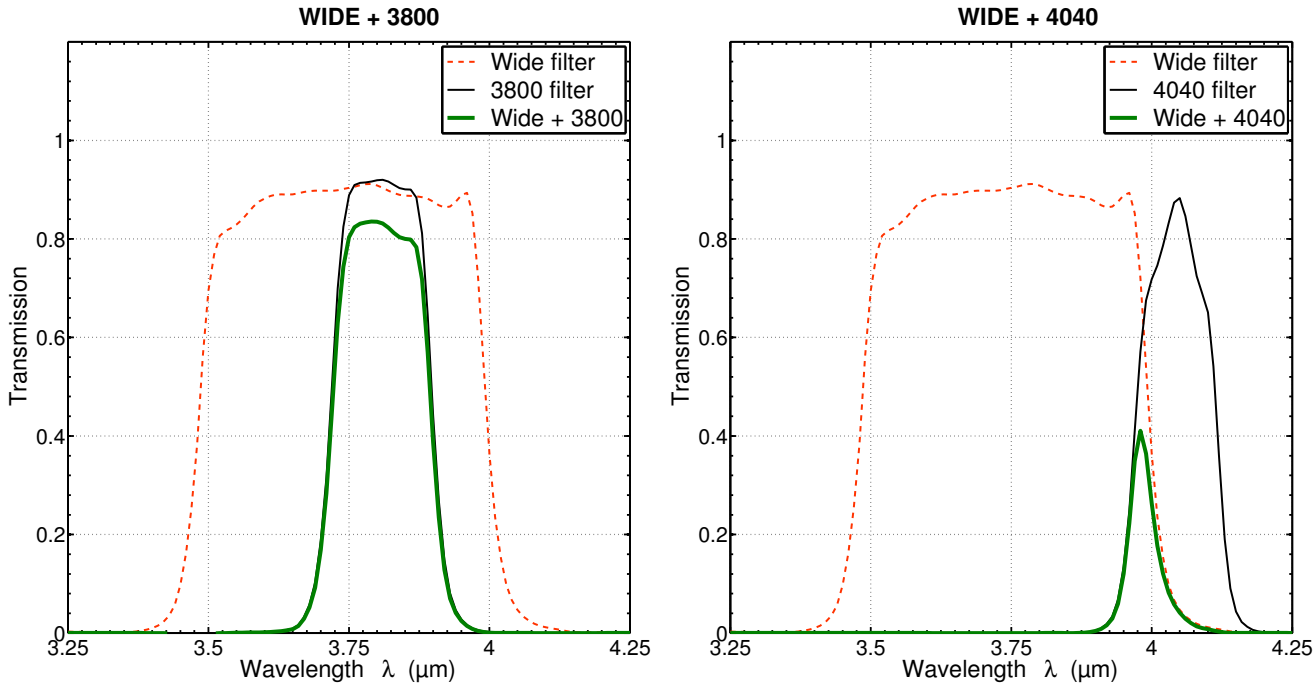

Figure 5.11: L-band filters acquired from SPECTROGON. One wide filter (3.5-4.0 μm) used together with two narrow filters, centered at 3.8 μm (left) and 4.04 μm (right).

5.3.3 Publication: Laboratory demonstration of a mid-infrared AGPM vector vortex coronagraph

In the following paper (Delacroix et al. 2013), published in May 2013 in the peer-reviewed journal Astronomy and Astrophysics, we present the complete laboratory assessment of our manufactured L-band AGPMs. We describe the design parameters, the antireflective grating, and the RCWA-simulated total null depth, including the ghost contribution. The optical layout of the test bench, as well as the measurement principles are explained. We focus on the best component: AGPM-L4. The measured null depth is very close to the expected 2×10^{-3} across the band. This is the best broadband performance demonstrated for a mid-infrared phase mask to date and is very promising for future exoplanet observations. Installation of this component in the LMIRCam instrument at the Large Binocular Telescope in Arizona is underway.

A&A 553, A98 (2013)
DOI: 10.1051/0004-6361/201321126

Astronomy & Astrophysics

Laboratory demonstration of a mid-infrared AGPM vector vortex coronagraph

C. Delacroix[1], O. Absil[1], P. Forsberg[2], D. Mawet[3], V. Christiaens[1], M. Karlsson[2], A. Boccaletti[4], P. Baudoz[4], M. Kuittinen[5], I. Vartiainen[6], J. Surdej[1], and S. Habraken[1]

[1] Département d'Astrophysique, Géophysique et Océanographie, Université de Liège, Allée du Six Août 17, 4000 Liège, Belgique
e-mail: cdelacroix@ulg.ac.be
[2] Department of Engineering Sciences, Ångström Laboratory, Uppsala University, Lägerhyddsvägen 1, 75121 Uppsala, Sweden
[3] European Southern Observatory, Alonso de Cordova 3107, Casilla 19001, Vitacura, Santiago 19, Chile
[4] LESIA-Observatoire de Paris, CNRS, UPMC Univ. Paris 06, Univ. Paris-Diderot, 5 Pl. J. Janssen, 92195 Meudon, France
[5] Department of Physics and Mathematics, University of Eastern Finland, PO Box 111, 80101 Joensuu, Finland
[6] Paul Scherrer Institut, 5232 Villigen PSI, Switzerland

Received 18 January 2013 / Accepted 29 March 2013

ABSTRACT

Context. Coronagraphy is a powerful technique to achieve high contrast imaging, hence to image faint companions around bright targets. Various concepts have been used in the visible and near-infrared regimes, while coronagraphic applications in the mid-infrared nowadays remain largely unexplored. Vector vortex phase masks based on concentric subwavelength gratings show great promise for such applications.
Aims. We aim at producing and validating the first high-performance broadband focal plane phase mask coronagraphs for applications in the mid-infrared regime, and in particular the L band with a fractional bandwidth of ~16% (3.5–4.1 μm).
Methods. Based on rigorous coupled wave analysis, we designed an annular groove phase mask (AGPM) producing a vortex effect in the L band, and etched it onto a series of diamond substrates. The grating parameters were measured by means of scanning electron microscopy. The resulting components were then tested on a mid-infrared coronagraphic test bench.
Results. A broadband raw null depth of 2×10^{-3} was obtained for our best L-band AGPM after only a few iterations between design and manufacturing. This corresponds to a raw contrast of about 6×10^{-5} (10.5 mag) at $2\lambda/D$. This result is fully in line with our projections based on rigorous coupled wave analysis modelling, using the measured grating parameters. The sensitivity to tilt and focus has also been evaluated.
Conclusions. After years of technological developments, mid-infrared vector vortex coronagraphs have finally become a reality and live up to our expectations. Based on their measured performance, our L-band AGPMs are now ready to open a new parameter space in exoplanet imaging at major ground-based observatories.

Key words. instrumentation: high angular resolution – planetary systems – planets and satellites: detection

1. Introduction

Direct imaging of exoplanets and close environments of stars has recently made a long-awaited breakthrough (Marois et al. 2008; Kalas et al. 2008; Lagrange et al. 2009a, 2010; Absil & Mawet 2010). While coronagraphs have sometimes been part of these discoveries, their role has been restricted to merely mitigate detector saturation. The reason for the still limited impact of stellar coronagraphs on direct imaging is twofold. First, the wavefront quality and stability provided by current instruments on most ground-based telescopes at short wavelengths (up to the near-infrared) is not high enough (Strehl ratio of the order of 50%). Second, the coronagraphic devices offered until a few years ago date back to the original century-old invention by French astronomer Bernard Lyot (Lyot 1939). Paradoxically, the diversity of new coronagraphs developed in the lab during past 15 years is far greater than the number of real science discoveries that they have enabled so far (Guyon et al. 2006). It is also fair to say that, with very few exceptions (Riaud et al. 2006; Mawet et al. 2009, 2011; Serabyn et al. 2009, 2010; Lagrange et al. 2009b; Quanz et al. 2010; Boccaletti et al. 2012), investments have mainly been made to develop the technologies in the laboratory rather than actually bringing them to the telescope for actual on-sky tests and operations (Mawet et al. 2012), from which so much can be learned while enabling limited, but actual science despite the average image quality in the near-infrared.

As a few dedicated experiments have already suggested (Mawet et al. 2010; Serabyn et al. 2010), this situation is about to change. Indeed, second-generation instruments have started rolling in at major observatories, e.g., the Gemini Planet Imager (GPI, Macintosh et al. 2008), VLT/SPHERE (Beuzit et al. 2008; Kasper et al. 2012), and a few others. They promise far greater image quality and stability, enabling new-generation coronagraphs to deliver their best performances. Not to be forgotten are first-generation instruments, which still possess untapped potential, which only ten years or so of operation and understanding have allowed us to fully unleash (Girard et al. 2012; Mawet et al. 2012).

Here we present the successful outcome of eight years of technological developments to make the so-called annular groove phase mask coronagraph (AGPM, Mawet et al. 2005a) into a reality ready to be installed at the telescope. The AGPM is an optical vortex made out of a subwavelength grating. The vortex coronagraph is one of the most advanced new-generation

coronagraphs, and its interest lies in its ability to reach high contrast at very small inner working angles (IWA), while maintaining high throughput over a full 360° field of view. This has already been proved in the literature with several successful demonstrations and results, both in the laboratory and on sky (Mawet et al. 2010; Serabyn et al. 2010) but at shorter wavelengths (visible and near-infrared). This paper tackles the difficult problem of designing and manufacturing vector vortex coronagraphs for the mid-infrared, where the demand for efficient coronagraphs is increasing following the recent success of high-contrast imaging of exoplanets and circumstellar disks in the L band around 4 μm (Moerchen et al. 2007; Lagrange et al. 2010; Quanz et al. 2010, 2011; Kenworthy et al. 2013). The L band is indeed an ideal filter for exoplanet searches on ground-based telescopes for the following reasons.

- The L-band contrast of planetary-mass companions with respect to their host stars is predicted to be more favourable than at shorter wavelengths (Baraffe et al. 2003; Fortney et al. 2008; Spiegel & Burrows 2012) so that lower mass, older objects can be addressed.
- An additional advantage of L band over shorter wavelengths is the better adaptive optics image quality, with Strehl ratios typically between 70% and 90%.

These advantages by far compensate for the increased sky background in the thermal infrared. In this context, the AGPM will be competitive, for it is designed to reduce the stellar contribution by $\Delta L' \geq 7.5$ mag at very small IWA (down to $0.9\lambda/D$). An L-band AGPM on an AO-assisted 10-m class telescope should be capable of imaging giant planets at a projected separation of only about 1 AU from stars located at 10 pc.

After reviewing the principle of vortex coronagraphs and of the AGPM in Sect. 2, we describe in Sect. 3 the design, manufacturing, and expected performance of L-band AGPM coronagraphs. In Sect. 4, we detail the optical setup of the coronagraphic testbench and present the measured performance of our best L-band AGPM. Finally, we conclude by discussing the perspectives of on-sky applications and of future improvements.

2. The AGPM: a vector vortex coronagraph

Optical vortices occur when the phase structure of light is affected by a helical ramp around the optical axis, $e^{\imath l\theta}$, where θ is the focal plane azimuthal coordinate and l the vortex topological charge, i.e., the number of times the geometric phase $\phi_{\rm p}$ (Pancharatnam 1956, see also below) accumulates 2π along a closed path s surrounding the phase singularity:

$$l = \frac{1}{2\pi} \oint \nabla \phi_{\rm p} \, {\rm d}s. \tag{1}$$

The phase dislocation forces the amplitude to zero at its centre, which is a singularity. Nature indeed prevents the phase from having an infinite number of values at a single point in space, which is non-physical, by simply nulling the light locally. When centred on the diffraction pattern of a star seen through a telescope, optical vortices affect the subsequent propagation by redirecting the on-axis starlight outside the geometric image of the pupil. This diffracted starlight is then blocked when passing through a diaphragm in the so-called Lyot stop (LS) plane, slightly undersized compared to the input pupil.

The perfect starlight attenuation of an optical vortex coronagraph has been proven analytically (Mawet et al. 2005a; Foo et al. 2005; Jenkins 2008) for any non-zero even values of l by applying the result of the Weber-Schafheitlin integral[1] (Abramowitz & Stegun 1972; Sneddon 1951) to the Fourier transform of the product of a vortex ramp phase ($e^{\imath l\theta}$) with an ideal Airy pattern ($\frac{2J_1(k\rho R)}{k\rho R}$), where R is the circular input pupil radius, k the wave number, and ρ the radial coordinate in the focal plane. For instance, with a topological charge $l = 2$, the amplitude of the electric field in the Lyot stop plane, with (r, γ) coordinates, becomes

$$E_{\rm LS}(r,\gamma) = \begin{cases} 0, & r < R \\ e^{\imath 2\gamma} \left(\frac{R}{r}\right)^2, & r \geq R \end{cases}. \tag{2}$$

The signal is perfectly nulled inside the pupil area, while the redirected light outside the pupil area is blocked by the Lyot stop. Naturally, this occurs only for the on-axis starlight, whereas light from off-axis objects misses the centre of the vortex and propagates normally. The vortex coronagraph is known for its near-perfect coronagraphic properties: small IWA (down to $0.9\lambda/D$), high throughput, clear off-axis 360° discovery space, and simplicity.

An optical vortex can be either scalar or vectorial. Scalar optical vortices are based on a structural phase ramp such as a piece of glass shaped as a helix. The accuracy to be achieved in the glass thickness is a definite technological challenge that remains poorly mastered, even using the most recent micro-fabrication techniques. More importantly, the induced phase profile of scalar vortices is highly dependent on the wavelength of the incoming light. Therefore, these are not suitable for significantly wide spectral bands, such as those commonly used as astronomical filters. A vectorial (or vector) vortex coronagraph (VVC), on the other hand, can overcome these limitations. Instead of a structural phase ramp, the VVC is based on a circularly symmetric halfwave plate, i.e., a mask that affects the transverse polarisation state cyclicly around the centre. This creates a geometric phase $\phi_{\rm p}$ known as the Pancharatnam-Berry phase, which is half of the solid angle subtended by the polarisation cycle on the Poincaré sphere (Pancharatnam 1956; Berry 1987). It was rigorously shown (Mawet et al. 2005a; Niv et al. 2006) that vectorial vortices present the same phase ramp as scalar vortices.

Different types of VVCs exist. A technology using liquid crystal polymers (LCP-VVC) recently showed excellent results (Serabyn et al. 2010; Mawet et al. 2010). Nevertheless, this technology has been limited so far to the visible and near-infrared wavelength regimes (up to 2.4 μm), and is not suitable for the highly coveted mid-infrared region. Another technological route is the annular groove phase mask (AGPM, see Fig. 1) using subwavelength gratings (SG-VVC), which are particularly adapted to longer wavelengths (Mawet et al. 2005b; Delacroix et al. 2010). Subwavelength gratings (SGs) are gratings with a period Λ shorter than the illuminating wavelength λ divided by the refractive index n of the substrate (assuming that the incident light is perpendicular to the grating surface and that the surrounding medium is air). Thanks to their property of form birefringence, which gives two different refractive indices $n_{\rm TE}$ (transverse electric) and $n_{\rm TM}$ (transverse magnetic), such SGs can produce a phase shift between the two polarisation components:

$$\Delta\Phi_{\rm TE-TM}(\lambda) = \frac{2\pi}{\lambda} h \, \Delta n_{\rm form}(\lambda). \tag{3}$$

By carefully selecting the grating parameters (substrate and geometry), this phase shift can be made quasi-independent of the

[1] This integral reduces to Sonine's for the $l = 2$ case.

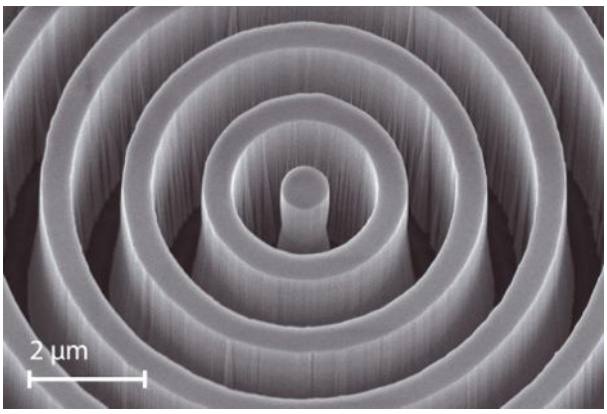

Fig. 1. Scanning electron microscope (SEM) picture of the centre of an annular groove phase mask (AGPM) made out of diamond and dedicated to coronagraphic applications in the *L* band.

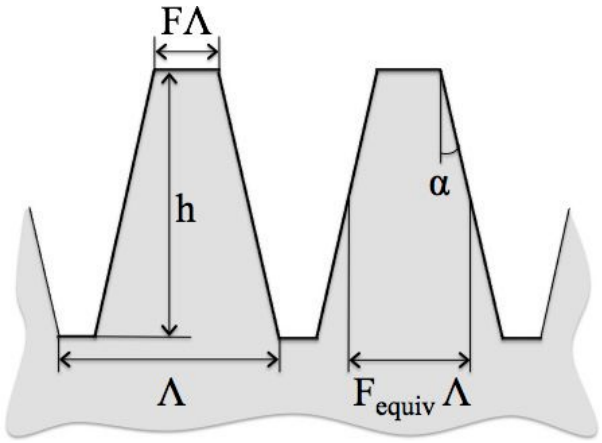

Fig. 2. Schematic diagram of a trapezoidal grating. The grating sidewalls have an angle α and an average width $F_{\rm equiv}\Lambda$.

wavelength over a wide spectral bandwidth, thereby synthesising an artificial birefringent achromatic wave plate (Kikuta et al. 1997). We have recently shown (Delacroix et al. 2012b) that diamond is a good material for manufacturing achromatic half-wave plates for mid-infrared wavelengths (e.g., *L* and *N* bands centred respectively around 3.8 μm and 10 μm). Here, we focus on applications in the *L* band, ranging from 3.5 to 4.1 μm.

3. AGPM-L design and manufacturing

3.1. Design

The design of the grating was conducted in complete synergy with the manufacturing process, described in Sect. 3.2. We performed realistic numerical simulations using the rigorous coupled wave analysis (RCWA), which resolves the Maxwell equations in the frequency domain and gives the entire diffractive characteristics of the studied structure (Moharam & Gaylord 1981). Although the theory states that a perfectly achromatic coronagraph would provide a perfect nulling of the on-axis starlight, in practice, imperfections remain. In this paper, we use the *null depth* metrics instead of the peak-to-peak attenuation. The null depth quantifies the contrast provided by the coronagraph, integrated over the whole point spread function (PSF). As explained further in Sect. 4.3, this metrics is well suited to coronagraphy since it takes the changes induced by the coronagraph itself to the PSF profile into account. The theoretical null depth $N_{\rm theo}$ is given by the following wavelength-dependent expression (Mawet et al. 2005a):

$$N_{\rm theo}(\lambda) = \frac{I_{\rm coro}(\lambda)}{I_{\rm off}(\lambda)} = \frac{[1 - \sqrt{q(\lambda)}]^2 + \epsilon(\lambda)^2\sqrt{q(\lambda)}}{[1 + \sqrt{q(\lambda)}]^2}, \quad (4)$$

where $I_{\rm coro}$ (resp. $I_{\rm off}$) is the signal intensity when the input beam is centred on (resp. off) the coronagraph, $\epsilon(\lambda)$ is the phase error with respect to π, and $q(\lambda)$ is the flux ratio between the two polarisation components, TE and TM. In the theoretical case where the coronagraphic profile remains identical to the original PSF profile, this formula of the null depth is also valid for the peak-to-peak attenuation, which was demonstrated in an ideal case by Mawet et al. (2005a).

Equation (4) involves all the geometrical parameters of the grating (period Λ, filling factor F, depth h, sidewall angle α), which are illustrated in Fig. 2. The period Λ is the only fixed parameter in our design. It is determined by the subwavelength limit (λ/n). Considering a little margin for the spectral band lower bound ($\simeq$3.4 μm), and considering the refractive index of diamond ($\simeq$2.38), the period should be $\leqslant$1.42 μm. The other parameters of the manufactured grating are free parameters whose values are provided by numerical optimisation. Some of the parameters, like the depth h, the filling factor F and the sidewall angle α, may vary slightly during the etch process. The only way to measure them precisely is by cracking the sample along a diameter. By doing so, we measured that the angle α is usually 2.95° ± 0.25°. Owing to the uncertainty on the slope, we sought a robust design that performs well even slightly outside of the optimal parameter set. To find the target design parameters, we computed two-dimensional maps of the theoretical null depth as a function of the filling factor F and of the depth h, for several values of the angle α ranging from 2.7° to 3.2°. The mean of all these maps (see Fig. 3) gives the targeted specifications, i.e., the optimal parameters set region: period $\simeq$1.42 μm, filling factor $\simeq$0.45, depth $\simeq$5.2 μm, and sidewall angle $\simeq$2.95°. For these optimal parameters, the mean null depth over the whole *L* band (3.5–4.1 μm) equals 5×10^{-4}.

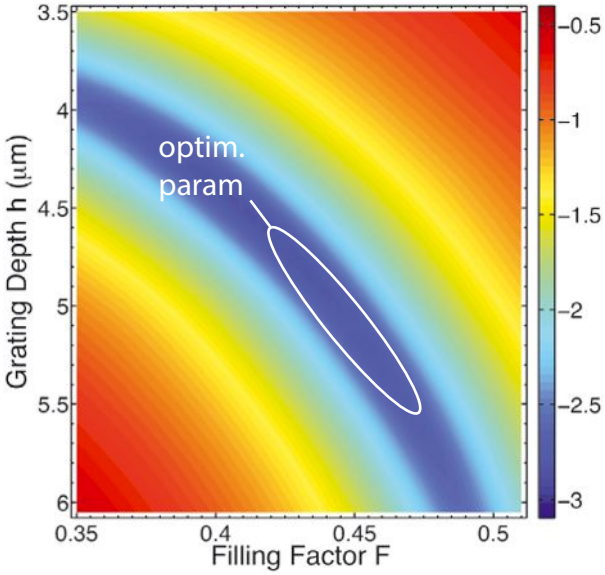

Fig. 3. RCWA multi-parametric simulation: mean null depth (logarithmic scale) over the whole *L* band (3.5–4.1 μm) with α ranging from 2.7° to 3.2°. The period is set to Λ = 1.42 μm (SG limit).

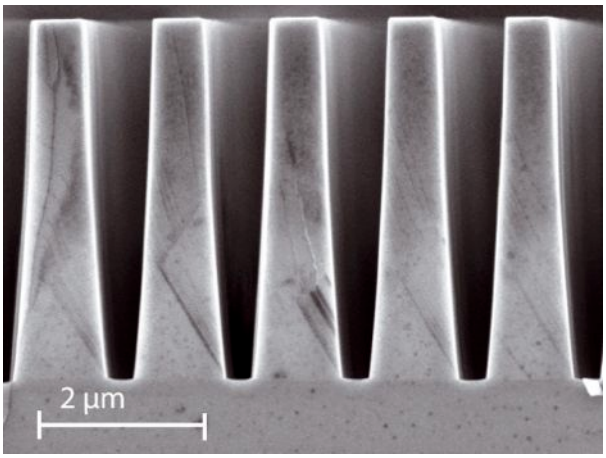

Fig. 4. SEM picture of the cleaved subwavelength grating, from which the geometric parameters of the AGPM-L4 profile are deduced: line width ≃0.58 μm (i.e., filling factor ≃0.41) and depth ≃4.7 μm.

3.2. Manufacturing and metrology

The AGPM pattern is etched onto a commercial optical-grade polycrystalline diamond window of 10 mm diameter and 300 μm thick, grown by chemical vapour deposition (Element Six Ltd.). The etching of the grooves involves techniques inherited from the micro-electronics industry. Electron-beam lithography was used to produce the pattern on a silicon wafer. Metal masking layers were deposited on the diamond by sputtering, and nano-imprint lithography was used to transfer the pattern to the top of the mask. Finally, reactive ion etching was used to etch the pattern first into the metal mask and then into the diamond. A similar manufacturing process has been described before (Karlsson et al. 2010; Delacroix et al. 2010). This process was painstakingly optimised to achieve the high pattern homogeneity, precision, and aspect ratio necessary for half-wave plates and AGPMs in the *N* band (Delacroix et al. 2012a). This included introducing a soft silicone stamp in the nano-imprint process and adding masking layers to better control the mask thickness and profile.

For the *L*-band AGPM only minor adjustments had to be made to take the difficulties of etching a finer grating into account. In particular, the etch rate and sidewall angle were both more sensitive to variations in groove width, and the depth of the grooves was even more difficult to measure with sufficient precision. To make precise measurements of the profile and depth, the sample had to be cracked and the cross-section imaged by scanning electron microscopy (SEM), as seen in Fig. 4. In the *N*-band case, the depth could be estimated with reasonable precision without cracking the sample or removing the mask, so etching could be carried out in steps with depth measurements in between until the correct depth was reached. For the *L*-band, this was not possible so a slightly different approach had to be taken. After etching the metal mask, the sample was imaged by SEM in order to measure the line width. This width did not change noticeably during diamond etching, so the top width ($F\Lambda$ in Fig. 2) of the final structure was known beforehand. Test samples with identical masks as the AGPM sample were then etched and cracked to determine the etch rate and sidewall angle. Two samples etched to different depths close to the final depth were required, because the etch rate slows when the grooves get deeper. The optimal depth was then recalculated by RCWA with the measured top width and sidewall angle fixed. Finally, the AGPM was etched for an appropriate length of time to achieve the desired depth. A detailed account of the masking and etching process used both for the *N* band and the *L* band is provided by Forsberg & Karlsson (2013). The grating depth of the finished components was confirmed by careful parallax measurements between SEM pictures at five different tilt angles.

Table 1. Measured profile parameters and simulated raw null depth for the four manufactured *L*-band AGPMs, and comparison with the optimal design.

Name	Period Λ	Fill F	Depth h	Angle α	$N_{\rm theo}$
AGPM-L1	1.42 μm	0.35	4.2 μm	2.40°	0.0267
AGPM-L2	1.42 μm	0.36	3.6 μm	2.65°	0.0116
AGPM-L3	1.42 μm	0.44	5.8 μm	3.25°	0.0048
AGPM-L4	1.42 μm	0.41	4.7 μm	3.10°	0.0010
Optimum	1.42 μm	0.45	5.2 μm	2.95°	0.0005

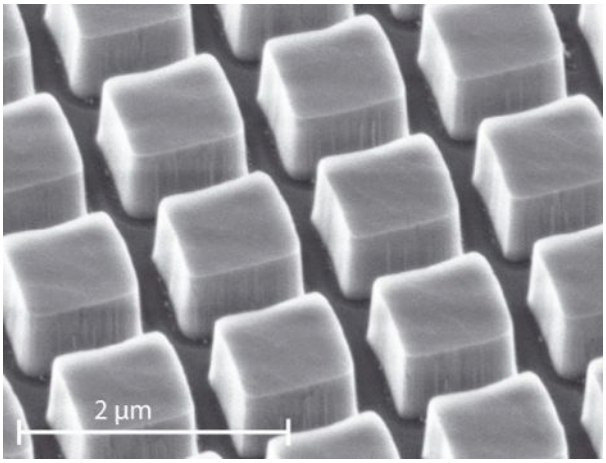

Fig. 5. SEM picture of the antireflective grating (ARG) etched on the backside of the AGPM.

Four finished components have been made to date. The first two, AGPM-L1 and AGPM-L2, were initial tests. These were etched with the exact same methods as *N*-band components. Moreover, the e-beam-written master used in the patterning of these two had lines that are too narrow. AGPM-L3 was an experiment with a different etch recipe giving a grating profile of trapezoidal walls with a triangular tops, designed to reduce the problem of ghost reflections (see Sect. 3.4). AGPM-L4 finally, was produced using the method described above to achieve a close to optimal depth for its actual fill factor and sidewall angle. That we were able to produce nearly optimal grating parameters with so few trials directly reflects the maturity of the fabrication process. The grating parameters of all four components and their simulated raw null depth can be found in Table 1 (with AGPM-L3 profile approximated as trapezoidal). In the rest of this paper, only the best component, AGPM-L4, will be discussed.

3.3. Antireflective grating

To avoid incoherent reflections on the internal sides of the AGPM, which would not be cancelled by the optical vortex, an anti-reflective grating (ARG) was etched on the backside of the component, using a very similar diamond-etching technique (Karlsson & Nikolajeff 2003) with a binary square-shaped structure as can be seen in Fig. 5. The backside reflection, which is high for diamond in the *L* band (~17%), is significantly reduced (~1.9%) thanks to the use of the ARG. The total transmission of the AGPM was measured on a Perkin-Elmer 983 spectrophotometer and compared to the theoretical transmission

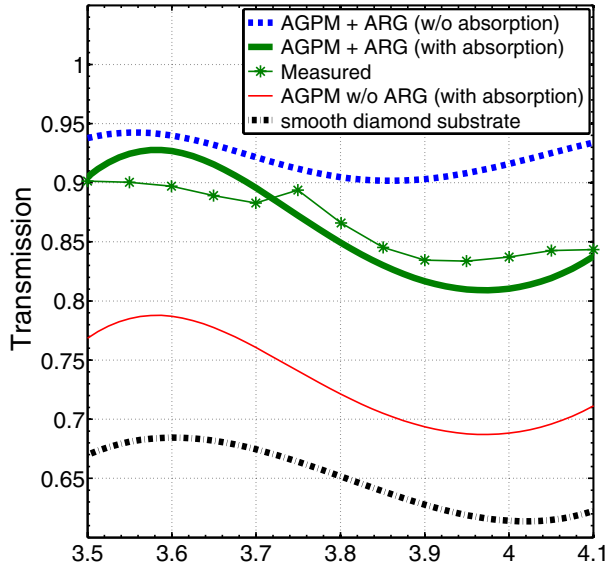

Fig. 6. *L*-band transmission measurements of AGPM-L4 with an antireflective grating (ARG) etched on its backside. The figure also shows the calculated transmission curves with/without the absorption, with/without the ARG, and for a smooth diamond substrate.

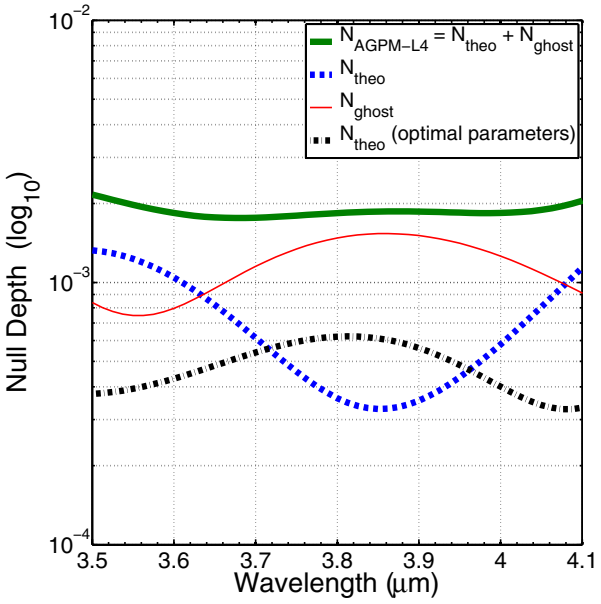

Fig. 7. *L*-band expected performance of AGPM-L4, calculated as the sum of the theoretical raw null depth N_{theo} and the ghost contribution N_{ghost}. The figure also shows the theoretical raw null depth obtained with the optimal design presented in Table 1.

calculated with RCWA (Fig. 6). The absorption, which is significant in the *L* band (especially around 4 μm), was taken into account in the calculation. The result is very satisfying, with an average total transmission of ~87%.

3.4. Expected performance

The performance of the coronagraph, i.e., the measured raw null depth N_{AGPM}, can be described as the sum of two terms:

$$N_{AGPM} = N_{theo} + N_{ghost}. \quad (5)$$

The first term is the theoretical null depth (Eq. (4)), which is limited by the manufacturing accuracy. The second term is induced by the ghost, i.e., the unwanted internal double reflection described in Sect. 3.3. The ghost contribution N_{ghost} is the ratio between the ghost intensity and the signal intensity when the input beam is centred off the coronagraph:

$$N_{ghost} = \frac{I_{ghost}}{I_{off}} = \frac{T_{SG}T_{ARG}R_{ARG}R_{SG}}{T_{SG}T_{ARG}} = R_{ARG}R_{SG}, \quad (6)$$

where T_{SG}, T_{ARG}, R_{SG}, and R_{ARG} are the transmittances and reflectances for both the subwavelength grating (SG) and antireflective grating (ARG) interfaces. In our case $R_{ARG}R_{SG} \simeq 10^{-3}$, which is quite small but not negligible in the case of the best component (AGPM-L4), whose theoretical null depth is also 10^{-3} (see Table 1). The expected performance of AGPM-L4 was calculated and is presented in Fig. 7. The mean null depth over the whole *L* band (3.5–4.1 μm) is 2×10^{-3}.

4. Laboratory results

After the manufacturing of different AGPMs with slightly varying grating heights and filling factors, coronagraphic tests were carried out in the *L* band at the Observatoire de Meudon, on the same optical bench (YACADIRE) as the one used for characterising the VLT-SPHERE coronagraphs (Boccaletti et al. 2008).

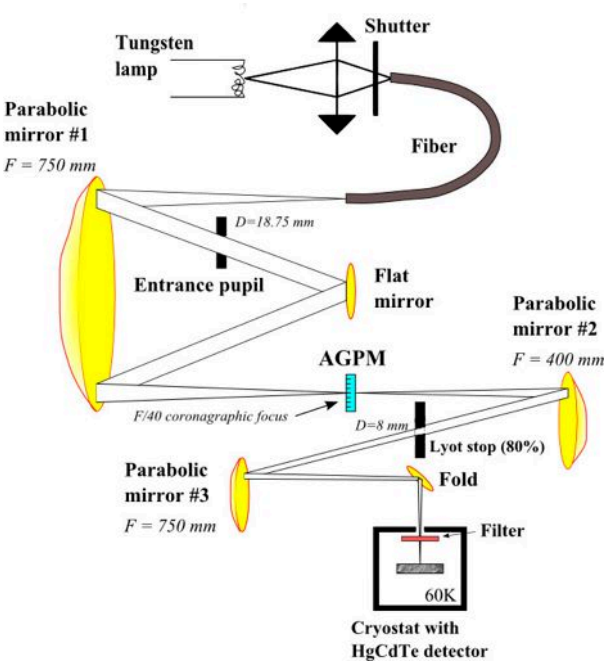

Fig. 8. Optical layout of the YACADIRE coronagraphic test bench.

4.1. Description of the coronagraphic test bench

The setup of the coronagraphic test bench, taking some minor modifications into account, is represented in Fig. 8. The bench is approximately 1.5 m long and located in a clean room. A tungsten lamp is used to feed a single-mode fibre (our star simulator) transmitting wavelengths up to 5 μm. Gold-coated parabolic and flat mirrors are placed successively in the light path between the fibre and the detector, so that the beam alternates from pupil to focal planes. This choice of a complete set of reflective optical components avoids inherent chromatic aberrations. The AGPM to be tested is placed in an intermediate focal plane between two

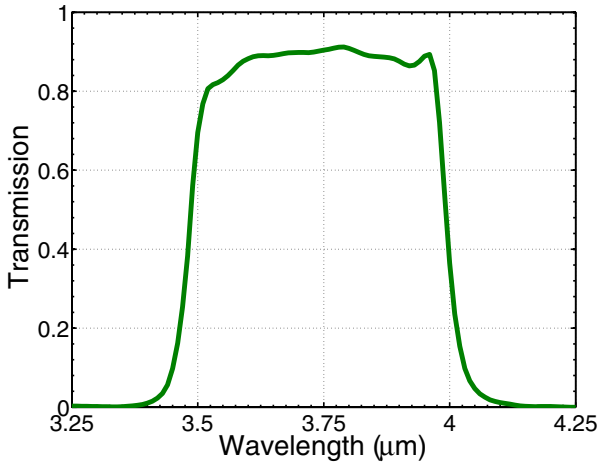

Fig. 9. Transmission curve measured at cold for the wide L-band filter (Spectrogon BBP-3500-4000 nm).

parabolic mirrors. With a focal distance of $F = 750$ mm for the first parabola and a beam diameter of 18.75 mm, the f-number of the beam impinging on the AGPM is $F/40$. The core of the Airy spot created on the AGPM is $F\lambda/D \simeq 150$ μm wide. A Lyot stop blocking the diffracted light is then located after the second parabolic mirror, reducing the pupil to 80% of its diameter. The beam is subsequently focussed at $F/94$ with the third parabolic mirror on an HgCdTe infrared detector placed in a cryostat cooled down to 60 K. Inside the cryostat, the beam first passes through a wide L-band filter (3.5–4.0 μm), whose transmission characteristics are given in Fig. 9.

4.2. Working and measurement principles

We started our coronagraphic tests by placing the AGPM precisely at the focus of the beam. A coarse positioning was achieved using a visible laser, by looking at the diffraction rings created upon propagation through the AGPM grating. The fine positioning was then performed in the L band, by minimising the flux reaching the camera. A second figure of merit in this optimisation was the shape of the coronagraphic PSF, which is expected to be symmetric when the AGPM is properly centred on $x = 0$ and $y = 0$ (the horizontal and vertical axes). The adjustment of the focus (z axis) was then based solely on the quality of the on-axis light extinction.

Series of 100 frames of 40 ms were recorded with the AGPM placed at the optimal position (referred to hereafter as the coronagraphic frames) and subsequently with the AGPM far from this position (typically at 1 mm) to measure a reference PSF without coronagraphic effect, but with the beam still propagating through the diamond substrate (referred to hereafter as the off-axis frames). These two sorts of frames (coronagraphic and off-axis) were used to evaluate the null depth as described hereafter (Sect. 4.3). Series of 100 frames were also recorded for various offsets of the AGPM from the optimal position in x, y, and z. In each case, 10 to 20 background frames were recorded to allow a basic treatment of our images. All exposure times were limited to 40 ms due to the saturation of the thermal background.

4.3. Data processing

The first step consisted in computing the median of the background images, before subtracting it from either the coronagraphic or the off-axis frames. Since we noticed that the background was sometimes slightly over-subtracted (resulting in negative values in the reduced images), a scaling of the background was implemented by using the ratio of the mean intensity in identical rings in both the coronagraphic (or off-axis) and the background frames. A flat field was measured and subsequently divided from the background-subtracted images. Noting $f_{\rm scal}$ the aforementioned scaling factor, the reduced images $I_{{\rm red},j}$ are given by

$$I_{{\rm red},j} = \frac{I_j - f_{\rm scal} I_{B,{\rm med}}}{i_F} \quad \text{with} \quad f_{\rm scal} = \frac{\langle {\rm ring}(I_{\rm coro}) \rangle}{\langle {\rm ring}(I_{B,{\rm med}}) \rangle}, \tag{7}$$

where I_j is the jth image within the coronagraphic or off-axis frames, $I_{B,{\rm med}}$ the median of the background images, $i_{\rm F}$ the normalised flat field, and $\langle\rangle$ represents the average over a number of pixels. Next, bad pixels and cosmic rays were adequately eliminated. Finally, all the reduced images were stacked to increase the signal-to-noise ratio of both the off-axis and coronagraphic images. Aperture photometry was then carried out on these final images in order to measure the flux in the coronagraphic and off-axis PSF, and thereby estimate the performance of our AGPM across the full L band.

Although the peak-to-peak attenuation is a widely used metrics to quantify the coronagraphic performance, the presence of the AGPM slightly changes the PSF profile near the axis. This phenomenon is characteristic of all coronagraphs. Therefore, a more robust metric needs to be used, taking both the coronagraphic and the off-axis frames mentioned in Sect. 4.2 into account. In our case, the figure of merit is the raw null depth, defined as the ratio between the integrated flux over a certain area around the centre of the final coronagraphic image and the integrated flux over the same area in the off-axis image. The question of the relevant size of this area is interesting. Using the full images would lead to a pessimistic result since it would integrate a lot of background and high frequency artefacts. Using the sole central peak seems to be more appropriate. As we wish to compare our results with the theoretical predictions of Riaud & Hanot (2010), we decided to use an area of radius equal to the FWHM of the PSF ($\sim\lambda/D$). This generally results in a good agreement with the theoretical formula (Eq. (5)), because most of the intensity in the image is contained within the FWHM. Our raw null depth is thus defined as

$$N_{\rm AGPM} = \frac{\int_0^{\rm FWHM} \int_0^{2\pi} \tilde{I}_{\rm coro}(r,\theta)\, r\, {\rm d}r\, {\rm d}\theta}{\int_0^{\rm FWHM} \int_0^{2\pi} \tilde{I}_{\rm off}(r,\theta)\, r\, {\rm d}r\, {\rm d}\theta} \tag{8}$$

where $\tilde{I}_{\rm off}$ and $\tilde{I}_{\rm coro}$ are the medians of the reduced off-axis and coronagraphic images, respectively. This definition would be perfectly equivalent to Eq. (5) if the coronagraphic profile was identical to the original PSF profile.

4.4. Measured performance and comparison with theory

The raw null depth measured by the described procedure was 2×10^{-3} over the L band (or alternatively, a rejection ratio $R = 1/N \simeq 500$), which is perfectly in line with the expected performance based on our RCWA modelling (see Sect. 3.4). In Fig. 10, the measured radial profile for the coronagraphic PSF is compared to the off-axis PSF profile. These profiles were obtained by computing the azimuthal medians in concentric rings of various sizes in our images, with a subsequent normalisation to the peak value of the off-axis PSF. We computed a confidence

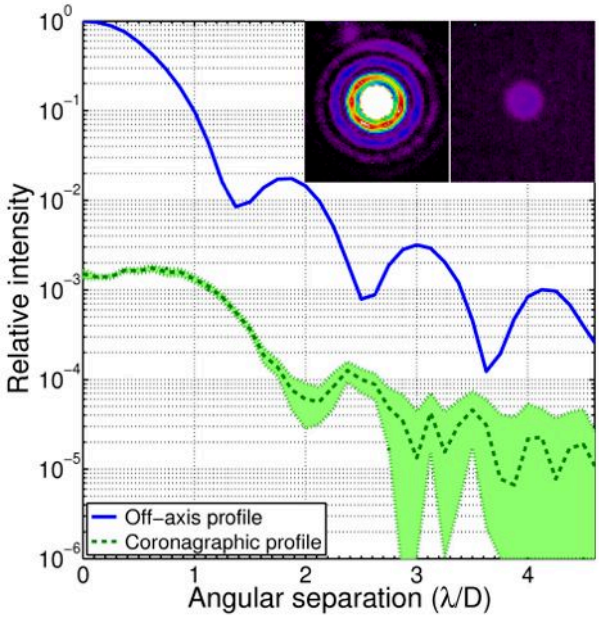

Fig. 10. Azimuthally averaged PSF (blue curve) and coronagraphic profiles (dash green curve) with confidence interval (green shaded region). The top-right inset shows the off-axis (*left*) and coronagraphic (*right*) images on a common linear scale. The off-axis image is thresholded and the coronagraphic image underexposed, conveying the true raw dynamic range achieved by the coronagraph, with a measured raw null depth of 2×10^{-3} and a raw contrast of 6×10^{-5} measured at $2\lambda/D$.

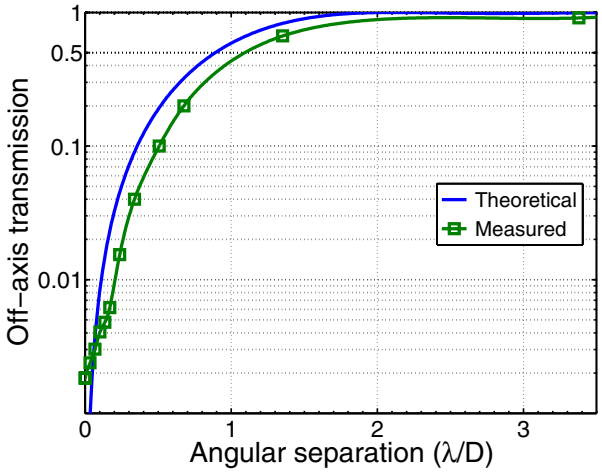

Fig. 11. Theoretical and measured off-axis transmission as a function of the angular separation between the beam and AGPM centre, expressed in resolution elements (λ/D).

interval on our median coronagraphic profile by measuring a series of 45 coronagraphic profiles on an integration time of about 40 s each (i.e., 1000 frames) and by computing the standard deviation of the profiles in each individual ring. The main source of fluctuations in the coronagraphic profile level is associated to background instabilities. The confidence interval in Fig. 10 shows that the coronagraphic profile is measured with a sufficient signal-to-noise ratio up to about $3\lambda/D$. Beyond this point, the intensity in the median coronagraphic profile is dominated by background subtraction residuals. The raw contrast delivered by the AGPM at $2\lambda/D$ equals 6×10^{-5}, which corresponds to 10.5 mag. Beyond $3\lambda/D$, the contrast quickly falls below 10^{-5} (i.e., 12.5 mag) and cannot be measured any more.

In a second phase, we explored the dependency of the coronagraphic attenuation as a function of the offset of the AGPM with respect to the optimal position. The results of these measurements are shown in Fig. 11. The agreement with the theoretical off-axis transmission profile of Riaud & Hanot (2010) is reasonable, which further suggests that our AGPMs produce the textbook vortex effect. Finally, we measured the sensitivity of the null depth to the focus. The null depth was divided by a factor 2 for a defocus of about ±1.5 mm at $F/40$, translating to a defocus aberration of ±120 nm peak-to-valley (∼30 nm rms).

5. Conclusions and perspectives

In this paper, we have presented the design, manufacturing, and measured performance of the first vortex phase mask coronagraphs based on the use of subwavelength gratings. Our annular groove phase masks, etched on diamond substrates, produce on-axis light rejection reaching a factor up to 500 across the L band (3.5–4.0 μm), which represents the best broadband performance of any mid-infrared phase mask to our knowledge. Assuming a high-quality input wave front, the use of our L-band AGPM on a telescope would result in an achievable raw contrast ranging from about 10^{-3} (7.5 mag) at an angular separation of $1\lambda/D$ to about 6×10^{-5} (10.5 mag) at $2\lambda/D$, and 10^{-5} (12.5 mag) at $3\lambda/D$. This underlines the strong potential of AGPM-L for exoplanet detection and characterisation at small angular separations from bright nearby stars.

In November 2012, AGPM-L3 was installed at the focus of NAOS-CONICA, the infrared adaptive-optics camera of the VLT (Lenzen et al. 2003; Rousset et al. 2003). Although the NACO image quality is not perfect in the L band, with a Strehl ratio around 70–85%, the very first on-sky tests suggest that the AGPM coronagraphic mode lives up to our expectations. These recent results will be presented in a forthcoming paper (Mawet et al. 2013). The installation of AGPM-L4 on LMIRCam, the L-band camera of the LBTI (Skrutskie et al. 2010), is currently going on. Thanks to the very high Strehl ratio delivered by the LBT adaptive optics at L band (>95%, Esposito et al. 2011), we expect that AGPM-L4 will realise its full potential on this instrument.

There are currently two main limitations to the performance of our L-band AGPMs. The first one is the presence of a ghost, reflected back and forth between the parallel faces of the diamond substrate. To reach starlight extinction better than 1000, a more aggressive antireflective solution will need to be used, based e.g. on an improved subwavelength structure or on a combination of the current design with an appropriate coating. The second limitation resides in the control of the grating parameters during manufacturing, including the slope of the grating walls. RCWA simulations show that, if the grating parameters can be made perfect, a theoretical on-axis attenuation of almost 10^{-4} could be reached. It is, however, expected that for such deep extinction, local phenomena not taken into account by RCWA simulations could become dominant. Such considerations will be fully investigated when designing and manufacturing second-generation AGPMs, for applications on future extremely large telescopes.

Acknowledgements. The first author is grateful to the financial support of the Belgian Fonds de la Recherche Scientifique (FRIA) and Fonds de solidarité ULg. S.H. and J.S. acknowledge support from the Belgian FRS-FNRS FRFC. We also gratefully acknowledge financial support from the Swedish Diamond Centre (financed by Uppsala University), and the Communauté française de Belgique – Actions de recherche concertées – Académie universitaire Wallonie-Europe.

References

Abramowitz, M., & Stegun, I. A. 1972, Handbook of Mathematical Functions (New York: Dover)
Absil, O., & Mawet, D. 2010, A&ARv, 18, 317
Baraffe, I., Chabrier, G., Barman, T. S., Allard, F., & Hauschildt, P. H. 2003, A&A, 402, 701
Berry, M. V. 1987, J. Mod. Opt., 34, 1401
Beuzit, J.-L., Feldt, M., Dohlen, K., et al. 2008, in Proc. SPIE, 7014, 41
Boccaletti, A., Abe, L., Baudrand, J., et al. 2008, in Proc. SPIE, 7015, 34
Boccaletti, A., Augereau, J.-C., Lagrange, A.-M., et al. 2012, A&A, 544, A85
Delacroix, C., Forsberg, P., Karlsson, M., et al. 2010, in Proc. SPIE, 7731, 157
Delacroix, C., Absil, O., Mawet, D., et al. 2012a, in Proc. SPIE, 8446, 8
Delacroix, C., Forsberg, P., Karlsson, M., et al. 2012b, Appl. Opt., 51, 5897
Esposito, S., Riccardi, A., Pinna, E., et al. 2011, in Proc. SPIE, 8149, 1
Foo, G., Palacios, D. M., & Swartzlander, Jr., G. A. 2005, Opt. Lett., 30, 3308
Forsberg, P., & Karlsson, M. 2013, Diam. Relat. Mater., 34, 19
Fortney, J. J., Marley, M. S., Saumon, D., & Lodders, K. 2008, ApJ, 683, 1104
Girard, J. H. V., O'Neal, J., Mawet, D., et al. 2012, in Proc. SPIE, 8447, 1
Guyon, O., Pluzhnik, E. A., Kuchner, M. J., Collins, B., & Ridgway, S. T. 2006, ApJS, 167, 81
Jenkins, C. 2008, MNRAS, 384, 515
Kalas, P., Graham, J. R., Chiang, E., et al. 2008, Science, 322, 1345
Karlsson, M., & Nikolajeff, F. 2003, Optics Express, 11, 502
Karlsson, M., Vartianen, I., Kuittinen, M., & Nikolajeff, F. 2010, Microelectron. Eng., 87, 2077
Kasper, M., Beuzit, J.-L., Feldt, M., et al. 2012, The Messenger, 149, 17
Kenworthy, M. A., Meshkat, T., Quanz, S. P., et al. 2013, ApJ, 764, 7
Kikuta, H., Ohira, Y., & Iwata, K. 1997, Appl. Opt., 36, 1566
Lagrange, A.-M., Gratadour, D., Chauvin, G., et al. 2009a, A&A, 493, L21
Lagrange, A.-M., Kasper, M., Boccaletti, A., et al. 2009b, A&A, 506, 927
Lagrange, A.-M., Bonnefoy, M., Chauvin, G., et al. 2010, Science, 329, 57
Lenzen, R., Hartung, M., Brandner, W., et al. 2003, in Proc. SPIE, 4841, 944
Lyot, B. 1939, MNRAS, 99, 580
Macintosh, B. A., Graham, J. R., Palmer, D. W., et al. 2008, Adaptive Optics Systems, ed. N. Hubin, 7015, 31
Marois, C., Macintosh, B., Barman, T., et al. 2008, Science, 322, 1348
Mawet, D., Riaud, P., Absil, O., & Surdej, J. 2005a, ApJ, 633, 1191
Mawet, D., Riaud, P., Surdej, J., & Baudrand, J. 2005b, Appl. Opt., 44, 7313
Mawet, D., Serabyn, E., Stapelfeldt, K., & Crepp, J. 2009, ApJ, 702, L47
Mawet, D., Serabyn, E., Liewer, K., et al. 2010, ApJ, 709, 53
Mawet, D., Mennesson, B., Serabyn, E., Stapelfeldt, K., & Absil, O. 2011, ApJ, 738, L12
Mawet, D., Pueyo, L., Lawson, P., et al. 2012, in Proc. SPIE, 8442, 04
Mawet, D., Absil, O., Delacroix, C., et al. 2013, A&A, 552, L13
Moerchen, M. M., Telesco, C. M., De Buizer, J. M., Packham, C., & Radomski, J. T. 2007, ApJ, 666, L109
Moharam, M. G., & Gaylord, T. K. 1981, J. Opt. Soc. Am., 71, 811
Niv, A., Biener, G., Kleiner, V., & Hasman, E. 2006, Optics Express, 14, 4208
Pancharatnam, S. 1956, in Proc. Ind. Acad. Sci. A, 44, 247
Quanz, S. P., Meyer, M. R., Kenworthy, M. A., et al. 2010, ApJ, 722, L49
Quanz, S. P., Kenworthy, M. A., Meyer, M. R., Girard, J. H. V., & Kasper, M. 2011, ApJ, 736, L32
Riaud, P., & Hanot, C. 2010, ApJ, 719, 749
Riaud, P., Mawet, D., Absil, O., et al. 2006, A&A, 458, 317
Rousset, G., Lacombe, F., Puget, P., et al. 2003, in Proc. SPIE, 4839, 140
Serabyn, E., Mawet, D., Bloemhof, E., et al. 2009, ApJ, 696, 40
Serabyn, E., Mawet, D., & Burruss, R. 2010, Nature, 464, 1018
Skrutskie, M. F., Jones, T., Hinz, P., et al. 2010, in Proc. SPIE, 7735, 118
Sneddon, I. 1951, Fourier Transforms (New York: McGraw-Hill)
Spiegel, D. S., & Burrows, A. 2012, ApJ, 745, 174

6

AGPM first light at the telescope

Contents

Abstract. *In the previous chapters, the design and the manufacturing of several AGPMs dedicated to the mid-infrared regime have been detailed. A laboratory demonstration at L band has allowed to validate the principle of the AGPM, and to confirm its theoretical performance based on the rigorous coupled wave analysis. The present and last chapter of this thesis is dedicated to the recent installation of AGPMs on three world-class infrared cameras: VISIR and NACO at the VLT, and LMIRCam at the LBT. After exposing the preliminary steps of certification and preparation of the coronagraphs, we detail the context of the implementation of these new AGPM modes, and show the first-light results.*

6.1 Preparing the device

6.1.1 Centering marks

Installing a coronagraph such as the AGPM on a telescope requires some preparation. We had to develop a system for centering the AGPM, once installed at the telescope. Indeed, the phase mask is very sensitive to tip-tilt, and it should be centered with a precision of several microns. In theory, the center of the vortex is supposed to affect the background. Therefore, it should be visible, allowing to center the AGPM manually. In practice, however, it is preferable to ensure that centering the device can be carried out properly (and rapidly).

One solution to help identifying the center of the vortex, is to add some fiducials (i.e. centering marks) visible while observing a flat field. Afterwards, the centering is done in real time by looking at the image on the detector. The centering marks were realized in collaboration with Sirris, a research center from Liège specialized in different fields of materials engineering and nanotechnology. We have printed 100 microns wide lines on our N-band AGPMs using Aerosol Jet Printing (AJP). This is a particularly innovative technology for selective deposition of materials at micron-scale. We have used silver ink, and defined sintering conditions for optimum adhesion. Indeed, the marks must be strongly fixed to the diamond surface, even at cryogenic temperatures as will be discussed here after.

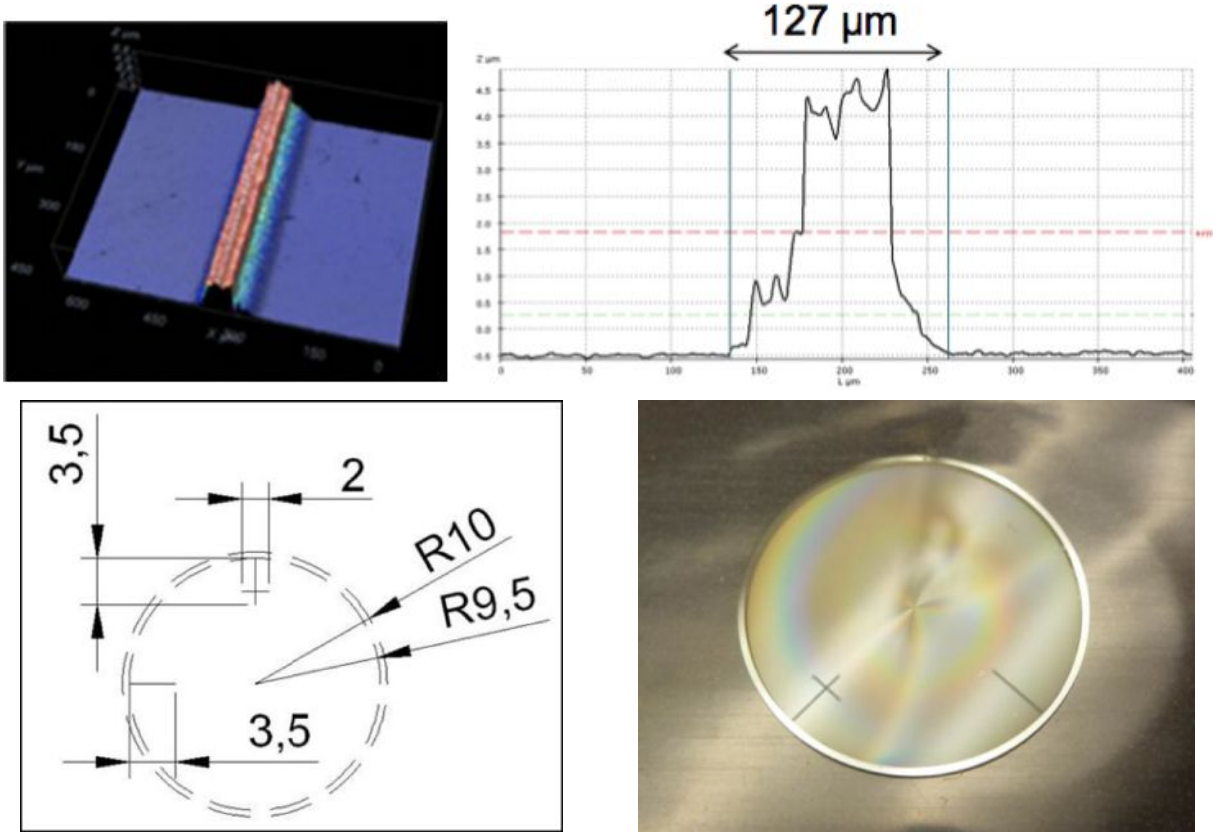

Figure 6.1: Top: Micrograph of a line deposited by AJP (left), with height determined by interferometric profilometry (right). Bottom left: Schematic diagram of the fiducials used for centering the AGPM. Bottom right: Lines (centering marks) deposited by AJP on an N-band AGPM coronagraph. Courtesy of Sirris.

6.1.2 Stress tests

Once installed on the instrument, the component must fit safely in its mount. Any risk of breaking the device should be avoided, otherwise it could damage severely the instrument. The AGPM is subject to two major constraints: (i) the pressure applied to it in its holder, and (ii) the thermal stresses occurring at cryogenic temperatures.

Pressure tests

We performed pressure stress tests in the laboratory, on a spare component of poor quality but of same material size and grating structure. We did not want to take the risk of breaking a good quality AGPM. The objective was twofold. The first goal was to validate the AGPM resistance against the stiffness of the spring maintaining the component in its mount. This was especially useful for implementing AGPM-N4 on VLT/VISIR, as will be discussed in Section 6.2. In that case, the spring applies a 2.5 N force on the coronagraph at room temperature, and even less when the device is cooled. The pressure test was done by placing a 10 mm diameter spare AGPM between two slightly undersized 1 mm thick hollow cylinders. We then applied a 20 N force on the top of the stack. The AGPM resisted well. We even increased the weight up to ∼25 N and it did not break or deform.

The second goal was to test whether the AGPM was able to withstand a maximum acceleration of 6 G, which corresponds to the usual resistance to earthquakes. The mass of an AGPM is very low, less than 0.5 g. While subjected to such an acceleration, its weight translates into a force of only ∼0.03 N. Thie earthquake-induced force is thus negligible compared to the spring pressure.

Cryogenic tests

The AGPM had to be tested at very low temperatures. Cryogenic stress tests were made with a spare AGPM, with centering marks imprinted by AJP on it. The tests were carried out at the Montefiore Institute, from the University of Liège (courtesy of Jean-Françis Fagnard). The AGPM was cooled down to 20 K with a ∼2 K/min temperature ramp. The cool-down lasted for approximately three hours. Again, the tests were successful and the component was not altered. Interferometric profilometry after cryogenic tests showed no deterioration of the printed lines. Indeed, one of the major advantages of diamond is its extremely low thermal dilatation. However, these were only primary cryogenic tests. For the use of AGPM-N4 on VISIR, we also needed to carry out final cryogenic tests with the AGPM inside its mount (see Section 6.2.2). These tests were performed at CEA Saclay. The mount was equipped with a representative diamond component, and placed on a dummy filter wheel. This subassembly was then cycled five times from 300 K to 4 K, with a maximum 10 K/min temperature ramp. Subsequent inspection showed no damage to the diamond component.

6.2 Validation of an N-band AGPM on VLT/VISIR

6.2.1 Motivations for the N band

The N band offers important advantages for AGPM coronagraphy. First and foremost, the manufacturing can be achieved with a much better precision than at lower wavelength, since the grating specifications are relaxed. The period and depth of the gratings are indeed proportional to the wavelength. The constraints are thus reduced by a factor of three compared to the L band. Besides, the N-band AGPM provides an exclusive and original solution for achromatic coronagraphy, where no other technique can currently compete. In this sense, the N band represents an ideal niche for the AGPM. As of today, an N-band coronagraph does not provide much improvement, due to the very high level of background. It can only enhance the detection performances for very small inner working angles, around very bright stars. However, this situation is about to change thanks to upcoming extremely large telescopes such as the E-ELT. Finally, the structure of blocked-impurity-band (BIB) detectors, usually used at mid-infrared wavelengths, generally induces multiple ghosts around point sources. The coronagraph is a good way to eliminate them, and to allow a better view of the companions.

As already stated before, testing the N-band AGPMs in the laboratory was impractical, as they work at a too long wavelength for the usual test benches. Preliminary tests had to be directly carried out at the telescope. Therefore, we proposed our best N-band coronagraph, AGPM-N4, to be installed in the VISIR (VLT Imager and Spectrograph for the mid-InfraRed) instrument, on the Melipal unit telescope at the VLT. The early results obtained with a calibration source during commissioning are presented in Section 6.2.3.

The new implemented modes in VISIR (see hereafter) not only provide new scientific applications, but can be seen as an N-band experimental demonstration. Indeed, the VISIR upgrade project will bring confirmation of the technical readiness and scientific value of several aspects of potential mid-infrared instrumentation at future ambitious astronomical projects such as the E-ELT. In particular, the upgraded VISIR will be a pathfinder for METIS (Mid-infrared E-ELT Imager and Spectrograph, Brandl et al. 2008, 2010a). The METIS instrument baseline includes imaging and spectroscopy at L, M and N bands with a possible extension to Q band imaging. METIS features an exoplanet characterization program, and therefore a coronagraphic mode.

In this context, our team, in close collaboration with CEA Saclay, is now involved in the METIS project, for which we naturally propose the AGPM as a baseline for the coronagraphic mode. This coronagraph concept is potentially one of the most efficient coronagraphic solutions for METIS. The technology is also particularly adapted to this wavelength range. Besides, the theoretical performance study was confirmed in August 2012 at the telescope (see Section 6.2.3), and more AGPMs are to come. METIS is currently undergoing a phase-A study. The AGPM could be selected for phase B (preliminary design), which might start mid-2014.

6.2.2 VISIR upgrade: implementing new observing modes

The VISIR-AGPM project was integrated to the VISIR Upgrade Project (Lagage et al. 2004; Kerber et al. 2012), in collaboration with members of the VISIR consortium. In particular, we worked together with CEA Saclay. Among the many contributions of CEA Saclay to the VISIR upgrade (e.g., detector, water vapor sensor, new spectroscopic mode), one was the implementation of three new observation modes: (i) the sub-aperture masking (SAM) interferometric mode, (ii) the 4QPM coronagraphic mode, and (iii) the AGPM coronagraphic mode. The two 4QPMs were designed to work at 10.65 and 11.3 μm respectively. The AGPM was designed for broadband operation (11.6-13.2 μm). Each of these modes needed equipment (filter, mask or/and diaphragm) which have to be mounted respectively on the existing filter wheel or/and diaphragm wheel of VISIR. The development of the 4QPM and SAM modes was taken care of by the Observatoire de Paris, while our group (Institut d'Astrophysique et de Géophysique de Liège) was responsible for the AGPM mode.

The existing focal plane wheel (diaphragm wheel) and filter wheel of VISIR were recycled to implement the new modes. The AGPM mount was installed in place of a small field (SF) slot in the diaphragm wheel (see Figure 6.2, left), whereas the broadband N-band filter was installed in the filter wheel, together with the Lyot stop diaphragm. The filter was specified such that its lower and upper bounds are above 11.6 μm and below 13.3 μm respectively. To guarantee an appropriate mounting of the filter, a new CAD model was designed with as-built geometry (see Figure 6.2, right). Two 0.15 mm thick gold washers were interposed to ensure a good contact between the filter and the mask. Two elastic straps, centered on the outer diameter of the mask, were used to fix the mask on the filter, preventing differential expansion between the filter (optical substrate) and the wheel (aluminum). The centering of the filter and of the mask were not crucial for the different modes, so no specific accuracy was provided. The Lyot mask dimensions were slightly undersized (with 15% margin) to take any pupil misalignment and diaphragm centering effect into account.

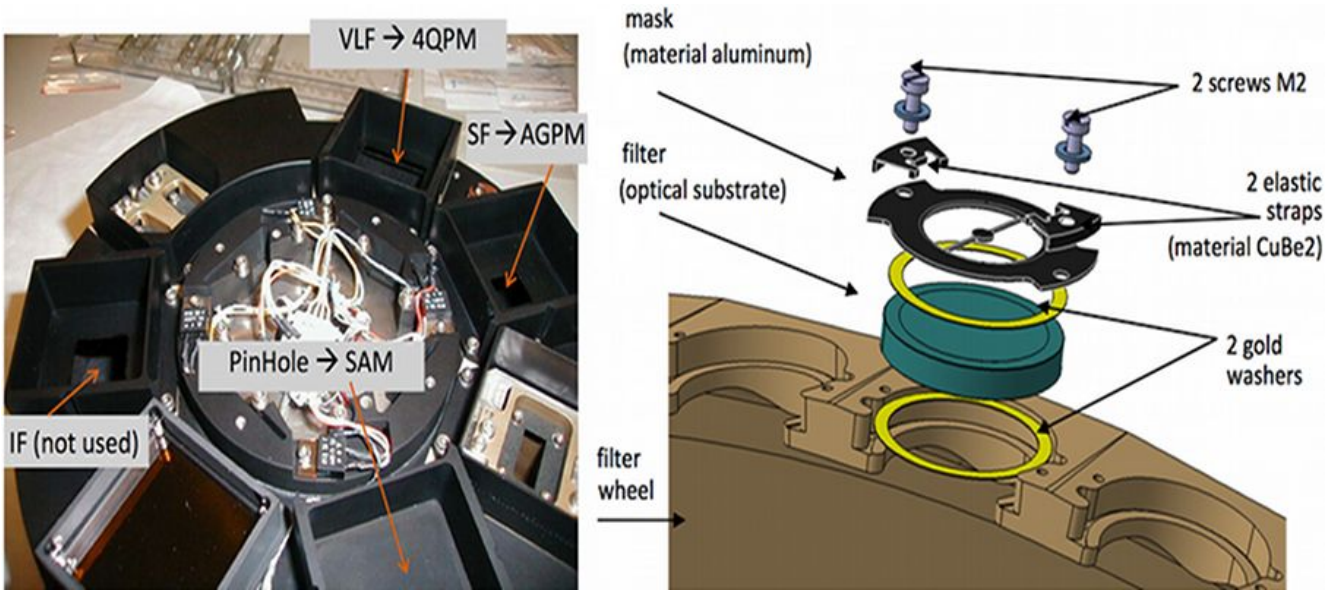

Figure 6.2: Left: VISIR focal plane/diaphragm wheel. Right: CAD model of the filter wheel, with mounting of the filter. Courtesy of Vincent Moreau, CEA Saclay.

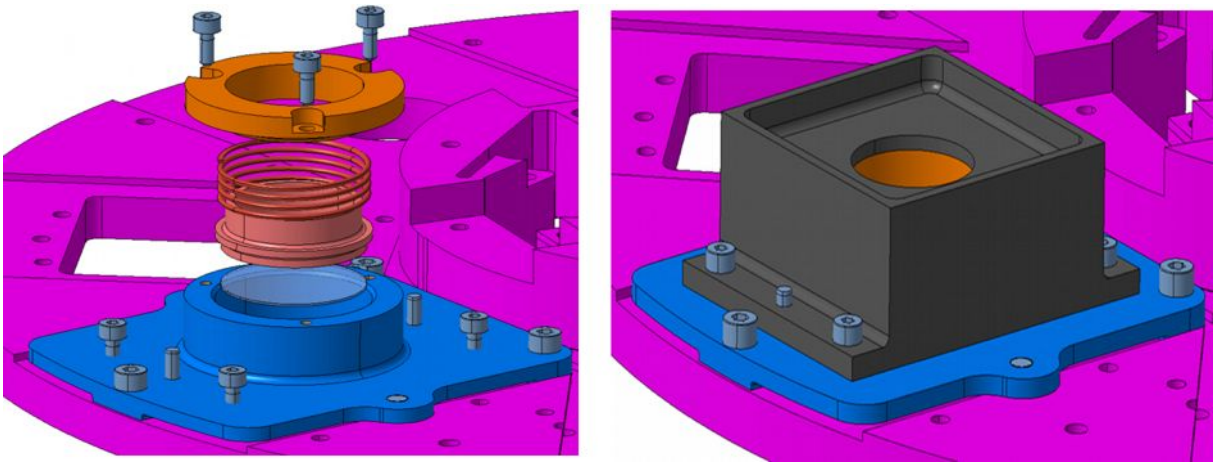

Figure 6.3: CAD model of the AGPM mount. Left: Assembly of the AGPM in its mount. The thin diamond optical component is pressed between two gold washers for thermal contact and mechanical stress relief in the bottom of the holder (note: the 2 washers are not shown on the figure). Right: The AGPM mount with its baffle. Courtesy of GDTech.

The AGPM mount was produced in collaboration with GDTech, a company from Liège specialized in mechanical design and engineering consultancy. Figure 6.3 illustrates the assembly of the mount. A *CuBe* spring was dimensioned to apply a 2.5 N force on the substrate. The focus was adjusted by an accurate tolerancing (± 50 μm) of the mechanical parts, allowing the annular grooves surface to be positioned on the focal plane within the tolerance. Finally, a baffle was mounted on the top of the assembly, to avoid any parasitic light path.

6.2.3 First coronagraphic test (and first light)

VISIR was successfully re-assembled and mounted back on Melipal in June 2012. Re-commissioning of the upgraded VISIR started on July 28th. In early August 2012, the newly implemented coronagraphs were tested our team represented by Eric Pantin, Ulli Käeufl, and Dimitri Mawet. Two tests have been carried out: one on an artificial star (see Figure 6.4), and the other one (a few nights later) on sky (see Figure 6.5).

For the very first time, taking advantage of bad whether conditions (the telescopes were closed because of high wind), our team tested the AGPM with the internal calibration source of VISIR. To our great relief, the artificial star disappeared behind the vortex. The star was not well centered under the coronagraph, but the peak attenuation was measured where the arrow points on Figure 6.4 (right), that is the brightest part of the attenuated PSF. Besides, it was difficult to precisely measure the attenuation because of the background. After normalization by the PSF, the brightest pixel was $\sim$0.0405 on the raw background subtracted coronagraphic image. Since the image was very noisy and oversampled, it was convolved with a 3-pixel wide Gaussian, leading to a $\sim$0.0323 brightest resel (resolution element), which corresponds to an estimated peak rejection 30:1.

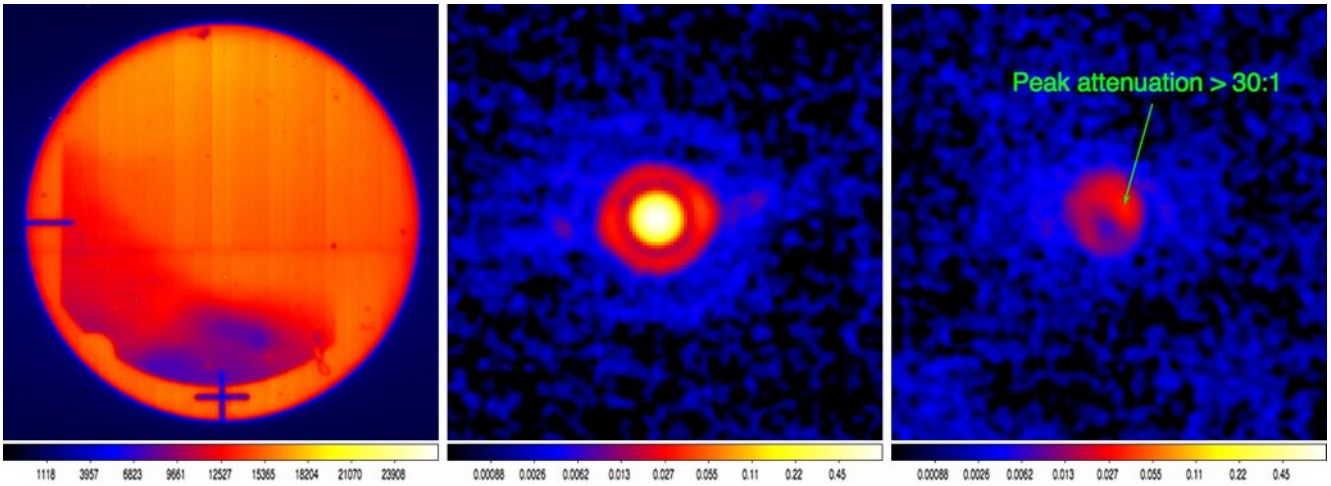

Figure 6.4: First test on VISIR internal calibration star. Left: VISIR field of view showing the fiducials imprinted on the AGPM. Middle: PSF of the artificial star. Right: PSF attenuation with the AGPM. Courtesy of Dimitri Mawet.

A few nights later, the N-band AGPM has seen first light during a quick test. The seeing was not impressive (∼0.9 arcsec) but both the AGPM and 4QPM ave shown good performance in stellar light attenuation. Moreover, the telescope had a slight tracking drift that should be corrected in the future. The AGPM provided a peak attenuation of ∼40 and an integrated energy (total) attenuation of ∼4. The 4QPM provided a peak attenuation of ∼23 and an integrated energy (total) attenuation of ∼2.3.

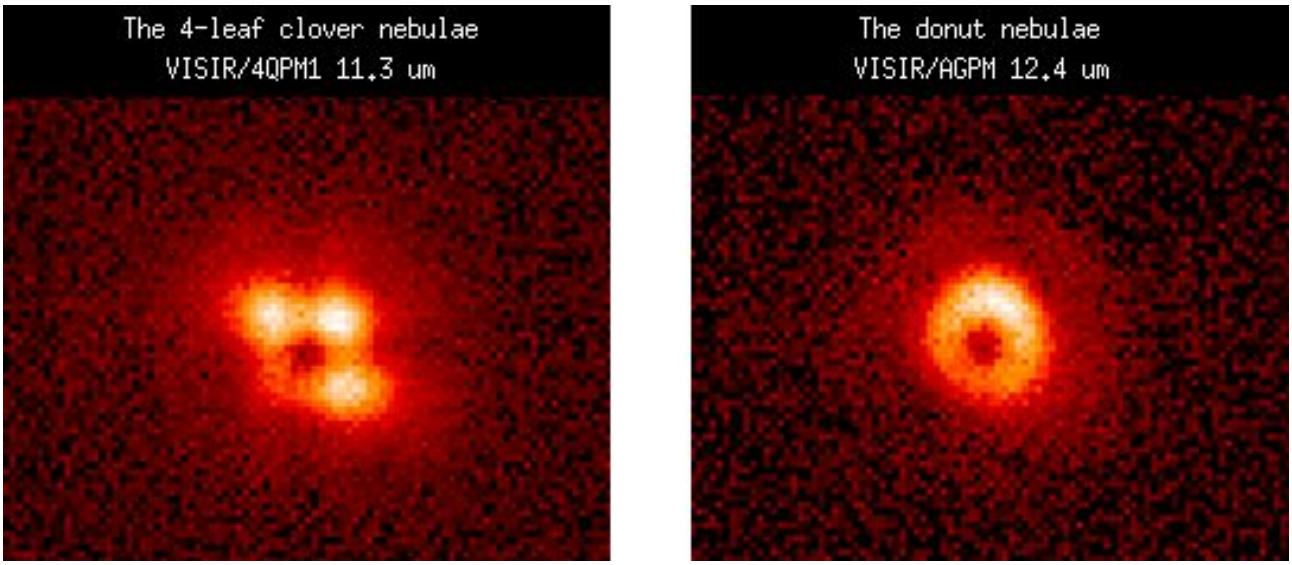

Figure 6.5: Coronagraphic images of a bright standard star, obtained with the new modes of VISIR. The 4QPM (left) has a peak attenuation ∼23 at 11.3 μm, and the AGPM (right) has a peak attenuation of ∼40 over the whole 11.6 - 13.2 μm band. Courtesy of Eric Pantin, CEA Saclay.

6.2.4 Perspectives with VISIR-AGPM

These numbers are of course preliminary and need to be re-estimated in better seeing and centering conditions. A better alignment could improve this result substantially, most likely by a factor ∼2-3. Nevertheless, these early results are promising. The device is (most probably) within specs. The fiducials do show nicely and are useful to locate the vortex center (see Figure 6.4, left). It is also the demonstration that the coronagraphic attenuation will be sufficient for on-sky observation with this level of background.

Further tests are needed to show just how good the component is. In this context, our team (led by PI Olivier Absil) has made a proposal to ESO for resolving the warm inner dust component of the Fomalhaut planetary system, during period P89. This proposal has been accepted. Unfortunately, a couple of weeks after the first recommissioning run, VISIR had to be dismounted from Melipal because of performance problems of the new AQUARIUS detector (made by Raytheon Vision Systems). In its present state the instrument does not meet the sensitivity expectations. VISIR is thus not ready for science operations yet.

Consequently to this bad news, our team has submitted a similar proposal for period P91. Our VISIR observing program on Fomalhaut was accepted, but has been delayed once again due to the continued unavailability of VISIR. At present, VISIR is not expected to come back online before 2014, and no VISIR proposals are accepted for ESO periods 91 and 92.

6.3 First light with an L-band AGPM on VLT/NACO

6.3.1 NAOS-CONICA: a sharp ground-based imager

New-generation vortex coronagraphs, such as the AGPM, provide a small IWA to enable detection down to 1 λ/D from the central star. Therefore, they require exquisite image quality and stability to perform efficiently. Next generation instruments like LMIRCam at the LBT, SPHERE at the VLT, the Gemini Planet Imager (GPI), or future instruments at the E-ELT, have been designed accordingly. However, first-generation instruments such as NACO possess excellent mid-infrared imaging capabilities that no other instrument can replace at the moment, allowing the follow-up of the very red galactic center region, and the L-band exoplanet imaging and characterization (Girard et al. 2012). Besides, the recent high contrast upgrades performed on NACO have opened a new parameter space and increased the chance to find planetary mass companions around nearby young stars. With the new calibrations performed by Girard et al. (2012), NACO provides a good and consistent PSF on night to night basis, with Strehl ratios usually 75 - 85%.

Following the recent successful installation of AGPM-N4 on VISIR, our team (led by Olivier Absil) proposed to take advantage of an upcoming refurbishment of NACO to install AGPM-L3 in the slit wheel of CONICA. The proposal was accepted, and our diamond vortex was thus installed in the so-called small slot, replacing an obsolete SDI mask unused for several years. As for VISIR-AGPM and LMIRCam-AGPM, a dedicated fully certified mount (see cryogenic tests, Section 6.1.2) was specially designed by GDTech.

6.3.2 Publication: L'-band AGPM vector vortex coronagraph's first light on VLT/NACO. Discovery of a late-type companion at two beam-widths from an F0V star

In November 2012, AGPM-L3 was inserted inside CONICA. The vortex coronagraph is optimized for 4 μm, and can be used with the narrow bands NB_3.74, NB_4.05, and with the broadband L' filters. The first on-sky tests carried out by Dimitri Mawet have been successful. Not only the AGPM has seen first light, but it also imaged a putative faint M2V companion at $\sim 0\farcs19$ ($< 2\lambda/D$) of an F-type star. In this section, we present the publication of the first-light with the AGPM coronagraph, published in April 2013 in the peer-reviewed journal Astronomy and Astrophysics (Mawet, Absil, Delacroix et al. 2013). The paper describes the observation method, and presents the intensity profile of the coronagraphic image, with the use of PCA-ADI technique. A high contrast of $\Delta L' > 7.5$ mag can be reached from the IWA of $0\farcs09$ onwards.

A&A 552, L13 (2013)
DOI: 10.1051/0004-6361/201321315

Astronomy & Astrophysics

Letter to the Editor

L'-band AGPM vector vortex coronagraph's first light on VLT/NACO

Discovery of a late-type companion at two beamwidths from an F0V star

D. Mawet[1], O. Absil[2], C. Delacroix[2], J. H. Girard[1], J. Milli[1], J. O'Neal[1], P. Baudoz[5], A. Boccaletti[5], P. Bourget[1], V. Christiaens[2], P. Forsberg[4], F. Gonte[1], S. Habraken[2], C. Hanot[2], M. Karlsson[4], M. Kasper[3], J.-L. Lizon[3], K. Muzic[1], R. Olivier[6], E. Peña[1], N. Slusarenko[1], L. E. Tacconi-Garman[3], and J. Surdej[2]

[1] European Southern Observatory, Alonso de Cordova 3107, Casilla 19001, Vitacura, Santiago 19, Chile
e-mail: dmawet@eso.org
[2] Département d'Astrophysique, Géophysique et Océanographie, Université de Liège, 17 Allée du Six Août, 4000 Liège, Belgium
[3] European Southern Observatory Headquarters, Karl-Schwarzschild-Str. 2, 85748 Garching bei München, Germany
[4] Department of Engineering Sciences, Ångström Laboratory, Uppsala University, Box 534, 751 21 Uppsala, Sweden
[5] LESIA, Observatoire de Paris, 5 pl. J. Janssen, 92195 Meudon, France
[6] GDTech s.a., LIEGE Science Park, rue des Chasseurs Ardennais, 4031 Liège, Belgium

Received 18 February 2013 / Accepted 1 April 2013

ABSTRACT

Context. High contrast imaging has thoroughly combed through the limited search space accessible with first-generation ground-based adaptive optics instruments and the *Hubble* Space Telescope. Only a few objects were discovered, and many non-detections reported and statistically interpreted. The field is now in need of a technological breakthrough.
Aims. Our aim is to open a new search space with first-generation systems such as NACO at the Very Large Telescope, by providing ground-breaking inner working angle (IWA) capabilities in the L' band. The L' band is a sweet spot for high contrast coronagraphy since the planet-to-star brightness ratio is favorable, while the Strehl ratio is naturally higher.
Methods. An annular groove phase mask (AGPM) vector vortex coronagraph optimized for the L' band made from diamond subwavelength gratings was manufactured and qualified in the lab. The AGPM enables high contrast imaging at very small IWA, potentially being the key to unexplored discovery space.
Results. Here we present the installation and successful on-sky tests of an L'-band AGPM coronagraph on NACO. Using angular differential imaging, which is well suited to the rotational symmetry of the AGPM, we demonstrated a $\Delta L' > 7.5$ mag contrast from an IWA $\simeq 0\farcs09$ onwards, during average seeing conditions, and for total integration times of a few hundred seconds.

Key words. instrumentation: high angular resolution – planetary systems – binaries: close

1. Introduction

The goal of high contrast imaging is primarily to discover and characterize extra-solar planetary systems. For technical motives rather than scientific ones, most surveys have targeted young and nearby stars. This search space is already limited, and imaging surveys have only explored its surface, strongly limited by contrast and inner working angle (IWA) capabilities (Absil & Mawet 2010). Despite the few spectacular objects discovered and insightful lessons learned from the majority of non detections, hunting for long-period planets has mostly been a hard and unfruitful task, with a very low yield (Lafrenière et al. 2007; Chauvin et al. 2010; Vigan et al. 2012). It is expected that opening the parameter space to fainter/smaller planets closer to their parent stars will bring many new objects (Crepp & Johnson 2011). The new sample is critical to exoplanet science because it will shed some light on planet formation mechanisms at or within the snow line, and help bridge the gap between the population of close planets discovered by radial velocity or transit techniques and the free-floating planets discovered by microlensing observations (Quanz et al. 2012). This intermediate parameter space should be opened by the second-generation coronagraphic instruments that have started to arrive at major observatories (Macintosh et al. 2012; Kasper et al. 2012; Oppenheimer et al. 2012; Martinache et al. 2012). Coronagraphy promises to be high contrast imaging's sharpest tool, but requires exquisite image quality and stability to perform efficiently. These new instruments have thus been designed accordingly. However, first-generation instruments still possess untapped potential that only ten years of operations and understanding allow us to exploit fully (Girard et al. 2012), especially in the mid-infrared (L' band, from 3.5 to 4.2 μm). This wavelength range offers significant advantages compared to shorter wavelengths (Kasper et al. 2007): (i) the L'-band contrast of planetary-mass companions with respect to their host stars is predicted to be more favorable than in the H band (Baraffe et al. 2003; Fortney et al. 2008; Spiegel & Burrows 2012) so that lower-mass, older objects can be addressed; and (ii) the L'-band provides better and more stable image quality, with Strehl ratios well above 70% and sometimes as high as 90%, thus reducing

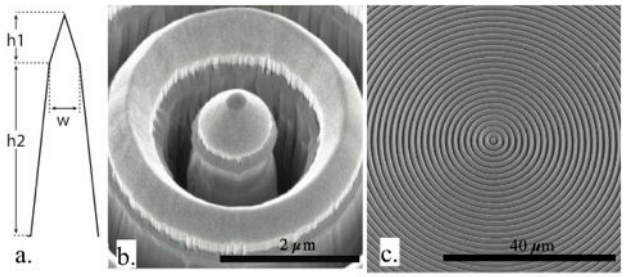

Fig. 1. Scanning electron microscope (SEM) images of the NACO AGPM. **a)** Structure profile schematic, with $h_2 = 5 \pm 0.1$ μm, $h_1 = 1 \pm 0.1$ μm, and $w = 0.65 \pm 0.03$ μm (the grating pitch is 1.42 μm). **b)** Zoom on the center of the diamond AGPM. **c)** Overview of the structure showing the uniformity and original cleanliness of this particular device.

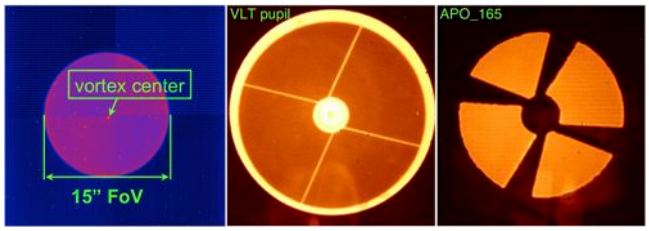

Fig. 2. *Left*: view from inside CONICA, showing the 9 mm clear aperture corresponding to a 15″ field of view (diameter), fully contained within the 27″ field of view of the L27 objective. *Middle*: full oversized stop of CONICA, showing the VLT pupil (including the central obscuration and struts). *Right*: APO165 pupil mask (diameter = $0.87 \times D_{\rm pup}$) available inside CONICA, aligned to cover the diffraction and thermal background from the central obscuration and struts.

speckle noise. These advantages certainly compensate for the increased sky background in the thermal infrared and the loss in resolution, especially if small IWA phase-mask coronagraphs are available.

Here we describe the successful implementation of an L'-band annular groove phase mask (AGPM; Mawet et al. 2005) vector vortex coronagraph on NACO (Lenzen et al. 2003; Rousset et al. 2003), the adaptive optics instrument of ESO's Very Large Telescope (VLT). To our knowledge it is the first time that an image-plane phase-mask coronagraph has been used in the mid-infrared.

2. An AGPM vector vortex coronagraph on NACO

The AGPM is an optical vortex made from diamond subwavelength gratings (Fig. 1). When centered on the diffraction pattern of a star seen by a telescope, optical vortices affect the subsequent propagation to the downstream Lyot stop by redirecting the on-axis starlight outside the pupil (e.g., Mawet et al. 2005). The advantages of the AGPM coronagraph over classical Lyot coronagraphs or phase/amplitude apodizers are small IWA, down to $0.9\lambda/D$ (e.g., 0.″09 in the L' band at the VLT, slightly smaller than the diffraction limit); clear 360° off-axis field of view/discovery space; outer working angle set only by the instrument and/or mechanical/optical constraints; achromatic over the entire working waveband (here L' band); high throughput (here ≃88%); and optical/operational simplicity. After eight years of intense technological development, the AGPM has reached a sufficient readiness level for telescope implementation (Delacroix et al. 2013; Forsberg & Karlsson 2013a). The AGPM selected for NACO was the third one in a series of four realizations (AGPM-L3). Its theoretical raw null depth limited by its intrinsic chromatism was estimated (assuming a trapezoidal profile[1], see Fig. 1) and measured to be around 5×10^{-3} (corresponding to a raw contrast of 2.5×10^{-5} at $2\lambda/D$), which is more than needed for on-sky operations where the limit is set by the residual wavefront aberrations.

The AGPM was installed inside NACO as part of a planned overhaul in November 2012. The AGPM was mounted on the entrance slit wheel by means of a dedicated aluminum mount, designed by GDTech s.a. The assembly of the mount and AGPM was done on site at Paranal observatory in a clean room environment. Prior to on-sky tests and operations, a CONICA internal image of the mask was done (see Fig. 2, left), revealing significant dust contamination, marginally affecting the background noise. The slit wheel was set so that the center of the AGPM falls close to but slightly away from CONICA's detector quadrant intersection. The AGPM field of view is ≃15″, corresponding to an outer working angle (OWA) of 7.″5. The OWA is only limited by the size of the device (10 mm in diameter) and its mount. The mask transmittance at L' band was measured on the sky to be 85% ± 5%, which is consistent with the theoretical value and laboratory measurements, both ≃88%, limited by imperfect antireflective treatments and mild absorption features around 4 μm (Delacroix et al. 2013). To stabilize speckles, we used the pupil tracking mode enabling angular differential imaging (ADI, Marois et al. 2006), which is perfectly adapted to the circular symmetry and 360° field of view of the AGPM. The CONICA camera is equipped with a pupil mask which blocks the telescope central obscuration and spiders. Once correctly aligned with the pupil (in x, y, and θ), this mask is optimal for use with the AGPM in pupil tracking mode (see Fig. 2). The measured throughput of the APO165 mask used here is ≃60%. In terms of sensitivity, it is worth noting that the throughput loss is almost entirely compensated by the improved thermal background. The pupil obscuration is responsible for more than 25% of the thermal emissivity of the telescope, even though its area only covers ≃5%. Therefore, instead of loosing $1 - \sqrt{0.6} \approx 0.225$ in sensitivity, only $1 - 0.6/\sqrt{0.6 \times 0.75} \approx 0.1$ is actually lost. To maintain its high contrast capabilities, the centering of the star on the AGPM must be within $(\lambda/D)/10$, or ≃10 mas (a third of a pixel at L27). This level of centering capability is now routinely obtained with NACO, both in pupil and field tracking modes; we typically measure ≃1 mas/min drifts across the meridian.

Table 1. Observing log.

Date	09/12/2012	11/02/2013
Star	HD 4691	HD 123888
Spectral type	F0V	K1III
V mag	6.79	6.62
L app. mag	5.86	4.01
DIT/NDIT/# fr	0.2s/10/100	0.25s/80/40
Seeing	1″–1.″5	0.″8–0.″9
τ_0	2–4 ms	4–5 ms
Strehl ratio	65–80%	75–80%
PA range	≃30°	≃30°

[1] This AGPM differs from the one tested in Delacroix et al. (2013). The tops of the grating walls are triangular to improve the transmittance (Fig. 1). This profile was etched with a process similar to the fabrication of broadband antireflective structures (Forsberg & Karlsson 2013b).

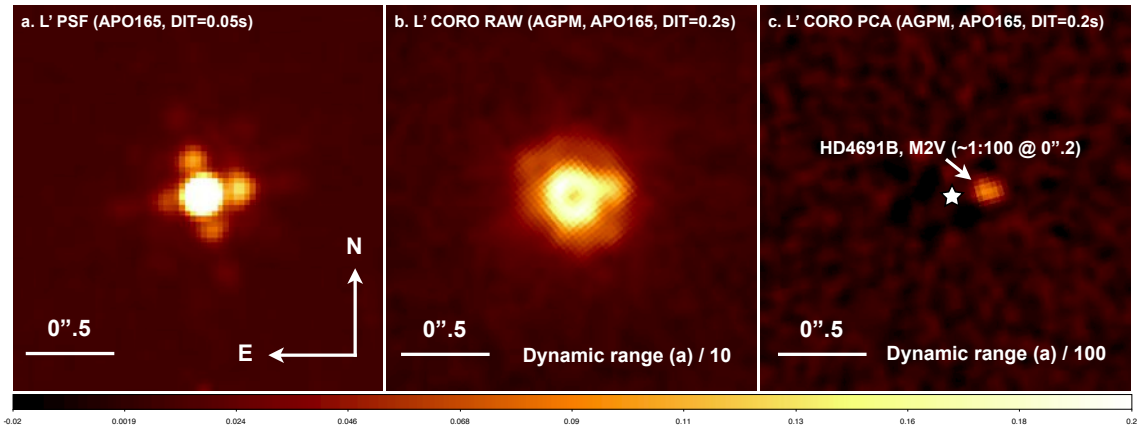

Fig. 3. **a)** L'-band NACO PSF with the APO165 pupil mask in the beam. **b)** L'-band NACO coronagraphic image with the star centered on the AGPM (the dynamic range and corresponding colorbar/scale are a factor of 10 smaller than in image **a)**). **c)**: Result of our PCA-ADI data reduction pipeline, revealing a putative faint off-axis M2V companion at only ≃0.″19 (the dynamic range and corresponding colorbar/scale are a factor of 100 smaller than in image **a)**). The scale is linear on all images (and scaled down by a factor of 10 and 100 for **b)** and **c)**, respectively), illustrating in sequence the benefits of coronagraphy and optimized data reduction technique. The bottom color bar refers to figure **a)**).

3. First light

On December 9, 2012, a representative observing sequence was performed on the 1.9-Gyr old main sequence standard star HD 4691 (see Table 1), under ≃1.″2 visual seeing conditions. This star was chosen to maximize brightness and field rotation during the short time allocated for this technical test. A ≃30-min ADI sequence was obtained with a parallactic angle (PA) range of 30° and for a total exposure time of 200 s on source; the efficiency was mediocre for technical reasons. After acquiring an off-axis PSF for photometric reference, we measured an instantaneous contrast of ≃50 peak-to-peak (despite the average-to-bad conditions, see Table 1). The attenuation is about 5 times higher than measured with NACO's four-quadrant phase-mask coronagraph at Ks (Boccaletti et al. 2004). The coronagraph diffraction control yields two instantaneous benefits compared to classical imaging: (i) the peak saturation limit is decreased by a factor ≃50; and (ii) the level of quasi-static speckles pinned to the PSF and the stellar photon noise limit are potentially decreased by a factor $\simeq\sqrt{50} \approx 7$, both within the AO control radius of $7\lambda/D$. All in all, the L'-band AGPM coronagraph allows the background limit to be reached much closer in.

3.1. Detection of a candidate companion

After applying basic cosmetic treatment to our sequence of 100 frames (background subtraction, flat fielding, and bad pixel/cosmic ray correction), we decided to use the quality and stability of the L'-band PSF provided by NACO to perform a sophisticated speckle subtraction. We used the very efficient principal component analysis (PCA) algorithm presented in Soummer et al. (2012). The result, using the whole image and retaining three main components, is presented in Fig. 3. By pure chance, the object has a ≃1:100 (or $\Delta L' \simeq 5$) off-axis companion located at ≃0.″19 ($<2\lambda/D$), making this our first unexpected scientific result. The companion flux and astrometry were obtained by using the fake negative companion technique (Marois et al. 2010). The method proceeds as follows: (i) estimate the (biased) position and flux of the companion from the first reduced image; (ii) use the measured off-axis PSF as a template to remove this first estimate from the cleaned data cube before applying PCA; and (iii) iterate on the position x, y and flux until a well-chosen figure of merit is minimized (χ^2 in a pie chart aperture centered on the first estimate of the companion position, $2.44\lambda/D$ in radius and $6 \times 1.22\lambda/D$ in azimuth). The minimization was performed with the Simplex-Amoeba optimization.

Table 2. Properties of HD 4691B.

Distance	62 pc
Age (Holmberg et al. 2009)	1.9 Gyr
Companion abs. L' mag	6.65 ± 0.1
Mass	≃0.3 $M_\odot$
Temperature	≃3450 K
Sp type	M2V
Angular sep.	$0.''190 \pm 0.''007$
Proj. angular sep.	11.8 ± 0.4 AU
Position angle	$279° \pm 0.°6$

Close to the center where the speckle field is intense, the companion flux can be overestimated because the minimization tries to subtract underlying speckles. To estimate our error bars, we decided to proceed with an alternative method called smart-ADI PCA: the frames used to construct the component basis are selected according to a minimum azimuthal separation criterion (here $N_\delta = 0.7\lambda/D$). With this technique, flux is much better preserved. We measured up to 200% additional flux compared to normal ADI PCA. However, fake planet tests still indicate a 25% flux loss, confirming that this method underestimates the flux and thus provides our lower bound. Finally, the coronagraph off-axis attenuation profile, measured in the lab (Delacroix et al. 2013) was also taken into account. Using the BCAH98 model (Baraffe et al. 1998), we derived the properties of the newly discovered candidate companion, assuming association. Note that the TRILEGAL starcount model (Girardi et al. 2005) yields a probability of 4×10^{-7} that it is an unrelated background object. At an absolute L'-band magnitude of 6.65, and 1.9 Gyr for the system, the putative companion would most likely be an M2V star at projected separation of 11.8 ± 0.4 AU, and $354.°5 \pm 0.°6$ position angle (see Table 2).

3.2. Representative NACO AGPM detection limits

Since the presence of the companion affects the contrast, we took another similar representative ADI sequence on a different

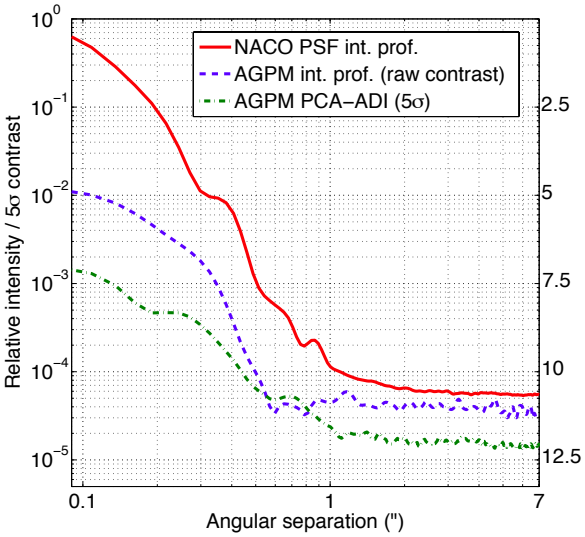

Fig. 4. Normalized azimuthally averaged relative intensity profiles and contrast curve. The plain red curve shows the intensity profile of a typical saturated NACO L' PSF (similar brightness and exposure time). The blue dashed curve shows the AGPM intensity profile before PCA, demonstrating the instantaneous contrast gain provided by the coronagraph at all spatial frequencies within the AO control radius (≃0.″7). The green dash-dot curve presents the reduced PCA-ADI 5σ detectability limits (40 frames, 800 s, ΔPA $\approx$ 30°), taking both the coronagraph off-axis transmission and the PCA-ADI flux losses into account.

standard star (HD 123888, see Table 1). This technical test was performed under better conditions, and benefited from our improved mastering of the new mode (efficiency was four times better than during the first light). A similar instantaneous attenuation was confirmed. To calibrate our detection limits against flux losses induced by PCA, we injected fake companions (at 15σ) prior to PCA and measured their throughput after PCA. We used the derived throughput map to renormalize the initial contrast curve a posteriori (see Fig. 4). Figure 4 shows excellent detection capabilities down to the IWA of the AGPM. The final calibrated contrast presented here (green dash-dot curve), is limited by the small PA range, especially at small angles. The floor reached beyond 1″ is due to the background at L', and will be lower for brighter targets and/or longer integrations.

We would like to raise several flags that we will thoroughly address in subsequent papers: (i) Classical tools assuming Gaussian statistics, perfectly valid at large separation, lose significance close to the center simply because the sample size decreases dramatically. At a given angular separation r (in λ/D), there are $2\pi r$ resolution elements, i.e., only 6 at $r = 1\lambda/D$, 12 at $r = 2\lambda/D$, etc. (ii) The probability density function (PDF) of speckle noise and associated confidence level for detection depend on radius. ADI was shown to transform speckles' modified Rician PDF into quasi-Gaussian PDF at large separations, but it is expected that this property of ADI does not hold true at small angles (Marois et al. 2008). (iii) The flux attenuation induced by ADI, potentially significant at small angles, does not scale linearly with the companion brightness, which makes its calibration more difficult. These points should be kept in mind when interpreting contrast curves such as those presented in Fig. 4, but also all contrast/detectivity plots that have been presented so far in the literature for very small angles.

4. Conclusions

The AGPM was designed to provide exquisite IWA (and OWA) capabilities, down to 0.9λ/D (0.″09 at L'), as demonstrated in Fig. 4. The downside of the AGPM's small IWA is its sensitivity to the Strehl ratio (as all coronagraphs) and to pointing errors. The apodizing phase plate (APP) is another advanced coronagraph offered at L' (Quanz et al. 2010; Kenworthy et al. 2013). The only, but significant, benefit of this pupil plane phase apodizer over the AGPM is its intrinsic immunity to tip-tilt errors. This advantage, which has to be traded off with the significantly limited field of view provided by the APP, is decisive when tip-tilt is an issue as was the case with NACO prior to November 2011 (Girard et al. 2012). However, it is less obvious when the instrument provides nominal PSF stability.

In a single technical run, the L'-band AGPM has proved to be a reliable coronagraphic solution, and one of the best high-contrast imaging modes of NACO (and most likely worldwide). Combined with ADI, we demonstrated that high contrast of the order of $\Delta L' > 7.5$ mag can be reached from the IWA of 0.″09 onwards, even with very modest on-source integration time, PA variation, and average conditions. The field of view is a clear 360° discovery space 15″ in diameter. The coronagraph is optimized for pupil tracking and is easy to use, thanks to the stability of the NACO L'-band PSF.

Acknowledgements. This work was carried out at the European Southern Observatory (ESO) site of Vitacura (Santiago, Chile). O.A. and J.S. acknowledge support from the Communauté française de Belgique – Actions de recherche concertées – Académie universitaire Wallonie-Europe. We would like to thank the referee, Dr Christian Marois, for his constructive comments.

References

Absil, O., & Mawet, D. 2010, A&ARv, 18, 317
Baraffe, I., Chabrier, G., Allard, F., & Hauschildt, P. H. 1998, A&A, 337, 403
Baraffe, I., Chabrier, G., Barman, T. S., Allard, F., & Hauschildt, P. H. 2003, A&A, 402, 701
Boccaletti, A., Riaud, P., Baudoz, P., et al. 2004, PASP, 116, 1061
Chauvin, G., Lagrange, A.-M., Bonavita, M., et al. 2010, A&A, 509, A52
Crepp, J. R., & Johnson, J. A. 2011, ApJ, 733, 126
Delacroix, C., Absil, O., Forsberg, P., et al. 2013, A&A, in press, DOI: 10.1051/0004-6361/201321126
Forsberg, P., & Karlsson, M. 2013a, Diamond & Related Materials, 34, 19
Forsberg, P., & Karlsson, M. 2013b, Opt. Exp., 21, 2693
Fortney, J. J., Marley, M. S., Saumon, D., & Lodders, K. 2008, ApJ, 683, 1104
Girard, J. H. V., O'Neal, J., Mawet, D., et al. 2012, in Proc. SPIE, 8447
Girardi, L., Groenewegen, M. A. T., Hatziminaoglou, E., & da Costa, L. 2005, A&A, 436, 895
Holmberg, J., Nordström, B., & Andersen, J. 2009, A&A, 501, 941
Kasper, M., Apai, D., Janson, M., & Brandner, W. 2007, A&A, 472, 321
Kasper, M., Beuzit, J.-L., Feldt, M., et al. 2012, The Messenger, 149, 17
Kenworthy, M. A., Meshkat, T., Quanz, S. P., et al. 2013, ApJ, 764, 7
Lafrenière, D., Doyon, R., Marois, C., et al. 2007, ApJ, 670, 1367
Lenzen, R., Hartung, M., Brandner, W., et al. 2003, in Proc. SPIE, eds. M. Iye, & A. F. M. Moorwood, 4841, 944
Macintosh, B. A., Anthony, A., Atwood, J., et al. 2012, in Proc. SPIE, 8446
Marois, C., Lafrenière, D., Doyon, R., Macintosh, B., & Nadeau, D. 2006, ApJ, 641, 556
Marois, C., Lafrenière, D., Macintosh, B., & Doyon, R. 2008, ApJ, 673, 647
Marois, C., Macintosh, B., & Veran, J.-P. 2010, Adaptive Optics Systems II, eds. B. L. Ellerbroek, M. Hart, N. Hubin, & P. L. Wizinowich, Proc. SPIE, 7736, 52
Martinache, F., Guyon, O., Clergeon, C., Garrel, V., & Blain, C. 2012, in Proc. SPIE, 8447
Mawet, D., Riaud, P., Absil, O., & Surdej, J. 2005, ApJ, 633, 1191
Oppenheimer, B. R., Beichman, C., Brenner, D., et al. 2012, in Proc. SPIE, 8447
Quanz, S. P., Meyer, M. R., Kenworthy, M. A., et al. 2010, ApJ, 722, L49
Quanz, S. P., Lafrenière, D., Meyer, M. R., Reggiani, M. M., & Buenzli, E. 2012, A&A, 541, 133
Rousset, G., Lacombe, F., Puget, P., et al. 2003, in Proc. SPIE 4839, eds. P. L. Wizinowich, & D. Bonaccini, 140
Soummer, R., Pueyo, L., & Larkin, J. 2012, ApJ, 755, L28
Spiegel, D. S., & Burrows, A. 2012, ApJ, 745, 174
Vigan, A., Patience, J., Marois, C., et al. 2012, A&A, 544, A9

6.3.3 Perspectives with NACO-AGPM

A half-night science verification was conducted by our team (led by Olivier Absil) on 31st January 2013, to observe β Pictoris. The weather conditions were poor to fair, with seeing $\approx 1''$. Based on a preliminary data processing, a performance comparison study with other techniques used on NACO has been carried out (see Figure 6.6). Using the data from β Pic, and simulating an ADI-PCA sequence, the simulation predicts a dynamic range better than 8 magnitudes at an angular distance of $0''.1$. Furthermore, the AGPM enables high contrast imaging in the whole 360°field-of-view, contrary to the APP which is restricted to a hemisphere and has a constraining outer working angle of a few resolution elements.

This is a preliminary result, which should be confirmed by further data analysis. A paper is being prepared (Absil et al. 2013).

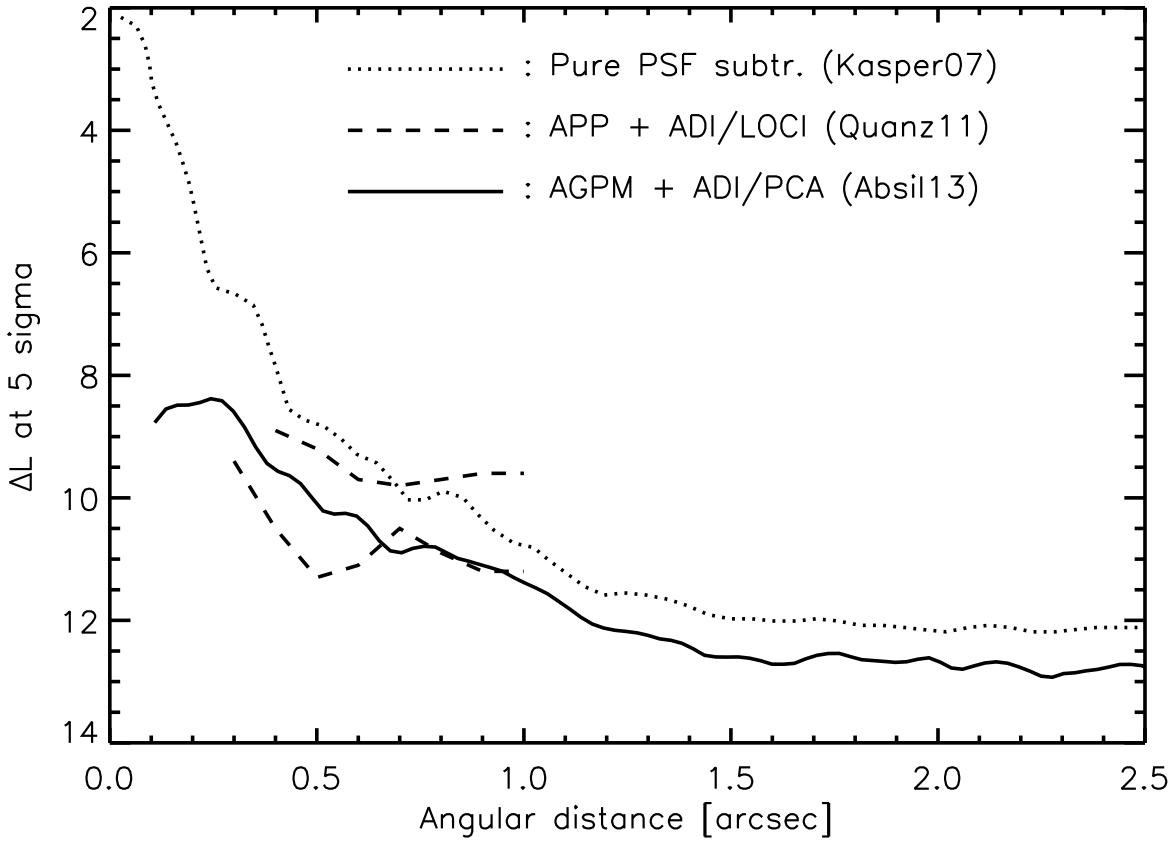

Figure 6.6: Estimated sensitivity of the AGPM in terms of magnitude difference, based on β Pic observation preliminary results, and comparison with a simple PSF subtraction (Kasper et al. 2007) and with two representative APP observations (Quanz et al. 2011). Courtesy of Olivier Absil.

Furthermore, a sensitivity analysis of the new NACO-AGPM mode was performed by our team (Hanot 2011), using a modified version of the official SPHERE simulator. The simulations show that in the case of young K and M dwarfs belonging to nearby moving groups, with ages between 8 and 200 Myr and at a distance $d < 50$ pc, the detection level is excellent and overlaps nicely with the SPHERE search space (see Figure 6.7). For older stars and higher masses, NACO-AGPM is expected to reach similar performances as SPHERE.

The intent of the new mode is truly to extend the scientific coverage of the VLT to the L band, providing insightful photometric information in that domain. Even if NACO were to be removed within less than two years, the implementation of the AGPM is worth the effort as: (i) E-ELT/METIS and other future high-contrast imagers will benefit from the experience, and (ii) original results should come out within this time frame.

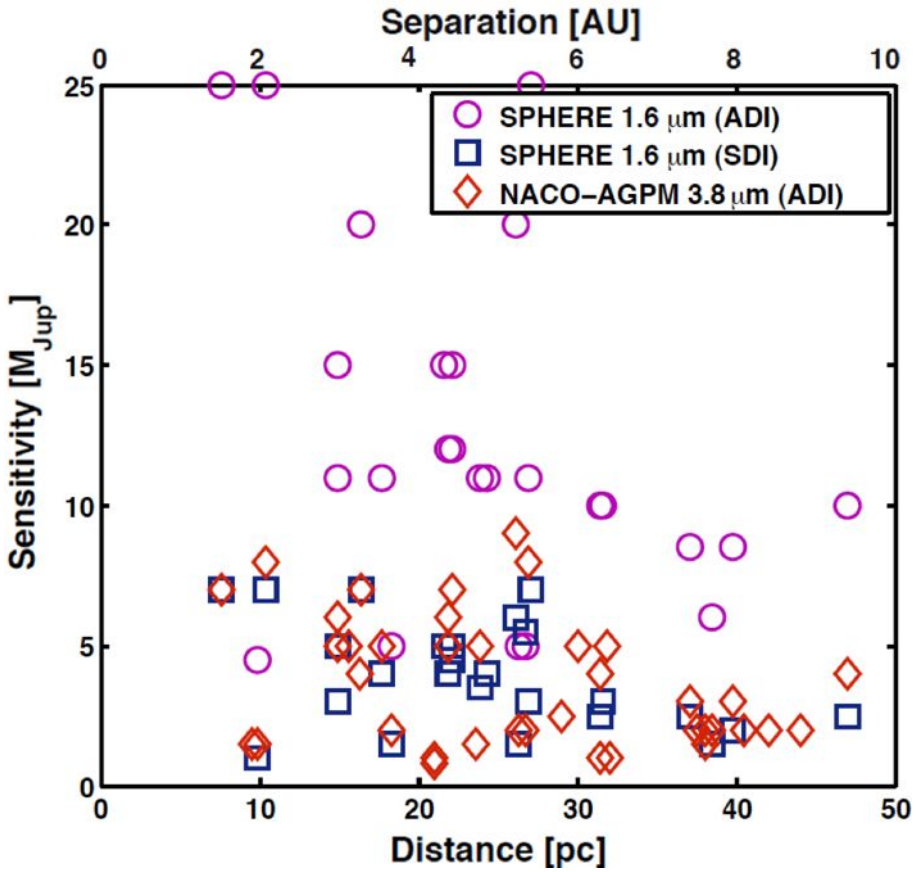

Figure 6.7: Estimated sensitivity of SPHERE (at 1.6 μm, H band) and NACO-AGPM (at 3.8 μm, L band) in terms of planetary mass, for low-mass stars in nearby young moving groups. From Hanot (2011)

6.4 Installation of an L-band AGPM on LBT/LMIRCam

Sitting on top Mount Graham (3260 m), a mountain in south-eastern Arizona, the Large Binocular Telescope (LBT) utilizes two giant 8.4 m primary mirrors that allow astronomers to explore distant planets in our galaxy and obtain crucial knowledge of the origins of our universe. The telescope first came online in 2010. The LBT next generation adaptive optics system is one of the best currently existing, with nearly 700 voice-coil magnets glued-on to the back of the 1.6 mm thick secondary mirror (Riccardi et al. 2010; Hill et al. 2012).

In this context, we proposed to install our best L-band component, AGPM-L4, at the LBT. This coronagraph was proved to deliver a 2×10^{-3} raw null depth, measured on the LESIA test bench (Delacroix et al. 2013). The installation of AGPM-L4 on LMIRCam, the L-band camera of the LBTI (Skrutskie et al. 2010) was accomplished in March 2013. The mount was designed by GDTech, similarly to VISIR-AGPM and NACO-AGPM, as shown on Figure 6.8. First light is expected in September 2013, due to little technical time available on LMIRCam. Thanks to the very high Strehl ratio delivered by the LBT adaptive optics at L band (>95%, Esposito et al. 2011), we expect that AGPM-L4 will unleash its full potential on this instrument.

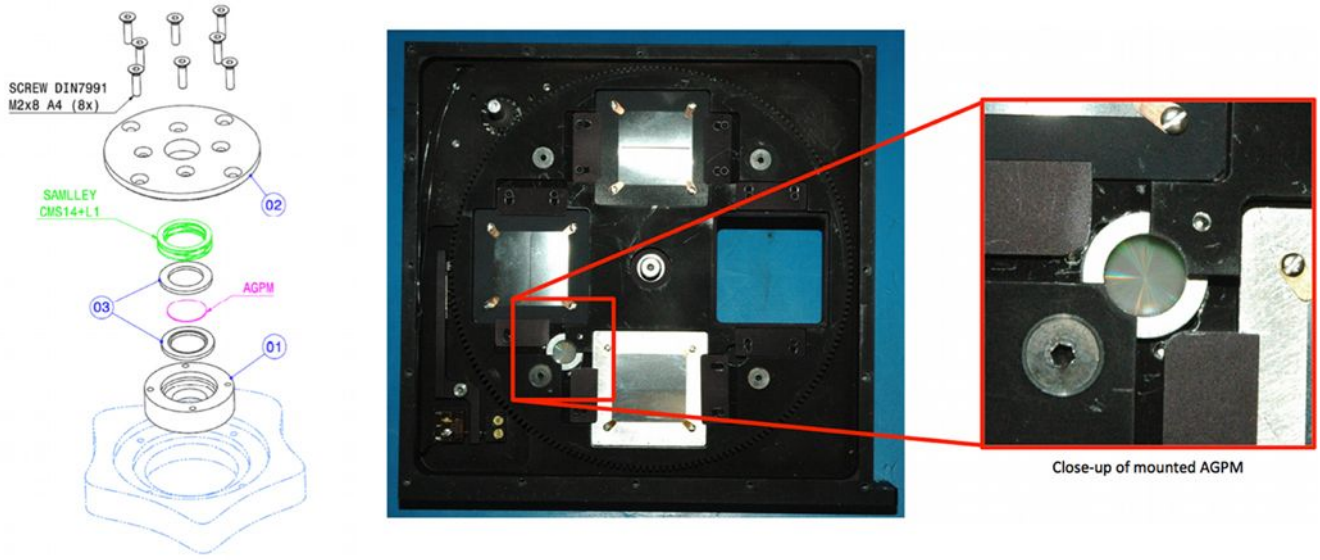

Figure 6.8: Left: GDTech mount design and assembly for the LMIRCam-AGPM. Right: LMIRCam field stop wheel, with a close-up of the mounted AGPM. Courtesy of Oli Durney, University of Arizona.

Conclusion and perspectives

In this dissertation, we have presented our work on the elaboration of the first annular groove phase mask (AGPM) coronagraphs, providing a detailed discussion at every stage of the development process.

In the first part of this thesis, beyond the introduction of the different indirect detection methods, we reviewed the theoretical details of the high dynamic range imaging techniques. Although important breakthrough results have recently been achieved by means of adaptive optics and data reduction algorithms, these were performed under specific conditions of moderate contrast and/or large angular separation between the planets and their host star. Ideally, coronagraphy should be used together with the techniques mentioned above to provide a powerful tool in order to detect exoplanets at smaller angular distances (Marois et al. 2006). After having set the scene in Chapter 1, we presented in Chapter 2 the theoretical aspects and existing technologies for producing vector vortex coronagraphs (VVCs). We showed that the annular groove phase mask (AGPM), based on subwavelength gratings, is a unique VVC solution at mid-infrared regimes, especially at L band (3.5 - 4.1 μm) which offers significant advantages compared to shorter wavelengths (Kasper et al. 2007), including higher planet/star contrast and reduced speckle noise.

In the second part of our work, we first reviewed the optical properties and advantages of subwavelength gratings (SGs), and presented a powerful theoretical tool for designing and analyzing those gratings, the so-called rigorous coupled wave analysis (RCWA). The use of RCWA at the University of Liège dates back to the early 1990s. The RCWA code has been enhanced repeatedly by several generations of researchers, and reprogrammed into different languages such as LabVIEW® (Lenaerts 2005) and MATLAB® (Mawet 2006). In this context, we contributed to the ongoing evolution and continuous improvement of the RCWA software with the performing and versatile language of MATLAB®. We have implemented new functionalities, such as: (i) updated grating profiles adequately adapted to the manufacturing capabilities, (ii) a multi-parametric algorithm running through the whole field of parameters, and generating 3D-maps of the optimal broadband performance (μ in the case of AGPMs, σ in the case of half-wave plates), and (iii) the integration of both the absorption and the multiple internal reflections occurring in the substrate media, hence estimating precisely the unwanted contribution of the so-called ghost signal. As new profiles have been recently developed at the Ångström laboratory (triangles on top of the walls, reducing reflections), we think that adapting the RCWA software to these profiles may constitute an interesting perspective for further improvements.

Chapter 3 was also devoted to the study and development of broadband half-wave plates (HWPs). Considering a selection of various substrates and micro-lithography techniques, we studied the feasibility of achromatic HWPs in the infrared regimes, where the fabrication constraints of SGs are relaxed. In the context of a long-term investment, one of our criteria was to use a material that is transparent down to the visible regime, allowing us to address the shorter wavelengths in the more distant future. We followed two parallel paths, silica (SiO_2) and diamond. Regarding the silica route, we contributed to the development process of K-band components, within the framework of the SPHERE project of ESO. We designed the components and estimated their performances for several spectral bandwidths, from the K band down to the visible regime ($\sim 5 \times 10^{-4}$ total raw null depth), and we took part in the setup of the technological stack within a wide consortium.

As the silica route was discontinued, we focussed on diamond, a prime candidate for mid-infrared applications, and we successfully managed to develop broadband HWPs (Delacroix et al. 2012b), hence fabricated the first N-band (11 - 13.2 μm) AGPM coronagraph (Chapter 4, Delacroix et al. 2012a). Our main contribution here was the thorough design study in synergy with the manufacturability. To a lesser extent, we participated to the manufacturing itself, at the Ångström laboratory (Uppsala University, Sweden) in summer 2009, during our first trials (Delacroix et al. 2010a,b). Later on, we took part in some metrology processes carried out at the University of Liège (HOLOLAB optics laboratory and Centre Spatial de Liège). Since conclusive results were obtained with the diamond manufacturing process, we pursued our developments of N-band AGPMs, and started to work in parallel on much finer gratings meant for the L band (3.5 - 4.1 μm) which is more constraining for two reasons: (i) the required precision is three times higher, and (ii) the etch rate and sidewall angle depend more strongly on the groove width as the grooves get narrower (Forsberg & Karlsson 2013a). Several iterations between design and manufacturing successfully led to eight manufactured components, four of them (AGPM-N3, AGPM-N4, AGPM-L3, AGPM-L4) being close to the optimal specifications and delivering an estimated total raw null depth $\approx 2 \times 10^{-3}$.

The results presented in the second part of this thesis bring interesting perspectives, with respect to several parameters: (i) the working wavelength, (ii) the grating shape, and (iii) the topological charge. First, based on the established manufacturing process, we defined in Chapter 4 the complete set of optimal parameters for several spectral bandwidths, downscaling our first results from the mid-infrared down to the visible regime. Our next target is clearly the K band (2 - 2.4 μm), which corresponds to a $\sim$60% scaling with respect to the L band. Such a goal is in theory not impossible to reach, but will require more process optimization, starting with a new high precision e-beam mask. The second aspect is the possible efficient gain provided by very recent grating profiles, such as the one etched on AGPM-L3 as an attempt to reduce the reflection on the AGPM side (Forsberg & Karlsson 2013b), and which could be better optimized from a coronagraphic point of view. The third aspect concerns the manufacturing of higher topological charge vortices ($l = 4, 6, 8, ...$). Up to now, we have chosen the $l = 2$ case mainly for two reasons. Firstly, its technical simplicity makes it easier to fabricate, and it is the only case to afford the required symmetry for the grating parameters to remain constant over the whole surface, thereby guarantying both the phase shift stability and the subwavelength regime. Secondly, it allows smaller IWA, typically $0.9\lambda/D$, compared to a charge-4 vortex $\approx 1.75\lambda/D$ (Mawet et al. 2009a). However, higher charges are mandatory to reduce the sensibility to low order aberrations (tip-tilt, focus, coma, astigmatism). A possible solution to build a charge-4 SG-VVC avoiding the difficult geometries, could be an embedded component made of two stacked AGPMs with a HWP in between.

In the third and last part of this dissertation, we presented our contribution to the validation of the AGPM technology. In Chapter 5 first, we showed the laboratory results of our L-band coronagraphs. We contributed directly to these results by performing the tests at the optical bench of the Observatoire de Paris. We noticed that the internal multiple reflections were producing a so-called ghost signal that was not cancelled by the optical vortex, therefore reducing the nulling performance. This observation motivated our choice to etch binary rectangular antireflective gratings on the backside of the components. When we returned to the laboratory, we successfully confirmed the expected performances of the tested AGPMs (Delacroix et al. 2013). Chapter 6 was dedicated to the recent installation of our components on three world-class infrared cameras (VISIR, NACO and LMIRCam), for which we contributed by taking part in the preliminary steps of certification and preparation of the coronagraphs. Finally, we presented the very first on-sky results of both N-band and L-band AGPMs, and the discovery and successful imaging of a faint stellar companion at two beamwidths from an F-type star (Mawet, Absil, Delacroix et al. 2013).

After many years of design, simulations, trials and also errors, this is the starting point of a demonstration. The demonstration that a powerful tool such as the AGPM can be created and operated. I remember the time when I was a child, my uncle Heniek would insist on me helping him in fixing the leaky sink, or cutting firewood with a sharp saw. From the many things I learned from my beloved uncle, I will surely never forget one of his favorite quotes: “the right tool for the right job”.

Part IV

Appendix

A

Infrared materials optical curves

An exhaustive survey of transparent materials in the thermal infrared has already been conducted by Mawet (2006) during his PhD. In our thesis, we have completed Mawet's work by computing reflectance and transmittance curves using the following equations demonstrated in Section 3.2.4

$$R_{tot} = R\left(1 + \frac{(1-R)^2\, e^{-2\alpha h}}{1 - R^2\, e^{-2\alpha h}}\right) \tag{A.1}$$

$$T_{tot} = \frac{(1-R)^2 e^{-\alpha h}}{1 - R^2\, e^{-2\alpha h}} \tag{A.2}$$

which consider absorption occurring in a substrate of thickness h. We have also extended Mawet's survey to SiO_2 and diamond, which are the materials we have selected upon criteria listed in Section 3.2.4, to synthesize achromatic half-wave plates using subwavelength gratings, dedicated to the manufacturing of vector vortex coronagraphs such as the annular groove phase mask.

The following curves show the optical coefficients, as well as reflectance and transmittance, of some of the principal materials which have been considered. As stated in section 3.2.4, we have exploited data from Pilon (2002) for SiO_2, and from Hawkins (1998) for diamond, Si, Ge, ZnS, and $ZnSe$, using polynomial regressions and Sellmeier equations with the corresponding coefficients given in Tables A.1 to A.5.

IR-grade fused silica Infrasil® (SiO_2)

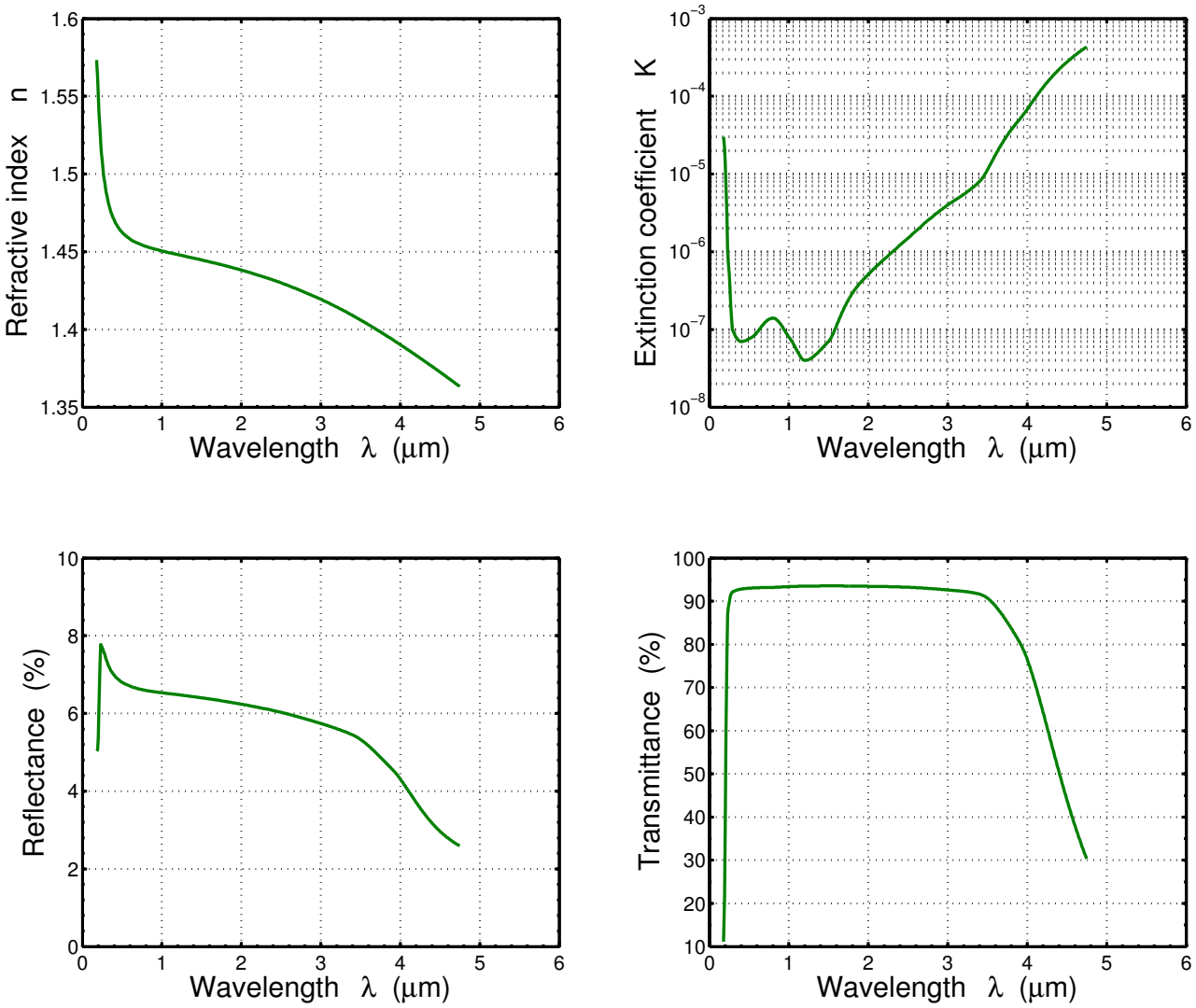

Figure A.1: Fused silica optical properties at room temperature. Top: refractive index (left) and extinction coefficient (right) dispersions, with data from Pilon (2002). Bottom: computed total reflectance (left) and transmittance (right) for a 1 mm thick substrate.

Chemical vapor deposited (CVD) diamond

$$n_{\text{diamond}}(\lambda, T) = \sqrt{A + \frac{B\lambda^2}{(\lambda^2 - C)} + \frac{D\lambda^2}{(\lambda^2 - E)}} \tag{A.3}$$

Table A.1: Sellmeier coefficients for diamond index representation at room temperature.

Coefficient	CVD diamond
A	1
B	0.3306
C	0.030625
D	4.3356
E	0.011236

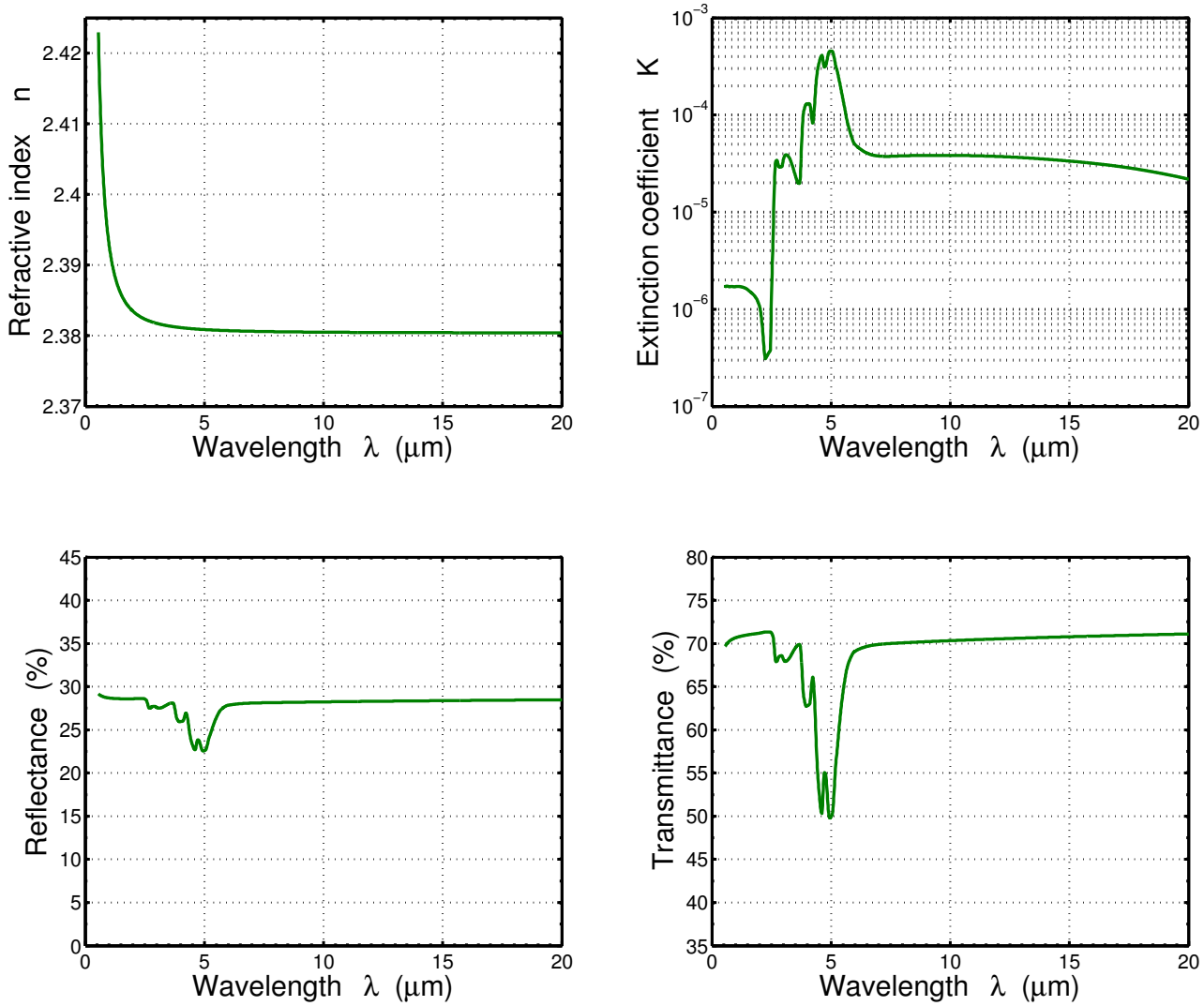

Figure A.2: CVD diamond optical properties at room temperature. Top: refractive index (left) and extinction coefficient (right) dispersions, with data from Dore et al. (1998) and Hawkins (1998). Bottom: computed total reflectance (left) and transmittance (right) for a 300 μm thick substrate.

Silicon (Si)

$$n_{\mathrm{Si}}(\lambda, T) = A + B\lambda + C\lambda^2 + D\lambda^3 + E\lambda^4 \tag{A.4}$$

Table A.2: Polynomial coefficients for silicon temperature-dependent index representation.

Coefficient	Si
A	$1.600 \times 10^{-4}T + 3.431$
B	-2.643×10^{-2}
C	4.324×10^{-3}
D	-3.194×10^{-4}
E	8.835×10^{-6}

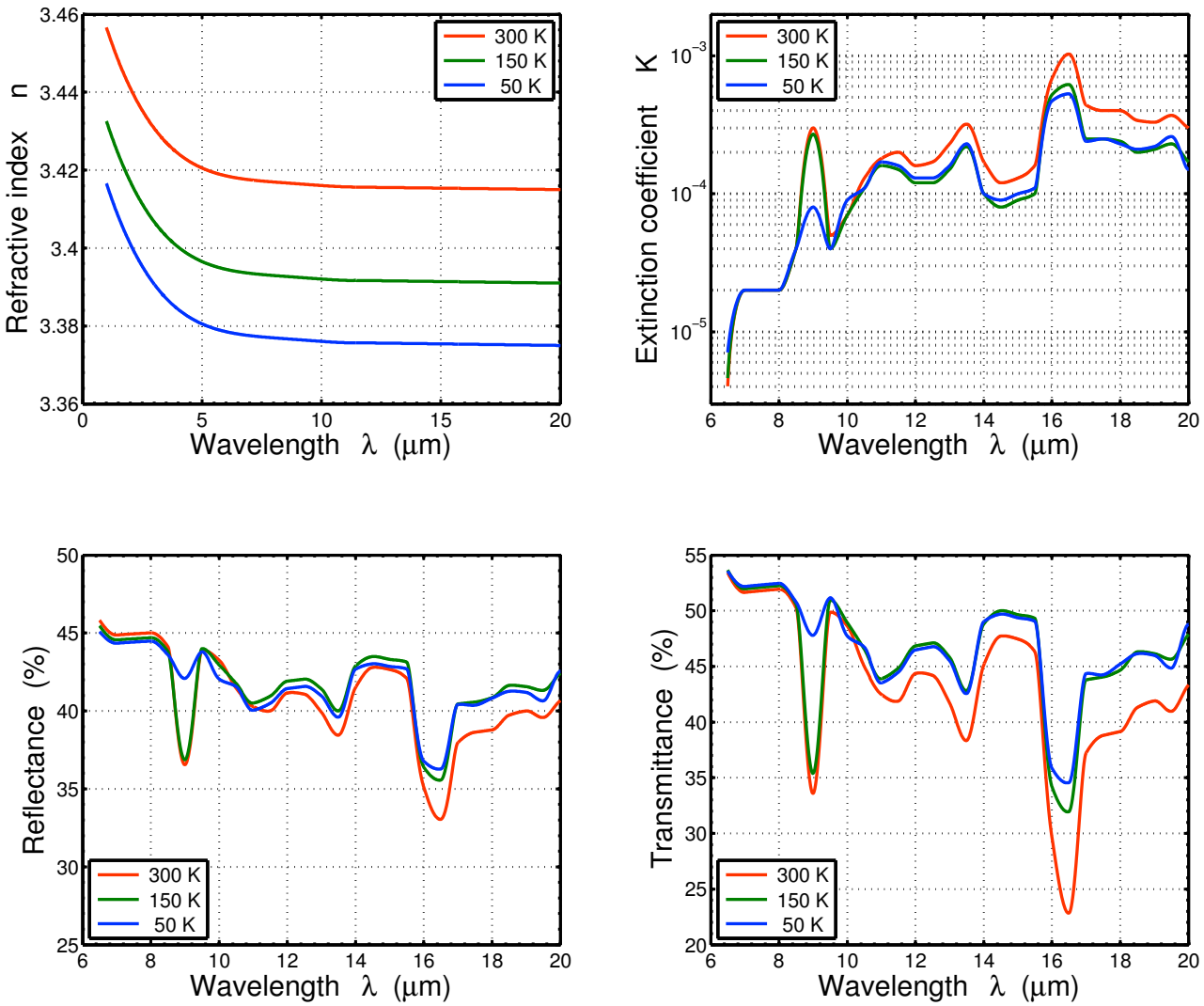

Figure A.3: Silicon optical properties at three different temperatures. Top: refractive index (left) and extinction coefficient (right) dispersions, with data from Hawkins (1998). Bottom: computed total reflectance (left) and transmittance (right) for a 1 mm thick substrate.

Germanium (Ge)

$$n_{\mathrm{Ge}}(\lambda, T) = \sqrt{A + \frac{B\lambda^2}{(\lambda^2 - C)} + \frac{D\lambda^2}{(\lambda^2 - E)}} \tag{A.5}$$

Table A.3: Sellmeier coefficients for germanium temperature-dependent index representation.

Coefficient	Ge
A	$-6.040 \times 10^{-3} T + 11.05128$
B	$9.295 \times 10^{-3} T + 4.00536$
C	$-5.392 \times 10^{-4} T + 0.599034$
D	$4.151 \times 10^{-4} T + 0.09145$
E	$1.51408\, T + 3426.5$

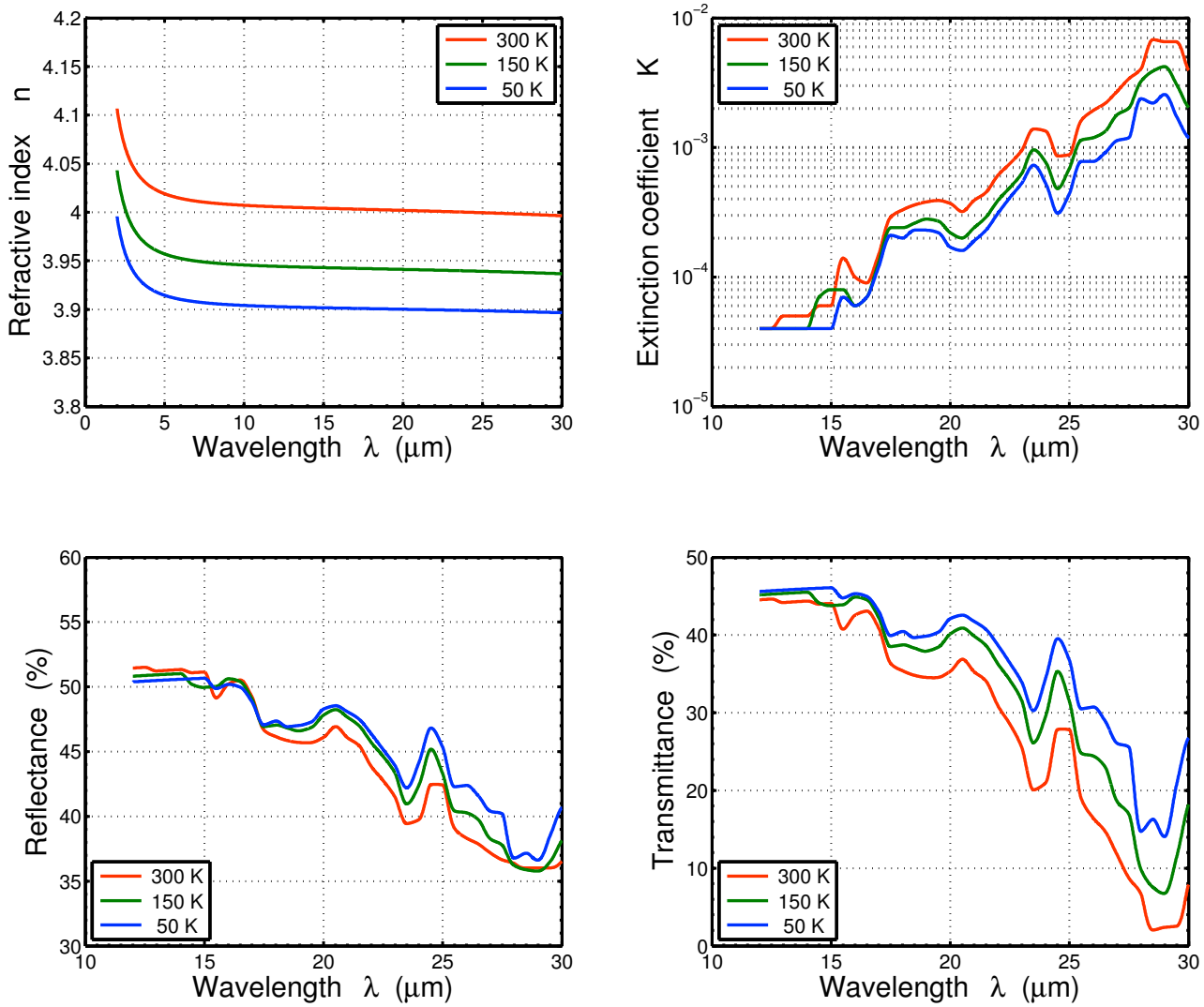

Figure A.4: Germanium optical properties at three different temperatures. Top: refractive index (left) and extinction coefficient (right) dispersions, with data from Hawkins (1998). Bottom: computed total reflectance (left) and transmittance (right) for a 1 mm thick substrate.

Zinc Sulfide (ZnS)

$$n_{\mathrm{ZnS}}(\lambda, T) = A + B\lambda + C\lambda^2 + D\lambda^3 + E\lambda^4 \tag{A.6}$$

Table A.4: Polynomial coefficients for zinc sulfide temperature-dependent index representation.

Coefficient	ZnS
A	$5.608 \times 10^{-5}T + 2.282$
B	$-8.671 \times 10^{-6}T - 1.563 \times 10^{-2}$
C	$5.549 \times 10^{-7}T + 2.067 \times 10^{-3}$
D	$2.597 \times 10^{-8}T - 1.714 \times 10^{-4}$
E	$-9.798 \times 10^{-10}T + 2.884 \times 10^{-6}$

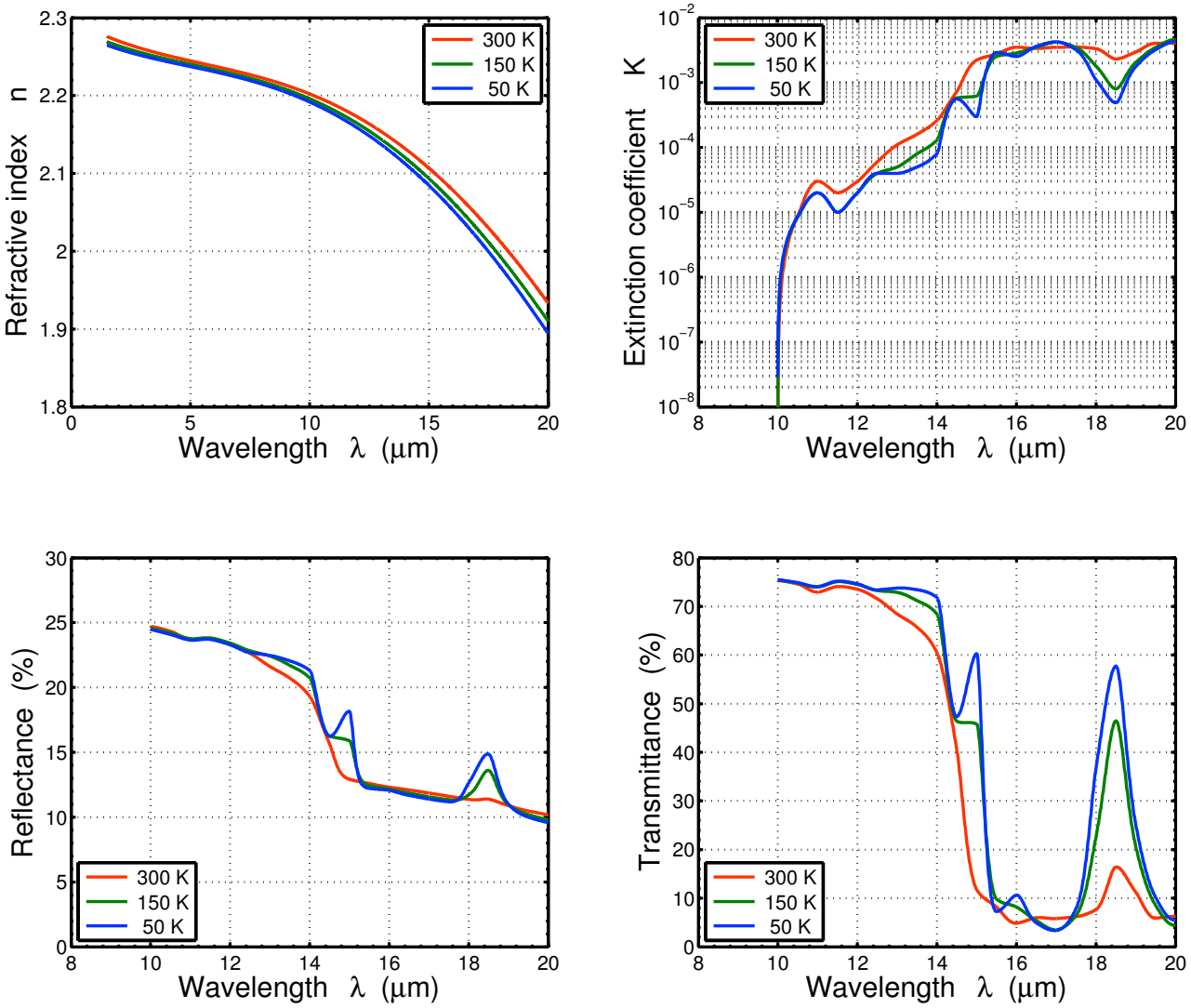

Figure A.5: Zinc sulfide optical properties at three different temperatures. Top: refractive index (left) and extinction coefficient (right) dispersions, with data from Hawkins (1998). Bottom: computed total reflectance (left) and transmittance (right) for a 1 mm thick substrate.

Zinc Selenide ($ZnSe$)

$$n_{\mathrm{ZnSe}}(\lambda, T) = A + B\lambda + C\lambda^2 + D\lambda^3 \tag{A.7}$$

Table A.5: Polynomial coefficients for zinc selenide temperature-dependent index representation.

Coefficient	$ZnSe$
A	$1.509 \times 10^{-4}T + 2.407$
B	$-1.801 \times 10^{-5}T - 2.564 \times 10^{-4}$
C	$1.300 \times 10^{-6}T - 1.308 \times 10^{-5}$
D	$-3.878 \times 10^{-8}T - 1.480 \times 10^{-5}$

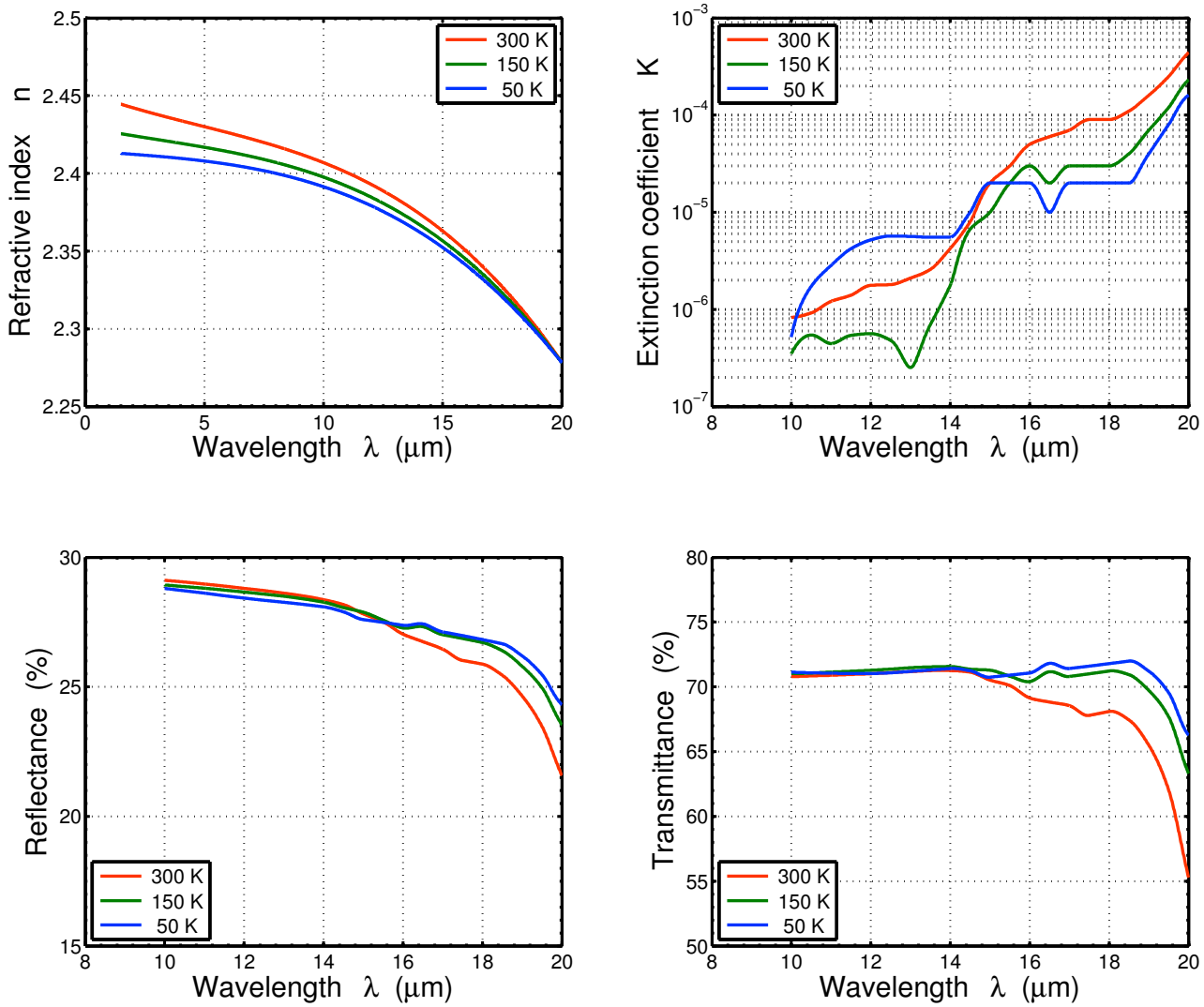

Figure A.6: Zinc selenide optical properties at three different temperatures. Top: refractive index (left) and extinction coefficient (right) dispersions, with data from Hawkins (1998). Bottom: computed total reflectance (left) and transmittance (right) for a 1 mm thick substrate.

B

Study of gravitational lensing inversion

B.1 Publication: The Optimal Gravitational Lens Telescope

In the present appendix, we expose the results of a project we took part in during our master thesis (Delacroix 2007) and the first years of our PhD (Surdej, Claeskens, Delacroix et al. 2008), called the optimal gravitational lens telescope (OGLT). At the end of one lecture, Richard Feynman once asked his students to reflect on a poet who once said: "The whole universe is in a glass of wine." This sentence may also be understood from an optical point of view. The refraction produced by the foot of some glasses of wine is similar to the deflection produced by a point mass gravitational lens.

We present a paper, published in the Astronomical Journal (Surdej, Delacroix, Coleman et al. 2010), that shows how to make use of an ad hoc optical device at the telescope in order to directly invert an observed gravitational lens mirage. Our contribution to this publication was twofold: (i) a laboratory demonstration of the gravitational lens inversion, and (ii) the creation of a software for simulating the same phenomenon. We managed, in the first part of this work, to obtain an Einstein ring, a doubly or a quadruply imaged source in the laboratory, and then to invert the latter ones in order to retrieve the original source image. In the second part, we used the performing language of MATLAB® to develop a gravitational lens simulator from scratch. Our three-dimensional simulations can reproduce the same gravitational mirages as the ones simulated on the laboratory test bench, and the numerical inversion implemented in the software properly restores the original source image. The paper also presents a possible design for the optimal gravitational lens telescope (OGLT) which can directly invert an observed gravitational lens mirage using an ad hoc optical instrument placed at the focus of a large telescope. This concept would first necessitate to extinguish the direct light from the foreground deflector by use of a phase mask coronagraph such as an annular groove phase mask (AGPM).

The Astronomical Journal, 139:1935–1941, 2010 May doi:10.1088/0004-6256/139/5/1935

THE OPTIMAL GRAVITATIONAL LENS TELESCOPE

J. Surdej[1], C. Delacroix[2], P. Coleman[3], M. Dominik[4,9], S. Habraken[2], C. Hanot[1], H. Le Coroller[5], D. Mawet[6], H. Quintana[7], T. Sadibekova[1], and D. Sluse[8]

[1] Department of Astrophysics, Geophysics and Oceanography (AGO), AEOS Group, Liège University, Allée du 6 Août 17, 4000 Liège, Belgium; surdej@astro.ulg.ac.be
[2] Department of Physics (DEPHY), Hololab Group, Liège University, Allée du 6 Août 17, 4000 Liège, Belgium
[3] Institute for Astronomy, University of Hawaii, 2680 Woodlawn Drive, Honolulu, HI 96822, USA
[4] SUPA, University of St Andrews, School of Physics & Astronomy, North Haugh, St Andrews, KY16 9SS, UK
[5] Observatoire de Haute Provence, F-04870 Saint Michel l'Observatoire, France
[6] Jet Propulsion Laboratory, California Institute of Technology, 4800 Oak Grove Drive, Pasadena, CA 91109, USA
[7] Departmento de Astronomia y Astrofisica, Pontificia Universidad Católica de Chile, Casilla 306, CL 22 Santiago, Chile
[8] Astronomisches Rechen-Institut am Zentrum für Astronomie der Universität Heidelberg, Mönchhofstrasse 12-14, 69120 Heidelberg, Germany
Received 2009 November 30; accepted 2010 March 2; published 2010 April 8

ABSTRACT

Given an observed gravitational lens mirage produced by a foreground deflector (cf. galaxy, quasar, cluster, . . .), it is possible via numerical lens inversion to retrieve the real source image, taking full advantage of the magnifying power of the cosmic lens. This has been achieved in the past for several remarkable gravitational lens systems. Instead, we propose here to invert an observed multiply imaged source directly at the telescope using an ad hoc optical instrument which is described in the present paper. Compared to the previous method, this should allow one to detect fainter source features as well as to use such an optimal gravitational lens telescope to explore even fainter objects located behind and near the lens. Laboratory and numerical experiments illustrate this new approach.

Key words: gravitational lensing: strong – methods: laboratory – quasars: general – techniques: high angular resolution

Online-only material: color figures

1. INTRODUCTION

Zwicky (1937a, 1937b) first proposed to use foreground galaxies as natural telescopes to observe otherwise too distant and faint background objects. The idea was either to take advantage of the gravitational lens amplification of the multiple unresolved images in order to obtain higher signal-to-noise ratio observations of the background object(s) or to directly re-image, with a significantly improved angular resolution, the real extended source from the observed gravitational lens mirage. In the past numerical lens inversions have been successfully applied to several cases among which are the famous radio Einstein ring MG 1131+0456 (Kochanek et al. 1989), the triply imaged giant arc in the galaxy cluster Cl 0024+1654 (Wallington et al. 1995), the radio Einstein ring MG 1654+134 (Wallington et al. 1994, 1996), the optical Einstein ring 0047-2808 (Dye & Warren 2005), the multiply imaged double source B1608+656 (Suyu et al. 2006), and the quadruply imaged quasar RXS J1131−1231 (Claeskens et al. 2006), or still more recently, the large sample of lensed galaxies observed by the SLACS collaboration (Bolton et al. 2008). In the present paper, we show how to make use of an ad hoc optical device at the telescope in order to directly invert an observed gravitational lens mirage.

First of all, in Section 2 we lay out the basic principles of gravitational lensing inversion based upon straightforward ray-tracing diagrams. Then in Section 3 we show how to use a point mass lens optical simulator to invert a gravitational lens mirage produced by a point mass deflector. After simulating an Einstein ring, a doubly or a quadruply imaged source in the laboratory, in Section 4 we show how to invert the latter ones in order to retrieve the original source image. In Section 5, we have made use of numerical simulations to confirm the expected properties of this type of hardware inversion. In Section 6, we present a possible design for the optimal gravitational lens telescope and discuss the future prospects of gravitational lensing inversion using more sophisticated optical devices. Some general conclusions form the last section.

2. BASIC PRINCIPLES OF GRAVITATIONAL LENSING INVERSION

In Figure 1 we have illustrated the possible deflection of light rays coming from a very distant source (S) by a foreground cosmic deflector (D, a galaxy here). We have assumed that in the present case, the observer located at left sees three lensed images of the distant source (S).

If one would set three little mirrors at the observer location, each mirror parallel to the incoming wave fronts associated with each of the three beams of parallel light rays, the latter would travel back toward the source along their original trajectories in accordance with the principle of inverse travel of light, assuming of course the case of a static universe. Instead, let us suppose that at the location of the observer we just set a pinhole screen (PS) in order to only let the three incoming beams of parallel light rays continue their travels toward the left. The size of the pinhole is typically that of the telescope aperture used to directly image the cosmic mirages. Furthermore, let us place at a symmetric location with respect to the pinhole a galaxy (D2) similar to the original deflector (D1), but turned around by 180°. We then obtain the ray-tracing diagram depicted in Figure 2.

Let us now assume that we could set the deflector at left (D2) much closer to the pinhole (PS, see Figure 3). The deflector at left is still supposed to be perfectly aligned with the deflector at right (D1) and the pinhole. Let us suppose that the D2 deflector is now three times closer to the pinhole compared with the distance to

[9] Royal Society University Research Fellow.

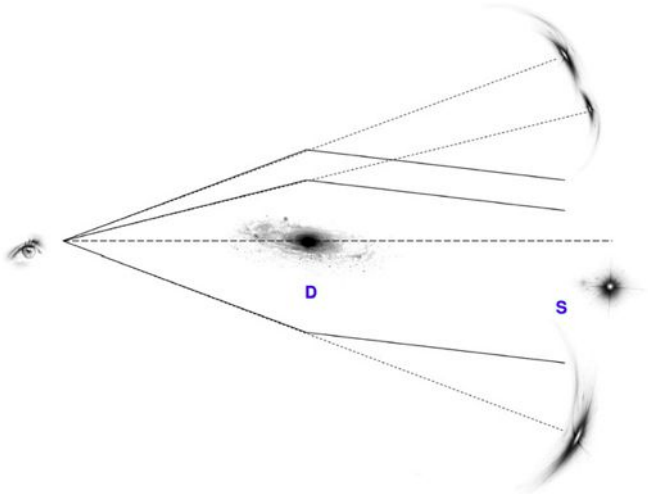

Figure 1. Formation of a three lensed image mirage by gravitational lensing.
(A color version of this figure is available in the online journal.)

the D1 galaxy. In order to preserve the same deflection angles α for the outgoing light rays at left, one simply needs to decrease the mass of the D2 deflector also by a factor of 3, since r has been reduced itself by the same factor, of course keeping the relative mass distribution between D2 and D1 identical. Indeed, for the case of a symmetric mass distribution, we have $\alpha = 4GM(r)c^{-2}\,r^{-1}$, where $M(r)$ represents the mass of the galaxy located within the impact parameter r; G and c being the universal constant of gravitation and the velocity of light (Refsdal & Surdej 1994). If the ratio $M(r)/r$ is kept constant, the deflection angle α remains unaltered.

It is interesting to note that the ray-tracing diagram shown in Figure 3 is very reminiscent of the propagation of light rays through a classical refractor, the main objective (cf. D1) being located at right from the PS and the eyepiece (D2) at left. However, let us note a big difference: in the present case, it is as if the main objective were diluted since only three (and not an infinity of) beams of parallel light rays propagate through such a gravitational lens refractor. Furthermore, these beams reaching the PS (or the observer) are mutually incoherent.

For convenience and simplicity, we shall consider in the remainder that the deflector is a point mass lens. In this case, the corresponding gravitational lens refractor is similar to that in Figure 3 with the exception that, in general, only two beams of parallel light rays go through the PS (see Figure 4). Indeed, due to the singularity of this type of lens, the third "central image" is simply being suppressed (Refsdal & Surdej 1994). If we were now capable of setting the point mass lens object (P2) at left at a still much closer distance from the pinhole (PS), also accordingly decreasing its mass, the separation between the two outgoing parallel beams of light rays at left would get similarly smaller. Let us assume that this separation gets so small that it matches the size of an optical lens.

Could we then replace the point mass lens object P2 by a laboratory lens simulator that would perfectly mimic the light deflection of the former? To our knowledge, Liebes (1969) was the first to propose using an optical lens having the shape of the foot of a wine glass to simulate the light deflection by a point mass lens. The design and construction of such optical lenses corresponding to any type of axially symmetric mass distributions have been presented and discussed by Refsdal & Surdej (1994). These authors have also described how to use such lenses to produce the various configurations of cosmic mirages observed in the universe.

3. THE POINT MASS LENS OPTICAL SIMULATOR AND INVERSION OF A GRAVITATIONAL LENS MIRAGE

Figure 5 illustrates (a) the typical shape of the foot of a wine glass and (b) a corresponding simulator made of Plexiglas which has been used to simulate the light deflection of a point mass

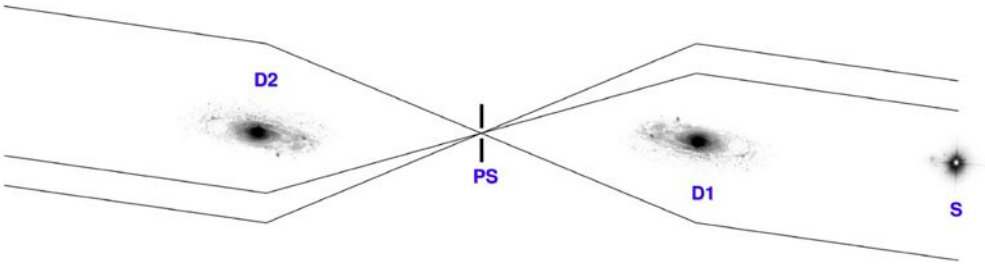

Figure 2. This figure results from the superposition of the ray-tracing diagram shown in Figure 1 and a copy of it, rotated by 180°. In this way, we clearly see that the light rays passing through the pinhole screen (PS) get similarly deflected, but in an opposite direction, to those coming from the distant source (S). The three beams of light rays passing the second, inverted, deflecting galaxy (D2), thus continue their travel as three parallel beams of light rays.
(A color version of this figure is available in the online journal.)

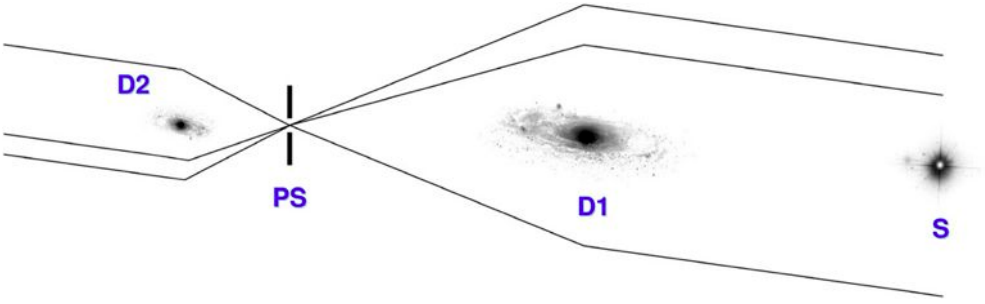

Figure 3. Same as in Figure 2 but for the case of a deflector (D2) at left being located at a distance three times closer to the pinhole screen (PS) and being also three times less massive than the original deflector (D1).
(A color version of this figure is available in the online journal.)

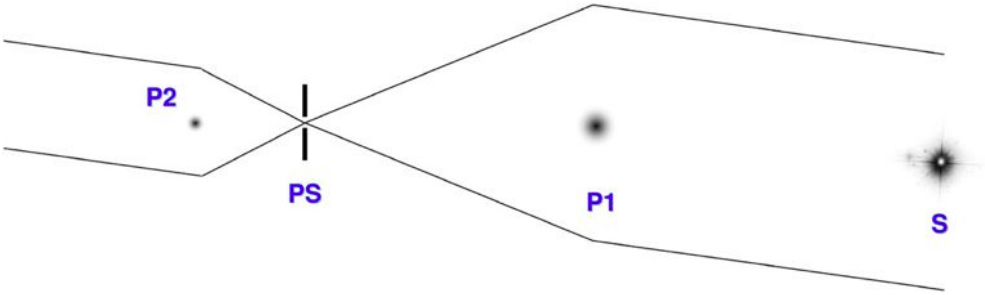

Figure 4. Two lensed image mirage produced by a cosmic point mass lens (P1) at right. The two incoming beams of parallel light rays pass through the pinhole screen (PS) and get deflected by a point mass lens object (P2) at left, at a distance three times closer from the pinhole and which mass is also three times smaller than that of the original cosmic point mass lens (P1). As with the case discussed in Figure 3, the outgoing light rays are again parallel.

(A color version of this figure is available in the online journal.)

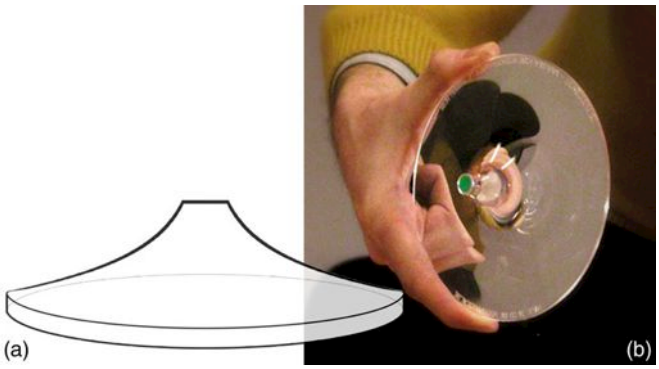

Figure 5. Shape (a) and photograph (b) of an optical lens simulator corresponding to the case of a point mass lens. Such a lens is made of Plexiglas and its shape, similar to that of the foot of a wine glass, is essentially determined by the mass of the point mass deflector (Refsdal & Surdej 1994). For the lens shown on the photograph, the corresponding mass is approximately 2/3 the mass of the Earth.

(A color version of this figure is available in the online journal.)

lens having approximately 2/3 the mass of the Earth when set at a distance of 1 m from an observer's eye.

In Figure 4 we may now conveniently replace the small size cosmic point mass lens (P2) at left by an optical point mass gravitational lens simulator (S2) characterized by the same mass (see Figure 6).

Still further at left, we set a converging lens (CL) so that a perfect image of the distant source (S) is formed in its focal plane. The real gain in proceeding so is to observe the recombined image of the distant source with a significant increase in angular resolution, corresponding to the highest magnification(s) provided by the point mass cosmic lens (P1), at right. A simple laboratory experiment illustrating these principles is proposed in the next section.

4. THE LABORATORY GRAVITATIONAL LENS EXPERIMENT FOR THE CASE OF A POINT MASS LENS

For purely didactical purposes, the Faculty of Sciences from the Liège University has proceeded to the manufacturing of a large series of optical gravitational

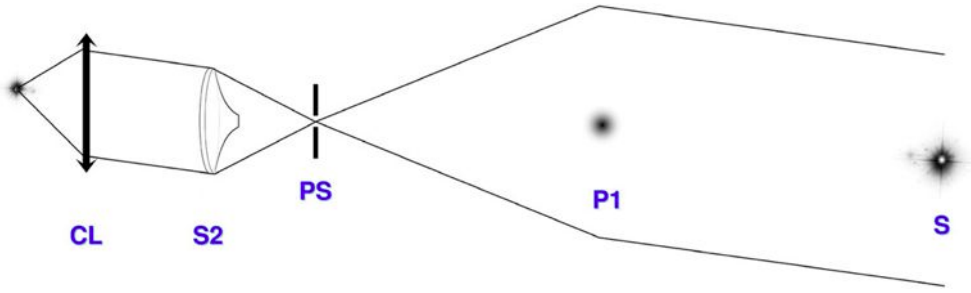

Figure 6. Same as Figure 4 but the small size cosmic lens at left (P2) has been replaced by an optical point mass lens simulator (S2) corresponding to the same mass. Since the separation between the two outgoing parallel beams of light rays is now reduced to several tens of centimeters, or even smaller, it is easy to place at left a classical converging lens (CL) so that a perfect, lens inverted, image of the distant source at right (S) is formed in its focal plane.

(A color version of this figure is available in the online journal.)

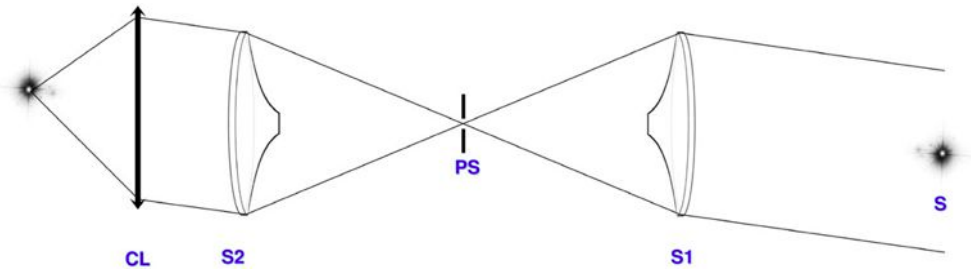

Figure 7. First point mass gravitational lens simulator (S1) at right produces a doubly imaged source as seen from the pinhole (PS), while the second lens simulator (S2) inverts the mirage into two parallel beams of light rays which are then focused at left by a classical converging lens (CL).

(A color version of this figure is available in the online journal.)

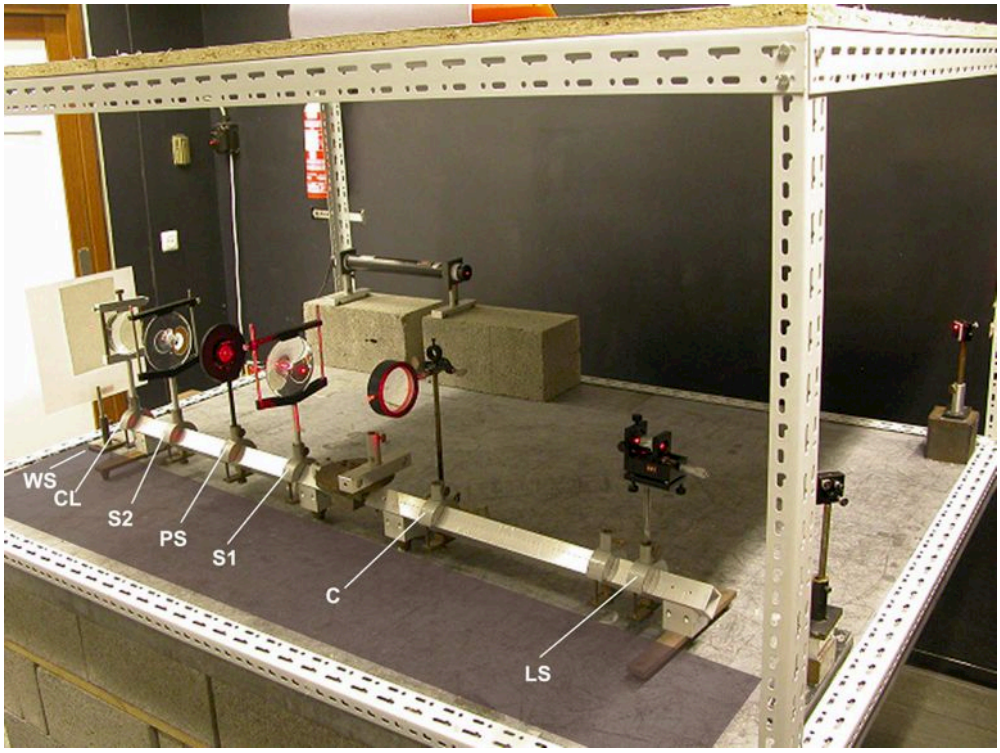

Figure 8. Optical bench in the laboratory showing from right to left the laser point source (LS) obtained with a spatial filter (microscope objective combined with a pinhole screen), followed by a lens (C) that collimates the light rays into a parallel beam which enters the first point mass gravitational lens simulator (S1). Some of the deflected rays then encounter the pinhole screen (PS) and enter the second optical lens simulator (S2). The outgoing light rays are finally focused by means of a converging lens (CL) on the white screen (WS) set at the extreme left.

(A color version of this figure is available in the online journal.)

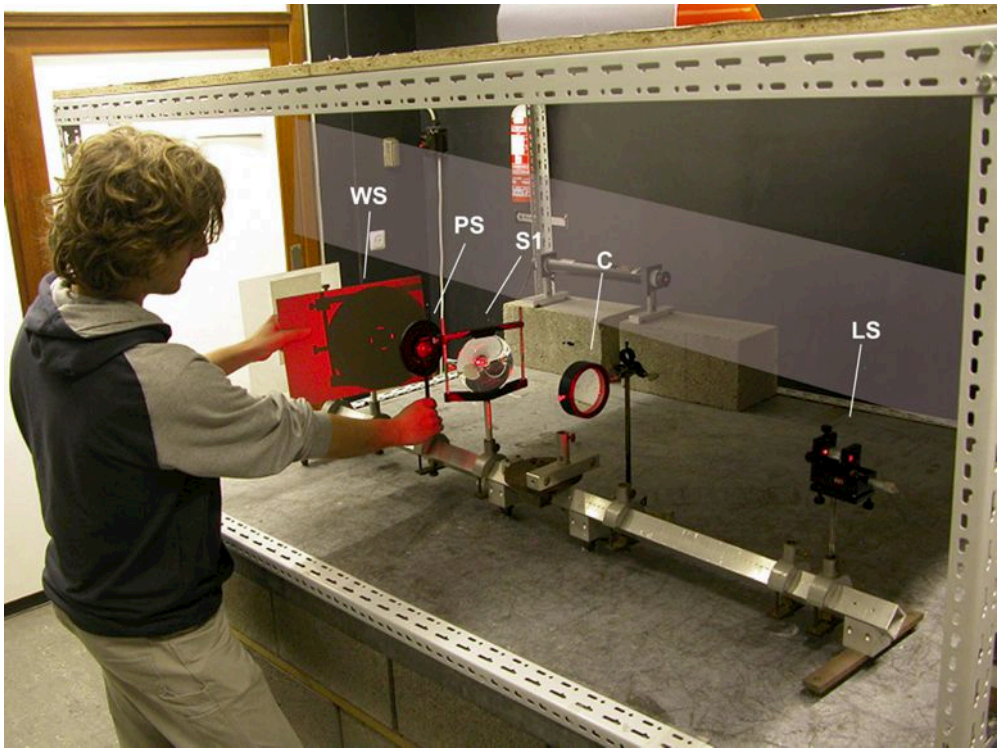

Figure 9. Another view of the laboratory optical bench (see also Figure 8). In this case, the first point mass gravitational lens simulator (S1) has been somewhat tilted with respect to the axis of the optical bench. By placing a white screen (WS) just behind the pinhole screen (PS), one sees the formation of a quadruply imaged source, in accordance with the predictions made for the case of a point mass lens in presence of an external shear (Refsdal & Surdej 1994).

(A color version of this figure is available in the online journal.)

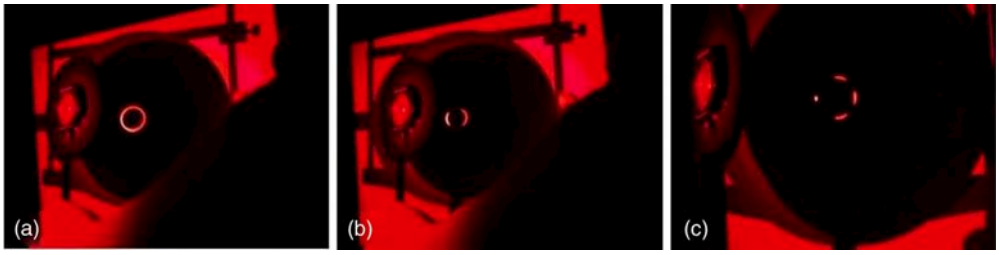

Figure 10. In the case of perfect alignment between the source (LS), the pinhole (PS), and the optical lens (S1), set perpendicularly with respect to the axis of the optical bench, the formation of an Einstein ring results (a) as seen on the white screen (WS) set between the pinhole (PS) and the S2 lens (cf. Figure 9). If we slightly translate the S1 lens, along a direction transverse to the axis of the optical bench, the Einstein ring breaks in two lensed images (b). If instead we slightly tilt the S1 lens with respect to the axis of the optical bench, the Einstein ring breaks into four lensed images (c) (Refsdal & Surdej 1994).

(A color version of this figure is available in the online journal.)

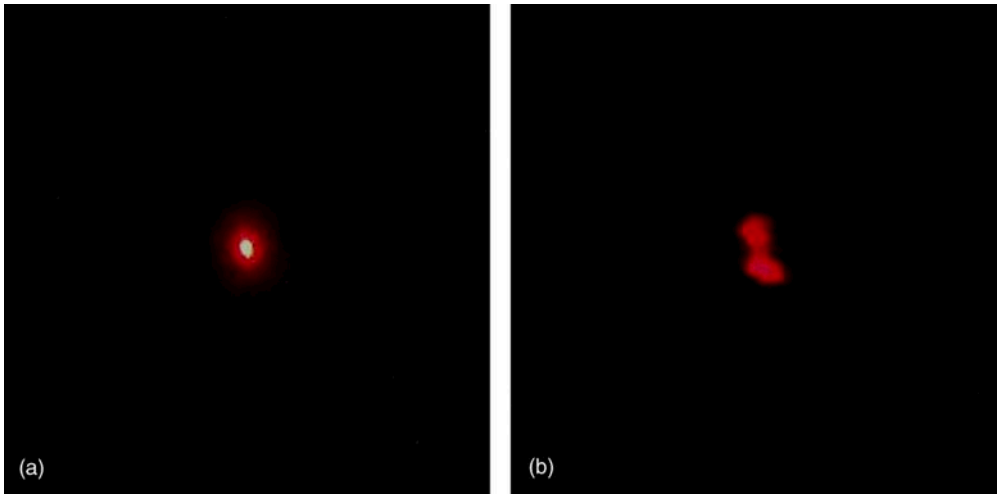

Figure 11. Inverted lensed images of the laser source on the white screen (WS) placed at the extreme left in Figure 8, for the case of a single (a) point-like source image S and that of a double one (b). The double source was obtained by means of a beam splitter. The diameter of the spot(s) seen in (a) and (b) is approximately 2 mm. In these two cases, the S1 and S2 lenses were set perpendicularly to the optical bench axis, slightly translated in opposite transverse directions and symmetrically placed with respect to the pinhole (PS).

(A color version of this figure is available in the online journal.)

lens simulators like the one shown in Figure 5(b) (see http://www2.ulg.ac.be/sciences/lentille/dp-lentilleweb.pdf). In order to illustrate the principles exposed in the previous section, we have thus decided to use two such optical lenses in the laboratory: one (S1) to produce a mirage and the second one (S2) to invert the resulting lensed images. The corresponding ray-tracing diagram is shown in Figure 7, while the laboratory experiment is shown in Figures 8 and 9.

Various experiments have been carried out in the laboratory, by tilting (or not) and/or translating (or not) with respect to each other the two optical point mass gravitational lens simulators S1 and S2, also for the case of a double point-like laser source image S. We have illustrated in Figure 10 some of the resulting lensed images seen on the intermediate white screen (WS) placed between the PS and the S2 lens (cf. Figure 9). Finally, always keeping the S1 and S2 lenses parallel to each other and symmetrically placed with respect to the pinhole, we have observed the images formed on the WS placed at the extreme left position on the optical bench for various configurations as shown in Figure 8. In all cases, we either observe (see Figure 11) the formation of a single point-like image or that of a double one, in case the original source (LS) consisted of a double point-like laser source. We have thus succeeded in inverting the multiple lensed images produced by the S1 point mass lens simulator into the original, single or double, laser source image.

5. NUMERICAL SIMULATIONS

Matlab software applications have been developed to simulate the propagation of light rays through two optical point mass lens simulators like those used in the laboratory. The ray tracings have been performed considering the refractive properties of the optical simulators (shapes, refractive index $n = 1.49$, etc.). Numerical two-dimensional and three-dimensional simulations have been carried out for various tilts and translations of the S1 and S2 simulators, and also for different sizes of these lenses and their positions with respect to the pinhole. Typical examples of such simulations are illustrated in Figures 12 and 13. Such simulations have been carried out for various source positions as well as for the case of multiple point-like sources. In all cases, the inversions by the optical gravitational lens simulator S2 of the mirages produced by the simulator S1 have properly restored in the focal plane of the CL, the original source images.

6. THE OPTIMAL GRAVITATIONAL LENS TELESCOPE: DESIGN AND FUTURE PROSPECTS

We propose to directly invert an observed gravitational lens mirage using an ad hoc optical instrument placed at the focus of a large telescope as follows. The idea is first to extinguish the direct light from the foreground deflector which might be a galaxy, a star, a quasar, etc. as much as possible. To do so, we center the light of the deflector on the mask of a coronagraphic

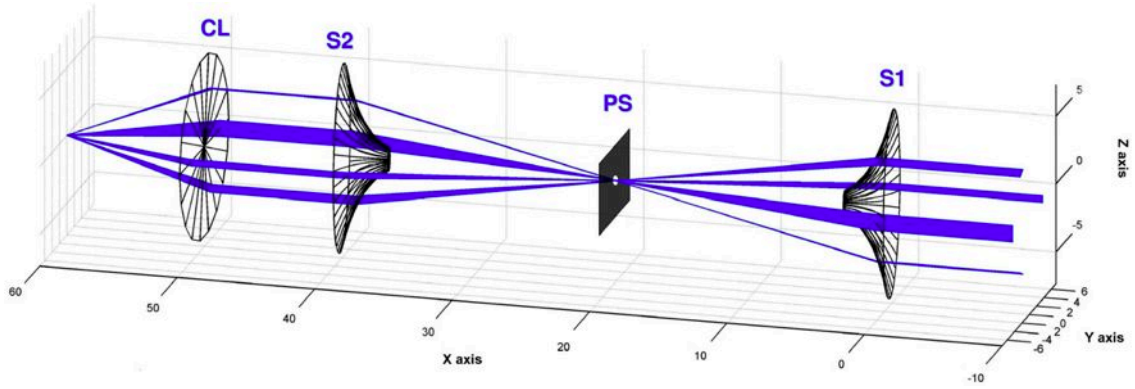

Figure 12. Three-dimensional ray-tracing simulations performed with the Matlab software for the case of two similar optical point mass lens simulators (S1 and S2) which centers have been properly aligned with the pinhole (PS). The two simulators have been kept parallel to each other but slightly tilted (10°) with respect to the axis of the optical bench.

(A color version of this figure is available in the online journal.)

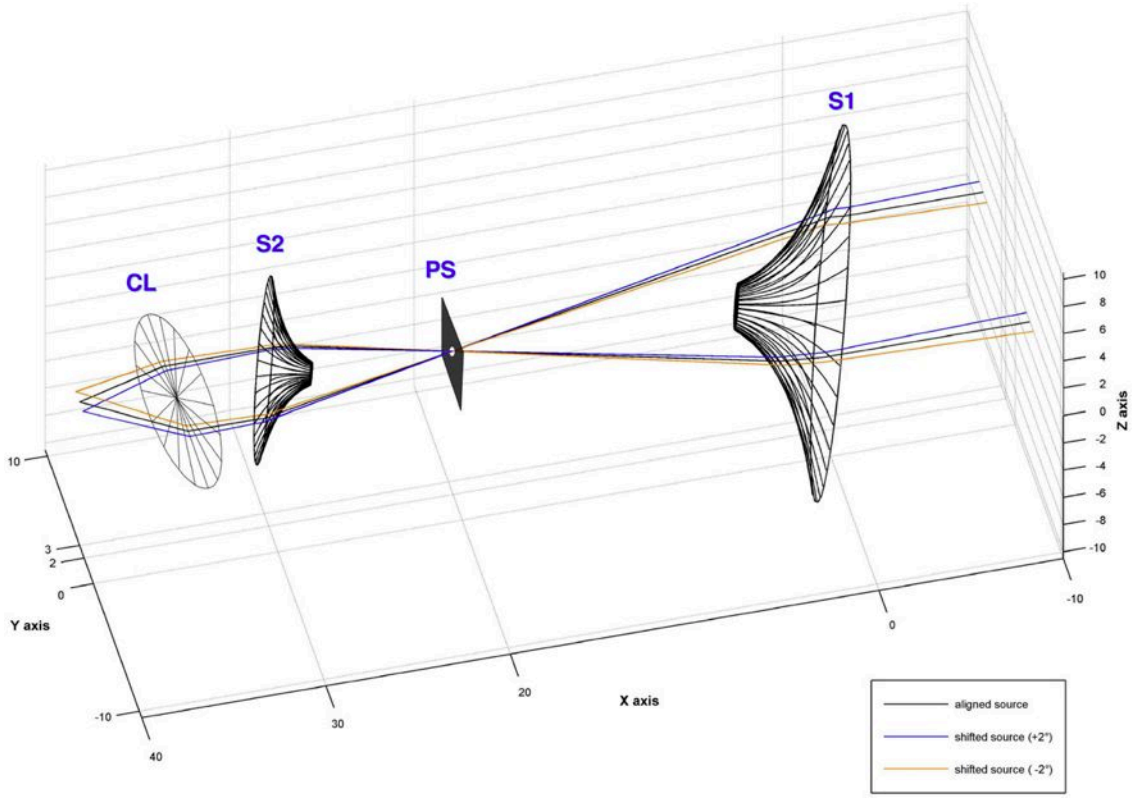

Figure 13. Another example of three-dimensional ray-tracing simulations performed with the Matlab software for the case of the two optical point mass lens simulators (S1 and S2) whose centers have been properly aligned with the pinhole (PS). The two simulators have been kept parallel to each other but slightly tilted (20°) and translated along a transverse direction with respect to the axis of the optical bench. Note that one of the lenses (S2) is half as massive as the other one (S1) and placed at half the distance with respect to the pinhole in order to provide an overall optimal gravitational lens telescope.

(A color version of this figure is available in the online journal.)

device. The mask could be either a classical Lyot one if the foreground deflector is resolved or a phase mask like an annular groove phase mask in case the deflector is point-like (Mawet et al. 2005); see Figure 14. Just behind, a lens (C) collimates the light rays from the observed mirage (a doubly imaged point-like source for the case shown in Figure 14) and forms an exit pupil of the telescope aperture where a Lyot stop is placed. The optical point mass lens simulator (S2), or another ad hoc optical device adapted to the specific mass distribution of the lens, then inverts the mirage and produces two (or more) parallel beams of light rays. Finally, a classical CL produces in its focal plane a single image of the multiply imaged distant source. This is a possible design for the optimal gravitational lens telescope which ideally restores in its focal plane a single real and faithful image from the direct imaging of a multiply imaged source.

As can be seen in Figure 14, only very small regions of the lens simulator (S2 in the present case) are actually involved in the lens inversion process. One could therefore think of possibly replacing this lens simulator by a computer-generated holographic lens or even a deformable mirror such that the entropy of the recombined image in the focal plane of the CL gets minimized. Conversely, one could use the lens model inferred from the numerical lens inversion of a known gravitational lens system to design the corresponding optical lens inversion

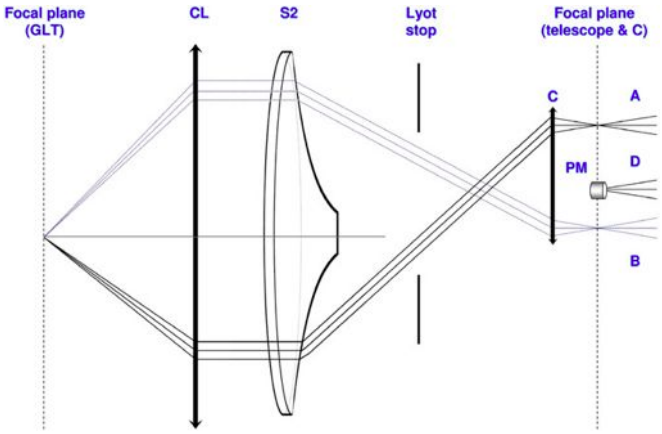

Figure 14. Simple unfolded model of the optimal gravitational lens telescope. It is here assumed that the astronomical telescope pointed toward a gravitational lens system produces in its focal plane at right two lensed images (A and B) of a distant source as well as the image of the deflector (D). The latter has been centered on the Lyot or phase mask (PM) of the coronagraphic device shown in this figure. The lens C collimates the light, forming also an exit pupil where a Lyot stop is placed. The optical point mass lens simulator S2 then inverts the observed gravitational lens mirage into two parallel beams of light rays which are then focused at left by a classical converging lens (CL). A single image of the original source, originally observed as a multiple imaged object, has thus been restored in the focal plane of CL.

(A color version of this figure is available in the online journal.)

simulator. Direct imaging of the gravitational lens mirage with such an optical device would then permit the direct observation of the original source image as well as to possibly detect still much fainter objects located behind and near the foreground deflector. Compared to the numerical inversion method, the sensitivity should be higher since the light from the source is now concentrated on a smaller number of pixels compared to the spread of the multiple images over a larger number of pixels. This is especially true whenever the noise in the faint lensed images is dominated by the CCD read-out-noise. Moreover, the coronagraphic device removes the light from the deflector that would otherwise be spread over the detector. As far as the final angular resolution is concerned, we should select a pixel size and/or adapt the focal length of the CL lens (see Figure 14) in such a way that the most magnified image of the source is not undersampled.

For the particular case of nearby stars, assuming that their mass and distance are precisely known, one could directly design optical lens simulators like those shown in Figure 5 and search for very faint and distant background objects located behind and near these stellar cosmic lenses. Note that some of the cosmological lenses may turn out to have a complex structure. For these, the corresponding optical lens inversion simulators ought to be more sophisticated.

Many other applications might be envisaged.

7. CONCLUSIONS

In the present paper we have shown how Zwicky's proposition (Zwicky 1937a, 1937b) to use foreground deflectors as giant cosmic lenses could be directly achieved at the telescope, using a phase mask coronagraph equipped with an ad hoc optical lens simulator in order to invert in real time an observed gravitational lens mirage into its real source image. The resulting optimal gravitational lens telescope is thus simply composed of the cosmic gravitational lens producing the observed cosmic mirage, the observer's telescope, and a coronagraphic lens inversion instrument placed at its focus. Based upon the gravitational lens modeling of known resolved mirages, it should be straightforward to design the corresponding optical lens simulators associated with the mass distribution of the corresponding deflectors in order to directly invert the former ones at the telescope. The use of such ad hoc instruments should allow one to directly re-image the real source at much fainter levels as well as to detect even fainter background objects located behind and near the foreground deflector(s). We have the aim to design and test such an instrument in the near future for the case of the well-resolved quintuply imaged quasar SDSS J1004+4112 at $z = 1.734$ produced by a foreground cluster at $z = 0.68$ (Inada et al. 2003; Liesenborgs et al. 2009). We also intend to test the use of deformable mirrors as well as computer generated holograms in order to properly restore in the focal plane of the optimal gravitational lens telescope the real image source(s) of observed gravitational lens mirages.

The authors wish to dedicate the present work to the memory of Prof. Sjur Refsdal (1935–2009) who has been a pioneer in the field of gravitational lensing theory. Sjur Refsdal has also been a very keen friend and collaborator. The authors from the Liège University acknowledge support from the Communauté française de Belgique—Actions de recherche concertées—Académie Universitaire Wallonie-Europe and thank the Faculty of Sciences (Liège University), in particular Prof. J.-M. Bouquegneau, for making a mass production of gravitational lens simulators possible. D.S. acknowledges the support of a Humboldt Fellowship and H.Q. acknowledges partial support from the Belgian F.R.S.-FNRS during his sabbatical stay in the Liège University and the FONDAP Centro de Astrofisica.

REFERENCES

Bolton, A. S., Treu, T., Koopmans, L. V. E., Gavazzi, R., Moustakas, L. A., Burles, S., Schlegel, D. J., & Wayth, R. 2008, ApJ, 684, 248
Claeskens, J., Sluse, D., Riaud, P., & Surdej, J. 2006, A&A, 451, 865
Dye, S., & Warren, S. J. 2005, ApJ, 623, 31
Inada, N., et al. 2003, Nature, 426, 810
Kochanek, C. S., Blandford, R. D., Lawrence, C. R., & Narayan, R. 1989, MNRAS, 238, 43
Liebes, F. 1969, Am. J. Phys., 37, 103
Liesenborgs, J., de Rijcke, S., Dejonghe, H., & Bekaert, P. 2009, MNRAS, 397, 341
Mawet, D., Riaud, P., Absil, O., & Surdej, J. 2005, ApJ, 633, 1191
Refsdal, S., & Surdej, J. 1994, Rep. Prog. Phys., 57, 117
Suyu, S. H., Marshall, P. J., Hobson, M. P., & Blandford, R. D. 2006, MNRAS, 371, 983
Wallington, S., Kochanek, C. S., & Koo, D. C. 1995, ApJ, 441, 58
Wallington, S., Kochanek, C. S., & Narayan, R. 1996, ApJ, 465, 64
Wallington, S., Narayan, R., & Kochanek, C. S. 1994, ApJ, 426, 60
Zwicky, F. 1937a, Phys. Rev., 51, 290
Zwicky, F. 1937b, Phys. Rev., 51, 679

C

List of publications

C.1 Peer-reviewed journals

1. **C. Delacroix**, O. Absil, P. Forsberg, D. Mawet, V. Christiaens, M. Karlsson, A. Boccaletti, P. Baudoz, M. Kuittinen, I. Vartiainen, J. Surdej, and S. Habraken, "Laboratory demonstration of a mid-infrared AGPM vector vortex coronagraph," accepted for publication in *Astronomy and Astrophysics* [Impact factor for 2011, 4.587]

2. D. Mawet, O. Absil, **C. Delacroix**, J. H. Girard, J. Milli, J. O'Neal, P. Baudoz, A. Boccaletti, P. Bourget, V. Christiaens, P. Forsberg, F. Gonte, S. Habraken, C. Hanot, M. Karlsson, M. Kasper, J.-L. Lizon, K. Muzic, R. Olivier, E. Peña, N. Slusarenko, L. E. Tacconi-Garman, and J. Surdej, "L'-band AGPM vector vortex coronagraph's first light on VLT/NACO. Discovery of a late-type companion at two beamwidths from an F0V star," *Astronomy and Astrophysics*, **552**, L13 (2013) [Impact factor for 2011, 4.587]

3. **C. Delacroix**, P. Forsberg, M. Karlsson, D. Mawet, O. Absil, C. Hanot, J. Surdej, and S. Habraken, "Design, manufacturing, and performance analysis of mid-infrared achromatic half-wave plates with diamond subwavelength gratings," *Applied Optics*, **51**, 5897-5902 (2012) [Impact factor for 2011, 1.748]

4. J. Surdej, **C. Delacroix**, P. Coleman, M. Dominik, S. Habraken, C. Hanot, H. Le Coroller, D. Mawet, H. Quintana, T. Sadibekova, and D. Sluse, "The Optimal Gravitational Lens Telescope," *The Astronomical Journal*, **139**, 1935-1941 (2010) [Impact factor for 2011, 4.035]

C.2 Non-peer-reviewed journals and contributions to international conferences

1. D. Mawet, O. Absil, J. H. Girard, J. Milli, J. O'Neal, **C. Delacroix**, P. Baudoz, A. Boccaletti, P. Bourget, V. Christiaens, P. Forsberg, F. Gonté, S. Habraken, C. Hanot, M. Karlsson, M. Kasper, A.-M. Lagrange, J.-L. Lizon, K. Muzic, E. Peña, R. Olivier, N. Slusarenko, L. E. Tacconi-Garman, J. Surdej, "High contrast imaging with the new vortex coronagraph of NACO," submitted for publication in *The Messenger* (2013)

2. **C. Delacroix**, O. Absil, D. Mawet, C. Hanot, M. Karlsson, P. Forsberg, E. Pantin, J. Surdej, and S. Habraken, "A diamond AGPM coronagraph for VISIR," in Proceedings of the Society of Photo-Optical Instrumentation Engineers (SPIE) Conference, Volume 8446, Ground-based and Airborne Instrumentation for Astronomy IV, pp. 84468K, Amsterdam, Netherlands, 1 – 6 July 2012

3. **C. Delacroix**, S. Habraken, M. Karlsson, O. Absil, C. Hanot, J. Surdej, and D. Mawet, "Development of diamond AGPM coronagraphs for VISIR and NACO," presented at the Belgian (exo)-planet meeting, Leuven, Belgium, 22 mars 2012

4. D. Mawet, N. Murakami, **C. Delacroix**, E. Serabyn, O. Absil, N. Baba, J. Baudrand, A. Boccaletti, R. Burruss, R. Chipman, P. Forsberg, S. Habraken, S. Hamaguchi, C. Hanot, A. Ise, M. Karlsson, B. Kern, J. Krist, A. Kuhnert, M. Levine, K. Liewer, S. McClain, S. McEldowney, B. Mennesson, D. Moody, H. Murakami, A. Niessner, J. Nishikawa, N. O'Brien, K. Oka, P. Park, P. Piron, L. Pueyo, P. Riaud, M. Sakamoto, M. Tamura, J. Trauger, D. Shemo, J. Surdej, N. Tabirian, W. Traub, J. Wallace, and K. Yokochi, "Taking the vector vortex coronagraph to the next level for ground- and space-based exoplanet imaging instruments: review of technology developments in the USA, Japan, and Europe," in Proceedings of the Society of Photo-Optical Instrumentation Engineers (SPIE) Conference, Volume 8151, Techniques and Instrumentation for Detection of Exoplanets V, pp. 815108, San Diego, USA, 21 – 25 August 2011

5. **C. Delacroix**, S. Habraken, M. Karlsson, F. Nikolajeff, P. Forsberg, M. Kuittinen, and I. Vartiainen, "Diamond subwavelength gratings for mid-infrared AGPM coronagraph: manufacturing assessment," presented at The third Scientific European Optical Society (EOS) Annual Meeting, Paris, France, 26 – 29 October 2010

6. **C. Delacroix**, P. Forsberg, M. Karlsson, D. Mawet, C. Lenaerts, S. Habraken, O. Absil, C. Hanot, and J. Surdej, "First manufactured diamond AGPM vector vortex for the L- and N-bands: metrology and expected performances," presented at the In the Spirit of Lyot Conference, Paris, France, 25 – 29 October 2010

7. O. Absil, **C. Delacroix**, C. Hanot, D. Mawet, S. Habraken, J. Surdej, and M. Karlsson, "Development of an L-band vector vortex coronagraph for NACO," presented at the In the Spirit of Lyot Conference, Paris, France, 25 – 29 October 2010

8. **C. Delacroix**, P. Forsberg, M. Karlsson, D. Mawet, C. Lenaerts, S. Habraken, C. Hanot, J. Surdej, A. Boccaletti, and J. Baudrand, "Annular groove phase mask coronagraph in diamond for mid-IR wavelengths: manufacturing assessment and performance analysis," in Proceedings of the Society of Photo-Optical Instrumentation Engineers (SPIE) Conference, Volume 7731, Space Telescopes and Instrumentation 2010: Optical, Infrared, and Millimeter Wave, pp. 77314W, San Diego, USA, 27 June – 2 July 2010

9. **C. Delacroix**, D. Mawet, J. Surdej, J. Baudrand, M. Karlsson, C. Lenaerts, and S. Habraken, "Annular Groove Phase Mask coronagraph in diamond for mid-IR wavelengths," presented at the European Interferometry Initiative VLTI training school, Porquerolles Island, France, 17 – 28 April 2010

10. J. Surdej, J.-F. Claeskens, **C. Delacroix**, T. Sadibekova, P. Bartczak, P. H. I. Coleman, A. Magette, J. Poels, D. Ricci, and D. Sluse, "Gravitational Lensing, Dark Matter and the Optical Gravitational Lens Experiment," in Proceedings of the American Institute of Physics Conference, Volume 1038, Hadronic Physics: Joint Meeting Heidelberg-Liège-Paris-Wroclaw, pp. 173-182, Spa, Belgium, 6 – 8 March 2008

11. N. Théret, J.-F. Aubrun, G. Lassalle-Balier, I. Sebbag, N. Descouvemont, and **C. Delacroix**, "Guidance with Avoidance during Maneuver Elaboration (GAME)," in Proceedings of the Advances in the Astronautical Sciences Conference, Volume 129, AAS/AIAA Astrodynamics Conference 2007, pp. 2275-2295, Mackinac Island, USA, 19 – 23 August 2007

Bibliography

Abe, L., Beaulieu, M., Vakili, F. et al., 2007, On-sky observations with an achromatic hybrid phase knife coronagraph in the visible, *Astron. & Astrophys.* **461**, 365–371.

Abe, L., Domiciano de Souza, A., Jr., Vakili, F. & Gay, J., 2003, Phase Knife Coronagraph. II - Laboratory results, *Astron. & Astrophys.* **400**, 385–392.

Abe, L., Murakami, N., Nishikawa, J. & Tamura, M., 2006, Removal of central obscuration and spider arm effects with beam-shaping coronagraphy, *Astron. & Astrophys.* **451**, 363–373.

Abe, L., Vakili, F. & Boccaletti, A., 2001, The achromatic phase knife coronagraph, *Astron. & Astrophys.* **374**, 1161–1168.

Abramowitz, M. & Stegun, I. A., 1972, *Handbook of Mathematical Functions*, Dover Publications, New York.

Absil, O., 2006, *Astrophysical studies of extrasolar planetary systems using infrared interferometric techniques*, Ph.D. thesis, Université de Liège.

Absil, O., Coudé du Foresto, V., Barillot, M. & Swain, M. R., 2007, Nulling interferometry: performance comparison between Antarctica and other ground-based sites, *Astron. & Astrophys.* **475**, 1185–1194.

Absil, O., Delacroix, C., Hanot, C. et al., 2010, Development of an L-band vector vortex coronagraph for NACO, in *In the Spirit of Lyot 2010: Direct Detection of Exoplanets and Circumstellar Disks* (A. Boccaletti, ed.).

Absil, O., den Hartog, R., Gondoin, P. et al., 2006, Performance study of ground-based infrared Bracewell interferometers. Application to the detection of exozodiacal dust disks with GENIE, *Astron. & Astrophys.* **448**, 787–800.

Absil, O., Le Bouquin, J.-B., Berger, J.-P. et al., 2011, Searching for faint companions with VLTI/PIONIER. I. Method and first results, *Astron. & Astrophys.* **535**, A68.

Absil, O. & Mawet, D., 2010, Formation and evolution of planetary systems: the impact of high-angular resolution optical techniques, *A&A Rev.* **18**, 317–382.

Absil, O., Mennesson, B., Le Bouquin, J.-B. et al., 2009, An Interferometric Study of the Fomalhaut Inner Debris Disk. I. Near-Infrared Detection of Hot Dust with VLTI/VINCI, *Astrophysical Journal* **704**, 150–160.

Agol, E., 2007, Rounding up the wanderers: optimizing coronagraphic searches for extrasolar planets, *Mon. Not. of the Royal Astron. Soc.* **374**, 1271–1289.

Aime, C. & Soummer, R., 2004, The Usefulness and Limits of Coronagraphy in the Presence of Pinned Speckles, *Astrophysical Journal, Letters* **612**, L85–L88.

Aime, C., Soummer, R. & Ferrari, A., 2001, Interferometric apodization of rectangular apertures. Application to stellar coronagraphy, *Astron. & Astrophys.* **379**, 697–707.

Aime, C., Soummer, R. & Ferrari, A., 2002, Total coronagraphic extinction of rectangular apertures using linear prolate apodizations, *Astron. & Astrophys.* **389**, 334–344.

Allen, P. R. & Reid, I. N., 2008, Spitzer/irac Search for Companions to Nearby, Young M Dwarfs, *Astronomical Journal* **135**, 2024–2032.

Allouche, F., Glindemann, A., Aristidi, E. & Vakili, F., 2009, APIC. Absolute Position Interfero-Coronagraph for direct exoplanet detection, *Astron. & Astrophys.* **500**, 1277–1280.

Allouche, F., Glindemann, A., Aristidi, E. & Vakili, F., 2010, APIC: Absolute Position Interfero Coronagraph for direct exoplanet detection: first laboratory results, in *Ground-based and Airborne Instrumentation for Astronomy III* (I. S. McLean, S. K. Ramsay & H. Takami, eds.), *Proceedings of the Society of Photo-Optical Instrumentation Engineers (SPIE) Conference Series*, vol. 7735, 773587–14.

Anglada-Escudé, G., Arriagada, P., Vogt, S. S. et al., 2012, A Planetary System around the nearby M Dwarf GJ 667C with At Least One Super-Earth in Its Habitable Zone, *Astrophysical Journal, Letters* **751**, L16.

Apai, D., Janson, M., Moro-Martín, A. et al., 2008, A Survey for Massive Giant Planets in Debris Disks with Evacuated Inner Cavities, *Astrophysical Journal* **672**, 1196–1201.

Azzam, R. M. A. & Spinu, C. L., 2004, Achromatic angle-insensitive infrared quarter-wave retarder based on total internal reflection at the Si-SiO_2 interface, *Journal of the Optical Society of America A* **21**, 2019–2022.

Babcock, H. W., 1953, The Possibility of Compensating Astronomical Seeing, *Publ. of the Astron. Soc. Pac.* **65**, 229.

Baraffe, I., Chabrier, G., Allard, F. & Hauschildt, P. H., 1998, Evolutionary models for solar metallicity low-mass stars: mass-magnitude relationships and color-magnitude diagrams, *Astron. & Astrophys.* **337**, 403–412.

Baraffe, I., Chabrier, G., Barman, T. S. et al., 2003, Evolutionary models for cool brown dwarfs and extrasolar giant planets. The case of HD 209458, *Astron. & Astrophys.* **402**, 701–712.

Barnes, J. W. & O'Brien, D. P., 2002, Stability of Satellites around Close-in Extrasolar Giant Planets, *Astrophysical Journal* **575**, 1087–1093.

Basri, G., Borucki, W. J. & Koch, D., 2005, The Kepler Mission: A wide-field transit search for terrestrial planets, *New A Rev.* **49**, 478–485.

Baudoz, P., Boccaletti, A., Rabbia, Y. & Gay, J., 2005, Stellar Coronagraphy: Study and Test of a Hybrid Interfero-Coronagraph, *Publ. of the Astron. Soc. Pac.* **117**, 1004–1011.

Baudoz, P., Boccaletti, A., Riaud, P. et al., 2004, Cryogenic IR test of the 4QPM coronagraph, in *EAS Publications Series* (C. Aime & R. Soummer, eds.), *EAS Publications Series*, vol. 12, 185–194.

Baudoz, P., Boccaletti, A., Riaud, P. et al., 2006, Feasibility of the Four-Quadrant Phase Mask in the Mid-Infrared on the James Webb Space Telescope, *Publ. of the Astron. Soc. Pac.* **118**, 765–773.

Baudoz, P., Galicher, R., Baudrand, J. & Boccaletti, A., 2008, Theory and laboratory tests of the multi-stage phase mask coronagraph, in *Adaptive Optics Systems* (N. Hubin, C. E. Max & P. L. Wizinowich, eds.), *Proceedings of the Society of Photo-Optical Instrumentation Engineers (SPIE) Conference Series*, vol. 7015, 70156C–9.

Beder, E. C., Bass, C. D. & Shackleford, W. L., 1971, Transmissivity and absorption of fused quartz between 0.22 mu and 3.5 mu from room temperature to 1500 degree C, *Applied Optics* **10**, 2263–2268.

Belikov, R., Give'on, A., Kern, B. et al., 2007, Demonstration of high contrast in 10% broadband light with the shaped pupil coronagraph, in *Techniques and Instrumentation for Detection of Exoplanets III* (D. R. Coulter, ed.), *Proceedings of the Society of Photo-Optical Instrumentation Engineers (SPIE) Conference Series*, vol. 6693, 66930Y–11.

Berry, M. V., 1987, The Adiabatic Phase and Pancharatnam's Phase for Polarized Light, *Journal of Modern Optics* **34**, 1401–1407.

Beuzit, J.-L., Feldt, M., Dohlen, K. et al., 2006, SPHERE: A 'Planet Finder' Instrument for the VLT, *The Messenger* **125**, 29.

Beuzit, J.-L., Feldt, M., Dohlen, K. et al., 2007, SPHERE: A Planet Finder Instrument for the VLT, in *In the Spirit of Bernard Lyot: The Direct Detection of Planets and Circumstellar Disks in the 21st Century* (P. Kalas, ed.).

Beuzit, J.-L., Feldt, M., Dohlen, K. et al., 2008, SPHERE: a 'Planet Finder' instrument for the VLT, in *Ground-based and Airborne Instrumentation for Astronomy II* (I. S. McLean & M. M. Casali, eds.), *Proceedings of the Society of Photo-Optical Instrumentation Engineers (SPIE) Conference Series*, vol. 7014, 701418–12.

Biener, G., Gorodetski, Y., Niv, A. et al., 2006, Manipulation of polarization-dependent multivortices with quasi-periodic subwavelength structures, *Optics Letters* **31**, 1594–1596.

Biller, B. A., Close, L. M., Masciadri, E. et al., 2007, An Imaging Survey for Extrasolar Planets around 45 Close, Young Stars with the Simultaneous Differential Imager at the Very Large Telescope and MMT, *Astrophysical Journal, Suppl.* **173**, 143–165.

Boccaletti, A., Abe, L., Baudrand, J. et al., 2008, Prototyping coronagraphs for exoplanet characterization with SPHERE, in *Adaptive Optics Systems* (N. Hubin, C. E. Max & P. L. Wizinowich, eds.), *Proceedings of the Society of Photo-Optical Instrumentation Engineers (SPIE) Conference Series*, vol. 7015, 70151B–10.

Boccaletti, A., Augereau, J.-C., Lagrange, A.-M. et al., 2012, Morphology of the very inclined debris disk around HD 32297, *Astron. & Astrophys.* **544**, A85.

Boccaletti, A., Riaud, P., Baudoz, P. et al., 2004, The Four-Quadrant Phase Mask Coronagraph. IV. First Light at the Very Large Telescope, *Publ. of the Astron. Soc. Pac.* **116**, 1061–1071.

Boccaletti, A., Riaud, P., Moutou, C. & Labeyrie, A., 2000, Snapshot coronagraphy with an interferometer in space, *Icarus* **145**, 628–636.

Bolton, A. S., Treu, T., Koopmans, L. V. E. et al., 2008, The Sloan Lens ACS Survey. VII. Elliptical Galaxy Scaling Laws from Direct Observational Mass Measurements, *Astrophysical Journal* **684**, 248–259.

Bond, I. A., Udalski, A., Jaroszyński, M. et al., 2004, OGLE 2003-BLG-235/MOA 2003-BLG-53: A Planetary Microlensing Event, *Astrophysical Journal, Letters* **606**, L155–L158.

Bonnefoy, M., Chauvin, G., Rojo, P. et al., 2010, Near-infrared integral-field spectra of the planet/brown dwarf companion AB Pictoris b, *Astron. & Astrophys.* **512**, A52.

Bonnefoy, M., Lagrange, A.-M., Boccaletti, A. et al., 2011, High angular resolution detection of β Pictoris b at 2.18 μm, *Astron. & Astrophys.* **528**, L15.

Bordé, P. J., Traub, W. A., Kern, B. D. et al., 2006, Speckle nulling for exoplanet detection with space-based coronagraphic telescopes, in *Space Telescopes and Instrumentation I: Optical, Infrared, and Millimeter* (J. C. Mather, H. A. MacEwen & M. W. M. de Graauw, eds.), *Proceedings of the Society of Photo-Optical Instrumentation Engineers (SPIE) Conference Series*, vol. 6265, 62651C.

Born, M. & Wolf, E., 1999, *Principles of Optics*, 7 edn., Cambridge University Press, Cambridge.

Borra, E. F., 2001, Astronomical Research with Liquid Mirror Telescopes, *ArXiv Astrophysics e-prints* .

Borucki, W. J., Agol, E., Fressin, F. et al., 2013, Kepler-62: A five-planet system with planets of 1.4 and 1.6 earth radii in the habitable zone, *Science* accepted for publication.

Borucki, W. J., Koch, D., Basri, G. et al., 2010, Kepler Planet-Detection Mission: Introduction and First Results, *Science* **327**, 977–.

Borucki, W. J., Koch, D. G., Basri, G. et al., 2011, Characteristics of Planetary Candidates Observed by Kepler. II. Analysis of the First Four Months of Data, *Astrophysical Journal* **736**, 19.

Borucki, W. J., Koch, D. G., Batalha, N. et al., 2012, Kepler-22b: A 2.4 Earth-radius Planet in the Habitable Zone of a Sun-like Star, *Astrophysical Journal* **745**, 120.

Boss, A. P., 2002, Stellar Metallicity and the Formation of Extrasolar Gas Giant Planets, *Astrophysical Journal, Letters* **567**, L149–L153.

Bouchez, A. H., Dekany, R. G., Roberts, J. E. et al., 2010, Status of the PALM-3000 high-order adaptive optics system, in *Adaptive Optics Systems II* (B. L. Ellerbroek, M. Hart, N. Hubin & P. L. Wizinowich, eds.), *Proceedings of the Society of Photo-Optical Instrumentation Engineers (SPIE) Conference Series*, vol. 7736, 77361Q–7.

Brandl, B., Blommaert, J., Glasse, A. et al., 2010a, METIS: A Mid-infrared E-ELT Imager and Spectrograph, *The Messenger* **140**, 30–31.

Brandl, B. R., Lenzen, R., Pantin, E. et al., 2008, METIS: the mid-infrared E-ELT imager and spectrograph, in *Ground-based and Airborne Instrumentation for Astronomy II* (I. S. McLean & M. M. Casali, eds.), *Proceedings of the Society of Photo-Optical Instrumentation Engineers (SPIE) Conference Series*, vol. 7014, 70141N–15.

Brandl, B. R., Lenzen, R., Pantin, E. et al., 2010b, Instrument concept and science case for the mid-IR E-ELT imager and spectrograph METIS, in *Ground-based and Airborne Instrumentation for Astronomy III* (I. S. McLean, S. K. Ramsay & H. Takami, eds.), *Proceedings of the Society of Photo-Optical Instrumentation Engineers (SPIE) Conference Series*, vol. 7735, 77352G–16.

Brown, T. M., Libbrecht, K. G. & Charbonneau, D., 2002, A Search for CO Absorption in the Transmission Spectrum of HD 209458b, *Publ. of the Astron. Soc. Pac.* **114**, 826–832.

Brundrett, D. L., Glytsis, E. N. & Gaylord, T. K., 1994, Homogeneous layer models for high-spatial-frequency dielectric surface-relief gratings: conical diffraction and antireflection designs, *Applied Optics* **33**, 2695–2706.

Bundy, F. P., 1962, Melting Point of Graphite at High Pressure: Heat of Fusion, *Science* **137**, 1055–1057.

Burke, C. J., 2013, Announcing 461 New Kepler Planet Candidates, in *Exoplanets Coming & Going Everywhere, the first AAS press conference*, *Proceedings of the American Astronomical Society Meeting*, vol. 221, in press.

Burke, D., Gladysz, S., Roberts, L. et al., 2009, An Improved Technique for the Photometry and Astrometry of Faint Companions, *Publ. of the Astron. Soc. Pac.* **121**, 767–777.

Burrows, A., Marley, M., Hubbard, W. B. et al., 1997, A Nongray Theory of Extrasolar Giant Planets and Brown Dwarfs, *Astrophysical Journal* **491**, 856.

Burrows, A., Sudarsky, D. & Hubeny, I., 2004, Spectra and Diagnostics for the Direct Detection of Wide-Separation Extrasolar Giant Planets, *Astrophysical Journal* **609**, 407–416.

Cady, E., Macintosh, B., Kasdin, N. J. & Soummer, R., 2009, Shaped Pupil Design for the Gemini Planet Imager, *Astrophysical Journal* **698**, 938–943.

Cameron, P. B., Britton, M. C. & Kulkarni, S. R., 2009, Precision Astrometry With Adaptive Optics, *Astronomical Journal* **137**, 83–93.

Carlotti, A., Ricort, G. & Aime, C., 2009, Phase mask coronagraphy using a Mach-Zehnder interferometer, *Astron. & Astrophys.* **504**, 663–671.

Carson, J., Thalmann, C., Janson, M. et al., 2013, Direct Imaging Discovery of a "Super-Jupiter" around the Late B-type Star κ And, *Astrophysical Journal, Letters* **763**, L32.

Cash, W., 2006, Detection of Earth-like planets around nearby stars using a petal-shaped occulter, *Nature* **442**, 51–53.

Cassan, A., Kubas, D., Beaulieu, J.-P. et al., 2012, One or more bound planets per Milky Way star from microlensing observations, *Nature* **481**, 167–169.

Cavarroc, C., Boccaletti, A., Baudoz, P. et al., 2006, Fundamental limitations on Earth-like planet detection with extremely large telescopes, *Astron. & Astrophys.* **447**, 397–403.

Cavarroc, C., Boccaletti, A., Baudoz, P. et al., 2008, Target Acquisition for MIRI Coronagraphs, *Publ. of the Astron. Soc. Pac.* **120**, 1016–1027.

Charbonneau, D., Berta, Z. K., Irwin, J. et al., 2009, A super-Earth transiting a nearby low-mass star, *Nature* **462**, 891–894.

Charbonneau, D., Brown, T. M., Noyes, R. W. & Gilliland, R. L., 2002, Detection of an Extrasolar Planet Atmosphere, *Astrophysical Journal* **568**, 377–384.

Charbonneau, D., Knutson, H. A., Barman, T. et al., 2008, The Broadband Infrared Emission Spectrum of the Exoplanet HD 189733b, *Astrophysical Journal* **686**, 1341–1348.

Chauvin, G., Lagrange, A.-M., Bonavita, M. et al., 2010, Deep imaging survey of young, nearby austral stars . VLT/NACO near-infrared Lyot-coronographic observations, *Astron. & Astrophys.* **509**, A52.

Chauvin, G., Lagrange, A.-M., Dumas, C. et al., 2004, A giant planet candidate near a young brown dwarf. Direct VLT/NACO observations using IR wavefront sensing, *Astron. & Astrophys.* **425**, L29–L32.

Chauvin, G., Lagrange, A.-M., Udry, S. et al., 2006, Probing long-period companions to planetary hosts. VLT and CFHT near infrared coronographic imaging surveys, *Astron. & Astrophys.* **456**, 1165–1172.

Chauvin, G., Lagrange, A.-M., Zuckerman, B. et al., 2005, A companion to AB Pic at the planet/brown dwarf boundary, *Astron. & Astrophys.* **438**, L29–L32.

Claeskens, J. F., Crampton, D., Filippenko, A. V. et al., 1993, Search for gravitational lenses in a large sample of highly luminous quasars and statistical determination of cosmological parameters, in *Liège International Astrophysical Colloquia* (J. Surdej, D. Fraipont-Caro, E. Gosset, S. Refsdal & M. Remy, eds.), vol. 31, 263.

Claeskens, J.-F., Sluse, D., Riaud, P. & Surdej, J., 2006, Multi wavelength study of the gravitational lens system RXS J1131-1231. II. Lens model and source reconstruction, *Astron. & Astrophys.* **451**, 865–879.

Claeskens, J.-F. & Surdej, J., 2002, Gravitational lensing in quasar samples, *A&A Rev.* **10**, 263–311.

Close, L. M. & Males, J. R., 2010, A Search for Wide Companions to the Extrasolar Planetary System HR 8799, *Astrophysical Journal* **709**, 342–348.

Cockell, C. S., Léger, A., Fridlund, M. et al., 2009, Darwin-A Mission to Detect and Search for Life on Extrasolar Planets, *Astrobiology* **9**, 1–22.

Codona, J. L. & Angel, R., 2004, Imaging Extrasolar Planets by Stellar Halo Suppression in Separately Corrected Color Bands, *Astrophysical Journal, Letters* **604**, L117–L120.

Codona, J. L., Kenworthy, M. A., Hinz, P. M. et al., 2006, A high-contrast coronagraph for the MMT using phase apodization: design and observations at 5 microns and 2 λ/D radius, in *Ground-based and Airborne Instrumentation for Astronomy* (I. S. McLean & M. Iye, eds.), *Proceedings of the Society of Photo-Optical Instrumentation Engineers (SPIE) Conference Series*, vol. 6269, 62691N–10.

Cox, B. & Forshaw, J., 2010, *Why Does E=mc^2 (And Why Should We Care?)*, Da Capo Press, Massachusetts.

Crampton, D., Simard, L. & Silva, D., 2009, TMT Science and Instruments, in *Science with the VLT in the ELT Era* (A. Moorwood, ed.), 279.

Crepp, J. R., Ge, J., Vanden Heuvel, A. D. et al., 2006, Laboratory Testing of a Lyot Coronagraph Equipped with an Eighth-Order Notch Filter Image Mask, *Astrophysical Journal* **646**, 1252–1259.

Crepp, J. R. & Johnson, J. A., 2011, Estimates of the Planet Yield from Ground-based High-contrast Imaging Observations as a Function of Stellar Mass, *Astrophysical Journal* **733**, 126.

Crepp, J. R., Mahadevan, S. & Ge, J., 2009, Direct Detection of Planets Orbiting Large Angular Diameter Stars: Sensitivity of an Internally Occulting Space-based Coronagraph, *Astrophysical Journal* **702**, 672–679.

Crepp, J. R., Vanden Heuvel, A. D. & Ge, J., 2007, Comparative Lyot Coronagraphy with Extreme Adaptive Optics Systems, *Astrophysical Journal* **661**, 1323–1331.

Cuby, J.-G., 2010, The European ELT: status report, in *SF2A-2010: Proceedings of the Annual meeting of the French Society of Astronomy and Astrophysics* (S. Boissier, M. Heydari-Malayeri, R. Samadi & D. Valls-Gabaud, eds.), 3.

Curtis, G. W. & Sacramento Peak Observatory Staff, 1966, Daylight observations of the 1965 F comet at the Sacramento Peak Observatory, *Astronomical Journal* **71**, 194.

Debes, J. H. & Ge, J., 2004, High-Contrast Imaging with Gaussian Aperture Pupil Masks, *Publ. of the Astron. Soc. Pac.* **116**, 674–681.

Deguzman, P. C. & Nordin, G. P., 2001, Stacked Subwavelength Gratings as Circular Polarization Filters, *Applied Optics* **40**, 5731–5737.

Dekany, R., Bouchez, A., Britton, M. et al., 2006, PALM-3000: visible light AO on the 5.1-meter Telescope, in *Advances in Adaptive Optics II* (B. L. Ellerbroek & D. Bonaccini Calia, eds.), *Proceedings of the Society of Photo-Optical Instrumentation Engineers (SPIE) Conference Series*, vol. 6272, 62720G–10.

Delacroix, C., 2006, *Manœuvres en attitude d'un satellite avec évitements de zones interdites*, Diploma thesis, Institut Supérieur de l'Aéronautique et de l'Espace (SUPAERO) and Université Libre de Bruxelles (ULB), research internship at the Centre National d'Etudes Spatiales (CNES).

Delacroix, C., 2007, *Inversion du phénomène de lentille gravitationnelle dans le cadre du projet de télescope à miroir liquide (ILMT)*, Master thesis, Institut Supérieur de l'Aéronautique et de l'Espace (SUPAERO), research internship at the Université de Liège (ULg).

Delacroix, C., Absil, O., Forsberg, P. et al., 2013, Laboratory demonstration of a mid-infrared AGPM vector vortex coronagraph, *Astron. & Astrophys.* **553**, A98.

Delacroix, C., Absil, O., Mawet, D. et al., 2012a, A diamond AGPM coronagraph for VISIR, in *Ground-based and Airborne Instrumentation for Astronomy IV* (I. S. McLean, S. K. Ramsay & H. Takami, eds.), *Proceedings of the Society of Photo-Optical Instrumentation Engineers (SPIE) Conference Series*, vol. 8446, 84468K–9.

Delacroix, C., Forsberg, P., Karlsson, M. et al., 2010a, Annular groove phase mask coronagraph in diamond for mid-IR wavelengths: manufacturing assessment and performance analysis, in *Space Telescopes and Instrumentation 2010: Optical, Infrared, and Millimeter Wave* (M. C. Clampin, H. A. MacEwen & J. M. Oschmann, Jr., eds.), *Proceedings of the Society of Photo-Optical Instrumentation Engineers (SPIE) Conference Series*, vol. 7731, 77314W–10.

Delacroix, C., Forsberg, P., Karlsson, M. et al., 2010b, First manufactured diamond AGPM vector vortex for the L- and N-bands: metrology and expected performances, in *In the Spirit of Lyot 2010: Direct Detection of Exoplanets and Circumstellar Disks* (A. Boccaletti, ed.).

Delacroix, C., Forsberg, P., Karlsson, M. et al., 2012b, Design, manufacturing, and performance analysis of mid-infrared achromatic half-wave plates with diamond subwavelength gratings, *Applied Optics* **51**, 5897.

Delacroix, E., 1977, *Effects of the Small Components of the Nuclear Wave Function on Threshold Pionic Disintegration of the Deuteron*, Ph.D. thesis, The College of William and Mary, Williamsburg.

Deng, X., Liu, F., Wang, J. J. et al., 2005, Achromatic wave plates for optical pickup units fabricated by use of imprint lithography, *Optics Letters* **30**, 2614–2616.

Des Marais, D. J., Allamandola, L. J., Benner, S. A. et al., 2003, The NASA Astrobiology Roadmap, *Astrobiology* **3**, 219–235.

Des Marais, D. J., Nuth, J. A., III., Allamandola, L. J. et al., 2008, The NASA Astrobiology Roadmap, *Astrobiology* **8**, 715–730.

Digby, A. P., Hinkley, S., Oppenheimer, B. R. et al., 2006, The Challenges of Coronagraphic Astrometry, *Astrophysical Journal* **650**, 484–496.

Dollfus, A. & Brunier, S., 1980, The focal coronograph and the observation of a new Saturn ring, *Academie des Sciences Paris Comptes Rendus Serie B Sciences Physiques* **290**, 261–263.

Dore, P., Nucara, A., Cannavò, D. et al., 1998, Infrared Properties of Chemical-Vapor Deposition Polycrystalline Diamond Windows, *Applied Optics* **37**, 5731–5736.

Dye, S. & Warren, S. J., 2005, Decomposition of the Visible and Dark Matter in the Einstein Ring 0047-2808 by Semilinear Inversion, *Astrophysical Journal* **623**, 31–41.

Edwards, D. F. & Philipp, H. R., 1991, Cubic carbon (diamond), in *Handbook of optical constants of solids I* (E. D. Palik, ed.), p. 665, Academic Press, California.

Ehrenfreund, P., McKay, C., Rummel, J. D. et al., 2012, Toward a global space exploration program: A stepping stone approach, *Advances in Space Research* **49**, 2–48.

Einstein, A., 1915, Die Feldgleichungen der Gravitation, *Sitzungsberichte der Königlich Preußischen Akademie der Wissenschaften (Berlin)* 844–847.

ESO Press Releases, 2013, http://www.eso.org/public.

Esposito, S., Riccardi, A., Pinna, E. et al., 2011, Large Binocular Telescope Adaptive Optics System: new achievements and perspectives in adaptive optics, in *Astronomical Adaptive Optics Systems and Applications IV* (R. K. Tyson & M. Hart, eds.), *Proceedings of the Society of Photo-Optical Instrumentation Engineers (SPIE) Conference Series*, vol. 8149, 814902–10.

Ferrari, A., 2007, Analytical Analysis of Lyot Coronagraphs Response, *Astrophysical Journal* **657**, 1201–1209.

Ferrari, A., Aime, C. & Soummer, R., 2010, Analytical Computation of the Lyot Coronagraph Response to an Extended Source, *Astrophysical Journal* **708**, 218–223.

Feynman, R. P., Leighton, R. B. & Sands, M., 1963, *The Feynman Lectures on Physics*, vol. 1, Addison-Wesley, Massachusetts.

Feynman, R. P., Leighton, R. B. & Sands, M., 1964, *The Feynman Lectures on Physics: Mainly electromagnetism and matter*, vol. 2, Addison-Wesley, Massachusetts.

Feynman, R. P., Leighton, R. B. & Sands, M., 1965, *The Feynman Lectures on Physics: Quantum mechanics*, vol. 3, Addison-Wesley, Massachusetts.

Fitzgerald, M. P. & Graham, J. R., 2006, Speckle Statistics in Adaptively Corrected Images, *Astrophysical Journal* **637**, 541–547.

Fitzgerald, M. P., Kalas, P. G. & Graham, J. R., 2007, A Ring of Warm Dust in the HD 32297 Debris Disk, *Astrophysical Journal* **670**, 557–564.

Fitzgerald, M. P., Kalas, P. G. & Graham, J. R., 2009, Orbital Constraints on the β Pic Inner Planet Candidate with Keck Adaptive Optics, *Astrophysical Journal, Letters* **706**, L41–L45.

Foo, G., Palacios, D. M. & Swartzlander, G. A., Jr., 2005, Optical vortex coronagraph, *Optics Letters* **30**, 3308–3310.

Forsberg, P., 2013, *Diamond Microfabrication for Applications in Optics and Chemical Sensing*, Ph.D. thesis, Uppsala Universitet.

Forsberg, P. & Karlsson, M., 2013a, High aspect ratio optical gratings in diamond, *Diamond and Related Materials* **34**, 19–24.

Forsberg, P. & Karlsson, M., 2013b, Inclined surfaces in diamond: broadband antireflective structures and coupling light through waveguides, *Optics Express* **21**(3), 2693–2700.

Fortney, J. J., Lodders, K., Marley, M. S. & Freedman, R. S., 2008a, A Unified Theory for the Atmospheres of the Hot and Very Hot Jupiters: Two Classes of Irradiated Atmospheres, *Astrophysical Journal* **678**, 1419–1435.

Fortney, J. J., Marley, M. S., Saumon, D. & Lodders, K., 2008b, Synthetic Spectra and Colors of Young Giant Planet Atmospheres: Effects of Initial Conditions and Atmospheric Metallicity, *Astrophysical Journal* **683**, 1104–1116.

Fressin, F., Torres, G. & Charbonneau, D., 2013a, At Least One in Six Stars Has an Earth-size Planet, in *Exoplanets Coming & Going Everywhere, the first AAS press conference*, *Proceedings of the American Astronomical Society Meeting*, vol. 221, in press.

Fressin, F., Torres, G., Charbonneau, D. et al., 2013b, The False Positive Rate of Kepler and the Occurrence of Planets, *Astrophysical Journal* **766**, 81.

Fridlund, M., Eiroa, C., Henning, T. et al., 2010, A Roadmap for the Detection and Characterization of Other Earths, *Astrobiology* **10**, 113–119.

Fukagawa, M., Itoh, Y., Tamura, M. et al., 2009, H-Band Image of a Planetary Companion Around HR 8799 in 2002, *Astrophysical Journal, Letters* **696**, L1–L5.

Fusco, T., Rousset, G., Sauvage, J.-F. et al., 2006, High-order adaptive optics requirements for direct detection of extrasolar planets: Application to the SPHERE instrument, *Optics Express* **14**, 7515.

Galicher, R., Baudoz, P. & Baudrand, J., 2011, Multi-stage four-quadrant phase mask: achromatic coronagraph for space-based and ground-based telescopes, *Astron. & Astrophys.* **530**, A43.

Galicher, R., Baudoz, P., Rousset, G. et al., 2010, Self-coherent camera as a focal plane wavefront sensor: simulations, *Astron. & Astrophys.* **509**, A31.

Galicher, R., Guyon, O., Otsubo, M. et al., 2005, Laboratory Demonstration and Numerical Simulations of the Phase-Induced Amplitude Apodization, *Publ. of the Astron. Soc. Pac.* **117**, 411–420.

Ghomchi, Y., Drossart, P., Sémery, A. et al., 1999, VIRTIS H: a high resolution channel for VIRTIS, the Rosetta infrared imaging spectrometer, in *AAS/Division for Planetary Sciences Meeting Abstracts #31*, *AAS/Division for Planetary Sciences Meeting Abstracts*, vol. 31, #08.07.

Gilbert, W., 1986, Origin of life: The RNA world, *Nature* **319**, 618.

Gilmozzi, R. & Spyromilio, J., 2007, The European Extremely Large Telescope (E-ELT), *The Messenger* **127**, 11–19.

Girard, J. H. V., O'Neal, J., Mawet, D. et al., 2012, Image quality and high contrast improvements on VLT/NACO, in *Adaptive Optics Systems III* (B. L. Ellerbroek, E. Marchetti & J.-P. Véran, eds.), *Proceedings of the Society of Photo-Optical Instrumentation Engineers (SPIE) Conference Series*, vol. 8447, 84470L–14.

Girardi, L., Groenewegen, M. A. T., Hatziminaoglou, E. & da Costa, L., 2005, Star counts in the Galaxy. Simulating from very deep to very shallow photometric surveys with the TRILEGAL code, *Astron. & Astrophys.* **436**, 895–915.

Girin, O. P., Kondratev, Y. N. & Raaben, E. L., 1970, Optical constants and spectral microcharacteristics of NaO_2-SiO_2 glasses in the IR region of the spectrum, *Opt. Spectrosc.* **29**, 397–403.

Gladysz, S. & Christou, J. C., 2009, Reference-Less Detection, Astrometry, and Photometry of Faint Companions with Adaptive Optics, *Astrophysical Journal* **698**, 28–42.

Gradie, J., 1986, A Search for Circum-Asteroidal Material Using a Stellar Coronagraph, in *Lunar and Planetary Institute Science Conference Abstracts*, *Lunar and Planetary Inst. Technical Report*, vol. 17, 277–278.

Gremaux, D. A. & Gallagher, N. C., 1993, Limits of scalar diffraction theory for conducting gratings, *Applied Optics* **32**, 1948–1953.

Guyon, O., 2003, Phase-induced amplitude apodization of telescope pupils for extrasolar terrestrial planet imaging, *Astron. & Astrophys.* **404**, 379–387.

Guyon, O., 2004, Imaging Faint Sources within a Speckle Halo with Synchronous Interferometric Speckle Subtraction, *Astrophysical Journal* **615**, 562–572.

Guyon, O., 2005, Limits of Adaptive Optics for High-Contrast Imaging, *Astrophysical Journal* **629**, 592–614.

Guyon, O., 2007, The Coronagraph Tree of Life, in *In the Spirit of Bernard Lyot: The Direct Detection of Planets and Circumstellar Disks in the 21st Century.*

Guyon, O., Bendek, E. A., Eisner, J. A. et al., 2012, High-precision Astrometry with a Diffractive Pupil Telescope, *Astrophysical Journal, Suppl.* **200**, 11.

Guyon, O., Martinache, F., Belikov, R. & Soummer, R., 2010a, High Performance PIAA Coronagraphy with Complex Amplitude Focal Plane Masks, *Astrophysical Journal, Suppl.* **190**, 220–232.

Guyon, O., Matsuo, T. & Angel, R., 2009, Coronagraphic Low-Order Wave-Front Sensor: Principle and Application to a Phase-Induced Amplitude Coronagraph, *Astrophysical Journal* **693**, 75–84.

Guyon, O., Pluzhnik, E., Martinache, F. et al., 2010b, High-Contrast Imaging and Wavefront Control with a PIAA Coronagraph: Laboratory System Validation, *Publ. of the Astron. Soc. Pac.* **122**, 71–84.

Guyon, O., Pluzhnik, E. A., Galicher, R. et al., 2005, Exoplanet Imaging with a Phase-induced Amplitude Apodization Coronagraph. I. Principle, *Astrophysical Journal* **622**, 744–758.

Guyon, O., Pluzhnik, E. A., Kuchner, M. J. et al., 2006, Theoretical Limits on Extrasolar Terrestrial Planet Detection with Coronagraphs, *Astrophysical Journal, Suppl.* **167**(1), 81–99.

Guyon, O. & Shao, M., 2006, The Pupil-swapping Coronagraph, *Publ. of the Astron. Soc. Pac.* **118**, 860–865.

Habraken, S., Lemaire, P. C., Blanche, P.-A. & Jamar, C. A., 2002, New facility for large-scale DCG transmission holographic gratings: status and evaluation, in *Optical Spectroscopic Techniques, Remote Sensing, and Instrumentation for Atmospheric and Space Research IV* (A. M. Larar & M. G. Mlynczak, eds.), *Proceedings of the Society of Photo-Optical Instrumentation Engineers (SPIE) Conference Series*, vol. 4485, 460–468.

Habraken, S., Michaux, O., Renotte, Y. & Lion, Y., 1995a, Polarizing holographic beam splitter on a photoresist, *Optics Letters* **20**, 2348–2350.

Habraken, S., Renotte, Y., Lion, Y. et al., 1995b, Design for polarizing holographic optical elements, *Applied Optics* **34**, 3595–3602.

Habraken, S., VanDormael, D., Carapelle, A. & Moreau, V., 2000, Holographic filter applied to LCD projector for improvement of laser pointer presentation, in *Diffractive/Holographic Technologies and Spatial Light Modulators VII* (I. Cindrich, S. H. Lee & R. L. Sutherland, eds.), *Proceedings of the Society of Photo-Optical Instrumentation Engineers (SPIE) Conference Series*, vol. 3951, 20–27.

Haguenauer, P., Serabyn, E., Bloemhof, E. E. et al., 2005, An off-axis four-quadrant phase-mask coronagraph for Palomar: high contrast near bright stars imager, in *Techniques and Instrumentation for Detection of Exoplanets II* (D. R. Coulter, ed.), *Proceedings of the Society of Photo-Optical Instrumentation Engineers (SPIE) Conference Series*, vol. 5905, 261–271.

Haguenauer, P., Serabyn, E., Mennesson, B. et al., 2006, Astronomical near-neighbor detection with a four-quadrant phase mask (FQPM) coronagraph, in *Space Telescopes and Instrumentation I: Optical, Infrared, and Millimeter* (J. C. Mather, H. A. MacEwen & M. W. M. de Graauw, eds.), *Proceedings of the Society of Photo-Optical Instrumentation Engineers (SPIE) Conference Series*, vol. 6265, 62651G–10.

Hanot, C., 2011, *Development of nulling interferometry devices for the detection and characterization of extrasolar planets*, Ph.D. thesis, Université de Liège.

Hawkins, G. J., 1998, *Spectral Characterisation of Infrared Optical Materials and Filters*, Ph.D. thesis, University of Reading.

Heinze, A. N., Hinz, P. M., Kenworthy, M. et al., 2008, Deep L'- and M-band Imaging for Planets around Vega and ϵ Eridani, *Astrophysical Journal* **688**, 583–596.

Heinze, A. N., Hinz, P. M., Kenworthy, M. et al., 2010a, Constraints on Long-period Planets from an L'- and M-band Survey of Nearby Sun-like Stars: Modeling Results, *Astrophysical Journal* **714**, 1570–1581.

Heinze, A. N., Hinz, P. M., Sivanandam, S. et al., 2010b, Constraints on Long-period Planets from an L'- and M-band Survey of Nearby Sun-like Stars: Observations, *Astrophysical Journal* **714**, 1551–1569.

Hill, J. M., Green, R. F., Ashby, D. S. et al., 2012, The Large Binocular Telescope, in *Ground-based and Airborne Telescopes IV* (L. M. Stepp, ed.), *Proceedings of the Society of Photo-Optical Instrumentation Engineers (SPIE) Conference Series*, vol. 8444, 84441A–12.

Hinz, P. M., Rodigas, T. J., Kenworthy, M. A. et al., 2010, Thermal Infrared MMTAO Observations of the HR 8799 Planetary System, *Astrophysical Journal* **716**, 417–426.

Hirayama, T. & Nakagomi, Y., 1974, Observations of Prominences in He II with a New 25 CM Coronagraph, *PASJ* **26**, 53.

Holmberg, J., Nordström, B. & Andersen, J., 2009, The Geneva-Copenhagen survey of the solar neighbourhood. III. Improved distances, ages, and kinematics, *Astron. & Astrophys.* **501**, 941–947.

Inada, N., Oguri, M., Pindor, B. et al., 2003, A gravitationally lensed quasar with quadruple images separated by 14.62arcseconds, *Nature* **426**, 810–812.

Jacquinot, P. & Roizen-Dossier, B., 1964, Apodisation, *American Journal of Physics* **32**, 899–899.

Janson, M., 2007, Celestial Exoplanet Survey Occulter: A Concept for Direct Imaging of Extrasolar Earth-like Planets from the Ground, *Publ. of the Astron. Soc. Pac.* **119**, 214–227.

Janson, M., Brandner, W., Henning, T. et al., 2007, NACO-SDI Direct Imaging Search for the Exoplanet ϵ Eri b, *Astronomical Journal* **133**, 2442–2456.

Jaubert, J., Julien, E., Lassalle-Balier, G. et al., 2005, Attitude Guidance Techniques Developed at CNES for Earth Observation and Scientific Missions, in *Guidance and Control 2005* (R. J. Proulx & T. F. Starchville, Jr., eds.), *Proceedings of the Advances in the Astronautical Sciences Conference Series*, vol. 121, 87–106.

Jenkins, C., 2008, Optical vortex coronagraphs on ground-based telescopes, *Mon. Not. of the Royal Astron. Soc.* **384**, 515–524.

Johns, M., 2008, Progress on the GMT, in *Ground-based and Airborne Telescopes II* (L. M. Stepp & R. Gilmozzi, eds.), *Proceedings of the Society of Photo-Optical Instrumentation Engineers (SPIE) Conference Series*, vol. 7012, 70121B–15.

Kalas, P., Graham, J. R., Chiang, E. et al., 2008, Optical Images of an Exosolar Planet 25 Light-Years from Earth, *Science* **322**, 1345–1348.

Kalas, P., Graham, J. R. & Clampin, M., 2005, A planetary system as the origin of structure in Fomalhaut's dust belt, *Nature* **435**, 1067–1070.

Kalas, P., Graham, J. R., Fitzgerald, M. P. & Clampin, M., 2013, STIS Coronagraphic Imaging of Fomalhaut: Main Belt Structure and the Orbit of Fomalhaut b, *ArXiv e-prints* .

Karlsson, M. & Nikolajeff, F., 2003, Diamond micro-optics: microlenses and antireflection structured surfaces for the infrared spectral region, *Optics Express* **11**, 502–507.

Karlsson, M., Vartiainen, I., Kuittinen, M. & Nikolajeff, F., 2010, Fabrication of sub-micron high aspect ratio diamond structures with nanoimprint lithography, *Microelectronic Engineering* **87**(11), 2077–2080.

Kasdin, N. J., Vanderbei, R. J., Spergel, D. N. & Littman, M. G., 2003, Extrasolar Planet Finding via Optimal Apodized-Pupil and Shaped-Pupil Coronagraphs, *Astrophysical Journal* **582**, 1147–1161.

Kasper, M., Amico, P., Pompei, E. et al., 2009, Direct Imaging of Exoplanets and Brown Dwarfs with the VLT: NACO Pupil-stabilised Lyot Coronagraphy at 4 μm, *The Messenger* **137**, 8–13.

Kasper, M., Apai, D., Janson, M. & Brandner, W., 2007, A novel L-band imaging search for giant planets in the Tucana and β Pictoris moving groups, *Astron. & Astrophys.* **472**, 321–327.

Kasper, M., Beuzit, J.-L., Feldt, M. et al., 2012, Gearing up the SPHERE, *The Messenger* **149**, 17–21.

Kasper, M., Beuzit, J.-L., Verinaud, C. et al., 2010, EPICS: direct imaging of exoplanets with the E-ELT, in *Ground-based and Airborne Instrumentation for Astronomy III* (I. S. McLean, S. K. Ramsay & H. Takami, eds.), *Proceedings of the Society of Photo-Optical Instrumentation Engineers (SPIE) Conference Series*, vol. 7735, 77352E–9.

Kasper, M. E., Beuzit, J.-L., Verinaud, C. et al., 2008, EPICS: the exoplanet imager for the E-ELT, in *Adaptive Optics Systems* (N. Hubin, C. E. Max & P. L. Wizinowich, eds.), *Proceedings of the Society of Photo-Optical Instrumentation Engineers (SPIE) Conference Series*, vol. 7015, 70151S–12.

Kasting, J. F. & Catling, D., 2003, Evolution of a Habitable Planet, *Annual Review of Astron. & Astrophys.* **41**, 429–463.

Kasting, J. F., Whitmire, D. P. & Reynolds, R. T., 1993, Habitable Zones around Main Sequence Stars, *Icarus* **101**, 108–128.

Kawakami, S., Kawashima, T. & Sato, T., 1999, Mechanism of shape formation of three-dimensional periodic nanostructures by bias sputtering, *Applied Physics Letters* **74**, 463–465.

Kawashima, T., Miura, K., Sato, T. & Kawakami, S., 2000, Self-healing effects in the fabrication process of photonic crystals, *Applied Physics Letters* **77**, 2613–2615.

Kenworthy, M., Quanz, S., Meyer, M. et al., 2010a, A New Coronagraph for NAOS-CONICA – the Apodising Phase Plate, *The Messenger* **141**, 2–4.

Kenworthy, M. A., Codona, J. L., Hinz, P. M. et al., 2007, First On-Sky High-Contrast Imaging with an Apodizing Phase Plate, *Astrophysical Journal* **660**(1), 762–769.

Kenworthy, M. A., Hinz, P. M., Codona, J. L. et al., 2010b, Developing achromatic coronagraphic optics for LMIRCam and the LBT, in *Optical and Infrared Interferometry II* (W. C. Danchi, F. Delplancke & J. K. Rajagopal, eds.), *Proceedings of the Society of Photo-Optical Instrumentation Engineers (SPIE) Conference Series*, vol. 7734, 77342P–11.

Kenworthy, M. A., Mamajek, E. E., Hinz, P. M. et al., 2009, MMT/AO 5 μm Imaging Constraints on the Existence of Giant Planets Orbiting Fomalhaut at $\sim$13-40 AU, *Astrophysical Journal* **697**, 1928–1933.

Kenworthy, M. A., Meshkat, T., Quanz, S. P. et al., 2013, Coronagraphic Observations of Fomalhaut at Solar System Scales, *Astrophysical Journal* **764**, 7.

Kenworthy, M. A., Quanz, S. P., Meyer, M. R. et al., 2010c, An apodizing phase plate coronagraph for VLT/NACO, in *Ground-based and Airborne Instrumentation for Astronomy III* (I. S. McLean, S. K. Ramsay & H. Takami, eds.), *Proceedings of the Society of Photo-Optical Instrumentation Engineers (SPIE) Conference Series*, vol. 7735, 773532–9.

Kerber, F., Käufl, H. U., Baksai, P. et al., 2012, VISIR upgrade overview and status, in *Ground-based and Airborne Instrumentation for Astronomy IV* (I. S. McLean, S. K. Ramsay & H. Takami, eds.), *Proceedings of the Society of Photo-Optical Instrumentation Engineers (SPIE) Conference Series*, vol. 8446, 84460E–12.

Kervella, P. & Domiciano de Souza, A., 2007, The environment of the fast rotating star Achernar. High-resolution thermal infrared imaging with VISIR in BURST mode, *Astron. & Astrophys.* **474**, L49–L52.

Kervella, P., Domiciano de Souza, A. & Bendjoya, P., 2008, The close-in companion of the fast rotating Be star Achernar, *Astron. & Astrophys.* **484**, L13–L16.

Kervella, P., Domiciano de Souza, A., Kanaan, S. et al., 2009, The environment of the fast rotating star Achernar. II. Thermal infrared interferometry with VLTI/MIDI, *Astron. & Astrophys.* **493**, L53–L56.

Kervella, P. & Thévenin, F., 2007, Deep imaging survey of the environment of α Centauri. II. CCD imaging with the NTT-SUSI2 camera, *Astron. & Astrophys.* **464**, 373–375.

Kervella, P., Thévenin, F., Coudé du Foresto, V. & Mignard, F., 2006, Deep imaging survey of the environment of α Centauri. I. Adaptive optics imaging of α Cen B with VLT-NACO, *Astron. & Astrophys.* **459**, 669–678.

Khashan, M. A. & Nassif, A. Y., 2001, Dispersion of the optical constants of quartz and polymethyl methacrylate glasses in a wide spectral range: 0.2-3 /μm, *Optics Communications* **188**, 129–139.

Kikuta, H., Ohira, Y. & Iwata, K., 1997, Achromatic quarter-wave plates using the dispersion of form birefringence, *Applied Optics* **36**, 1566–1572.

Kissler-Patig, M., 2010, Overall science goals and top level AO requirements for the E-ELT, in *Adaptative Optics for Extremely Large Telescopes*, 01001.

Knutson, H. A., Charbonneau, D., Allen, L. E. et al., 2007, A map of the day-night contrast of the extrasolar planet HD 189733b, *Nature* **447**, 183–186.

Koch, D. G., Borucki, W. J., Basri, G. et al., 2010, Kepler Mission Design, Realized Photometric Performance, and Early Science, *Astrophysical Journal, Letters* **713**, L79–L86.

Kochanek, C. S., Blandford, R. D., Lawrence, C. R. & Narayan, R., 1989, The ring cycle - an iterative lens reconstruction technique applied to MG1131+0456, *Mon. Not. of the Royal Astron. Soc.* **238**, 43–56.

Konopacky, Q. M., Barman, T. S., Macintosh, B. A. & Marois, C., 2013, Detection of Carbon Monoxide and Water Absorption Lines in an Exoplanet Atmosphere, *Science* **339**, 1398–1401.

Koomen, M. J., Detwiler, C. R., Brueckner, G. E. et al., 1975, White light coronagraph in OSO-7, *Applied Optics* **14**, 743–751.

Kopparapu, R. K., Ramirez, R., Kasting, J. F. et al., 2013, Habitable Zones around Main-sequence Stars: New Estimates, *Astrophysical Journal* **765**, 131.

Kuchner, M. J., Crepp, J. & Ge, J., 2005, Eighth-Order Image Masks for Terrestrial Planet Finding, *Astrophysical Journal* **628**, 466–473.

Kuchner, M. J. & Spergel, D. N., 2003, Notch-Filter Masks: Practical Image Masks for Planet-finding Coronagraphs, *Astrophysical Journal* **594**, 617–626.

Kuchner, M. J. & Traub, W. A., 2002, A Coronagraph with a Band-limited Mask for Finding Terrestrial Planets, *Astrophysical Journal* **570**, 900–908.

Kuipers, J. B., 1999, *Quaternions and Rotation Sequences: A Primer With Applications to Orbits, Aerospace, and Virtual Reality*, Princeton University Press, New Jersey.

Lafrenière, D., Doyon, R., Marois, C. et al., 2007a, The Gemini Deep Planet Survey, *Astrophysical Journal* **670**, 1367–1390.

Lafrenière, D., Doyon, R., Nadeau, D. et al., 2007b, Improving the Speckle Noise Attenuation of Simultaneous Spectral Differential Imaging with a Focal Plane Holographic Diffuser, *Astrophysical Journal* **661**, 1208–1217.

Lafrenière, D., Jayawardhana, R. & van Kerkwijk, M. H., 2010, The Directly Imaged Planet Around the Young Solar Analog 1RXS J160929.1 - 210524: Confirmation of Common Proper Motion, Temperature, and Mass, *Astrophysical Journal* **719**, 497–504.

Lafrenière, D., Marois, C., Doyon, R. & Barman, T., 2009, HST/NICMOS Detection of HR 8799 b in 1998, *Astrophysical Journal, Letters* **694**, L148–L152.

Lafrenière, D., Marois, C., Doyon, R. et al., 2007c, A New Algorithm for Point-Spread Function Subtraction in High-Contrast Imaging: A Demonstration with Angular Differential Imaging, *Astrophysical Journal* **660**, 770–780.

Lagage, P. O., Pel, J. W., Authier, M. et al., 2004, Successful Commissioning of VISIR: The Mid-Infrared VLT Instrument, *The Messenger* **117**, 12–16.

Lagrange, A.-M., Boccaletti, A., Milli, J. et al., 2012, The position of β Pictoris b position relative to the debris disk, *Astron. & Astrophys.* **542**, A40.

Lagrange, A.-M., Bonnefoy, M., Chauvin, G. et al., 2010, A Giant Planet Imaged in the Disk of the Young Star β Pictoris, *Science* **329**, 57–59.

Lagrange, A.-M., Gratadour, D., Chauvin, G. et al., 2009a, A probable giant planet imaged in the β Pictoris disk. VLT/NaCo deep L'-band imaging, *Astron. & Astrophys.* **493**, L21–L25.

Lagrange, A.-M., Kasper, M., Boccaletti, A. et al., 2009b, Constraining the orbit of the possible companion to β Pictoris. New deep imaging observations, *Astron. & Astrophys.* **506**, 927–934.

Lalanne, P. & Lemercier-Lalanne, D., 1997, Depth dependence of the effective properties of subwavelength gratings, *Journal of the Optical Society of America A* **14**, 450–458.

Lalanne, P. & Morris, G. M., 1996, Highly improved convergence of the coupled-wave method for TM polarization, *Journal of the Optical Society of America A* **13**, 779–784.

Law, N. M., Mackay, C. D. & Baldwin, J. E., 2006, Lucky imaging: high angular resolution imaging in the visible from the ground, *Astron. & Astrophys.* **446**, 739–745.

Law, N. M., Mackay, C. D., Dekany, R. G. et al., 2009, Getting Lucky with Adaptive Optics: Fast Adaptive Optics Image Selection in the Visible with a Large Telescope, *Astrophysical Journal* **692**, 924–930.

Lawson, P. R., Poyneer, L., Barrett, H. et al., 2012, On advanced estimation techniques for exoplanet detection and characterization using ground-based coronagraphs, in *Adaptive Optics Systems III* (B. L. Ellerbroek, E. Marchetti & J.-P. Véran, eds.), *Proceedings of the Society of Photo-Optical Instrumentation Engineers (SPIE) Conference Series*, vol. 8447.

Leconte, J., Soummer, R., Hinkley, S. et al., 2010, The Lyot Project Direct Imaging Survey of Substellar Companions: Statistical Analysis and Information from Nondetections, *Astrophysical Journal* **716**, 1551–1565.

Lee, J. W., Kim, S.-L., Kim, C.-H. et al., 2009, The sdB+M Eclipsing System HW Virginis and its Circumbinary Planets, *Astronomical Journal* **137**, 3181–3190.

Léger, A., Ollivier, M., Altwegg, K. & Woolf, N. J., 1999, Is the presence of H_2O and O_3 in an exoplanet a reliable signature of a biological activity?, *Astron. & Astrophys.* **341**, 304–311.

Léger, A., Rouan, D., Schneider, J. et al., 2009, Transiting exoplanets from the CoRoT space mission. VIII. CoRoT-7b: the first super-Earth with measured radius, *Astron. & Astrophys.* **506**, 287–302.

Lenaerts, C., 2005, *Etude et réalisation de filtres spectraux: Application à la résonance de mode guidé et à la résonance des plasmons de surface*, Ph.D. thesis, Université de Liège.

Lenaerts, C., Michel, F., Tilkens, B. et al., 2005, High transmission efficiency for surface plasmon resonance by use of a dielectric grating, *Applied Optics* **44**, 6017–6022.

Lenzen, R., Hartung, M., Brandner, W. et al., 2003, NAOS-CONICA first on sky results in a variety of observing modes, in *Instrument Design and Performance for Optical/Infrared Ground-based Telescopes* (M. Iye & A. F. M. Moorwood, eds.), *Proceedings of the Society of Photo-Optical Instrumentation Engineers (SPIE) Conference Series*, vol. 4841, 944–952.

Li, L., 1993, Multilayer modal method for diffraction gratings of arbitrary profile, depth, and permittivity, *Journal of the Optical Society of America A* **10**, 2581–2591.

Li, L., 1994, Multilayer modal method for diffraction gratings of arbitrary profile, depth, and permittivity: addendum, *Journal of the Optical Society of America A* **11**, 1685.

Liebes, S., 1969, Gravitational Lens Simulator, *American Journal of Physics* **37**, 103–104.

Liesenborgs, J., de Rijcke, S., Dejonghe, H. & Bekaert, P., 2009, Non-parametric strong lens inversion of SDSS J1004+4112, *Mon. Not. of the Royal Astron. Soc.* **397**, 341–349.

Lin, D. N. C., Bodenheimer, P. & Richardson, D. C., 1996, Orbital migration of the planetary companion of 51 Pegasi to its present location, *Nature* **380**, 606–607.

Lissauer, J. J., Fabrycky, D. C., Ford, E. B. et al., 2011, A closely packed system of low-mass, low-density planets transiting Kepler-11, *Nature* **470**, 53–58.

Lloyd, J. P., Gavel, D. T., Graham, J. R. et al., 2003, Four-quadrant phase mask coronagraph: analytical calculation and pupil geometry, in *High-Contrast Imaging for Exo-Planet Detection* (A. B. Schultz, ed.), *Proceedings of the Society of Photo-Optical Instrumentation Engineers (SPIE) Conference Series*, vol. 4860, 171–181.

Lozi, J., Martinache, F. & Guyon, O., 2009, Phase-Induced Amplitude Apodization on Centrally Obscured Pupils: Design and First Laboratory Demonstration for the Subaru Telescope Pupil, *Publ. of the Astron. Soc. Pac.* **121**, 1232–1244.

Lyot, B., 1932, Étude de la couronne solaire en dehors des éclipses. Avec 16 figures dans le texte., *ZAp* **5**, 73.

Lyot, B., 1939, The study of the solar corona and prominences without eclipses (George Darwin Lecture, 1939), *Mon. Not. of the Royal Astron. Soc.* **99**, 580–594.

Macintosh, B., Graham, J., Palmer, D. et al., 2007, Adaptive optics for direct detection of extra-solar planets: the Gemini Planet Imager, *Comptes Rendus Physique* **8**, 365–373.

Macintosh, B., Zuckerman, B., Becklin, E. E. & McLean, I. S., 1992, Searches for Brown Dwarfs in the Hyades, in *American Astronomical Society Meeting Abstracts #180*, *Bulletin of the American Astronomical Society*, vol. 24, 773.

Macintosh, B. A., Anthony, A., Atwood, J. et al., 2012, The Gemini Planet Imager: integration and status, in *Ground-based and Airborne Instrumentation for Astronomy IV* (I. S. McLean, S. K. Ramsay & H. Takami, eds.), *Proceedings of the Society of Photo-Optical Instrumentation Engineers (SPIE) Conference Series*, vol. 8446, 84461U–9.

Macintosh, B. A., Becklin, E. E., Kaisler, D. et al., 2003, Deep Keck Adaptive Optics Searches for Extrasolar Planets in the Dust of ϵ Eridani and Vega, *Astrophysical Journal* **594**, 538–544.

Macintosh, B. A., Graham, J. R., Palmer, D. W. et al., 2008, The Gemini Planet Imager: from science to design to construction, in *Adaptive Optics Systems* (N. Hubin, C. E. Max & P. L. Wizinowich, eds.), *Proceedings of the Society of Photo-Optical Instrumentation Engineers (SPIE) Conference Series*, vol. 7015, 701518–13.

Maher, K. A. & Stevenson, D. J., 1988, Impact frustration of the origin of life, *Nature* **331**, 612–614.

Malbet, F., Yu, J. W. & Shao, M., 1995, High-Dynamic-Range Imaging Using a Deformable Mirror for Space Coronography, *Publ. of the Astron. Soc. Pac.* **107**, 386.

Mamajek, E. E., Kenworthy, M. A., Hinz, P. M. & Meyer, M. R., 2010, Discovery of a Faint Companion to Alcor Using MMT/AO 5 μm Imaging, *Astronomical Journal* **139**, 919–925.

Marchis, F., Hestroffer, D., Descamps, P. et al., 2006, A low density of 0.8gcm^{-3} for the Trojan binary asteroid 617Patroclus, *Nature* **439**, 565–567.

Marois, C., Doyon, R., Nadeau, D. et al., 2003, Effects of Quasi-Static Aberrations in Faint Companion Searches, in *EAS Publications Series* (C. Aime & R. Soummer, eds.), *EAS Publications Series*, vol. 8, 233–243.

Marois, C., Doyon, R., Nadeau, D. et al., 2005, TRIDENT: An Infrared Differential Imaging Camera Optimized for the Detection of Methanated Substellar Companions, *Publ. of the Astron. Soc. Pac.* **117**, 745–756.

Marois, C., Doyon, R., Racine, R. & Nadeau, D., 2000, Efficient Speckle Noise Attenuation in Faint Companion Imaging, *Publ. of the Astron. Soc. Pac.* **112**, 91–96.

Marois, C., Lafrenière, D., Doyon, R. et al., 2006, Angular Differential Imaging: A Powerful High-Contrast Imaging Technique, *Astrophysical Journal* **641**, 556–564.

Marois, C., Lafrenière, D., Macintosh, B. & Doyon, R., 2008a, Confidence Level and Sensitivity Limits in High-Contrast Imaging, *Astrophysical Journal* **673**, 647–656.

Marois, C., Macintosh, B. & Barman, T., 2007, GQ Lup B Visible and Near-Infrared Photometric Analysis, *Astrophysical Journal, Letters* **654**, L151–L154.

Marois, C., Macintosh, B., Barman, T. et al., 2008b, Direct Imaging of Multiple Planets Orbiting the Star HR 8799, *Science* **322**, 1348–1352.

Marois, C., Zuckerman, B., Konopacky, Q. M. et al., 2010, Images of a fourth planet orbiting HR 8799, *Nature* **468**, 1080–1083.

Martinache, F., Guyon, O., Clergeon, C. & Blain, C., 2012a, Speckle Control with a Remapped-Pupil PIAA Coronagraph, *Publ. of the Astron. Soc. Pac.* **124**, 1288–1294.

Martinache, F., Guyon, O., Clergeon, C. et al., 2012b, The Subaru coronagraphic extreme AO project: first observations, in *Adaptive Optics Systems III* (B. L. Ellerbroek, E. Marchetti & J.-P. Véran, eds.), *Proceedings of the Society of Photo-Optical Instrumentation Engineers (SPIE) Conference Series*, vol. 8447, 84471Y–8.

Martinache, F., Guyon, O., Pluzhnik, E. A. et al., 2006, Exoplanet Imaging with a Phase-induced Amplitude Apodization Coronograph. II. Performance, *Astrophysical Journal* **639**, 1129–1137.

Martinache, F., Lloyd, J. P., Ireland, M. J. et al., 2007, Precision Masses of the Low-Mass Binary System GJ 623, *Astrophysical Journal* **661**, 496–501.

Martinez, P., Carpentier, E. A. & Kasper, M., 2010, Laboratory Demonstration of Efficient XAO Coronagraphy in the Context of SPHERE, *Publ. of the Astron. Soc. Pac.* **122**, 916–923.

Martinez, P., Dorrer, C., Aller Carpentier, E. et al., 2009, Design, analysis, and testing of a microdot apodizer for the Apodized Pupil Lyot Coronagraph, *Astron. & Astrophys.* **495**, 363–370.

Mascaro, J., 2011, Earth Similarity Index Provides a Logical Breakpoint for Naming Planets, *Astrobiology* **11**, 1053–1053.

Masciadri, E., Mundt, R., Henning, T. et al., 2005, A Search for Hot Massive Extrasolar Planets around Nearby Young Stars with the Adaptive Optics System NACO, *Astrophysical Journal* **625**, 1004–1018.

Masson, J.-B. & Gallot, G., 2006, Terahertz achromatic quarter-wave plate, *Optics Letters* **31**, 265–267.

Matin, A., 1978, Organic nutrition of chemolithotrophic bacteria., *Annu Rev Microbiol* **32**.

Mawet, D., 2006, *Subwavelength gratings for extrasolar planetary system imaging and characterization*, Ph.D. thesis, Université de Liège.

Mawet, D., Absil, O., Delacroix, C. et al., 2013, L'-band AGPM vector vortex coronagraph's first light on VLT/NACO. Discovery of a late-type companion at two beamwidths from an F0V star, *Astron. & Astrophys.* **552**, L13.

Mawet, D., Mennesson, B., Serabyn, E. et al., 2011a, A Dim Candidate Companion to ϵ Cephei, *Astrophysical Journal, Letters* **738**, L12.

Mawet, D., Murakami, N., Delacroix, C. et al., 2011b, Taking the vector vortex coronagraph to the next level for ground- and space-based exoplanet imaging instruments: review of technology developments in the USA, Japan, and Europe, in *Techniques and Instrumentation for Detection of Exoplanets V* (S. Shaklan, ed.), *Proceedings of the Society of Photo-Optical Instrumentation Engineers (SPIE) Conference Series*, vol. 8151, 815108–14.

Mawet, D., Riaud, P., Absil, O. & Surdej, J., 2005a, Annular Groove Phase Mask Coronagraph, *Astrophysical Journal* **633**, 1191–1200.

Mawet, D., Riaud, P., Baudrand, J. et al., 2006, The four-quadrant phase-mask coronagraph: white light laboratory results with an achromatic device, *Astron. & Astrophys.* **448**, 801–808.

Mawet, D., Riaud, P., Surdej, J. & Baudrand, J., 2005b, Subwavelength surface-relief gratings for stellar coronagraphy, *Applied Optics* **44**, 7313–7321.

Mawet, D., Serabyn, E., Liewer, K. et al., 2009a, Optical Vectorial Vortex Coronagraphs using Liquid Crystal Polymers: theory, manufacturing and laboratory demonstration, *Optics Express* **17**, 1902–1918.

Mawet, D., Serabyn, E., Liewer, K. et al., 2010, The Vector Vortex Coronagraph: Laboratory Results and First Light at Palomar Observatory, *Astrophysical Journal* **709**, 53–57.

Mawet, D., Serabyn, E., Stapelfeldt, K. & Crepp, J., 2009b, Imaging the Debris Disk of HD 32297 with a Phase-Mask Coronagraph at High Strehl Ratio, *Astrophysical Journal, Letters* **702**, L47–L50.

Mawet, D., Serabyn, E., Wallace, J. K. & Pueyo, L., 2011c, Improved high-contrast imaging with on-axis telescopes using a multistage vortex coronagraph, *Optics Letters* **36**, 1506.

Mayor, M., Bonfils, X., Forveille, T. et al., 2009, The HARPS search for southern extra-solar planets. XVIII. An Earth-mass planet in the GJ 581 planetary system, *Astron. & Astrophys.* **507**, 487–494.

Mayor, M. & Queloz, D., 1995, A Jupiter-mass companion to a solar-type star, *Nature* **378**, 355–359.

Maystre, D., 1984, Rigorous theory of light scattering from rough surfaces, *Journal of Optics* **15**, 43–51.

McEldowney, S. C., Shemo, D. M. & Chipman, R. A., 2008a, Vortex retarders produced from photo-aligned liquid crystal polymers, *Optics Express* **16**, 7295.

McEldowney, S. C., Shemo, D. M., Chipman, R. A. & Smith, P. K., 2008b, Creating vortex retarders using photoaligned liquid crystal polymers, *Optics Letters* **33**, 134.

McKenzie, P. A., Hendrix, K., Shemo, D. & Tan, K., 2008, Hybrid optical retarders fabricated from liquid crystal polymer and form birefringent thin films, in *Polarization: Measurement, Analysis, and Remote Sensing VIII* (D. B. Chenault & D. H. Goldstein, eds.), *Proceedings of the Society of Photo-Optical Instrumentation Engineers (SPIE) Conference Series*, vol. 6972, 697206–10.

Metchev, S., Marois, C. & Zuckerman, B., 2009, Pre-Discovery 2007 Image of the HR 8799 Planetary System, *Astrophysical Journal, Letters* **705**, L204–L207.

Milli, J., Mouillet, D., Lagrange, A.-M. et al., 2012, Impact of angular differential imaging on circumstellar disk images, *Astron. & Astrophys.* **545**, A111.

Mills, J. P., Gaiser, S. L., Diner, D. J. & Watson, S. M., 1991, Direct imaging of nonsolar planets with infrared telescopes using apodized coronagraphs, *Applied Optics* **30**, 3253–3262.

Moerchen, M. M., Telesco, C. M., De Buizer, J. M. et al., 2007, 12 and 18 μm Images of Dust Surrounding HD 32297, *Astrophysical Journal, Letters* **666**, L109–L112.

Mohanty, S., Jayawardhana, R., Huélamo, N. & Mamajek, E., 2007, The Planetary Mass Companion 2MASS 1207-3932B: Temperature, Mass, and Evidence for an Edge-on Disk, *Astrophysical Journal* **657**, 1064–1091.

Moharam, M. G. & Gaylord, T. K., 1981, Rigorous coupled-wave analysis of planar-grating diffraction, *Journal of the Optical Society of America* **71**, 811–818.

Moharam, M. G. & Gaylord, T. K., 1982, Diffraction analysis of dielectric surface-relief gratings, *Journal of the Optical Society of America* **72**, 1385.

Moharam, M. G., Grann, E. B., Pommet, D. A. & Gaylor, T. K., 1995, Formulation for stable and efficient implementation of the rigorous coupled-wave analysis of binary gratings, *Journal of the Optical Society of America A* **12**, 1068–1076.

Murakami, N., Baba, N., Ise, A. et al., 2010a, Laboratory demonstration of an optical vortex mask coronagraph using photonic crystal, in *In the Spirit of Lyot 2010: Direct Detection of Exoplanets and Circumstellar Disks* (A. Boccaletti, ed.).

Murakami, N., Hamaguchi, S., Sakamoto, M. et al., 2013, Design and laboratory demonstration of an achromatic vector vortex coronagraph, *Optics Express* **21**, 7400.

Murakami, N., Nishikawa, J., Traub, W. A. et al., 2012, Coronagraph focal-plane phase masks based on photonic crystal technology: recent progress and observational strategy, in *Space Telescopes and Instrumentation 2012: Optical, Infrared, and Millimeter Wave* (M. C. Clampin, G. G. Fazio, H. A. MacEwen & J. M. Oschmann, Jr., eds.), *Proceedings of the Society of Photo-Optical Instrumentation Engineers (SPIE) Conference Series*, vol. 8442, 844205–9.

Murakami, N., Nishikawa, J., Yokochi, K. et al., 2010b, Achromatic Eight-octant Phase-mask Coronagraph using Photonic Crystal, *Astrophysical Journal* **714**, 772–777.

Murakami, N., Uemura, R., Baba, N. et al., 2008a, An Eight-Octant Phase-Mask Coronagraph, *Publ. of the Astron. Soc. Pac.* **120**, 1112–1118.

Murakami, N., Uemura, R., Baba, N. et al., 2008b, Four-Quadrant Phase Mask Coronagraph with a Jacquinot-Lyot Stop, *Astrophysical Journal* **677**, 1425–1432.

Muterspaugh, M. W., Lane, B. F., Kulkarni, S. R. et al., 2010, The Phases Differential Astrometry Data Archive. V. Candidate Substellar Companions to Binary Systems, *Astronomical Journal* **140**, 1657–1671.

Nakajima, T., 1994, Planet detectability by an adaptive optics stellar coronagraph, *Astrophysical Journal* **425**, 348–357.

Nakajima, T., Durrance, S. T., Golimowski, D. A. & Kulkarni, S. R., 1994, A coronagraphic search for brown dwarfs around nearby stars, *Astrophysical Journal* **428**, 797–804.

NASA Exoplanet Archive, 2013, http://www.exoplanetarchive.ipac.caltech.edu.

N'Diaye, M., Dohlen, K., Cuevas, S. et al., 2010, Experimental results with a second-generation Roddier & Roddier phase mask coronagraph, *Astron. & Astrophys.* **509**, A8.

Nelson, J. & Sanders, G. H., 2006, TMT status report, in *Ground-based and Airborne Telescopes* (L. M. Stepp, ed.), *Proceedings of the Society of Photo-Optical Instrumentation Engineers (SPIE) Conference Series*, vol. 6267, 626728.

Nersisyan, S. R., Tabiryan, N. V., Steeves, D. M. & Kimball, B. R., 2010, The Promise of Diffractive Waveplates, *Optics & Photonics News* **21**, 40.

Nielsen, E. L., Close, L. M., Biller, B. A. et al., 2008, Constraints on Extrasolar Planet Populations from VLT NACO/SDI and MMT SDI and Direct Adaptive Optics Imaging Surveys: Giant Planets are Rare at Large Separations, *Astrophysical Journal* **674**, 466–481.

Nikolajeff, F. K. & Karlsson, M., 2003, Diamond micro-optics, in *Lithographic and Micromachining Techniques for Optical Component Fabrication II* (E.-B. Kley & H. P. Herzig, eds.), *Proceedings of the Society of Photo-Optical Instrumentation Engineers (SPIE) Conference Series*, vol. 5183, 56–60.

Nikolajeff, F. K. & Karlsson, M., 2004, Diamond optics: fabrication and applications, in *Micromachining Technology for Micro-Optics and Nano-Optics II* (E. G. Johnson & G. P. Nordin, eds.), *Proceedings of the Society of Photo-Optical Instrumentation Engineers (SPIE) Conference Series*, vol. 5347, 38–43.

Nisenson, P. & Papaliolios, C., 2001, Detection of Earth-like Planets Using Apodized Telescopes, *Astrophysical Journal, Letters* **548**, L201–L205.

Nishikawa, J., Abe, L., Murakami, N. & Kotani, T., 2008, Precise wavefront correction with an unbalanced nulling interferometer for exo-planet imaging coronagraphs, *Astron. & Astrophys.* **489**, 1389–1398.

Niv, A., Biener, G., Kleiner, V. & Hasman, E., 2006, Manipulation of the Pancharatnam phase in vectorial vortices, *Optics Express* **14**, 4208–4220.

Niv, A., Biener, G., Kleiner, V. & Hasman, E., 2007, Polychromatic vectorial vortex formed by geometric phase elements, *Optics Letters* **32**, 847–849.

Nordin, G. P. & Deguzman, P. C., 1999, Broadband form birefringent quarter-wave plate for the mid-infrared wavelength region, *Optics Express* **5**, 163–168.

Olson, D. W., 2010, Diamond, Industrial, in *2010 Minerals Yearbook*, U.S. Geological Survey.

Oppenheimer, B. R., Baranec, C., Beichman, C. et al., 2013, Reconnaissance of the HR8799 Exosolar System. I. Near-infrared Spectroscopy, *Astrophysical Journal* **768**, 24.

Oppenheimer, B. R., Beichman, C., Brenner, D. et al., 2012, Project 1640: the world's first ExAO coronagraphic hyperspectral imager for comparative planetary science, in *Adaptive Optics Systems III* (B. L. Ellerbroek, E. Marchetti & J.-P. Véran, eds.), *Proceedings of the Society of Photo-Optical Instrumentation Engineers (SPIE) Conference Series*, vol. 8447, 844720–13.

Palacios, D. M., 2005, An optical vortex coronagraph, in *Techniques and Instrumentation for Detection of Exoplanets II* (D. R. Coulter, ed.), *Proceedings of the Society of Photo-Optical Instrumentation Engineers (SPIE) Conference Series*, vol. 5905, 196–205.

Palmer, C., 2000, *Diffraction grating handbook*, Richardson grating laboratory, New York.

Pancharatnam, S., 1955, Achromatic combinations of birefringent plates - Part II. An achromatic quarter wave plate, in *Proceedings of the Indian Academy of Science, Section A*, vol. 42, 24–31.

Pancharatnam, S., 1956, Generalized theory of interference and its applications, in *Proceedings of the Indian Academy of Science, Section A*, vol. 44, 247–262.

Paresce, F. & Burrows, C., 1986, Multi-color, High Spatial Resolution Imaging of the Beta Pictoris Circumstellar Disk, in *Bulletin of the American Astronomical Society*, *Bulletin of the American Astronomical Society*, vol. 18, 1027.

Paresce, F. & Burrows, C., 1987, Coronography at La Silla - High resolution imaging of faint features near bright objects, *The Messenger* **47**, 43–46.

Peck Jr, H., 1968, Energy-coupling mechanisms in chemolithotrophic bacteria., *Annu Rev Microbiol* **22**.

Pepe, F., Lovis, C., Ségransan, D. et al., 2011, The HARPS search for Earth-like planets in the habitable zone. I. Very low-mass planets around <ASTROBJ>HD 20794</ASTROBJ>, <ASTROBJ>HD 85512</ASTROBJ>, and <ASTROBJ>HD 192310</ASTROBJ>, *Astron. & Astrophys.* **534**, A58.

Petit, R., 1980, Electromagnetic Theory of Gratings, *Topics in Current Physics, Springer Berlin Heidelberg* **22**.

Petit, R. & Cadilhac, M., 1990, Electromagnetic theory of gratings: some advances and some comments on the use of the operator formalism, *Journal of the Optical Society of America A* **7**, 1666–1674.

Pilon, L., 2002, *Interfacial and transport phenomena in closed-cell foams*, Ph.D. thesis, Purdue University.

Piron, P., 2009, Banc polarimétrique de mesure de masques de phase pour la coronographie, Diploma thesis, Université de Liège.

Pisarenco, M., Maubach, J., Setija, I. & Mattheij, R., 2011, Modified S-matrix algorithm for the aperiodic Fourier modal method in contrast-field formulation, *Journal of the Optical Society of America A* **28**, 1364.

Plotnichenko, V., 2000, Hydroxyl groups in high-purity silica glass, *Journal of Non Crystalline Solids* **261**, 186–194.

Pluzhnik, E. A., Guyon, O., Ridgway, S. T. et al., 2005, Exoplanet Imaging with a Phase-induced Amplitude Apodization Coronagraph III. Hybrid Approach: Optical Design and Diffraction Analysis, *ArXiv Astrophysics e-prints* .

Pollack, J. B., 1984, Origin and History of the Outer Planets: Theoretical Models and Observations L Contraints, *Annual Review of Astron. & Astrophys.* **22**, 389–424.

Pollack, J. B., Hubickyj, O., Bodenheimer, P. et al., 1996, Formation of the Giant Planets by Concurrent Accretion of Solids and Gas, *Icarus* **124**, 62–85.

Pommet, D. A., Moharam, M. G. & Grann, E. B., 1994, Limits of scalar diffraction theory for diffractive phase elements, *Journal of the Optical Society of America A* **11**, 1827–1834.

Popova, S. I., Tolstykh, T. S. & Vorobev, V. T., 1972, Optical characteristics of amorphous quartz in the 1400-200 cm^{-1} region, *Opt. Spectrosc.* **33**, 444–445.

Quanz, S. P., Kenworthy, M. A., Meyer, M. R. et al., 2011, Searching for Gas Giant Planets on Solar System Scales: VLT NACO/APP Observations of the Debris Disk Host Stars HD172555 and HD115892, *Astrophysical Journal, Letters* **736**, L32.

Quanz, S. P., Lafrenière, D., Meyer, M. R. et al., 2012, Direct imaging constraints on planet populations detected by microlensing, *Astron. & Astrophys.* **541**, A133.

Quanz, S. P., Meyer, M. R., Kenworthy, M. A. et al., 2010, First Results from Very Large Telescope NACO Apodizing Phase Plate: 4 μm Images of The Exoplanet β Pictoris b, *Astrophysical Journal, Letters* **722**, L49–L53.

Queloz, D., Anderson, D., Collier Cameron, A. et al., 2010, WASP-8b: a retrograde transiting planet in a multiple system, *Astron. & Astrophys.* **517**, L1.

Quirrenbach, A., 2005, Coronographic Methods for the Detection of Terrestrial Planets, *ArXiv Astrophysics e-prints* .

Quirrenbach, A., 2009, Characterizing Other Earths: Why and How, in *Bioastronomy 2007: Molecules, Microbes and Extraterrestrial Life* (K. J. Meech, J. V. Keane, M. J. Mumma, J. L. Siefert & D. J. Werthimer, eds.), *Astronomical Society of the Pacific Conference Series*, vol. 420, 361.

Racine, R., 2006, The Strehl Efficiency of Adaptive Optics Systems, *Publ. of the Astron. Soc. Pac.* **118**, 1066–1075.

Racine, R., Walker, G. A. H., Nadeau, D. et al., 1999, Speckle Noise and the Detection of Faint Companions, *Publ. of the Astron. Soc. Pac.* **111**, 587–594.

Refsdal, S., 1964, On the possibility of determining Hubble's parameter and the masses of galaxies from the gravitational lens effect, *Mon. Not. of the Royal Astron. Soc.* **128**, 307.

Refsdal, S. & Surdej, J., 1994, Gravitational lenses, *Reports on Progress in Physics* **57**, 117–185.

Renn, J., Sauer, T. & Stachel, J., 1997, The origin of gravitational lensing: a postscript to Einstein's 1936 Science paper., *Science* **275**, 184–186.

Riaud, P., Boccaletti, A., Baudrand, J. & Rouan, D., 2003, The Four-Quadrant Phase-Mask Coronagraph. III. Laboratory performance, *Publ. of the Astron. Soc. Pac.* **115**, 712–719.

Riaud, P., Boccaletti, A., Rouan, D. et al., 2001, The Four-Quadrant Phase-Mask Coronagraph. II. Simulations, *Publ. of the Astron. Soc. Pac.* **113**, 1145–1154.

Riaud, P. & Hanot, C., 2010, Combining Coronagraphy with Interferometry as a Tool for Measuring Stellar Diameters, *Astrophysical Journal* **719**, 749–762.

Riaud, P., Mawet, D., Absil, O. et al., 2006, Coronagraphic imaging of three weak-line T Tauri stars: evidence of planetary formation around PDS 70, *Astron. & Astrophys.* **458**, 317–325.

Riccardi, A., Xompero, M., Briguglio, R. et al., 2010, The adaptive secondary mirror for the Large Binocular Telescope: optical acceptance test and preliminary on-sky commissioning results, in *Adaptive Optics Systems II* (B. L. Ellerbroek, M. Hart, N. Hubin & P. L. Wizinowich, eds.), *Proceedings of the Society of Photo-Optical Instrumentation Engineers (SPIE) Conference Series*, vol. 7736.

Ricci, D., Le Coroller, H. & Labeyrie, A., 2009, Extreme coronagraphy with an adaptive hologram. Simulations of exo-planet imaging, *Astron. & Astrophys.* **503**, 301–308.

Ricci, D., Le Coroller, H., Labeyrie, A. & Piron, P., 2010, Simulations of coronagraphy with a dynamic hologram for the direct detection of exo-planets, in *Space Telescopes and Instrumentation 2010: Optical, Infrared, and Millimeter Wave* (M. C. Clampin, H. A. MacEwen & J. M. Oschmann, Jr., eds.), *Proceedings of the Society of Photo-Optical Instrumentation Engineers (SPIE) Conference Series*, vol. 7731, 77314X–5.

Roddier, F. & Roddier, C., 1997, Stellar Coronograph with Phase Mask, *Publ. of the Astron. Soc. Pac.* **109**, 815–820.

Rouan, D., Baudrand, J., Boccaletti, A. et al., 2007, The Four Quadrant Phase Mask Coronagraph and its avatars, *Comptes Rendus Physique* **8**, 298–311.

Rouan, D., Riaud, P., Boccaletti, A. et al., 2000, The Four-Quadrant Phase-Mask Coronagraph. I. Principle, *Publ. of the Astron. Soc. Pac.* **112**, 1479–1486.

Rousset, G., Fontanella, J. C., Kern, P. et al., 1990, First diffraction-limited astronomical images with adaptive optics, *Astron. & Astrophys.* **230**, L29–L32.

Rousset, G., Lacombe, F., Puget, P. et al., 2003, NAOS, the first AO system of the VLT: on-sky performance, in *Adaptive Optical System Technologies II* (P. L. Wizinowich & D. Bonaccini, eds.), *Proceedings of the Society of Photo-Optical Instrumentation Engineers (SPIE) Conference Series*, vol. 4839, 140–149.

Sagan, C., Thompson, W. R., Carlson, R. et al., 1993, A search for life on Earth from the Galileo spacecraft, *Nature* **365**, 715–721.

Sasselov, D. D. & Lecar, M., 2000, On the Snow Line in Dusty Protoplanetary Disks, *Astrophysical Journal* **528**, 995–998.

Schirmer, J. & Schmidt-Kaler, T., 2000, Liquid crystal phase retarder with broad spectral range, *Optics Communications* **176**, 313–317.

Schneider, G., Silverstone, M. D. & Hines, D. C., 2005, Discovery of a Nearly Edge-on Disk around HD 32297, *Astrophysical Journal, Letters* **629**, L117–L120.

Schneider, G., Wood, K., Silverstone, M. D. et al., 2003, NICMOS Coronagraphic Observations of the GM Aurigae Circumstellar Disk, *Astronomical Journal* **125**, 1467–1479.

Schneider, J., 2013, The Extrasolar Planet Encyclopedia, http://www.exoplanet.eu.

Schneider, J., Boccaletti, A., Mawet, D. et al., 2009, Super earth explorer: a coronagraphic off-axis space telescope, *Experimental Astronomy* **23**, 357–377.

Schneider, J., Riaud, P., Tinetti, G. et al., 2006, SEE-COAST: The Super-Earth Explorer, in *SF2A-2006: Semaine de l'Astrophysique Francaise* (D. Barret, F. Casoli, G. Lagache, A. Lecavelier & L. Pagani, eds.), 429.

Selsis, F., Despois, D. & Parisot, J.-P., 2002, Signature of life on exoplanets: Can Darwin produce false positive detections?, *Astron. & Astrophys.* **388**, 985–1003.

Selsis, F., Kasting, J. F., Levrard, B. et al., 2007, Habitable planets around the star Gliese 581?, *Astron. & Astrophys.* **476**, 1373–1387.

Serabyn, E., 2009, High-contrast, Narrow-field Exoplanet Imaging with a Multi-aperture Telescope Phased-array Coronagraph, *Astrophysical Journal* **697**, 1334–1340.

Serabyn, E., Mawet, D., Bloemhof, E. et al., 2009, Imaging Faint Brown Dwarf Companions Close to Bright Stars with a Small, Well-corrected Telescope Aperture, *Astrophysical Journal* **696**, 40–46.

Serabyn, E., Mawet, D. & Burruss, R., 2010, An image of an exoplanet separated by two diffraction beamwidths from a star, *Nature* **464**, 1018–1020.

Serabyn, E., Mawet, D., Wallace, J. K. et al., 2011, Recent progress in vector vortex coronagraphy, in *UV/Optical/IR Space Telescopes and Instruments: Innovative Technologies and Concepts V* (L. Tsakalakos, ed.), *Proceedings of the Society of Photo-Optical Instrumentation Engineers (SPIE) Conference Series*, vol. 8146, 81460L–8.

Shaklan, S. B. & Green, J. J., 2005, Low-Order Aberration Sensitivity of Eighth-Order Coronagraph Masks, *Astrophysical Journal* **628**, 474–477.

Shectman, S. & Johns, M., 2010, GMT overview, in *Ground-based and Airborne Telescopes III* (L. M. Stepp, R. Gilmozzi & H. J. Hall, eds.), *Proceedings of the Society of Photo-Optical Instrumentation Engineers (SPIE) Conference Series*, vol. 7733.

Sheng, P., 1982, Boundary-layer phase transition in nematic liquid crystals, *Phys. Rev. A* **26**, 1610–1617.

Sheng, P., Stepleman, R. S. & Sanda, P. N., 1982, Exact eigenfunctions for square-wave gratings: Application to diffraction and surface-plasmon calculations, *Phys. Rev. B* **26**, 2907–2916.

Shimoda, S., Kubota, T. & Nakatani, I., 2004, Attitude control of two-wheel-satellite using riemannian geometry, in *Proceedings of the AIAA Guidance, Navigation, and Control Conference*.

Silvotti, R., Schuh, S., Janulis, R. et al., 2007, A giant planet orbiting the 'extreme horizontal branch' star V391 Pegasi, *Nature* **449**, 189–191.

Simard, L., Crampton, D., Ellerbroek, B. & Boyer, C., 2010, The TMT instrumentation program, in *Ground-based and Airborne Instrumentation for Astronomy III* (I. S. McLean, S. K. Ramsay & H. Takami, eds.), *Proceedings of the Society of Photo-Optical Instrumentation Engineers (SPIE) Conference Series*, vol. 7735, 773523–12.

Sivaramakrishnan, A. & Lloyd, J. P., 2005, Spiders in Lyot Coronagraphs, *Astrophysical Journal* **633**, 528–533.

Sivaramakrishnan, A., Soummer, R., Sivaramakrishnan, A. V. et al., 2005, Low-Order Aberrations in Band-limited Lyot Coronagraphs, *Astrophysical Journal* **634**, 1416–1422.

Sivaramakrishnan, A., Tuthill, P. G., Ireland, M. J. et al., 2010, Planetary System and Star Formation Science with Non-Redundant Masking on JWST, in *American Astronomical Society Meeting Abstracts #215*, *Bulletin of the American Astronomical Society*, vol. 42, #380.06.

Skrutskie, M. F., Jones, T., Hinz, P. et al., 2010, The Large Binocular Telescope mid-infrared camera (LMIRcam): final design and status, in *Ground-based and Airborne Instrumentation for Astronomy III* (I. S. McLean, S. K. Ramsay & H. Takami, eds.), *Proceedings of the Society of Photo-Optical Instrumentation Engineers (SPIE) Conference Series*, vol. 7735, 77353H–11.

Slepian, D., 1965, Analytic Solution of Two Apodization Problems, *Journal of the Optical Society of America (1917-1983)* **55**, 1110.

Smith, A., Bailey, J., Hough, J. H. & Lee, S., 2009, An investigation of lucky imaging techniques, *Mon. Not. of the Royal Astron. Soc.* **398**, 2069–2073.

Smith, B. A. & Terrile, R. J., 1984, A circumstellar disk around Beta Pictoris, *Science* **226**, 1421–1424.

Smith, W. H., 1987, Spectral differential imaging detection of planets about nearby stars, *Publ. of the Astron. Soc. Pac.* **99**, 1344–1353.

Sneddon, I. N., 1951, *Fourier Transforms*, McGraw-Hill, New York.

Snik, F., Otten, G., Kenworthy, M. et al., 2012, The vector-APP: a broadband apodizing phase plate that yields complementary PSFs, in *Modern Technologies in Space- and Ground-based Telescopes and Instrumentation II* (R. Navarro, C. R. Cunningham & E. Prieto, eds.), *Proceedings of the Society of Photo-Optical Instrumentation Engineers (SPIE) Conference Series*, vol. 8450, 84500M–11.

Solli, D. R., McCormick, C. F. & Hickmann, J. M., 2006, Polarization-Dependent Reflective Dispersion Relations of Photonic Crystals for Waveplate Mirror Construction, *Journal of Lightwave Technology* **24**, 3864–3867.

Soummer, R., 2005, Apodized Pupil Lyot Coronagraphs for Arbitrary Telescope Apertures, *Astrophysical Journal, Letters* **618**, L161–L164.

Soummer, R., Aime, C. & Falloon, P. E., 2003a, Stellar coronagraphy with prolate apodized circular apertures, *Astron. & Astrophys.* **397**, 1161–1172.

Soummer, R., Dohlen, K. & Aime, C., 2003b, Achromatic dual-zone phase mask stellar coronagraph, *Astron. & Astrophys.* **403**, 369–381.

Soummer, R., Ferrari, A., Aime, C. & Jolissaint, L., 2007, Speckle Noise and Dynamic Range in Coronagraphic Images, *Astrophysical Journal* **669**, 642–656.

Soummer, R., Pueyo, L., Ferrari, A. et al., 2009, Apodized Pupil Lyot Coronagraphs for Arbitrary Apertures. II. Theoretical Properties and Application to Extremely Large Telescopes, *Astrophysical Journal* **695**, 695–706.

Soummer, R., Pueyo, L. & Larkin, J., 2012, Detection and Characterization of Exoplanets and Disks Using Projections on Karhunen-Loève Eigenimages, *Astrophysical Journal, Letters* **755**, L28.

Spiegel, D. S. & Burrows, A., 2012, Spectral and Photometric Diagnostics of Giant Planet Formation Scenarios, *Astrophysical Journal* **745**, 174.

Spyromilio, J., Comerón, F., D'Odorico, S. et al., 2008, Progress on the European Extremely Large Telescope, *The Messenger* **133**, 2–8.

Sudarsky, D., Burrows, A. & Hubeny, I., 2003, Theoretical Spectra and Atmospheres of Extrasolar Giant Planets, *Astrophysical Journal* **588**, 1121–1148.

Sumi, T., Kamiya, K., Bennett, D. P. et al., 2011, Unbound or distant planetary mass population detected by gravitational microlensing, *Nature* **473**, 349–352.

Surdej, J., Absil, O., Bartczak, P. et al., 2006a, The 4m international liquid mirror telescope (ILMT), in *Ground-based and Airborne Telescopes* (L. M. Stepp, ed.), *Proceedings of the Society of Photo-Optical Instrumentation Engineers (SPIE) Conference Series*, vol. 6267, 626704–10.

Surdej, J., Claeskens, J.-F., Delacroix, C. et al., 2008, Gravitational Lensing, Dark Matter and the Optical Gravitational Lens Experiment, in *Hadronic Physics: Joint Meeting Heidelberg-Liège-Paris-Wroclaw – HLPW 2008* (J. Cugon, J.-P. Lansberg & N. Matagne, eds.), *Proceedings of the American Institute of Physics (AIP) Conference Series*, vol. 1038, 173–182.

Surdej, J., Claeskens, J.-F. & Sluse, D., 2006b, Gravitational lensing and anomalous redshifts, in *Current Issues in Cosmology* (J.-C. Pecker & J. Narlikar, eds.), 223–233, Cambridge University Press, Cambridge.

Surdej, J., Delacroix, C., Coleman, P. et al., 2010, The Optimal Gravitational Lens Telescope, *Astronomical Journal* **139**, 1935–1941.

Surdej, J., Magain, P., Swings, J.-P. et al., 1987, A new case of gravitational lensing, *Nature* **329**, 695.

Surdej, J., Refsdal, S. & Pospieszalska-Surdej, A., 1993, The optical gravitational lens experiment, in *Liège International Astrophysical Colloquia* (J. Surdej, D. Fraipont-Caro, E. Gosset, S. Refsdal & M. Remy, eds.), vol. 31, 199.

Surdej, J. & Surdej, A., 2001, Les mirages gravitationnels-IV, *Le Ciel* **63**, 21–26.

Susskind, L., 2008, *The Black Hole War: My Battle with Stephen Hawking to Make the World Safe for Quantum Mechanics*, Little, Brown and Company, New York.

Suyu, S. H., Marshall, P. J., Hobson, M. P. & Blandford, R. D., 2006, A Bayesian analysis of regularized source inversions in gravitational lensing, *Mon. Not. of the Royal Astron. Soc.* **371**, 983–998.

Swanson, G. J., 1989, Binary optics technology: The theory and design of multi-level diffractive optical elements, *Tech. rep.*, Instituto de Astronomía, México.

Swartzlander, G. A., Jr., 2009, The optical vortex coronagraph, *Journal of Optics A: Pure and Applied Optics* **11**(9), 094022.

Swartzlander, G. A., Jr., Ford, E. L., Abdul-Malik, R. et al., 2007, Advancements of the optical vortex coronagraph, in *Techniques and Instrumentation for Detection of Exoplanets III* (D. R. Coulter, ed.), *Proceedings of the Society of Photo-Optical Instrumentation Engineers (SPIE) Conference Series*, vol. 6693, 669311–6.

Swartzlander, G. A., Jr., Ford, E. L., Abdul-Malik, R. S. et al., 2008, Astronomical demonstration of an optical vortex coronagraph, *Optics Express* **16**, 10200.

Szeto, K., Roberts, S., Gedig, M. et al., 2008, TMT telescope structure system: design and development progress report, in *Ground-based and Airborne Telescopes II* (L. M. Stepp & R. Gilmozzi, eds.), *Proceedings of the Society of Photo-Optical Instrumentation Engineers (SPIE) Conference Series*, vol. 7012, 70122G–12.

Tamura, M., Hodapp, K., Takami, H. et al., 2006, Concept and science of HiCIAO: high contrast instrument for the Subaru next generation adaptive optics, in *Ground-based and Airborne Instrumentation for Astronomy* (I. S. McLean & M. Iye, eds.), *Proceedings of the Society of Photo-Optical Instrumentation Engineers (SPIE) Conference Series*, vol. 6269, 62690V–9.

Tanner, A. M., Gelino, C. R. & Law, N. M., 2010, A High-Contrast Imaging Survey of SIM Lite Planet Search Targets, *Publ. of the Astron. Soc. Pac.* **122**, 1195–1206.

Thalmann, C., Carson, J., Janson, M. et al., 2009, Discovery of the Coldest Imaged Companion of a Sun-like Star, *Astrophysical Journal, Letters* **707**, L123–L127.

Thalmann, C., Grady, C. A., Goto, M. et al., 2010, Imaging of a Transitional Disk Gap in Reflected Light: Indications of Planet Formation Around the Young Solar Analog LkCa 15, *Astrophysical Journal, Letters* **718**, L87–L91.

Thalmann, C., Janson, M., Buenzli, E. et al., 2013, Imaging Discovery of the Debris Disk around HIP 79977, *Astrophysical Journal, Letters* **763**, L29.

Théret, N., Aubrun, J.-F., Lassalle-Balier, G. et al., 2008, GAME: Guidance with Avoidance During Maneuver Elaboration, in *AAS/AIAA Astrodynamics Conference 2007* (R. J. Proulx & T. F. Starchville, Jr., eds.), *Proceedings of the Advances in the Astronautical Sciences Conference Series*, vol. 129, 2275–2294.

Thomas, M. E. & Tropf, W. J., 1994, Optical properties of diamond, in *Window and Dome Technologies and Materials IV* (P. Klocek, ed.), *Proceedings of the Society of Photo-Optical Instrumentation Engineers (SPIE) Conference Series*, vol. 2286, 144–151.

Todorov, K., Luhman, K. L. & McLeod, K. K., 2010, Discovery of a Planetary-mass Companion to a Brown Dwarf in Taurus, *Astrophysical Journal, Letters* **714**, L84–L88.

Touloukian, Y. S. & DeWitt, D. P., 1972, *Thermal properties of matter: Radiative, Thermal radiative properties of nonmetallic solids*, vol. 8, IFI/Plenum, New York.

Träger, F., 2012, *Springer Handbook of Lasers and Optics*, Springer.

Traub, W. A. & Vanderbei, R. J., 2003, Two-Mirror Apodization for High-Contrast Imaging, *Astrophysical Journal* **599**, 695–701.

Trauger, J., Moody, D., Gordon, B. et al., 2012, Complex apodization Lyot coronagraphy for the direct imaging of exoplanet systems: design, fabrication, and laboratory demonstration, in *Space Telescopes and Instrumentation 2012: Optical, Infrared, and Millimeter Wave* (M. C. Clampin, G. G. Fazio, H. A. MacEwen & J. M. Oschmann, Jr., eds.), *Proceedings of the Society of Photo-Optical Instrumentation Engineers (SPIE) Conference Series*, vol. 8442, 84424Q–13.

Trauger, J. T., 2000, High Contrast Coronagraphic Imaging with NGST, in *Next Generation Space Telescope Science and Technology* (E. Smith & K. Long, eds.), *Astronomical Society of the Pacific Conference Series*, vol. 207, 165.

Trauger, J. T., 2009, Direct detection: Seeking exoplanet colors and spectra, in *Innovative Approaches to Exoplanet Spectra*, Keck Institute for Space Studies Workshop.

Trauger, J. T., Stapelfeldt, K., Traub, W. et al., 2009, ACCESS – A Science and Engineering Assessment of Space Coronagraph Concepts for the Direct Imaging and Spectroscopy of Exoplanetary Systems, in *American Astronomical Society Meeting Abstracts #213*, *Bulletin of the American Astronomical Society*, vol. 41, #493.01.

Trauger, J. T. & Traub, W. A., 2007, A laboratory demonstration of the capability to image an Earth-like extrasolar planet, *Nature* **446**, 771–773.

Tropf, W. J., 1995, Temperature-dependent refractive index models for BaF2, CaF2, MgF2, SrF2, LiF, NaF, KCl, ZnS, and ZnSe, *Optical Engineering* **34**, 1369–1373.

Tuomi, M., 2011, Bayesian re-analysis of the radial velocities of Gliese 581. Evidence in favour of only four planetary companions, *Astron. & Astrophys.* **528**, L5.

Tuomi, M., Anglada-Escudé, G., Gerlach, E. et al., 2013a, Habitable-zone super-Earth candidate in a six-planet system around the K2.5V star HD 40307, *Astron. & Astrophys.* **549**, A48.

Tuomi, M., Jones, H. R. A., Jenkins, J. S. et al., 2013b, Signals embedded in the radial velocity noise. Periodic variations in the τ Ceti velocities, *Astron. & Astrophys.* **551**, A79.

Turner, N. H., ten Brummelaar, T. A., Roberts, L. C. et al., 2008, Adaptive Optics Photometry and Astrometry of Binary Stars. III. a Faint Companion Search of O-Star Systems, *Astronomical Journal* **136**, 554–565.

Udalski, A., 2003, The Optical Gravitational Lensing Experiment. Real Time Data Analysis Systems in the OGLE-III Survey, *Acta Astron.* **53**, 291–305.

Udalski, A., Pietrzynski, G., Szymanski, M. et al., 2003, The Optical Gravitational Lensing Experiment. Additional Planetary and Low-Luminosity Object Transits from the OGLE 2001 and 2002 Observational Campaigns, *Acta Astron.* **53**, 133–149.

Vanderbei, R. J., 2006, Diffraction Analysis of Two-dimensional Pupil Mapping for High-Contrast Imaging, *Astrophysical Journal* **636**, 528–543.

Vanderbei, R. J. & Traub, W. A., 2005, Pupil Mapping in Two Dimensions for High-Contrast Imaging, *Astrophysical Journal* **626**, 1079–1090.

Vandormael, D., Habraken, S. & Collette, J.-P., 2001, Diffractive microprism architecture for color fan-out beam splitter, in *Gradient Index, Miniature, and Diffractive Optical Systems II* (T. J. Suleski, ed.), *Proceedings of the Society of Photo-Optical Instrumentation Engineers (SPIE) Conference Series*, vol. 4437, 142–148.

Vandormael, D., Habraken, S., Loicq, J. et al., 2006, Anti-reflective sub-wavelength patterning of IR optics, in *Electro-Optical and Infrared Systems: Technology and Applications III* (R. G. Driggers & D. A. Huckridge, eds.), *Proceedings of the Society of Photo-Optical Instrumentation Engineers (SPIE) Conference Series*, vol. 6395, 63950L–7.

Vigan, A., Langlois, M., Moutou, C. & Dohlen, K., 2008, Exoplanet characterization with long slit spectroscopy, *Astron. & Astrophys.* **489**, 1345–1354.

Vigan, A., Patience, J., Marois, C. et al., 2012, The International Deep Planet Survey. I. The frequency of wide-orbit massive planets around A-stars, *Astron. & Astrophys.* **544**, A9.

Wagner, W. J., Hansen, R. T. & Hansen, S. F., 1974, Coronal Disturbances. II: The Fast Rearrangement of Coronal Magnetic Fields, *Sol. Phys.* **34**, 453–459.

Wald, G., 1964, The Origins of Life, *Proceedings of the National Academy of Science* **52**, 595–611.

Walsh, D., Carswell, R. F. & Weymann, R. J., 1979, 0957 + 561 A, B - Twin quasistellar objects or gravitational lens, *Nature* **279**, 381–384.

Wertz, J. R., 1997, *Spacecraft Attitude Determination and Control*, Kluwer Academic Publishers, Netherlands.

Whelan, E. & Garcia, P., 2008, Spectro-astrometry: The Method, its Limitations, and Applications, in *Jets from Young Stars II* (F. Bacciotti, L. Testi & E. Whelan, eds.), *Lecture Notes in Physics, Berlin Springer Verlag*, vol. 742, 123.

Williams, D. M. & Pollard, D., 2002, Earth-like worlds on eccentric orbits: excursions beyond the habitable zone, *International Journal of Astrobiology* **1**, 61–69.

Wolszczan, A. & Frail, D. A., 1992, A planetary system around the millisecond pulsar PSR1257 + 12, *Nature* **355**, 145–147.

Yang, W. & Kostinski, A. B., 2004, One-sided Achromatic Phase Apodization for Imaging of Extrasolar Planets, *Astrophysical Journal* **605**, 892–901.

Zolotarev, V. M., 1970, The optical constants of amorphous SiO_2 and GeO_2 in the valence band region, *Opt. Spectrosc.* **29**, 34–37.

Résumé

Ces vingt dernières années, les détections de planètes extrasolaires se sont multipliées de manière exponentielle pour atteindre près de 900 exoplanètes confirmées à ce jour. Ce nombre double tous les deux ou trois ans. Les découvertes les plus récentes effectuées par la mission Kepler ont permis de révéler deux exoplanètes de tailles similaires à la Terre, orbitant la même étoile, et remplissant toutes les conditions nécessaires pour être habitables. Les techniques d'imagerie ont également fait du chemin. Depuis la première détection directe en 2004, des images incroyables d'exoplanètes ont été capturées au télescope dans des conditions favorables de séparation angulaire et/ou de contraste modéré, grâce à l'apparition et à l'amélioration constante des techniques d'optique adaptative et de réduction de données. Dans ce contexte général, le besoin de techniques d'imagerie à haut contraste et faible séparation angulaire ne s'est jamais avéré aussi criant. La coronographie joue un rôle majeur car elle offre des outils qui rendent possible l'imagerie de planètes de tailles similaires à la Terre, et qui essaient de répondre à l'éternelle question sur la présence éventuelle de vie en dehors du système solaire.

Cette thèse est consacrée au développement du masque de phase à sillons annulaires (AGPM), un type de coronographe achromatique à vortex vectoriel, basé sur les réseaux sub-lambda. Considéré depuis plusieurs années comme une des meilleures solutions pour la construction de coronographes de moyen infrarouge à faibles séparations angulaires, l'AGPM n'a jamais été validé jusqu'à présent. Bien que plusieurs processus de fabrication soient possibles selon les matériaux et les techniques de lithographie envisagées, ils sont souvent soumis à des contraintes extrêmes. Dans ce travail, nous explorons la faisabilité de microcomposants achromatiques à base de réseaux sub-lambda, pour lesquels deux solutions technologiques sont envisagées: le quartz et le diamant. En concentrant nos efforts sur l'option diamant, dont les propriétés uniques en font un candidat de premier choix pour des applications de moyen infrarouge, nous avons réussi à développer des lames demi-onde achromatiques pour le moyen infrarouge, optimisées pour permettre la fabrication de vortex de charge topologique 2. A la suite de cette expérience concluante, nous avons poursuivi nos travaux et fabriqué plusieurs AGPM pour deux fenêtres spectrales astronomiques, les bandes N et L, et nous avons validé avec succès plusieurs AGPM de bande L sur un banc de tests coronographiques, à l'Observatoire de Paris. Dans le dernier chapitre, nous relatons la récente installation de nos composants sur trois caméras infrarouges de renommées mondiales, VISIR et NACO au VLT, au Chili, ainsi que LMIRCam au LBT, en Arizona. Nous terminons par la découverte et l'imagerie d'un compagnon stellaire à deux séparations angulaires d'une étoile de type F.

Mots-clés: planète extrasolaire – imagerie à haut contraste – coronographie à vortex vectoriel – masque de phase à sillons annulaires – lame demi-onde pour le moyen infrarouge – réseau sub-lambda

Abstract

During the past twenty years, detections of extrasolar planets have flourished and grown exponentially, reaching almost 900 confirmed exoplanets so far. This number is doubling every two or three years. The most recent discoveries made by the KEPLER mission have revealed two Earth-size exoplanets orbiting the same star, and fulfilling all the required conditions to be habitable. Imaging techniques have also come a long way. Since the first direct detection in 2004, some stunning exoplanet pictures have been captured at the telescope under special circumstances of moderate contrast and/or angular separation, thanks to the advent and continuous improvement of adaptive optics systems and data reduction methods. In this broad context, the need for high contrast imaging techniques with very small inner working angles has never been so strong. Coronagraphy has a key role to play in order to provide the means necessary for imaging Earth-size planets, and try to answer the recurring question of the possible presence of life outside the solar system.

The present thesis is dedicated to the development of the annular groove phase mask (AGPM), a specific type of broadband vector vortex coronagraph based on subwavelength gratings. Considered for several years as one of the best solutions for building high-performance mid-infrared coronagraphs with small inner working angles, the AGPM has never been validated up to now. Although various fabrication processes are available, depending on the substrates and micro-lithography techniques considered, they often face extremely challenging constraints. In the present work, we explored the feasibility of achromatic micro-components made out of subwavelength gratings, for which two technological solutions are followed: quartz and diamond. As we focussed on the diamond option, its unique material properties making it a prime candidate for mid-infrared applications, we managed to develop mid-infrared broadband half-wave plates, ideally optimized to enable the manufacturing of charge-2 vortices. Following this success, we continued our developments leading to the fabrication of several AGPMs for two astronomic windows, the L and N bands, and we successfully validated several L-band AGPMs on a coronagraphic test bench at the Observatoire de Paris. In the last chapter, we expose the recent installation of our components on three world-class infrared cameras, VISIR and NACO at the Very Large Telescope in Chile, and LMIRCam at the Large Binocular Telescope in Arizona. We conclude with the very first on-sky results of both N-band and L-band AGPMs, and the discovery and successful imaging of a faint stellar companion at two beamwidths from an F-type star.

Keywords: extrasolar planet – high contrast imaging – vector vortex coronagraphy – annular groove phase mask – mid-infrared half-wave plate – subwavelength grating